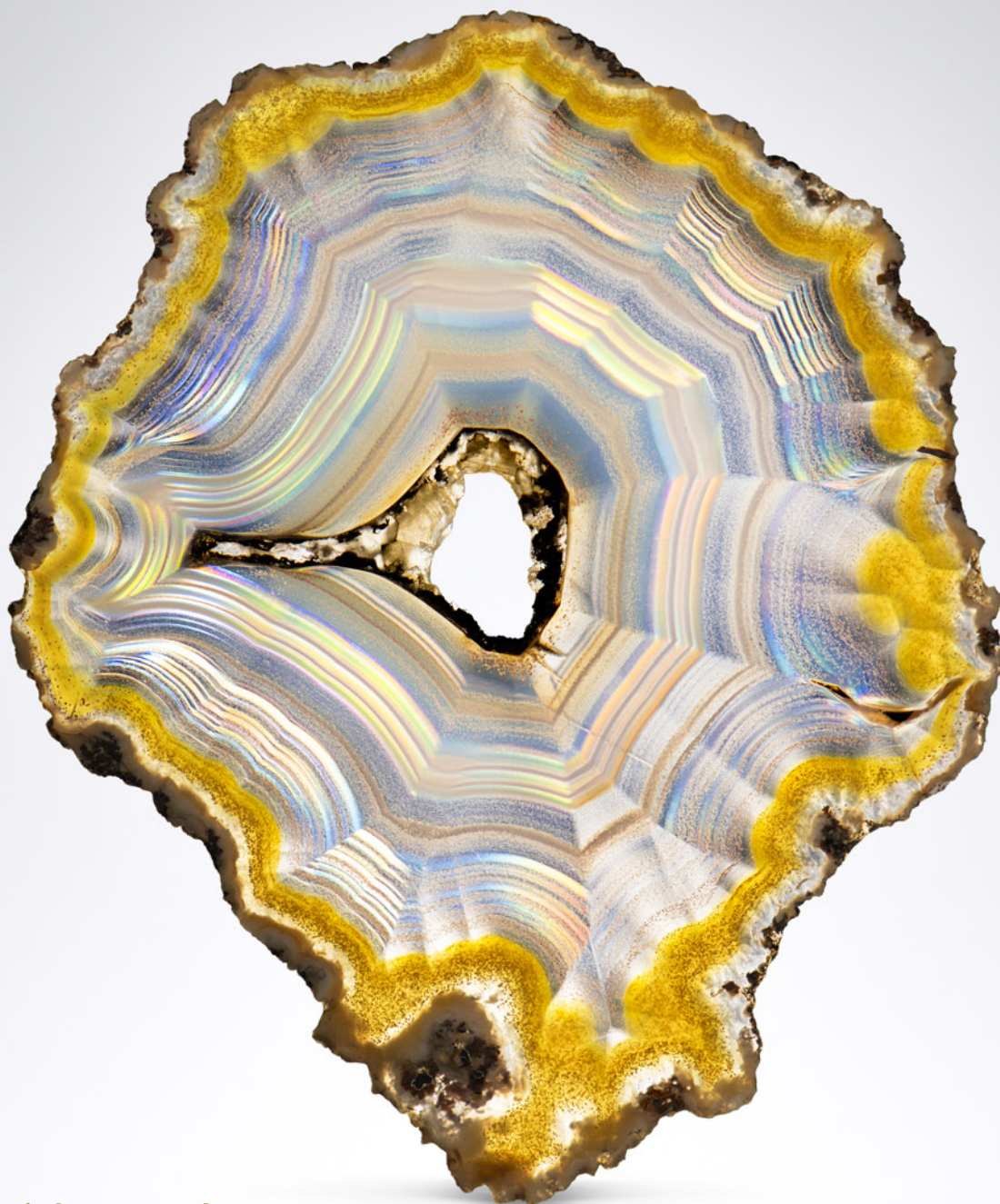


SUMMER 2025

GEMS & GEMOLOGY

VOLUME LXI

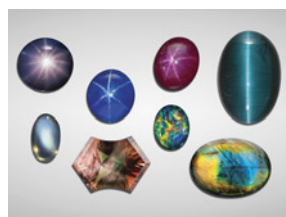


Review of Phenomenal Gemstones

Gem Granitic Pegmatites

Spotlight on Ben Kho

THE QUARTERLY JOURNAL OF THE GEMOLOGICAL INSTITUTE OF AMERICA



p. 111

EDITORIAL

109 The Science of Phenomenal Gems, a Summary of Pegmatites, and a Cutter's Remarkable Journey

Duncan Pay

FEATURE ARTICLE

110 Structures Behind the Spectacle: A Review of Optical Effects in Phenomenal Gemstones and Their Underlying Nanotextures

Shiyun Jin, Nathan D. Renfro, Aaron C. Palke, and James E. Shigley

Provides a comprehensive summary of the special optical effects in gemstones, including opalescence, chatoyancy, asterism, schiller, and iridescence, and investigates the submicron inclusions and nanotextures in each type of phenomenal stone.



p. 186

REGULAR FEATURES

172 Lab Notes

Unusual patterns in diamonds • Gold-plated gold • CVD-grown diamond with unusual cause of greenish color • HPHT-processed natural and laboratory-grown diamonds with counterfeit inscriptions • Three large natural hollow *Pinctada radiata* pearls • Imitation seed pearl with blue X-ray fluorescence • Pezzottaite with multiple cat's-eyes • Quartz assemblage imitating emerald



p. 195

184 G&G Micro-World

Anatase "dandelion" in agate • Diamond within a diamond within a diamond • "Goose bumps" on South Sea pearl • Iridescent pen shell • Colorless danburite crystals in phenakite from Myanmar • Lithiophilite in quartz • Monazite in quartz • Mystery pebbles in quartz • Rutile star in quartz • "Sugar plum" in titanium-diffused blue sapphire • "Soap bubbles" in yellow sphene • Quarterly Crystal: Unique phantom in diamond

192 Colored Stones Unearthed

Describes the geology, mineralogy, and formation of granitic-composition pegmatites and provides a summary of their worldwide occurrences.

206 Gem News International

Emeralds and beryl from Kazakhstan and Ukraine • Unique trapiche grossular from China • GIA 7 Pearl Value Factors: An update on nacre classification • Exceptional nacre thickness of hybrid akoya bead cultured pearls • Iridescent gems cut from hinge ligament of South Sea pearl oyster • Neptunite inclusions in rare poudretteite • New väyrynenite production from Nigeria • Multilayered laboratory-grown diamond • Diamond trader Ishaia Gol • Diffusion-induced blue spinel-like layer on natural sapphire



p. 224

224 In the Spotlight: Ben Kho: From Rough Beginnings to Brilliant Mastery

Jennifer Stone-Sundberg

Editorial Staff

Editor-in-Chief

Duncan Pay

Editorial Manager

Brooke Goedert

Associate Editor

Erica Zaidman

Senior Technical Editor

Jennifer Stone-Sundberg

Technical Editor

Tao Z. Hsu

Assistant Editor

Erin Hogarth

Editors, Lab Notes

Thomas M. Moses

Shane F. McClure

Sally Eaton-Magaña

Artitaya Homkrajae

Editors, Micro-World

Tyler Smith

John I. Koivula

Nathan Renfro

Editors, Gem News

Gagan Choudhary

Guanghai Shi

Editors, Colored Stones

Unearthed

Aaron C. Palke

James E. Shigley

Editor, Diamond Reflections

Evan M. Smith

Contributing Editors

James E. Shigley

Raquel Alonso-Perez

Editor-in-Chief Emerita

Alice S. Keller

Production Staff

Supervisor, Multimedia

Design

Michael Creighton

Photo/Video Producer

Kevin Schumacher

Video Production

Albert Salvato

Editorial Review Board

Ahmadjan Abduriyim

Tokyo, Japan

Timothy Adams

San Diego, California

James E. Butler

Washington, DC

Alan T. Collins

London, UK

Aurélien Delaunay

Paris, France

Dona Dirlam

Carlsbad, California

Sally Eaton-Magaña

Carlsbad, California

John L. Emmett

Brush Prairie, Washington

Emmanuel Fritsch

Nantes, France

Eloïse Gaillou

Paris, France

Al Gilbertson

Carlsbad, California

Gaston Giuliani

Nancy, France

Lee A. Groat

Vancouver, Canada

Yunbin Guan

Pasadena, California

George Harlow

New York, New York

Peter Heaney

University Park, Pennsylvania

Richard W. Hughes

Bangkok, Thailand

Jaroslav Hyršl

Prague, Czech Republic

Dorrit Jacob

Canberra, Australia

A.J.A. (Bram) Janse

Perth, Australia

Mary L. Johnson

San Diego, California

Robert E. Kane

Helena, Montana

Stefanos Karampelas

Thessaloniki, Greece

Lore Kiefert

Lucerne, Switzerland

Simon Lawson

Maidenhead, UK

Ren Lu

Wuhan, China

Thomas M. Moses

New York, New York

Laura Otter

Canberra, Australia

Aaron C. Palke

Carlsbad, California

Ilene Reinitz

Chicago, Illinois

Nathan Renfro

Carlsbad, California

George R. Rossman

Pasadena, California

Sudarast Saeseaw

Bangkok, Thailand

Karl Schmetzer

Petershausen, Germany

Andy Shen

Wuhan, China

Guanghai Shi

Beijing, China

Elisabeth Strack

Hamburg, Germany

Nicholas Sturman

Bangkok, Thailand

Tim Thomas

Portland, Oregon

D. Brian Thompson

Florence, Alabama

Fanus Viljoen

Johannesburg, South Africa

Wuyi Wang

New York, New York

Christopher M. Welbourn

Reading, UK

Chunhui Zhou

New York, New York

J.C. (Hanco) Zwaan

Leiden, The Netherlands

GEMS & GEMOLOGY®

gia.edu/gems-gemology

Customer Service

(760) 603-4200

gandg@gia.edu



Subscriptions

Copies of the current issue may be purchased for \$29.95 plus shipping. Subscriptions are \$79.99 for one year (4 issues) in the U.S. and \$99.99 elsewhere. Canadian subscribers should add GST. Discounts are available for renewals, group subscriptions, GIA alumni, and current GIA students. To purchase print subscriptions, visit store.gia.edu or contact Customer Service. For institutional rates, contact Customer Service.

Database Coverage

Gems & Gemology's impact factor is 2.6, according to the 2024 Journal Citation Reports by Clarivate Analytics (issued June 2025). *G&G* is abstracted in Thomson Reuters products (Current Contents: Physical, Chemical & Earth Sciences and Science Citation Index—Expanded, including the Web of Knowledge) and other databases. For a complete list of sources abstracting *G&G*, go to gia.edu/gems-gemology, and click on "Publication Information."

Manuscript Submissions

Gems & Gemology, a peer-reviewed journal, welcomes the submission of articles on all aspects of the field. Please see the Author Guidelines at gia.edu/gems-gemology or contact the editors (gandgeditorial@gia.edu). Letters on articles published in *G&G* are also welcome. Please note that Field Reports, Lab Notes, Gem News International, Micro-World, Colored Stones Unearthed, Diamond Reflections, Charts, and In the Spotlight are not peer-reviewed sections but do undergo technical and editorial review.

Copyright and Reprint Permission

Abstracting is permitted with credit to the source. Libraries are permitted to photocopy beyond the limits of U.S. copyright law for private use of patrons. Instructors are permitted to reproduce isolated articles and photographs/images owned by *G&G* for noncommercial classroom use without fee. Use of photographs/images under copyright by external parties is prohibited without the express permission of the photographer or owner of the image, as listed in the credits. For other copying, reprint, or republication permission, please contact the editors.

Gems & Gemology is published quarterly by the Gemological Institute of America, a nonprofit educational organization for the gem and jewelry industry.

Postmaster: Return undeliverable copies of *Gems & Gemology* to GIA, The Robert Mouawad Campus, 5345 Armada Drive, Carlsbad, CA 92008.

Our Canadian goods and service registration number is 126142892RT.

Any opinions expressed in signed articles are understood to be opinions of the authors and not of the publisher.

About the Cover

This issue's feature article reviews special optical effects in gemstones, including iridescence, which is displayed in the 7 x 5.7 mm iris agate slice on the cover. The rainbow color is caused by the interference of light as it passes through the fine banding in the agate. Photo by Kevin Schumacher; gift of the Hauser family, in memory of Joel and Barbara Hauser. On the back cover, another optical effect, chatoyancy, results from structural planes in a cat's-eye zircon from Sri Lanka. Photomicrograph by Nathan Renfro; field of view 1.44 mm.

Printing is by L+L Printers, Carlsbad, CA.

GIA World Headquarters The Robert Mouawad Campus 5345 Armada Drive Carlsbad, CA 92008 USA
© 2025 Gemological Institute of America All rights reserved. ISSN 0016-626X



The Science of Phenomenal Gems, a Summary of Pegmatites, and a Cutter's Remarkable Journey



In 1934, *Gems & Gemology* editor Robert Shipley made two promises to readers in our first issues: to enhance the knowledge and abilities of gem practitioners so they could better protect consumers' best interests, and to supplement the knowledge of gemology students. Our summer issue fits squarely within his vision.

We offer just one feature article on the broad and fascinating topic of phenomenal gems, which aims to deliver everything a practicing gemologist wants to know about these special gems but was afraid to ask. GIA authors Dr. Shiyun Jin, Nathan Renfro, Dr. Aaron Palke, and Dr. James Shigley provide a comprehensive review of gem

materials that display special optical phenomena, including iridescence, schiller, and

"...everything a practicing gemologist wants to know about these special gems but was afraid to ask."

asterism, under specific lighting or viewing conditions. The resolution and wider availability of

modern analytical techniques have enabled scientists to improve their studies of phenomenal gems dramatically. Unfortunately, much of this new knowledge hasn't transferred into the trade, leading to confusion and misinformation. The authors aim to help close the knowledge gap between the practical gemology world and mineralogy and physics research by reviewing scientific investigations into optical processes and submicron textures that cause phenomena. Their paper sorts phenomenal gems by the dimensionality and complexity of their underlying submicron structures and textures. We trust this article, along with its thorough list of references, will become a valuable resource for practitioners, researchers, and students of gemology alike.

To gemologists and mineral collectors, complex pegmatites are a cornucopia of rare elements and therefore may host uncommon minerals and remarkable crystal specimens. *Colored Stones Unearthed* dives into this important gem source.

In the Spotlight profiles the extraordinary life of gem cutter Ben Kho. His journey encompasses entrepreneurial origins as a gem trader and cutter through the adversity of Cambodia's Killing Fields to a fresh start and success in the United States—a unique tale of perseverance and the power of talent. Kho's artistry is exemplified by the award-winning colored gems he's faceted during his exceptional career.

G&G's regular columns provide the latest gemological findings. Noteworthy updates from GIA's laboratories are summarized in *Lab Notes*, including unusual patterns in diamonds composed of dark micro-inclusions, a pezzottaite with multiple cat's-eyes, and a quartz assemblage imitating emerald. *Micro-World's* inner landscapes of gemstones feature "goose bumps" on a South Sea pearl, mystery pebbles in quartz, and a unique phantom crystal in diamond. Finally, highlights from the *Gem News International* section include emerald and beryl from Kazakhstan and Ukraine and unique trapiche grossular from China.

Please enjoy the latest edition of *Gems & Gemology*!

Duncan Pay | Editor-in-Chief | dpay@gia.edu

STRUCTURES BEHIND THE SPECTACLE: A REVIEW OF OPTICAL EFFECTS IN PHENOMENAL GEMSTONES AND THEIR UNDERLYING NANOTEXTURES

Shiyun Jin, Nathan D. Renfro, Aaron C. Palke, and James E. Shigley

This article reviews all of the special optical effects of gemstones, including opalescence, chatoyancy, asterism, schiller, and iridescence. The physics of light scattering, reflection, diffraction, and interference is briefly described for qualitative explanations of these optical phenomena. The most up-to-date microscopic investigations of the submicron inclusions and nanotextures in each type of phenomenal stone, along with their mechanistic interpretations, are also summarized. Although the basic principles behind these phenomena are generally understood, quantitative descriptions that directly connect the optical effects and the submicron structures are still lacking for many of these stones. In addition, the formation mechanisms of some of the textures in phenomenal stones are still debated, if not completely elusive.

This article roughly sorts the optical effects by the dimensionality and complexity of their underlying submicron structures and textures. Zero-dimensional nanoparticles in diamond and corundum, though typically not considered phenomenal gemstones, produce milky or opalescent appearances by scattering light randomly; one-dimensional oriented needle-like inclusions in chrysoberyl and garnet create cat's-eye and star effects; two-dimensional platelets and layers in feldspar produce schiller and iridescence by reflection and interference; and three-dimensional photonic crystals in precious opal cause brilliant play-of-color by Laue and Bragg diffraction. The often-confusing past uses of the phenomenal terminology in the literature are also clarified in this article.

A gem lover might think that all gemstones are phenomenal by definition. However, the term *phenomenal gemstones* designates a specific group of gem materials that display special optical phenomena under certain lighting or viewing conditions (Shipley, 1945), such as iridescence, schiller, and asterism (figure 1). These gems exhibit a wide range of visual effects created by different internal structures of various sizes and shapes, from diffuse scattering of light by randomly oriented particles to highly directional light reflection or diffraction from aligned or periodic textures. These phenomena can

dramatically increase the value of an already valuable stone or even promote an otherwise common mineral into the gemstone category. Phenomenal gemstones substantially diversify the appearances of gemstones beyond the stereotypical sparkling crystals with attractive colors.

The optical effects of phenomenal gemstones reflect fine-scale structures and textures that interact with visible light in intricate ways, and they have drawn the attention of scientists for centuries. However, despite investigations by renowned scientists including David Brewster, C.V. Raman, and Robert Strutt, there is much that we do not understand about phenomenal gemstones, mainly due to the exceptionally small scales of the textures that create the phenomena. Most structures in phenomenal gemstones are internal (unlike the surface coloring structures in the animal kingdom, such as

See end of article for About the Authors and Acknowledgments.

GEMS & GEMOLOGY, Vol. 61, No. 2, pp. 110–170,

<http://dx.doi.org/10.5741/GEMS.61.2.110>

© 2025 Gemological Institute of America

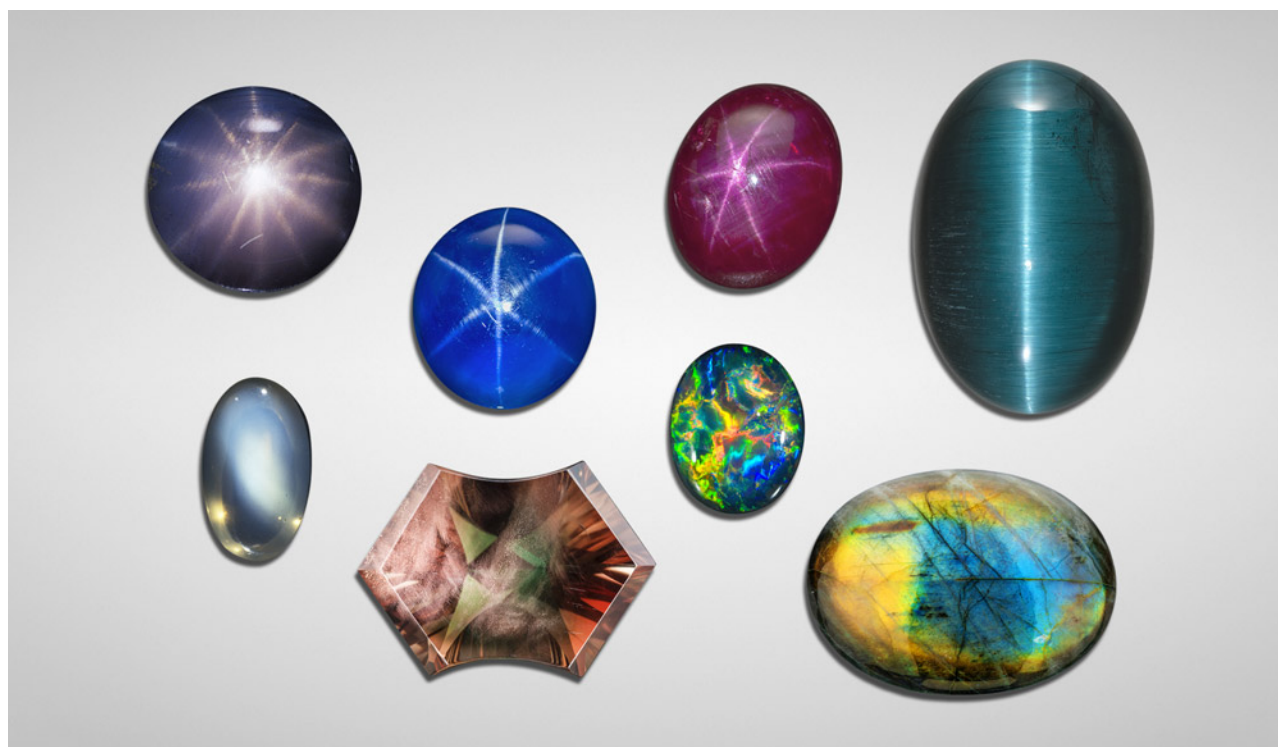


Figure 1. A variety of some of the most common phenomenal gemstones. Top row, left to right: 2.35 ct 12-rayed star sapphire from Sri Lanka, gift of Gordon Bleck, GIA Museum no. 17037; 18.18 ct blue star sapphire, courtesy of Evan Caplan; 18.29 ct star ruby from Myanmar, courtesy of the Natural History Museum of Los Angeles County; 36.76 ct cat's-eye tourmaline from Brazil, courtesy of Pala International. Bottom row, left to right: 7.60 ct moonstone from Sri Lanka; 11.0 ct Oregon sunstone displaying aventurescence over red and green bodycolors; 11.45 ct black opal from Australia displaying vibrant play-of-color; 30.82 ct Finnish labradorite cabochon from GIA's Dr. Edward J. Gübelin collection. Photos by Robert Weldon (six stones on the left) and Orasa Weldon (two stones on the right).

in butterfly wings and bird feathers) and require meticulous sample preparation before they can be studied by advanced imaging techniques such as electron microscopy. In addition, the extremely long geological timescales and complicated crystallization histories that are often required to create these convoluted structures make them challenging, if not impossible, to reproduce through laboratory synthesis.

Fortunately, studies of phenomenal gemstones have dramatically improved in recent decades, mainly due to the development of more advanced analytical techniques with increasing resolution and accessibility (box A). Professional support for these seemingly inconsequential research projects has historically been limited. However, recent studies have proven that the intricate structures are not only exciting to the curious mind, but they also contain important information regarding the geological processes that created them, which is critical to better understand the history of our planet. Moreover, as a flexible, durable, and environmentally friendly

alternative to traditional pigments, colors caused by structural interference have attracted a lot of interest in photonics and material sciences due to their wide

In Brief

- Nanoscale textures and structures in gemstones can create special optical effects that significantly affect their appearances and appeal.
- The dimensionality of the nanotextures in gemstones can range from zero (nanoparticles) to three (photonic crystals), resulting in drastically different optical phenomena.
- The nanotextures can form by many different mechanisms, reflecting the extreme range of thermodynamic conditions exhibited by geological processes.

range of applications in paints, cosmetics, fabrics, color sensors, wearable electronics, and anti-counterfeiting technologies. A better understanding of the

BOX A: ANALYTICAL TECHNIQUES FOR STUDYING PHENOMENAL GEMS

Some analytical techniques commonly used to study the structure of phenomenal stones will be repeatedly mentioned in this article, and it is not possible to fully explain how each one works. For simplicity, the abbreviations used in this article are listed here in order of relevance, along with a brief description of the information each method can provide regarding the analyzed material.

XRD: X-ray diffraction. Mainly used to identify crystalline phases by matching the measured diffraction pattern with known structures in a database. Can be used to refine the details of the crystal structure to reveal the atomic ordering state and the chemical composition of the studied mineral. Also can be used to directly determine the crystal structure of an unknown or new material.

SEM: Scanning electron microscopy. Can image submicron textures that cannot be resolved by an optical microscope, typically on a polished surface of a material. Image contrast reflects the chemical variations in the material. May also reveal textural contrasts on an etched or freshly broken surface.

TEM: Transmission electron microscopy. Can resolve nanoscale textures and even atomic-scale structures. Requires special sample preparation that slices the analyzed material into a very thin foil of less than 100 nm in thickness. Also can create an electron diffraction pattern that can be used to identify the phase and its crystallographic orientation.

EDS: Energy-dispersive X-ray spectroscopy (sometimes abbreviated as EDX). An instrumental component of SEM or TEM that collects the X-ray spectrum excited by a high-energy electron beam, which can be used to map the chemical composition of the material. Quantitative analysis is possible only using well-characterized reference materials.

EPMA: Electron probe microanalysis. Employs the excited X-ray spectrum as in EDS, but with much better precision for quantitative chemical analysis. Well-characterized standard materials are required for quantification.

EBSD: Electron backscatter diffraction. An instrumental component of SEM that collects electron diffraction patterns in the backscattered direction, which can be used to identify the crystalline phases and their relative crystallographic orientations. Has much lower resolution compared to the electron diffraction in TEM but can be used to map a much larger area of a sample for statistical analysis. A database of known material structures is required to match the data for phase identification and orientation determination.

AFM: Atomic force microscopy. Can resolve the surface texture of a material at the nanoscale by scanning the surface with a tiny mechanical probe. The image may look similar to an SEM image, but it contains quantitative information of the surface height, which cannot be acquired from SEM.

APT: Atom probe tomography. A method that can create three-dimensional elemental maps with nanometer resolution, revealing the size, shape, and distribution of tiny clusters, precipitates, or lamellar textures that are smaller than 100 nm. Often used as a complement to TEM.

FIB: Focused ion beam. A method that probes the sample using a high-energy beam of atomic ions (most commonly gallium ions). One of the most important applications of FIB is to prepare TEM and APT samples due to its ability to precisely cut the exact region of interest from the analyzed specimen. The secondary electrons created by FIB can also be used for imaging (similar to SEM), while the secondary ions can be analyzed by mass spectrometry.

submicron structures of minerals may help push the design and manufacture of these colorful materials beyond biomimicry.

Because of the sophistication of these recent studies, the knowledge gap between the gemology world and mineralogy and physics research is widening faster than ever. It is challenging for gemologists and gem consumers to stay current with the latest updates in the scientific literature, which may be filled with jargon and target only a few experts in their respective fields. Certain inaccurate descriptions and incorrect explanations of phenomenal gemstones from outdated publications are some-

times still cited in recent gemological literature. The new studies cannot be blindly trusted either, as many of them have not yet stood the test of time. Speculation without sufficient supporting evidence is another source of misinformation and confusion, with researchers still struggling to draw solid conclusions. Even experts sometimes fall victim to misinformation, and it is not uncommon to find mislabeled specimens of phenomenal gemstones in famous gem and mineral museums. Misinterpretation of data acquired using advanced techniques is also quite common, as they often exist in abstract and potentially misleading formats that require

BOX B: GLOSSARY

The terms used to describe the optical effects of gemstones are defined below, with the relationships among some of them illustrated in figure B-1. Note that the definitions provided here are closely linked to the underlying textures that create these effects, which is why they may seem different from the definitions found in other sources. Many of the previous definitions of these phenomenal terms are subjective descriptions of their appearances, which often lead to misuse and confusion.

Iridescence: Structural color(s) created by interference of reflected or diffracted light by submicron structures. Primarily used for prismatic colors but can be expanded to desaturated or even whitish colors to emphasize their interference origin (e.g., iridescence of moonstone). The term *iridescent color(s)* is used only for more saturated prismatic-colored iridescence.

Play-of-color: Iridescent colors created by diffraction that change (typically in the sequence of prismatic colors) when the stone is rotated relative to the light source or observing eye.

Schiller: A sudden strong reflection of light from within a crystal as it rotates relative to the light source and observing eye, caused by oriented platy inclusions or lamellar textures. Sometimes accompanied by iridescence from thin-film or multilayer interference.

Sheen: Similar to schiller but much less frequently used. Sheen may describe a schiller that is slightly diffuse or originates close to the surface.

Adularescence: Iridescent sheen of alkali feldspar (i.e., moonstone). Occurs primarily as a desaturated blue but sometimes light yellow or white, with a billowy, floating appearance resembling moonlight. This term is misleading as adularescence is not observed in adularia (a variety of potassium-rich feldspar).

Labradorescence: Iridescent schiller seen in plagioclase feldspar labradorite from plutonic rocks.

Peristerescence: Iridescent schiller of peristerite (sodium-rich plagioclase feldspar).

Aventurescence: Specular reflection from isolated, visually discernible flat interfaces (platy or thin-film inclusions, fractures, or facets of euhedral crystal inclusions) inside transparent minerals. Originally called “aventurization,” a now obsolete term. Most adventurescence is caused by oriented inclusions and appears as a schiller effect.

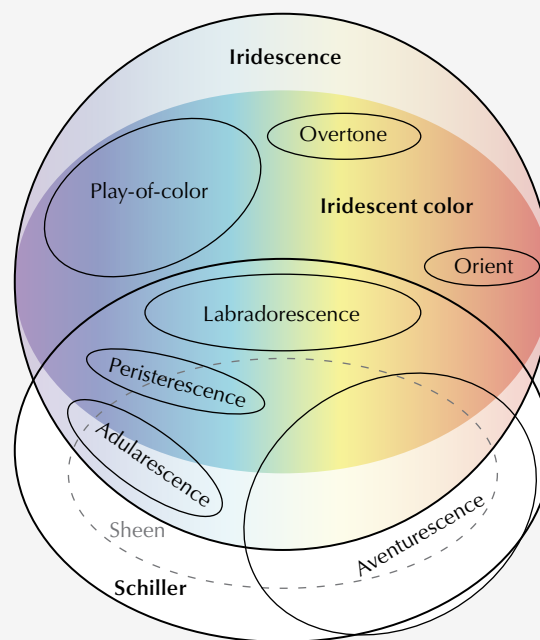


Figure B-1. Venn diagram showing the complicated relationships among the terms describing reflection- and interference-related optical phenomena in gemstones. Note that the overlaps among different terms indicate that they are not exclusive from one another, which means the same phenomena can often be described by several different terms.

Opalescence: Milky or hazy appearance of a mineral or gem material created by diffuse scattering of light by nanoparticles, such as that observed in common opal. This term is sometimes used colloquially to refer to the play-of-color of precious opal.

Chatoyancy/“Cat’s-eye”: A narrow band or thin line of reflected light on a cabochon-cut gemstone that moves as the stone rotates relative to the light source, created by parallel needle inclusions or fibrous textures. The term is named for the effect’s resemblance to the slit-shaped pupil of a cat’s eye.

Asterism/“Star”: Two or more chatoyant bands on a cabochon-cut gemstone that intersect at a single point to create a star-like shape, created by parallel needle inclusions along different directions. The number of rays of the star can range from 4 to 12.

Overtone: Single-color iridescence over the bodycolor of a nacreous pearl.

Orient: Multicolor iridescence over the bodycolor of a nacreous pearl.

The definitions of some terms related to crystal intergrowth of minerals are listed below. Many of these terms have a long history in mineralogy, but are not always clearly defined. Therefore, it is useful, even for experts familiar with the field, to clarify some of the subtleties and ambiguities of the terms before they are repeatedly used in this article.

Inclusion: A foreign material enclosed within a host mineral. Can be of any size or shape. Common types include mineral inclusions (crystals of different minerals), fluid inclusions (liquid and gaseous), and melt inclusions (solidified magmatic melt). Can be materials trapped during crystal growth of the host mineral (primary inclusions) or formed after the crystal stopped growing (secondary inclusions).

Exsolution: Unmixing of an initially homogeneous solid solution into two or more separated phases. If the crystal structures of the exsolved phases are similar, the intergrowth often has a lamellar texture, sometimes periodic or quasiperiodic, known as exsolution lamellae. Some argue that by definition, exsolution should be restricted to a chemically closed system, which means it can be caused only by temperature or pressure change. Nonetheless, phase separation due to change in oxidation state is often referred to as exsolution as well.

Precipitation: A special case of exsolution in which the minor phase, formed through nucleation and growth, makes up only a small fraction of the system, resulting in a suspension (or colloid) of small inclusions sprinkled in a continuous matrix of the dominant phase. The term is borrowed from the similar processes in aqueous chemistry and metallurgy, but the liquid solutions are replaced by mineral solid solutions. The inclusions created by precipitation are called precipitates, which are typically simple oxides or native elements.

Epitaxy: Growth of one mineral on the crystal face (or cleavage plane) of another mineral in an orderly manner, such that certain crystallographic directions of the two

minerals are aligned at the interface. Requires the two minerals to have similar atomic arrangements on the two-dimensional plane they share (low degree of lattice mismatch). The interface for epitactic¹ growth is either coherent (the lattices of the two minerals perfectly match one another) or semi-coherent (the lattices mostly match but with periodic dislocations).

Crystallographic orientation relation (COR): When two crystals grow next to each other, they are often oriented in a special way relative to one another, usually due to coherency constraints at the interface. This relative orientation is described by the crystallographic orientation relation (COR).² Depending on the symmetry of the two phases, there may be more than one way to describe the COR. Exsolution and epitactic growth can both create special CORs between two different phases.

Twinning: Two single crystals of the same phase growing into one another following a special COR. The specific COR describing a twinning intergrowth is known as a twin law. Twin laws are often named after the locality they were originally reported from (e.g., Brazil law, Carlsbad law) or the minerals that most commonly display them (e.g., Albite law, Spinel law). Note that the name of a twin law is always capitalized to avoid confusion (e.g., Albite-twinned anorthite, Spinel-twinned magnetite). Also note that a twin law always describes the relation between two single crystals in direct contact with each other. However, one single crystal may have twin relations with multiple other single crystals, resulting in repetitive twinning within the same specimen, such as polysynthetic (parallel boundaries) or cyclic (nonparallel boundaries) twins.

¹"Epitactic" (or "epitaxial") is the accepted adjective in the mineralogy field (Bailey, 1977), even though "epitaxial" appears to be more commonly used in other fields.

²COR is typically described in the form $\{h_1k_1l_1\}_a // \{h_2k_2l_2\}_b + \langle u_1v_1w_1 \rangle_a // \langle u_2v_2w_2 \rangle_b$, where $h_1k_1l_1$ and $h_2k_2l_2$ are the lattice planes of the two crystals at the interface and $u_1v_1w_1$ and $u_2v_2w_2$ are matching lattice directions within the $h_1k_1l_1$ and $h_2k_2l_2$ lattice planes, respectively.

special expertise for proper processing and interpretation. Finally, the situation is further complicated by often subjective descriptions of the phenomena in gemstones, resulting in poorly defined terminology that is often misused. Different optical effects sometimes look similar, and the same effect may appear dissimilar in different specimens. Multiple phenomena can also occur in the same gemstone, sometimes

at different orientations or on different surfaces. A glossary of optical phenomena in gemstones, along with some terms related to crystal intergrowth, is provided in box B in an attempt to clarify the often-confusing terminology.

With this comprehensive review of the status of scientific investigations into optical processes and submicron textures in phenomenal gemstones, the

BOX C: INTERACTION BETWEEN LIGHT AND SMALL PARTICLES

Visible light contains electromagnetic waves with wavelengths between approximately 400 and 700 nm. When light is intercepted by an object, it may be reflected, refracted, and/or absorbed. These interactions can modulate the intensity of specific wavelengths and redirect them to our eyes, allowing us to see the colorful world around us. The interaction between light and macroscopic objects can be described by relatively simple mathematical equations such as Snell's law and the Fresnel equations, using only the refractive indices of the materials involved. However, when an object is smaller than the wavelength of the light, the laws of reflection and refraction in geometrical optics stop working, as the light behaves more like a coherent wave instead of independent rays. In order to accurately compute the optical effects of small particles, light must be described using the more fundamental Maxwell's equations.

The process of light randomly bouncing off small particles is generally called "scattering." Unlike reflection or refraction, in which the direction of light is fixed by the incident direction relative to the interface (incident angle), light scattering is a more random process that can only be described by a probability distribution. In the simplest case, light scattering is modeled by particles that are spherical (the highest possible symmetry in three-dimensional space), as was solved analytically by Gustav Mie (1908) more than a century ago. For particle sizes (with diameter d) much smaller than the wavelength (λ) of light, Mie scattering can be approximated by the Rayleigh scattering equation (Bohren and Huffman, 1998):

$$I = I_0 \frac{1 + \cos^2 \theta}{2R^2} \left(\frac{2\pi}{\lambda} \right)^4 \left(\frac{n^2 - 1}{n^2 + 2} \right)^2 \left(\frac{d}{2} \right)^6 \quad (\text{C-1})$$

where I is the intensity of the scattered radiation, I_0 is the intensity before interaction with the particle, R is the distance to the particle, θ is the scattering angle, and n is the refractive index (RI) of the scattering particle relative to the surrounding medium. Note that the Rayleigh approximation applies only to very small particles ($d/\lambda < 0.1$), and the larger the particle size, the larger the error of the approximation. It also applies only to non-absorbing particles, of which the relative RI is a real number (because the RI of an absorbing/opaque material is a complex number). The equation

shows that the further n (relative RI) deviates from 1 (the larger the RI difference between the scattering particle and the surrounding matrix), the stronger the scattering intensity. The scattering intensity is proportional to the sixth power of the particle diameter (d^6 in equation C-1), which means that larger particles are much more efficient at scattering light than smaller particles. For instance, the scattering intensity from a 20 nm particle is 64 times that of a 10 nm particle, even though the volume is only 8 times larger. The scattering intensity is also proportional to $1/\lambda^4$, meaning that blue and violet light with shorter wavelengths is scattered much more intensely than red and orange light with longer wavelengths. The blue color of the sky is created by Rayleigh scattering from molecules in Earth's atmosphere. It is speculated that Rayleigh scattering from small particles in gemstones can contribute to blue hues, but there has been no direct experimental evidence suggesting that this effect is observable at such small scales.

A dispersion system containing evenly distributed particles smaller than a few hundred nanometers is called a colloid, so nanoparticles are sometimes called colloidal particles. Because colloidal particles scatter visible light randomly, they cannot be directly observed using even the best optical microscope. However, the scattering effect from these small particles, called the Tyndall effect, creates a hazy translucent appearance that distinguishes a colloid from a solution. Nanoparticle inclusions can sometimes be found in minerals and gemstones, and they can create a unique aesthetic different from that of gemstones with high clarity. These colloid gemstones are typically not considered phenomenal gemstones, but the special optical effects they display justify their inclusion in this article. This also sets a foundation for understanding some of the most complicated optical phenomena. The study of optical properties of colloid systems has been a very important subject in physics for over a century, mainly due to their significant applications in chemistry, biology, material optics, atmospheric and environmental science, oceanography, remote sensing, and astronomy. Related developments in optical theory and computational methods have allowed us to better understand the optical effects of some mineral colloids and colloid gemstones.

authors hope to clear up some of the confusion and misinformation. This article may also offer guidance for future investigations into optical phenomena in gemstones by providing a summary of what we understand so far and what is still unknown. In this review, the optical processes are only qualitatively explained,

with a few necessary mathematical equations, which should be sufficient for a basic understanding. Although some rudimentary knowledge of crystallography and thermodynamics of solid solutions may be required to fully understand every detail, we hope the general concepts are still accessible to anyone who is



Figure 2. A: Green, yellow, brown, and white Brazilian opals; courtesy of Cody Opal. B: Mexican opals showing ranges of color and clarity. C: Faceted fire opals with red (13.51 ct, Mexico), orange (3.14 ct, Mexico), and yellow (8.80 ct, United States) colors. D: Pink and blue Peruvian opal; courtesy of Hussain Rezayee, Rare Gem Co. E: Purple Mexican opals colored by fluorite inclusions (116 and 130 g rough pieces with 13.98 and 15.24 ct cabochons). F: A 10.22 ct prase opal cabochon from Central Tanzania; gift of Lithos Africa. Photos by Robert Weldon (A, C, and D), Tino Hammid (B), and C.D. Mengason (E and F).

interested in this subject. This review is also intended as a starting point for those who seek to expand their knowledge of the topic, as most of the relevant literature is referenced in this article.

This article is structured by roughly sorting the different phenomenal gemstones by the increasing dimensionality and complexity of their underlying submicron structures and textures, as outlined by the physical principles explained in boxes C–F. However, we resisted the temptation to firmly separate the phenomenal gemstones into distinct categories because the boundaries between different effects are not as distinct as most would expect (e.g., chatoyancy versus aventurescence). Moreover, many of the descriptions of optical phenomena are qualitative at best, if not outright ambiguous. This article's order is intended to optimize the logical flow for the reader. For example, the iridescence of pearl and shell is produced primarily by multilayer interference similar to that in labradorite, yet they are discussed last, along with other gemstones that exhibit effects based on diffraction, because the concept of diffraction must be explained first for the reader to appreciate the historical debates regarding the role of diffraction gratings on the surfaces of shells. Also, common opal and precious opal have similar submicron structures but are discussed separately (at the beginning and near the end, respectively) due to their dramatically different visual appearances and optical effects.

COMMON OPAL

Opal (Opl: $\text{SiO}_2 \cdot n\text{H}_2\text{O}$) is a silica mineral containing a variable amount of water. Although it is considered a valid mineral name by the International Mineralogical Association (IMA) for historical reasons, opal does not fit the technical definition of a mineral and is

commonly described as a mineraloid because it is not ordered at the atomic scale. As determined by X-ray diffraction (XRD) patterns, opals are generally classified into three groups of increasing order: opal-A (amorphous silica), opal-CT (poorly ordered intergrowths of cristobalite and tridymite with amorphous silica), and opal-C (poorly ordered cristobalite with amorphous silica), with many samples showing transitional characteristics between these end members (Curtis et al., 2019). Opal-A can be further divided into opal-AG (amorphous gel, composed of amorphous silica spheres) and opal-AN (amorphous network, also known as hyalite) based on their submicron textures. In general, opals form when meteoric and ground waters dissolve silica from igneous or sedimentary rocks and reprecipitate it within fissures of host rocks (Gaillou et al., 2008). The detailed processes controlling the texture and crystallinity of opal are still not fully understood (Gaillou, 2015), although different models have been proposed and tested (Brown, 2005). A recent study synthesized a material with similar composition and grain sizes to natural opal-AG under geologically relevant conditions (Gouzy et al., 2024). Because opal typically forms at low temperatures, kinetics rather than thermodynamics controls the precipitation process, and opals from different localities can have dramatically variable appearances as a result of diverse chemistries and nanostructures. Opals with no play-of-color are generally called “common opals,” which may also serve as gemstones due to their unique milky appearance (box C) and vibrant colors (figure 2).

Common opals may be considered the paradigm of colloid gemstones, as they consist almost entirely of nano-size silica spheres (figure 3; Gaillou et al., 2008), with the exception of opal-AN. The scattering of light from the randomly arranged nanospheres

Figure 3. SEM images showing the silica spheres in common opal. Instead of solid concentric spheres (A and B), opal-CT and opal-C may contain lepispheres (spherical aggregates of blades, C). The spheres in common opal scatter light completely randomly due to the irregular arrangement, creating the typical milky appearance. The sizes of the silica spheres in common opal may cover a wide range (A) or be very similar to each other (B and C). Image A from Gaillou (2015) and B and C from Gaillou et al. (2008).



gives common opal a hazy appearance (figure 2). In fact, the word *opalescent* is sometimes used to describe the hazy or milky appearance found in other gemstones containing nano-inclusions, such as fancy white diamonds (Eaton-Magaña et al., 2019).

The bodycolor of common opal is mainly controlled by the species of nano-inclusions. For instance, hematite inclusions create yellow, orange, or brown colors; fluorite inclusions can produce purple; and green opals may contain nickel-rich inclusions. The sky-blue color in some opals may be created by scattering, as they appear orange in strong transmitted light (Gaillou, 2015). It is highly debatable, however, whether this is Rayleigh scattering, because most of the nanospheres in opal are too large to scatter visible light (box C). Careful quantitative analysis of the scattered and transmitted spectrum will be necessary to accurately describe the effect (Kinoshita, 2008). Photoluminescence created by uranium (green), unsaturated silica frameworks (blue), or organic compounds (orange) may also affect the apparent color of opal under sunlight, if it is not quenched by high concentrations of iron (Gaillou, 2015).

FANCY WHITE AND FANCY BLACK DIAMOND

Among all milky and cloudy gemstones, fancy white and fancy black diamonds are perhaps the most valuable (figure 4). Although it is debated whether white and black are considered colors or not, these special diamonds are graded and reported similarly to other

fancy-color diamonds. Therefore, they are generally not considered phenomenal gems even though their “colors” are caused by special optical effects. The gemological properties of both natural fancy white and fancy black diamonds are best summarized by Eaton-Magaña et al. (2019).

Fancy white diamonds owe their hazy or cloudy appearance to dislocation loops and nano-inclusions (Gu and Wang, 2018; Gu et al., 2019). A dislocation is a linear crystallographic defect within the crystal structure where the atomic arrangement changes abruptly. Dislocations in diamond almost always exist as self-enclosed loops due to their localization and lower energy. Experiments at very high temperatures have shown that dislocation loops can form from platelet defects (planar or film defects containing aggregated nitrogen) in type IaB diamonds (Evans et al., 1995; Speich et al., 2017), and a similar process is believed to be responsible for dislocation loops in untreated natural diamonds. Because dislocations are one-dimensional misalignments of atoms in the crystal structure, they fall well below the imaging resolution of an optical microscope (figure 5A). However, they can still scatter light to create the hazy appearance due to the disrupted crystal lattice as well as the strain field around it.

The nano-inclusions found in fancy white diamonds are octahedral-shaped negative crystals, known as voidites, which are approximately 30 to 200 nm in size and contain nitrogen (Barry et al., 1987). These voidites are believed to have formed



Figure 4. Faceted fancy white and fancy black diamonds with different degrees of transparency. Photos by GIA staff.

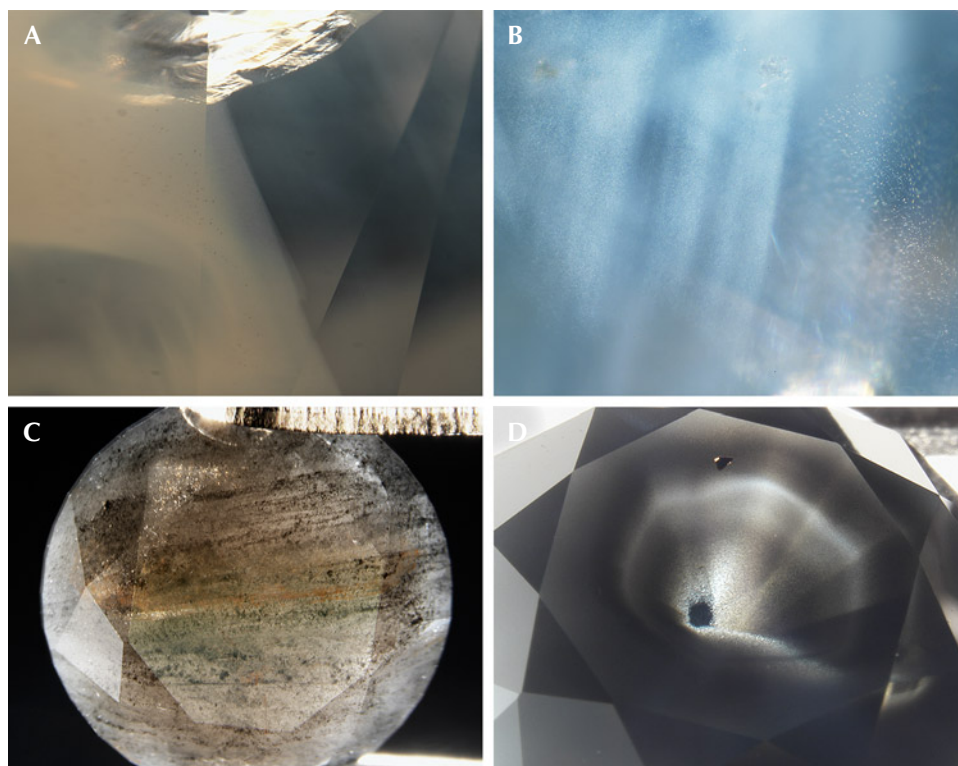


Figure 5. Cloudy regions in fancy white diamonds (top) and dark-colored particle and cloud inclusions in fancy black diamonds (bottom). Photomicrographs by Garrett McElhenny (A) and GIA staff (B–D); fields of view 2.3 mm (A), 1.6 mm (B), 6.7 mm (C), and 6.9 mm (D).

by the exsolution of excess nitrogen from the diamond lattice (Kiflawi and Bruley, 2000), and they contain mostly solid molecular nitrogen (cubic δ -N₂) (Navon et al., 2017; Sobolev et al., 2019; Tschauner et al., 2022). A recent study also showed that oxygen atoms dissolved within the diamond lattice can also exsolve to form voidites filled with CO₂ (Shiryaev et al., 2023). Unlike dislocation loops, voidite inclusions are three-dimensional particles, which can be seen as “pinpoints” under high magnification using an optical microscope (the size falls below the resolution of the optical microscope, so they appear as dots) (figure 5B).

Nitrogen defects in diamond crystals start as isolated single nitrogen atoms substituting for carbon atoms (C centers), which can coalesce into pairs (A centers) and eventually four-nitrogen clusters (B centers) over geological time (Boyd et al., 1995). Both dislocation loops and voidites in fancy white diamonds are strongly related to the aggregated nitrogen defects, which are produced by high concentrations of nitrogen impurities and prolonged annealing at high temperature. Therefore, fancy white diamonds are predominantly type IaB (diamonds old enough to contain only B centers), and they originate from Earth’s transition zone or the lower mantle. Because these aggregates form by annealing, no thermal treatment to mimic or

enhance the cloudy or hazy appearance of fancy white diamonds has been reported.

The cause of color in natural fancy black diamonds is more complicated, involving dark-colored inclusions such as graphite or iron oxide (hematite and magnetite), radiation stains, or a high density of absorption defects. Most inclusions in fancy black diamonds are much larger than the voidites in fancy white diamonds and are likely incorporated during rapid growth of the diamond crystal (figure 5, C and D). Unlike fancy white diamonds, the fancy black color can be created in diamonds by several different treatment methods, including heating at high temperatures under vacuum or heavy irradiation treatment. In fact, more than one-third of the black diamonds examined by GIA have been treated.

COPPER-COLORED PLAGIOCLASE FELDSPAR

The U.S. state of Oregon is the only confirmed source of natural copper-colored gem feldspar. Ethiopia has been reported as a newer source, which is likely valid given the stones’ consistently different chemistry from that of the Oregon material (Kiefert et al., 2019; Sun et al., 2020), but international gemological researchers have not yet visited the deposit to verify its authenticity. All the gem basaltic feldspars

from Oregon are sold as “Oregon sunstone” in the gem market, even though not all show aventurescence (figure 6).

Spherical colloidal copper is known to imbue a host material with hues of red, a technique used for centuries to make red glass (Durán et al., 1984; Freestone, 1987; Freestone et al., 2007). The less common green color of Oregon sunstone, however, has long remained an enigma to mineralogists. Metallic copper is electrically conductive and interacts with light quite differently compared to dielectric (insulating) particles, and therefore the interaction cannot be simply approximated with Rayleigh scattering. The free electrons in a copper nanoparticle could resonate with light of certain wavelengths and absorb its energy. These oscillating charges also create a strong electric field on the particle surface and enhance its scattering power. These complicated processes make the color of copper-bearing feldspars unique in the mineral world and challenging to study. Jin et al. (2022a) computed the absorption and scattering properties of spheroidal copper particles of various sizes and shapes embedded in feldspar, which validated the speculation by Hofmeister and Rossman (1983) that an anisotropic colloid is the cause of the strong pleochroism often observed in green-blue Oregon sunstone. The computation shows that the colloidal copper particles are strong and selective absorbers of visible light, and only a few parts per million by weight are sufficient to produce saturated colors in mostly transparent crystals.

The orientation of the copper particles in an Oregon sunstone from the Sunstone Butte mine, evidently controlled by the feldspar structure, has also been characterized in detail using polarized absorption spectroscopy (Jin et al., 2023). Interestingly, the transmission electron microscopy (TEM) analysis by Wang et al. (2025) revealed copper particles elongated along the [001] direction in a dichroic crystal from the same mine, instead of the [100] direction as shown by optical analysis (Jin et al.,

2023), suggesting that the feldspar structure may not be the only factor determining the particle shape and orientation. Note that optical analysis reveals the average orientation of all the copper particles collectively, whereas TEM can show only the projection of individual particles one at a time. Wang et al. (2025) oriented the samples crystallographically instead of optically and thus missed the opportunity to correlate the two types of analyses in the same study. More correlated TEM and optical studies are needed to better understand the relationship between the particle shapes and the feldspar structure.

The low (triclinic) symmetry of feldspar leaves its optical orientation unconstrained by its crystallography, resulting in complicated interactions between the highly directional absorption and scattering effects of the copper particles and the anisotropic feldspar optics (Jin et al., 2023). This creates a wide range of possible appearances that are heavily dependent on lighting and viewing directions, presenting more challenges and opportunities for faceting Oregon sunstone than for any other pleochroic gem. Depending on the aspect ratio of the copper particles, Oregon sunstone could be the most pleochroic gem material of all, often showing drastically contrasting colors on different facets of the same stone.

Copper diffusion treatments have been shown to create red and green colors in otherwise colorless feldspar crystals (Emmett and Douthit, 2009; Zhou et al., 2021, 2022), a discovery made after a large amount of red feldspar, purportedly from Asia or Africa, flooded the gem market more than a decade ago, creating controversy in the gem trade regarding the origin and authenticity of these gemstones (Abduriyim, 2009; Abduriyim et al., 2011; Rossman, 2011). The treatment process proves that the particles form by precipitation of copper dissolved in the feldspar lattice. Diffused feldspars generally contain much higher copper concentrations than natural Oregon sunstone (Sun et al., 2020; Jin et al., 2023).



Figure 6. Rough Oregon sunstone from the Sunstone Butte mine showing a wide range of colors. Photo by Robert Weldon.

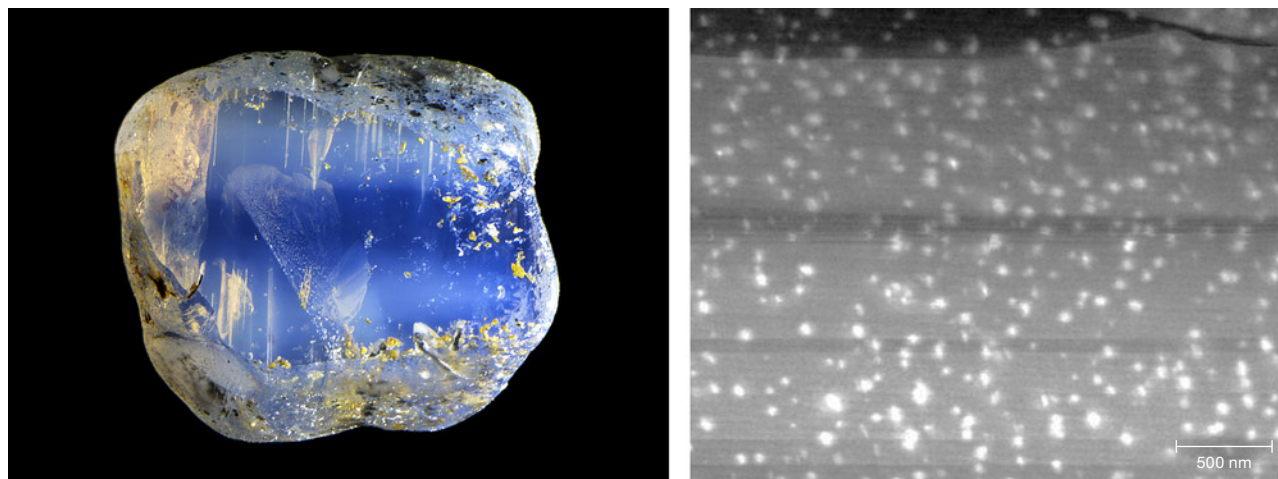


Figure 7. Left: A 1.25 ct sapphire from Ilakaka, Madagascar, containing cloudy areas correlated with higher concentrations of beryllium, niobium, and tantalum. Photo by Nathan Renfro. Right: A scanning TEM (high-angle annular darkfield) image of the cloudy area showing high-density titanium-rich nanoparticles with the riesite structure. The titanium oxide nanoparticles appear brighter than the corundum matrix. The horizontal stripes in the image are artifacts from sample preparation. Image from Shen (2011).

The size, shape, density, and zonation of the copper particles also appear noticeably different from diffused and untreated copper-colored feldspars as a result of different thermal histories (Jin et al., 2023). Natural Oregon sunstones typically show much stronger pleochroism than artificially diffused feldspars, likely due to the prolonged cooling in basaltic lava flows compared to the fast heating and cooling processes used in the laboratory.

MILKY SAPPHIRE AND RUBY

Corundum (Crn: $\alpha\text{-Al}_2\text{O}_3$) is another gem mineral that can show a milky or cloudy appearance due to nanoscale particle inclusions. Although translucence generally does not increase the attractiveness or value of sapphire or ruby crystals, which ideally are transparent, internal light scattering is often used as a special characteristic to help determine provenance (Palke et al., 2019a,b). Thin milky bands that do not impair the transparency can create an admirable sleepy, velvety appearance, which is best shown in Kashmir sapphires. Some sapphires with a homogeneous milky appearance are marketed as “opalescent sapphires,” which have increased in attraction and popularity in recent years. Most milky sapphires and rubies would display weak asterism if cut into cabochons, but they are more often faceted to enhance their visual transparency. Therefore, they are discussed separately from the star sapphires and rubies in this article due to their special appearance and mineralogy.

The included milky regions in natural corundum show a positive correlation with the titanium concentration, indicating that the nano-inclusions are most likely titanium-bearing phases. He et al. (2011) systematically studied the evolution of TiO_2 precipitates in synthetic titanium-doped sapphire, and their work supports several previous studies of synthetic or heated natural titanium-bearing corundum (Phillips et al., 1980; Jayaram, 1988; Moon and Phillips, 1991; Xiao et al., 1997). Titanium in sapphire would exsolve directly as rutile (Rt: $\alpha\text{-TiO}_2$) at 1350°C or higher, yet riesite¹ is the initial precipitated phase when annealed at 1300°C or lower, transforming eventually to rutile as the precipitates grow larger.

Unfortunately, studies of nano- and micro-inclusions in natural corundum are relatively limited. Shen and Wirth (2012) confirmed the presence of natural riesite precipitates (20–40 nm long and 5–10 nm wide) in the cloudy region of a sapphire from Ilakaka, Madagascar (figure 7). Baldwin et al. (2017) observed high-density nanoparticles (~10–20 nm long) enriched in high field strength elements (HFSEs) in the cloudy brown region of a basaltic sapphire crystal from Petersberg, Germany. Contrary to the authors’

¹Riesite is a high-pressure polymorph of TiO_2 with the scrutinyite ($\alpha\text{-PbO}_2$) structure. The mineral name was coined only recently (Tschauner et al., 2020), even though the phase had already been known for decades; thus the nomenclature in the literature is often confusing. It has been referred to as srilankite (Ti, Zr oxide with the same structure), $\text{TiO}_2\text{-II}$, $\alpha\text{-PbO}_2$ -type TiO_2 , and even $\alpha\text{-TiO}_2$, the last of which is incorrect because $\alpha\text{-TiO}_2$ is rutile.

interpretation, the preferred orientations and coherent boundaries shown in the TEM images of these nanoparticles are consistent with solid-state exsolution of HFSEs as riesite precipitates (Jin et al., 2024). Rutile inclusions in corundum crystals have been observed only with much larger sizes (at least 200 nm long) (Phillips et al., 1980; Moon and Phillips, 1991; Xiao et al., 1997; He et al., 2011). A recent atom probe tomography (APT) and TEM study reported an unknown phase of secondary beryllium-bearing nanoparticles (~10 nm) occurring together with riesite precipitates (~5 nm) in a Nigerian sapphire crystal containing high concentrations of heavy HFSEs and beryllium (Jin et al., 2024). A similar study of a Madagascar sapphire containing less beryllium showed only riesite precipitates (~20 nm), with beryllium concentrated at the boundary between the nanoparticles and the corundum matrix (Emori et al., 2024). Riesite is stable at pressures above 6 GPa (Olsen et al., 1999), which is much greater than the pressures associated with the growth conditions of most gem corundum (Giuliani et al., 2014). This suggests that all the riesite nano-inclusions in corundum form through solid-state exsolution, stabilized by the immense strain induced by the coherent boundary between riesite and corundum (Xiao et al., 1997; He et al., 2011).

Most (if not all) of these nano-inclusions in natural corundum contain titanium, which would dissolve into the corundum lattice under high-temperature heat treatment, turning the stones bluer due

to the newly formed titanium-iron pairs. In fact, the milky or cloudy appearance is commonly used by gem miners and traders to determine whether natural corundum may be color enhanced by heat treatment, with the geuda-type sapphire from Sri Lanka the best-known example (Gunaratne, 1981; Ediriweera et al., 1989; Perera et al., 1991).

Submicron and nanoscale inclusions are quite common in natural materials, as suggested by the few studies on sapphire and feldspar. Even though most of the nano-inclusions are optically invisible and may not affect the appearance of minerals and gemstones, they are of great importance for geological research, as they contain detailed information about the mineral's geological history that cannot be retrieved otherwise. More careful TEM and APT analysis of natural corundum and other minerals is needed to fully understand the nature of these nano-inclusions. More unknown phases likely are waiting to be discovered as new mineral species in these nano-inclusions.

STAR SAPPHIRE AND RUBY

Star sapphire and ruby are certainly the most popular asteriated gemstones (box D) and probably the best-known of all phenomenal gemstones. The asterism in star sapphire and ruby is created by thin needle-shaped inclusions known as “silk” in the corundum host (figure 8). It has long been speculated that these silk inclusions are rutile needles. However, prior to

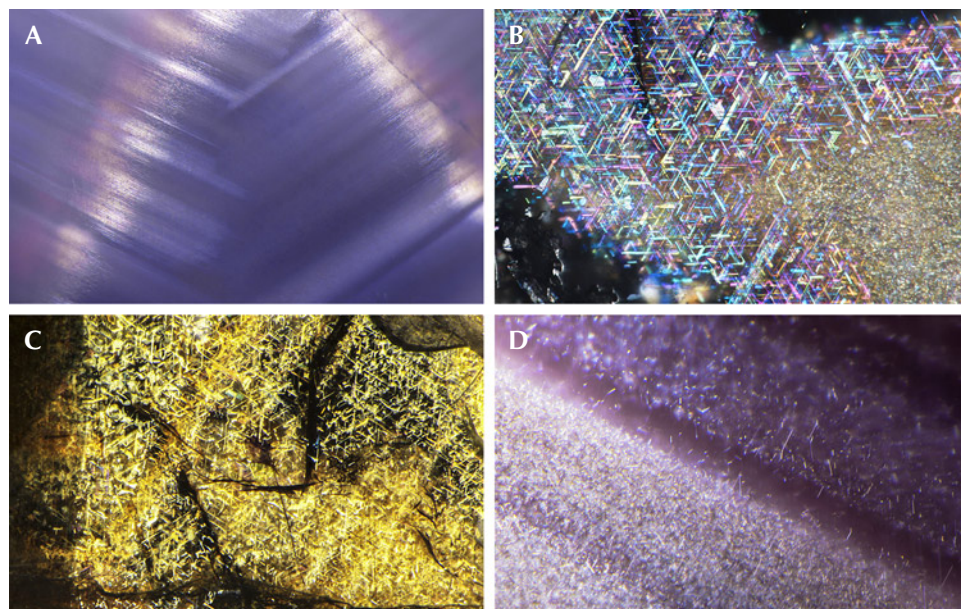


Figure 8. A: Fine rutile silk in a star sapphire. B: Rutile needles in a Burmese sapphire. C: Dense hematite and/or ilmenite needles in a sapphire from Kenya. D: Needle inclusions in a 12-rayed star sapphire. Photomicrographs by Nathan Renfro (A, C, and D) and Victoria Liliane Raynaud-Flattot (B); fields of view 4.62 mm (A), 0.97 mm (B), 2.44 mm (C), and 0.91 mm (D).

BOX D: SCATTERING AND DIFFRACTION OF LIGHT BY ACICULAR PARTICLES

Chatoyancy (“cat’s-eyes”) and asterism (“stars”) are optical phenomena that have been observed in gemstones for centuries. Their correlation with the minute needle-shaped inclusions in chatoyant and asteriated stones has been known since not long after the invention of the optical microscope. Surprisingly, the first qualitative explanation of the effect was not proposed until the early 1980s (Weibel et al., 1980; Wüthrich and Weibel, 1981; Wüthrich et al., 1983). When a beam of light intersects with a needle-shaped particle, the scattered light forms a cone with the needle as its axis (figure D-1A). The cabochon-cut surface of the stone acts as a convex lens, which focuses the scattered light from multitudes of needles inside the crystal into a bright line above the stone (figure D-1C) that can be observed by our eyes. Moon and Phillips (1984a and 1985) later described the phenomenon more quantitatively using Fraunhofer diffraction, which explains why thinner needle inclusions create sharper bright lines, as well as how the cat’s-eye or star can be sharpened by reducing the spherical aberration from the cabochon surface.

The redirection of light around an obstacle (or an aperture) is called diffraction, a phenomenon exhibited by all forms of waves (e.g., sound waves, water waves).

Basically, all optical phenomena in gemstones are created by light diffracting off the inclusions or textures with variable sizes and shapes. Note that the terms *scattering* and *diffraction* are often used to describe the same effect or physical process, with “scattering” emphasizing the random particle-like behavior of light, while “diffraction” stresses a wavelike nature that is more directional and predictable.

Because the bright line of scattered light is perpendicular to the needle direction (figure D-1), the number of bright lines (sometimes called branches or rays) in asterism and chatoyancy is dependent on the number of different orientations of the needle inclusions. The orientations of the needles are typically controlled by the crystallographic relation between them (the included phase) and the host mineral. Therefore, the distribution of the needles mostly follows the symmetry of the host mineral. This is why chatoyancy and 4-rayed stars are often observed in minerals of lower symmetry such as chrysoberyl (orthorhombic) and diopside (monoclinic), whereas 6-rayed and 12-rayed stars are mostly found in trigonal and hexagonal minerals such as corundum, quartz, and emerald.

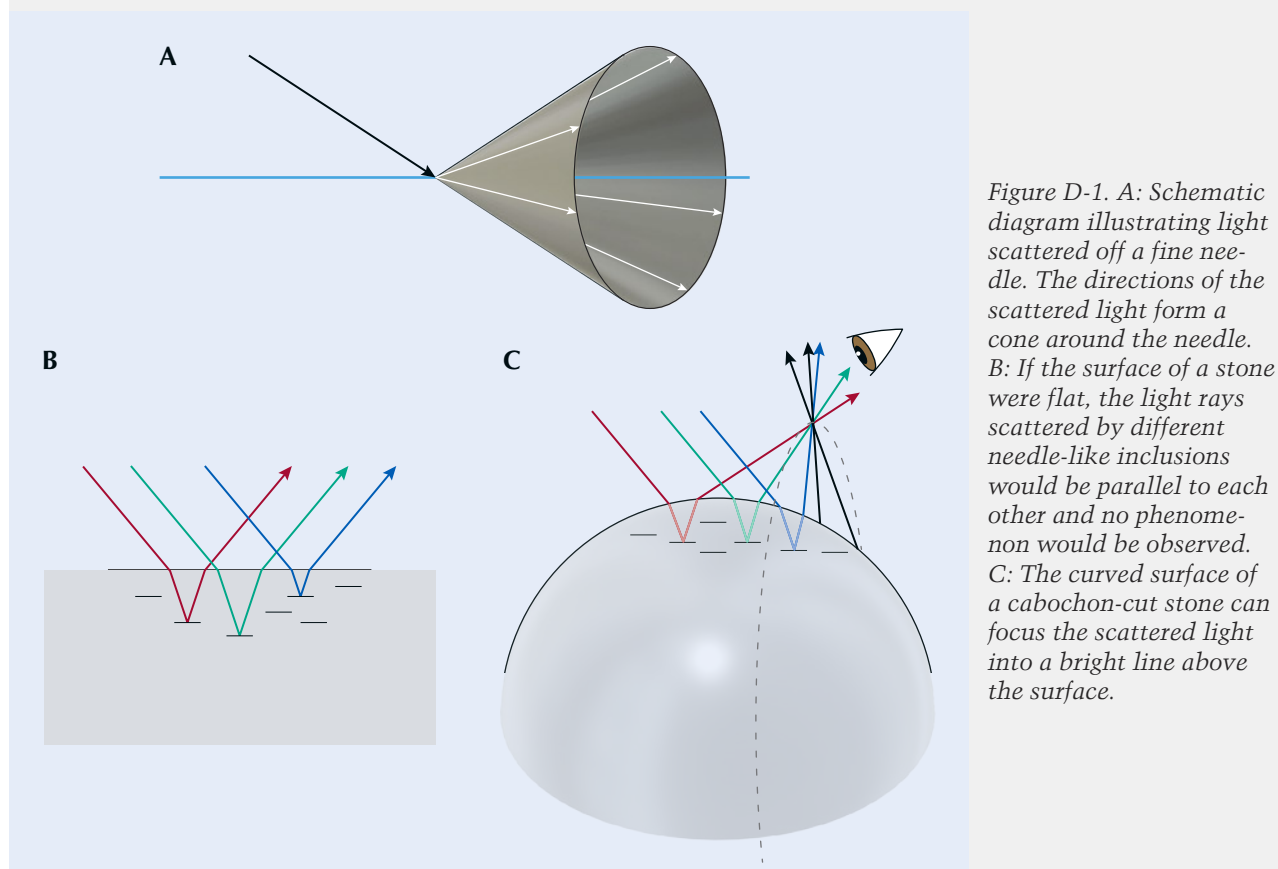


Figure D-1. A: Schematic diagram illustrating light scattered off a fine needle. The directions of the scattered light form a cone around the needle. B: If the surface of a stone were flat, the light rays scattered by different needle-like inclusions would be parallel to each other and no phenomenon would be observed. C: The curved surface of a cabochon-cut stone can focus the scattered light into a bright line above the surface.

The bright lines of different orientations intersect at a single point to form a star only when the needle directions lie in the same plane. Any two directions define a plane, and a third direction could be at an angle with the plane defined by the first two. The needles in cubic minerals, such as garnet and spinel, cannot all be coplanar. Moreover, the needles in some star quartz are oriented at an angle with the (001) plane. These non-coplanar needles can create a network of multiple stars connected to one another through their extended rays. Intergrowth between two crystals, such as twinning, can also misalign the needle planes and create double stars that are not connected to each other (figure D-2) (Koivula et al., 1993; McClure, 1998).

The illusion of the cat's-eye or star "floating" above the stone is sometimes described as the stereoscopic effect (Killingback, 2005; Bui et al., 2020), which is most noticeable on larger specimens due to the longer focal lengths of their less curved surfaces. The cat's-eye or star also moves dramatically when the stone is turned, as its position strongly depends on the direction of the incident light (figure D-1). When a chatoyant or asteriated stone is illuminated by multiple light sources,

corresponding numbers of cat's-eyes and stars can be seen moving synchronously because each light source shines from a different angle (see video 1 at <https://www.gia.edu/gems-gemology/summer-2025-phenomenal-gemstones>).

Thanks to the densely distributed needle inclusions, chatoyant and asteriated gems are often semitranslucent with dark bodycolor, which means that only light scattered by needles near the surface makes it out of the stone. The denser the needle inclusions are, the sharper the cat's-eye or star typically is, because the light contributing to the phenomenon is more localized. When chatoyancy is observed in transparent or translucent stones, light is scattered by needles deeper in the stone, creating a special appearance under oblique lighting known as "milk-and-honey" (or "coffee-and-cream"), where the stone appears to be separated by the cat's-eye into a brighter ("cream"/"milk") half and a darker ("coffee"/"honey") half (Killingback, 2015). Some star ruby, sapphire, and quartz are even sufficiently transparent to let light reflect off the base of the cabochon, creating a second star with the same hue as the stone's bodycolor (Schmetzer et al., 2015).

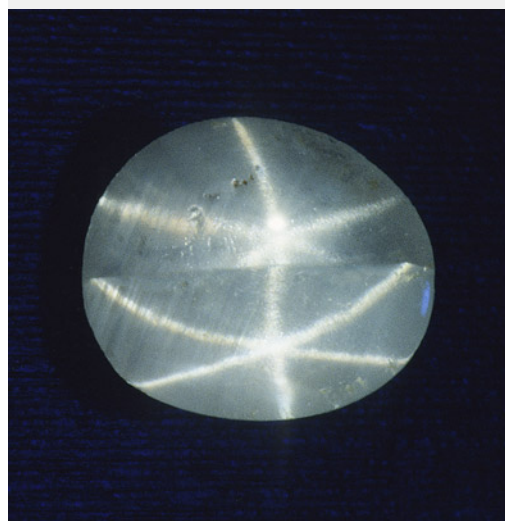


Figure D-2. Sapphire (left, 0.87 ct) and ruby (right, 8.19 ct) with double stars due to twinning. Note that the star sapphire contains only two twin domains, whereas the star ruby is polysynthetically twinned with microscopic twin domains. Photos by Robert Weldon (left) and Shane McClure (right).

TEM or micro-Raman spectroscopy, only circumstantial evidence of rutile could be found, such as the presence of titanium in the bulk composition as well as the high refractive index (RI) and brownish colors. Nassau (1968) suspected that the needles were tialite (Al_2TiO_5) due to the apparently lower symmetry but could not provide any evidence for this identification. Tialite is a synthetic material only stable at temperatures above $\sim 1300^\circ\text{C}$ and is thus unlikely to

be found in any natural corundum, which generally forms at lower temperatures (Giuliani et al., 2014). The presence of rutile in synthetic star sapphire was first confirmed by Frondel (1954) by chemical and XRD tests on crushed and centrifugation-separated precipitates. The first direct observation of rutile needles in synthetic sapphire using TEM was done by Phillips et al. (1980) nearly three decades later. Viti and Ferrari (2006) reported a "monoclinic polymorph

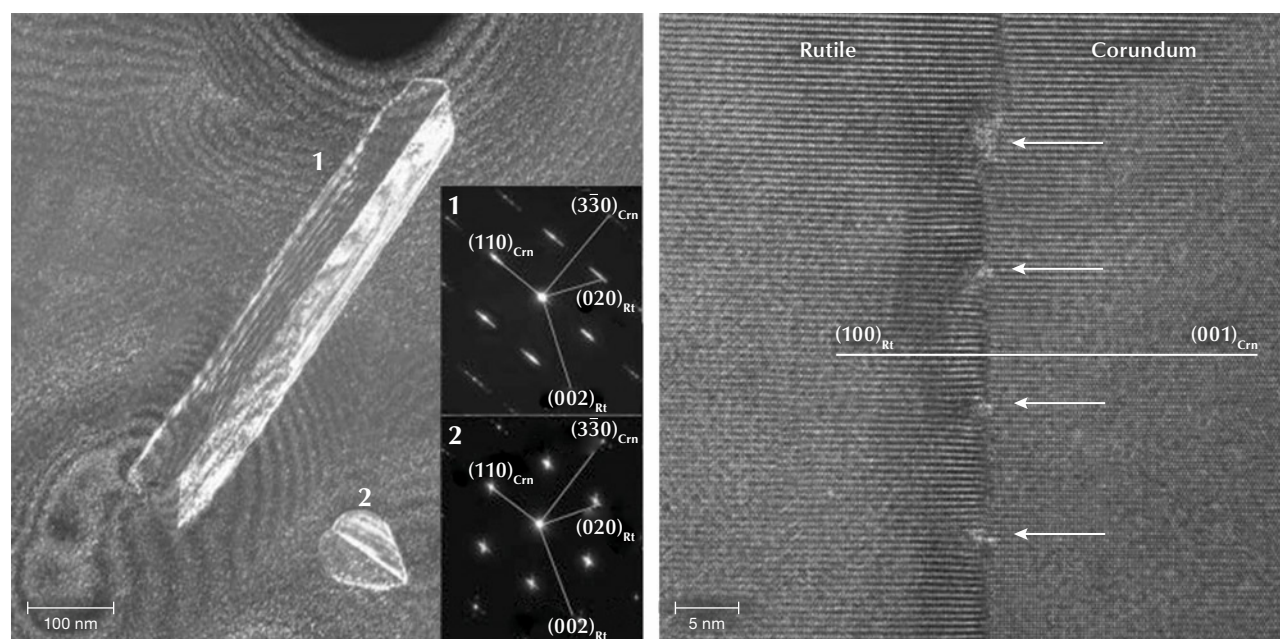
of TiO_2 in a Verneuil-grown star sapphire, although the TEM images and the electron diffraction patterns clearly show a twinned rutile structure. The behavior of titanium in synthetic titanium-doped corundum is relatively well understood after the study by He et al. (2011) showed only two types of titanium-containing precipitates, riesite and rutile, depending on the annealing temperature and time.

Similar to nanoprecipitates, needle inclusions in natural corundum are significantly understudied. Moon and Phillips (1984b) first applied TEM to natural black (star) Australian sapphire and surprisingly discovered hematite (Hem: $\alpha\text{-Fe}_2\text{O}_3$) and/or ilmenite (Ilm: FeTiO_3) as the star-creating needles, instead of rutile, supporting an earlier claim by Weibel and Wes-sicken (1981) on a Thai black star sapphire with no detectable titanium. The authors also reported that rutile was observed in blue and blue-green stones from Australia but did not publish the data. Needle-shaped hematite/ilmenite inclusions have been reported multiple times as the star-forming silk since the original discovery (Saminpanya, 2001; Izokh et al., 2010; Khamloet et al., 2014; Bui et al., 2015, 2017; Soonthorntantikul et al., 2017; Sorokina et al., 2017; Liu et al., 2022), including almost pure hematite in a

titanium-free corundum from Shandong, China (Zhao et al., 2022). On the other hand, despite mounting circumstantial evidence for the rutile needle inclusions in natural corundum, it was not until recently that direct confirmation using electron probe microanalysis (EPMA) and electron backscatter diffraction (EBSD) was first reported (Palke and Breeding, 2017). It appears that ilmenite and/or hematite inclusions are more common than rutile as the star-forming needles in corundum, which makes sense as natural corundum contains much more iron than titanium. However, there could also be a bias caused by rutile needles being generally smaller and harder to identify. As the studies on this subject are very limited, it is not possible to estimate the percentage of each type of inclusion in natural corundum.

TEM analyses show the ilmenite/hematite inclusions are elongated along the $\langle 100 \rangle$ direction (ilmenite and hematite have the same crystallographic orientation as corundum as they are isostructural) (Moon and Phillips, 1984b; Zhao et al., 2022), whereas the rutile needles are elongated along $\langle 011 \rangle_{\text{Rt}} \parallel \langle 210 \rangle_{\text{Cm}}$, with $\{100\}_{\text{Rt}} \parallel \{001\}_{\text{Cm}}$ (figures 9 and 10) (Phillips et al., 1980; Jayaram, 1988; Moon and Phillips, 1991; Xiao et al., 1997; Viti and Ferrari, 2006; He et al., 2011).

Figure 9. Left: $[001]_{\text{Cm}} ([100]_{\text{Rt}})$ zone axis darkfield TEM image showing needle-shaped and heart-shaped twinned rutile precipitates in titanium-doped synthetic sapphire annealed at 1300°C for 50 hours. The selected area electron diffraction patterns of the two precipitates are shown as insets. Right: $[210]_{\text{Cm}} ([011]_{\text{Rt}})$ zone axis high-resolution TEM image showing the $(110)_{\text{Cm}} \parallel (011)_{\text{Rt}}$ interface with periodic dislocations (white arrows) to accommodate the lattice mismatch between rutile and corundum crystal structures. Images from He et al. (2011).



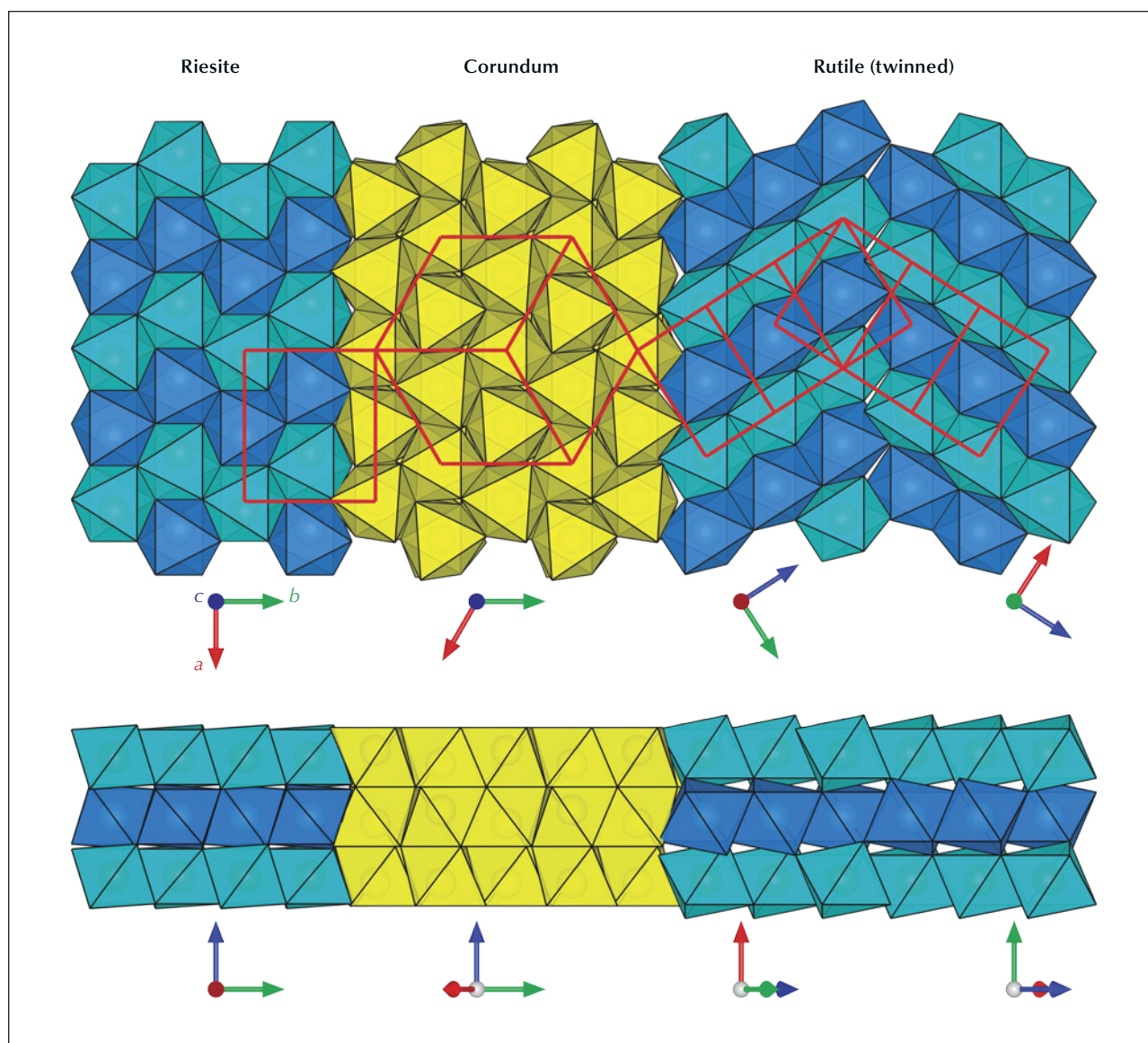


Figure 10. Structural relations between the corundum host and titanium oxide inclusions at the $\{110\}_{Cm}$ interface. The different layers of titanium octahedra are differentiated by two shades of blue. The unit cells of each structure domain are depicted by red boxes to highlight symmetry and orientation. The coherent boundaries between corundum and the needle inclusions determine the specific CORs. Note that the lattice match between corundum and riesite is much better, which is presumably why riesite precipitates first at low temperatures. Rutile, which is more stable at ambient pressure, eventually takes over with larger precipitates (or at higher temperatures), which requires periodic dislocations at the interface and twinning to accommodate the different lattice dimensions.

Therefore, the needles perpendicular to the growth zoning of corundum are ilmenite or hematite, whereas those parallel to the growth zoning are rutile (figure 11). Mayerson (2001) incorrectly claimed that all stars in untreated natural sapphire are parallel to the growth zoning, and thus mistakenly concluded that stars with rays perpendicular to growth zoning can be an indication of titanium-diffused star sapphire. When needles of both orientations are present

in the same corundum crystal, a rare 12-rayed star can be observed (again, see figure 1, top left). The two sets of 6 rays in a 12-rayed star may show different colors (Vertriest and Bruce-Lockhart, 2018), as rutile silk mostly appears silver white (figure 8A) and hematite/ilmenite silk can appear golden yellow depending on the iron content (figure 8, C and D). It should be noted that Bui et al. (2017) claimed that only ilmenite inclusions could be found in a 12-rayed

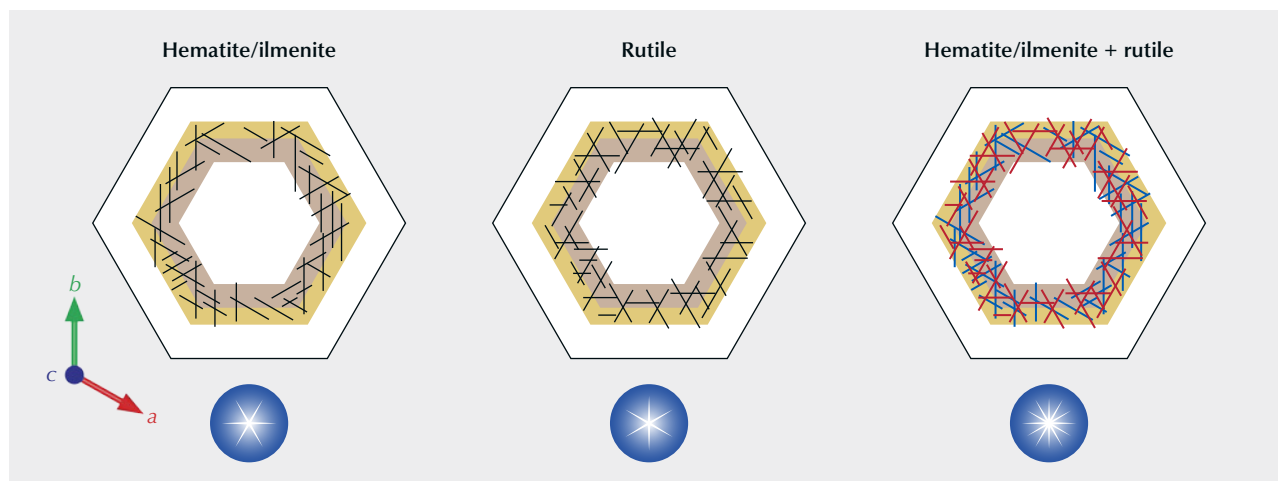


Figure 11. Schematic drawing showing the orientation relation between needle inclusions and growth zoning of corundum. Hematite and ilmenite needles are mostly perpendicular to the growth bands, creating a star with rays parallel to the banding; rutile needles are always parallel to the growth bands, and the rays are perpendicular. If both types of needles are present, a 12-rayed star is created.

star sapphire likely from Sri Lanka, although the Raman spectra presented in their paper do not conclusively exclude the presence of rutile.

Iron and titanium are among the most common trace elements in natural corundum, which is why it is generally believed that these needle inclusions form by solid-state precipitation of iron and/or titanium dissolved in the corundum structure. Natural rutile silk has the same crystallographic orientation relation (COR) as synthetic or titanium-diffused star sapphire, suggesting a similar formation mechanism. Little is known about the formation mechanism of the ilmenite/hematite needles, as heating an iron-rich corundum failed to produce any similar precipitates (Moon and Phillips, 1991). Iron is much more soluble in corundum than titanium and probably would not precipitate unless annealed at significantly lower temperatures for much longer periods than in the study by Moon and Phillips (1991), and exsolution may be achievable only in natural geological settings.

It should be noted that experiments of epitactic growth of rutile (Gao et al., 1992) and hematite (Wang et al., 2002) on a corundum substrate can also create coherent or semi-coherent interfaces similar to those observed for the needles exsolved in the corundum matrix (He et al., 2011; Zhao et al., 2022). Palke and Breeding (2017) first argued for epitactic coprecipitation of the oriented needle rutile inclusions containing heavy HFSEs, based on observations of glassy melt inclusions that indicate fast cooling, as well as the assumption that the heavy HFSEs are strongly incompatible and thus unlikely to be incor-

porated into the corundum lattice during crystal growth. However, this argument has been invalidated by a recent APT study showing that significant amounts of heavy HFSEs (e.g., tungsten, niobium, and tantalum) can not only be dissolved into the crystal structure of natural corundum but are also likely to be enriched beyond their solubility in corundum due to preferred adsorption on the growth surfaces (Jin et al., 2024). This means that the precipitation of HFSEs could occur when the already supersaturated host corundum is heated above its formation temperature, which would be a much faster process than previously thought.

Moreover, the distribution of rutile silk in natural corundum mostly correlates with fluctuating titanium concentrations associated with the hexagonal $\{110\}$ growth zoning, yet the basal $\{001\}_{\text{Crm}}//\{100\}_{\text{Rt}}$ interfaces of the needle inclusions are always wider than the vertical $\{110\}_{\text{Crm}}//\{011\}_{\text{Rt}}$ interfaces, as evidenced by the much stronger reflection seen on the $\{001\}_{\text{Crm}}$ surface (again, see figure 8, A and B). These observations are hard to reconcile with the epitactic coprecipitation mechanism, because if the epitaxy occurs on the basal $\{001\}_{\text{Crm}}$ surface, as suggested by the platy needle shape, its distribution should not correlate with the $\{110\}$ growth zoning.

The precipitation of rutile (or other iron/titanium oxide) from corundum should result in a rim deprived of titanium (and/or iron) immediately around the precipitation, a texture that in theory could be used to test the formation mechanism of the needle inclusions. Unfortunately, such small variations at the nanometer scale are difficult to detect using current techniques,

and the compositional gradient may have been erased by diffusion in any natural corundum. The nanoscale polysynthetic twinning of rutile needle inclusions (figure 9) (He, 2006; Viti and Ferrari, 2006) is also likely to be exclusive to solid-state exsolution as a mechanism to redistribute the strain, since similar structures have not been reported in epitactically coprecipitated rutiles (Gao et al., 1992). It is not clear, however, how such nanoscopic twinning would be preserved in natural corundum over geological timescales.

CAT'S-EYE AND STAR CHRYSOBERYL

Cat's-eye chrysoberyl is the most recognized and most valuable chatoyant gemstone, especially if it is accompanied by a color change (cat's-eye alexandrite; figure 12A). In fact, the term *cat's-eye* refers to chatoyant chrysoberyl by default if the mineral species is not specified. Chrysoberyl (Cbrl: BeAl_2O_4) is a beryllium aluminate mineral that crystallizes in an olivine-type structure, with hexagonal close-packed (HCP) oxygen atoms positioned as in the corundum and hematite structures. The cation arrangement in the chrysoberyl structure, with half of the octahe-

dral sites filled by aluminum and one-eighth of the tetrahedral sites filled by beryllium, results in a pseudo-hexagonal orthorhombic symmetry. The chrysoberyl structure has been reported in many different crystallographic axis settings, making it difficult to compare the orientation notations across the literature. The *Pmnb* ($a = 5.48 \text{ \AA}$, $b = 9.42 \text{ \AA}$, $c = 4.43 \text{ \AA}$) setting will be used in this article because it intuitively keeps the HCP stacked layers parallel to (001), making it easy to compare different close-packed structures (Drev et al., 2015). The Miller indices cited in the literature using other settings will be translated to the *Pmnb* setting.

Despite its long history as a prominent phenomenal gemstone, there had not been any serious investigation into the details of needle inclusions in chrysoberyl until recently. By using a combination of optical microscopy, scanning electron microscopy equipped with energy-dispersive X-ray spectroscopy (SEM-EDS), and Raman spectroscopy, Schmetzer et al. (2016) conducted a comprehensive survey of included chrysoberyl from different locations and showed that almost all needle inclusions in natural chrysoberyl are rutile, with the only exception of ilmenite needles

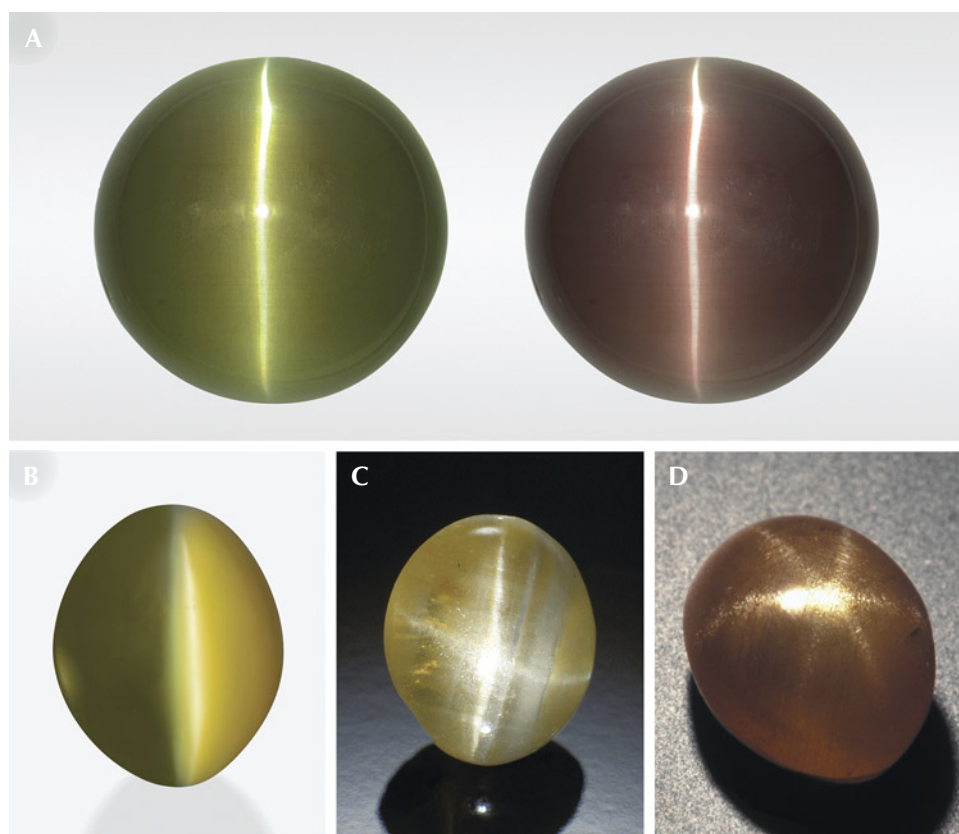


Figure 12. A: A 21.22 ct cat's-eye alexandrite under fluorescent light (left) and incandescent light (right). B: A 5.39 ct cat's-eye chrysoberyl displaying a "milk-and-honey" effect; courtesy of Tim Roark, Inc. C: A 1.54 ct four-rayed star chrysoberyl from Sri Lanka. D: A 2.29 ct natural six-rayed star chrysoberyl. Photos by Shunsuke Nagai (A), Orasa Weldon (B), Robert Weldon (C), and Maha Tannous (D).

found in a four-rayed star chrysoberyl from Sri Lanka. The oriented needle inclusions presumably form by precipitation of titanium originally dissolved in the chrysoberyl structure. Elongated cavities or channels may also exist along the same orientations as the rutile needles.

Three different needle orientations have been observed in chrysoberyl, elongated along the $[100]_{\text{Cbrl}}$, $\langle 110 \rangle_{\text{Cbrl}}$, and $[001]_{\text{Cbrl}}$ axes. The $[100]_{\text{Cbrl}}$ needles sometimes occur together with $\langle 110 \rangle_{\text{Cbrl}}$ needles, forming a pseudohexagonal array at a $\sim 60^\circ$ angle relative to one another. The $\langle 110 \rangle_{\text{Cbrl}}$ needles are often connected as twinned pairs to form a V shape, a heart shape, or a triangle, depending on needle width. Ilmenite needles are reported to occur only along the $[100]_{\text{Cbrl}}$ axis. No TEM analysis has been done on the needle inclusions parallel to the $(001)_{\text{Cbrl}}$ plane, but they most likely have an orientation similar to the rutile needles found in star sapphire in light of their similar HCP structures. The only atomic-resolution TEM study of the rutile precipitates in chrysoberyl, conducted on a twinned sample from Bahia, Brazil, showed a COR of $\{013\}_{\text{Rt}} // \{120\}_{\text{Cbrl}} + \langle 100 \rangle_{\text{Rt}} // \langle 001 \rangle_{\text{Cbrl}}$, which corresponds to the needles and striped plates elongated along the $[001]$ axis of chrysoberyl with L-shaped or zigzag cross sections observed by Schmetzer et al. (2016). It should be noted that these inclusions are quite unusual because they are elongated perpendicular to the stacked oxygen layers in the structure, rather than parallel to them.

Depending on the dominant needle orientation and the cut of the material, chrysoberyl can display chatoyancy or asterism with up to six rays (figure 12). It is not clear what process controls the orientation of the needle inclusions in chrysoberyl, but the temperature at which the titanium oxide starts precipitating out may play an important role. Synthetic cat's-eye and star chrysoberyl can be produced by growing Ti^{3+} -doped crystals in neutral or reducing atmospheres and then annealing in an oxygen atmosphere to precipitate TiO_2 . Only needles parallel to the $(001)_{\text{Cbrl}}$ plane have been observed in synthetic chrysoberyl (Schmetzer and Hodgkinson, 2011; Schmetzer et al., 2013, 2016). Titanium diffusion, as used to create artificial stars in sapphire, can also create chatoyancy in chrysoberyl. Another method, which uses a floating zone technique to create cat's-eye alexandrite with tubular fluid inclusions, has been patented by the Seiko Epson Corporation in Japan (Schmetzer et al., 2013).

STAR GARNET

Silicate garnet (Grt : $\text{X}_3^{2+}\text{Y}_2^{3+}[\text{SiO}_4]_3$) is a mineral group with one of the highest possible symmetries in three-dimensional space (space group 230, the last space group). The cubic symmetry allows the needle inclusions to be arranged in three dimensions, instead of coplanar as in corundum (figure 13). As a result, the bright lines constructing the asterism cannot all intersect at one point, which means multiple stars

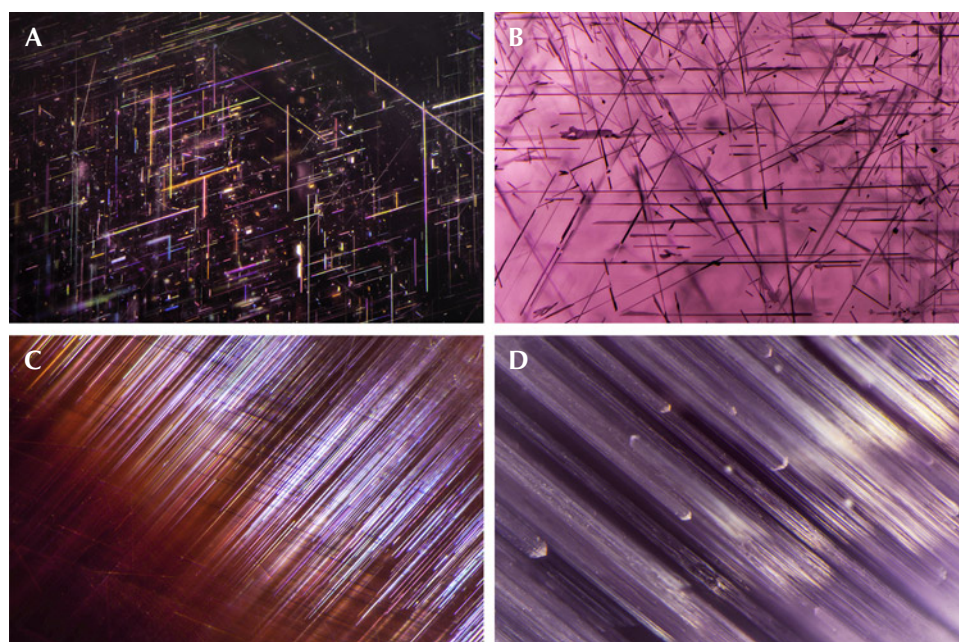


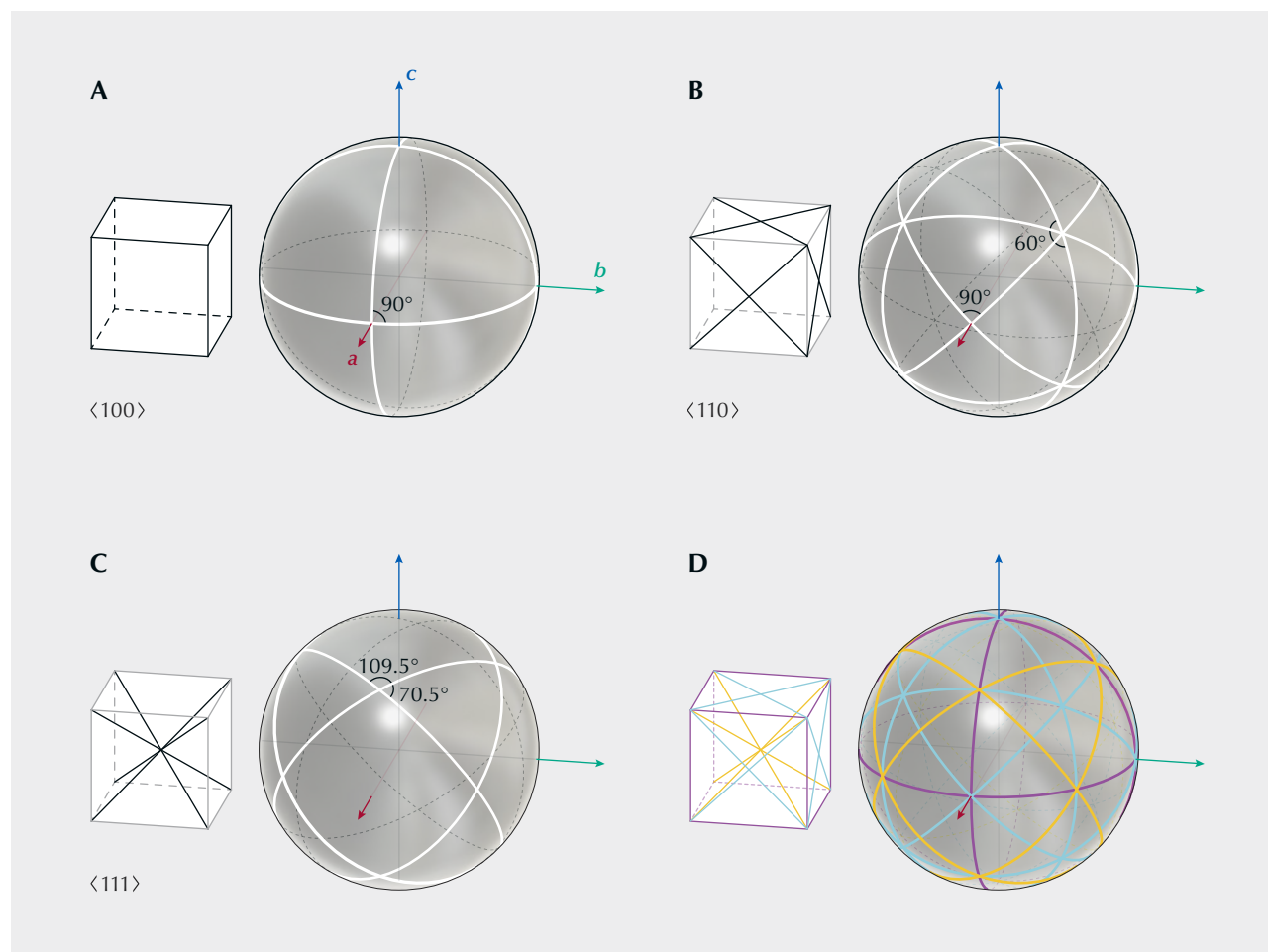
Figure 13. A: Rutile needles in star garnet. B: Needle inclusions in star spinel. C: Needle inclusions in cat's-eye garnet. D: Linear inclusions in cat's-eye spinel. Photomicrographs by Nathan Renfro; fields of view 3.35 mm (A), 3.38 mm (B), 1.95 mm (C), and 3.09 mm (D).

may be seen on a single garnet crystal. The best shape to demonstrate this “star network” is a sphere, as is commonly used when cutting a star garnet. Depending on the orientations of the needle inclusions, different asterism patterns may be observed on a polished spherical garnet crystal (figure 14). Therefore, the angles between the rays of the stars can be used to identify the orientations of the inclusions (Walcott, 1937; Kumaratilake, 1998; Schmetzer and Bernhardt, 2002; Schmetzer et al., 2002). Sometimes two different sets of inclusions can appear in the same garnet crystal, creating more complicated networks of stars (Guinel and Norton, 2006). Similar asterism patterns, although much rarer, can sometimes be observed in spinel crystals, which also

belong to the cubic crystal system (Walcott, 1937; Schmetzer, 1988; Kumaratilake, 1998; Schmetzer et al., 2000; Promwongnan et al., 2017; Hughes, 2018).

While rutile is the most common needle inclusion in garnet, other oriented inclusions such as ilmenite, magnetite, corundum, apatite, quartz, mica, olivine, pyroxene, and amphibole have also been observed (van Roermund et al., 2000; Hwang et al., 2010, 2013; Zhang et al., 2011; Ague and Eckert, 2012; Axler and Ague, 2015; Xu and Wu, 2017; Keller and Ague, 2019, 2020). However, the relation between asterism and inclusions other than rutile needles has yet to be confirmed. Most rutile needles are elongated along the $\langle 111 \rangle$ directions of garnet, creating four-rayed stars intersecting at $\sim 70^\circ/110^\circ$ angles

Figure 14. Schematic diagram showing the different needle orientations and their corresponding star networks in star garnet. A: $\langle 100 \rangle$ needles create six 4-rayed stars with 90° angles. B: $\langle 110 \rangle$ needles create six 4-rayed stars with 90° angles and eight 6-rayed stars with 60° angles. C: $\langle 111 \rangle$ needles create twelve 4-rayed stars with $\sim 70^\circ/110^\circ$ angles. D: Combinations of more than one set of needles can create more complicated networks. Note that almost all 6-rayed stars found in garnet are created by a combination of $\langle 100 \rangle$ and $\langle 111 \rangle$ needles (yellow and purple lines in D).



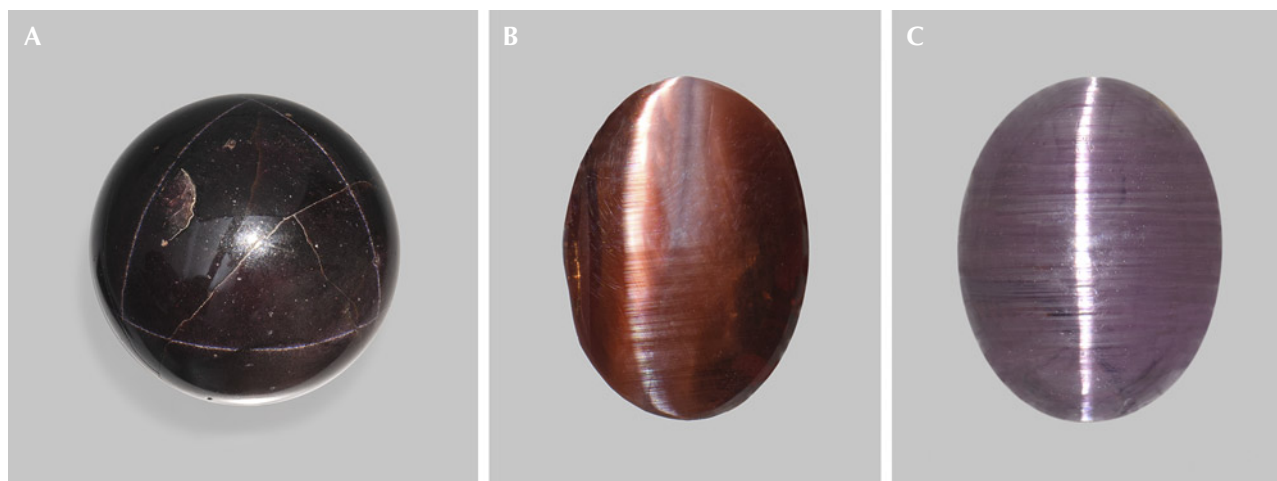


Figure 15. A: A 1,185 ct garnet sphere showing a star network of $\langle 111 \rangle$ needle inclusions (see figure 14). The star network under rotation is shown in video 2. Courtesy of GIA Museum, collection no. 4068. B: A 1.47 ct cat's-eye almandine garnet. C: A 9.39 ct cat's-eye spinel from Sri Lanka; courtesy of John I. Koivula. Photos by Emily Lane (A) and Annie Haynes (B and C).

(figures 14C and 15A; video 2). Rutile needles elongated along the $\langle 001 \rangle_{\text{Grt}}$ directions have also been reported (Hwang et al., 2015), producing asymmetric six-rayed stars with $\sim 70^\circ/55^\circ/55^\circ$ angles together with the $\langle 111 \rangle_{\text{Grt}}$ needles.² Although specific CORs between the rutile needles and the garnet host are commonly observed in TEM and EBSD analyses of star garnet, such as $\{100\}_{\text{Rt}} // \{134\}_{\text{Grt}} + \langle 013 \rangle_{\text{Rt}} // \langle 111 \rangle_{\text{Grt}}$ or $\{100\}_{\text{Rt}} // \{011\}_{\text{Grt}} + \langle 011 \rangle_{\text{Rt}} // \langle 100 \rangle_{\text{Grt}}$ (Keller and Ague, 2022), many of the $\langle 111 \rangle_{\text{Grt}}$ needles show nonspecific or “statistical” CORs, with $[001]_{\text{Rt}}$ falling onto a cone of $28.5^\circ \pm 2.5^\circ$ around $\langle 111 \rangle_{\text{Grt}}$ (Keller and Ague, 2019).

Most star garnets are in the almandine-pyropes-spessartine ($\text{Fe}_3\text{Al}_2\text{Si}_3\text{O}_{12}$ – $\text{Mg}_3\text{Al}_2\text{Si}_3\text{O}_{12}$ – $\text{Mn}_3\text{Al}_2\text{Si}_3\text{O}_{12}$) solid-solution series that form under high-pressure conditions deep in the earth. Due to its stability over a wide range of temperature and pressure conditions, garnet is an important indicator of evolving metamorphic conditions and underlying tectonic processes, and it has been studied extensively by metamorphic petrologists. Consequently, the formation mechanism of the needle inclusions is essential for the correct interpretation of the garnets' chemical data, which is why the CORs of the needles in garnet have drawn a lot of attention in the past decade. The complex crystal structure and chemistry of garnet, and the accordingly more diverse CORs of the needle inclusions, make this already controversial subject even more convoluted. As a result of the more complicated chemical reactions and structure-matching schemes, many different mechanisms have been proposed to explain the formation process of these needle inclusions, including solid-state precipitation,

interface-coupled dissolution-reprecipitation, and epitactic co-growth or overgrowth. Proyer et al. (2013) as well as Keller and Ague (2019) discussed all hypotheses in detail and concluded that (open-system) solid-state precipitation (exsolution) is the only process that withstands scrutiny. Other hypotheses either contradict observations or lack key supporting evidence. This conclusion is further supported by the successful prediction of CORs using an edge-to-edge matching model (Keller and Ague, 2022).

It should be noted that the asymmetrically oriented rutile needles intersecting the growth zones at steep angles (e.g., figure 13, C and D) are harder to explain by solid-state precipitation, which led to the interpretation of epitactic nucleation and co-growth (Griffiths et al., 2020). Precipitation within the crystal should fully observe the symmetry of the host mineral, whereas crystallization is one-dimensional along the growth surface, which reduces the local symmetry. However, as pointed out by Keller and Ague (2019), preexisting crystallographic defects, chemical gradients, as well as varying lattice parameters might also promote preferred precipitations along certain directions. Nonetheless, these parallel needles could create chatoyancy instead of asterism in the occasionally reported cat's-eye garnet (figures 13C and 15B). Similar linear features can also be found in cat's-eye spinel (figures 13D and 15C).

²The $\langle 011 \rangle_{\text{Grt}}$ needle orientation reported by Guinel and Norton (2006) is an error and should be $\langle 001 \rangle_{\text{Grt}}$ instead.

STAR QUARTZ

Although rutile is the most common needle-like inclusion in quartz (Qz : $\alpha\text{-SiO}_2$) and can create poor-quality asterism or chatoyancy with a strange shape (Johnson and McClure, 1997; Schmetzer and Steinbach, 2022, 2023; Gauthier et al., 2023), the high-quality stars observed in quartz are not related to titanium oxide. These star quartzes are only found as turbid massive quartz and never as clear euhedral quartz crystals (Goreva et al., 2001; White, 2015), although there may be a sampling bias because only massive anhedral quartz would be cut into cabochons or spheres to display the asterism. Most star quartz has pink color that varies from bright to pale; thus, it is called rose quartz. This name is sometimes also applied to euhedral pink quartz crystals, the color of which is photochemically unstable and can be bleached away easily with UV light or low heat. The pink color of massive star rose quartz, on the other hand, is stable up to $\sim 575^\circ\text{C}$, indicating a completely different coloring mechanism.

Sillimanite (Sil : Al_2SiO_5) was first identified using TEM as the needle inclusions in a star quartz from the Ratnapura district, Sri Lanka (Woensdregt et al., 1980), elongated along $\langle 001 \rangle_{\text{Sil}} \parallel \langle 100 \rangle_{\text{Qz}}$, with $\{110\}_{\text{Sil}} \parallel \{001\}_{\text{Qz}}$. Dumortierite (Dum : $\text{Al}_7\text{Si}_3\text{BO}_{18}$) was also identified as the fibrous residue observed after rose quartz was dissolved in hydrofluoric acid (Applin and Hicks, 1987; Ignatov et al., 1990; Goreva et al., 2001). Further study revealed that these dumortierite inclusions contain significant amounts of iron and titanium, and they show a superlattice structure likely due to cation ordering (Ma et al., 2002). The pink color of rose quartz turned out to result from the iron-titanium intervalence charge transfer in these nano-inclusions. It should be noted that the earlier reports of rutile nanoneedles in rose quartz (von Vultée, 1955, 1956; Eppler, 1958) were most likely incorrect, as none of the 29 rose quartz samples from different locations analyzed by Goreva et al. (2001) showed any evidence of rutile. Regrettably, the COR between these dumortierite needles

Figure 16. A: A 178 ct 12-rayed star rose quartz sphere in transmitted light; courtesy of Far Arden Essentials. B: An 8.51 ct double polished rose quartz cabochon showing double stars due to reflection from the back surface; courtesy of GIA Museum, collection no. 35214. C: A 31.37 ct star quartz from Sri Lanka shows a complex network of stars with a 12-rayed star in the center; courtesy of Michael Schramm. D: A 44.25 ct star smoky quartz with a network of stars; courtesy of GIA Museum, collection no. 31575. E: A 22 ct multi-star quartz with a strong 6-rayed star in the center. Photos by Lylith Aradia Moon (A), Emily Lane (B and D), Maha Tannous (C), and Andrew Quinlan (E).

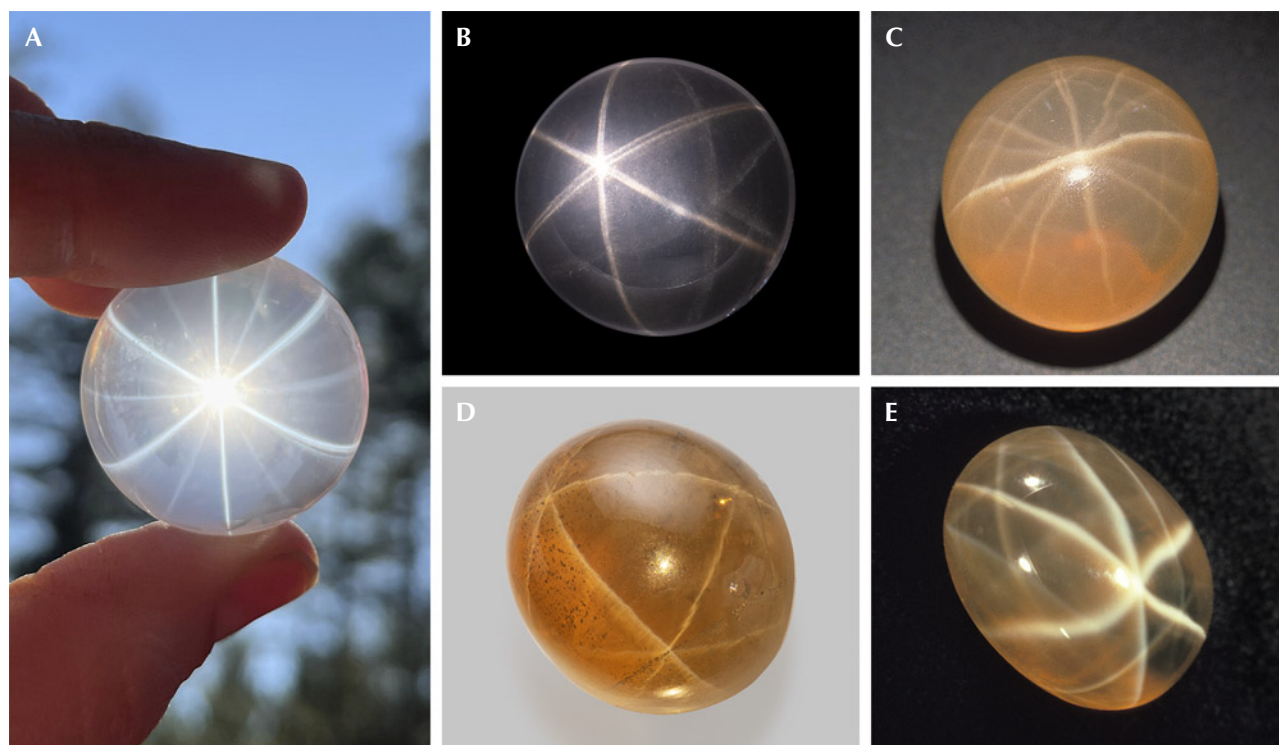




Figure 17. A: A 255 ct polished rectangular slice of tiger's-eye from South Africa. B: A 22.03 ct tiger's-eye cabochon from South Africa showing waves due to bent inclusions; courtesy of John I. Koivula. C: A 220 ct hawk's-eye oval cabochon. D: A 19.82 ct pietersite round cabochon showing chatoyant fragments of different colors. Photos by Emily Lane (A and C) and Annie Haynes (B and D).

and the quartz host is unknown, as all analyses were performed on residue fibers with all the quartz dissolved away.

The silicate needle inclusions, most likely formed by solid-state exsolution (Ma et al., 2002), have low RIs that are close to those of the quartz host, resulting in much weaker scattering power compared to the strongly refractive rutile or iron oxide inclusions in other gemstones. Therefore, star quartz has a more transparent appearance than star corundum or garnet. The star in rose quartz is often more strongly observed using light transmitted through the stone, an effect known as “diasterism” (figure 16A) (Killingback, 2006), whereas only “epiasterism” under reflected light can be observed in most other asteriated gemstones.

Some rose quartz crystals display 12-rayed stars, indicating two sets of needle inclusions with different crystallographic orientations (figure 16, A and C). It is possible that the two orientations are from different mineral inclusions, as both dumortierite and boron-bearing sillimanite were found as needles in a rose quartz from Brazil (Ma et al., 2002). Needle

inclusions elongated off the (001) plane are also occasionally observed in quartz (Johnson and Koivula, 1999; Schmetzer and Glas, 2003), creating complex star networks in sphere-cut crystals similar to star garnet (figure 16, D and E; video 3). Chatoyancy is also very rarely observed in quartz (Choudhary and Vyas, 2009; Choudhary, 2011), indicating needle inclusions elongated parallel to the *c*-axis. Unfortunately, the nature of these abnormally oriented needles is not clear.

TIGER'S-EYE AND PIETERSITE

Tiger's-eye is a chatoyant variety of quartz containing altered amphibole needle inclusions (figure 17, A and B). Unlike the other star or chatoyant gemstones in which the host is a single crystal, tiger's-eye consists of columnar polycrystalline quartz crystals that are 0.1–1.0 mm in diameter and 1–10 mm in length (Heaney and Fisher, 2003). As indicated by its orientation, the chatoyancy of tiger's-eye is created by fibrous mineral inclusions and not the columnar quartz crystals (figure 18). No special COR has been observed between the needle inclusions and the

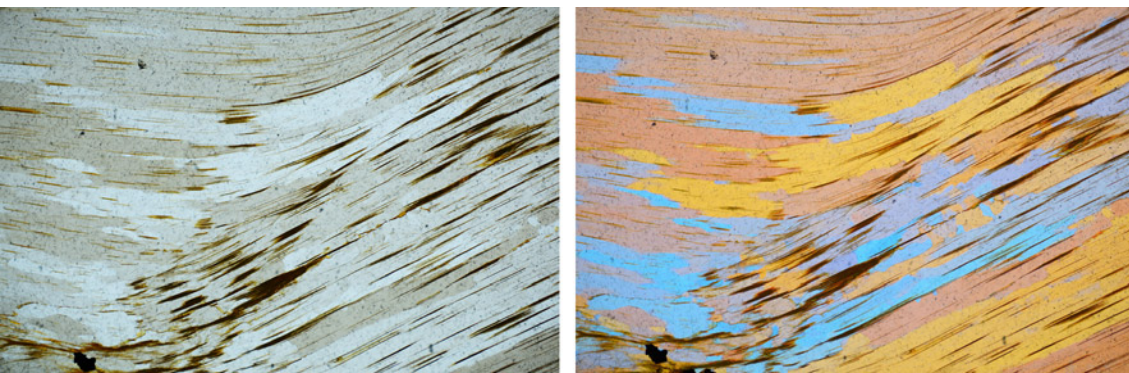


Figure 18. Thin section of tiger's-eye under cross-polarized light (left) and with a lambda plate inserted to enhance the contrast across grain boundaries (right). The dark brown needles are the iron oxide/hydroxide from weathered amphibole. Photomicrographs by Amir C. Akhavan; field of view 1.5 mm.

quartz crystals, suggesting that the aligned needle orientation must be controlled by crystal growth. The typical golden-brown color is caused by the iron-rich amphibole needles being weathered to iron (hydr)oxides. In the less common dark blue variety, commonly known as hawk's-eye (or falcon's-eye) (figure 17C), the amphibole needles are less altered and retain their original color.

Tiger's-eye has long been attributed to pseudomorphism with quartz replacing crocidolite, a blue asbestiform variety of the sodic amphibole riebeckite ($\text{Rbk: Na}_2\text{Fe}_5\text{Si}_8\text{O}_{22}(\text{OH})_2$) (Wibel, 1973). However, Heaney and Fisher (2003) proposed that quartz and riebeckite grew synchronously through an episodic crack-seal mechanism, as optical and electron microscopic observations failed to show any evidence for pseudomorphism.

Pietersite, reportedly found only in Namibia and China, is generally described as a brecciated variety of tiger's-eye (figure 17D). Although the chatoyancy

is also caused by crocidolite fibers, the silica that composes pietersite is in the form of chalcedony (discussed later in the section on iridescent agate) instead of columnar quartz. The chaotic texture of pietersite also indicates a formation mechanism different from that of tiger's-eye. Instead of pseudomorphism or a crack-seal mechanism, pietersite specimens are theorized to have formed as solution breccias, in which the crocidolite fibers form by late-stage reactions between chalcedony and hematite in a sodic fluid (Hu and Heaney, 2010).

OTHER ASTERIATED AND CHATOYANT STONES

Needle-like inclusions, which are the most common inclusion habits, can be found in almost any included mineral. The shape of an inclusion is often controlled by the lattice match across the boundary between the included mineral and the host, as demonstrated by the examples discussed above. A needle inclusion

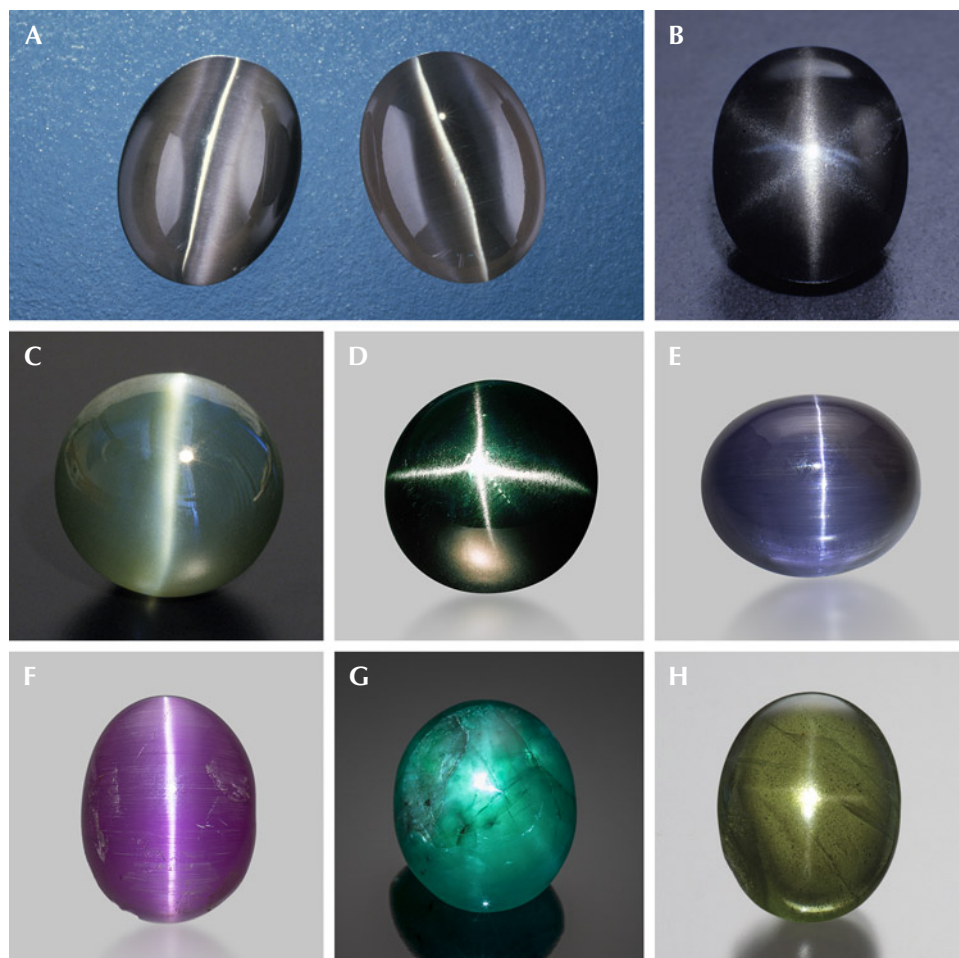


Figure 19. A: A 1.72 ct fiber-optic glass cabochon (left) looks visually identical to a 1.78 ct cat's-eye sillimanite (right). B: A black star scapolite. C: A 125.46 ct cat's-eye zircon. D: A four-rayed star diopside. E: A 2.69 ct cat's-eye tanzanite; courtesy of John I. Koivula. F: A 2.73 ct cat's-eye pezzottaite from Madagascar; courtesy of John I. Koivula. G: A 25.86 ct star emerald; courtesy of Manuel Marcial de Gomar. H: A 22.21 ct four-rayed star peridot. Photos by Shane F. McClure (A), Robert Weldon (B, G, and H), ICA (C), Mike Havstad (D), and Emily Lane (E and F).

requires only a near-perfect lattice match along one dimension, with the interfaces along the other two dimensions restrained to a very small scale by strain. Many defects generated during crystal growth or dissolution, such as growth tubes and etch channels, also have an oriented linear form, which may scatter light analogously to needle inclusions. In addition, some minerals—such as actinolite, hypersthene, sillimanite, and chrysotile—naturally adopt a columnar or fibrous habit similar to that observed in tiger’s-eye. Therefore, chatoyancy and asterism may be observed in almost any mineral host included with fibrous minerals or defects (figure 19). Even diamond has been reported to show asterism (Watts, 2021). There have been attempts to list all the gemstones that are reported to display asterism or chatoyancy (Kumaratilake, 1997; Steinbach, 2016, 2018), which will not be repeated here. Because the star and cat’s-eye effects can only be observed in a cabochon cut, it is highly probable that many chatoyant and asteriated minerals have not been discovered simply because no one has cut and polished them into a curved shape. In fact, many of the reported stars and cat’s-eyes in gemstones are so weak that they are only observable under strong fiber-optic light, which may attract the attention of niche collectors, but probably would not be an eye-catcher in the general gem market. The columnar or fibrous texture is also easy to fabricate in glass and plastic by simply pulling

and fusing together a bundle of optical fiber. Therefore, chatoyant glass (figure 19A, left) and plastic are very affordable imitations of cat’s-eye gemstones of any color. Nonetheless, there is yet to be a convincing glass or plastic imitation for asterism, as the crystallographic symmetry is necessary to force the fibers into multiple directions.

ADVENTURESCE IN GEMSTONES

The word *aventurine* derives from *a ventura* in Italian, meaning “by chance,” originating from the glittering glass “*avventurina*,” now known as “*aventurine glass*” or “*goldstone*” (figure 20A), which was allegedly invented by accident in eighteenth-century Italy (Moretti et al., 2013). The name was first adopted in mineralogy for quartzite (a metamorphic rock predominantly composed of polycrystalline quartz) containing glimmering mica crystals (figure 20B), although the best-known aventurescent mineral is aventurine feldspar. The term *aventurescence* is now used to describe the glittering effect created by isolated and visually discernible flat interfaces scattered in any transparent to translucent gemstone. Most aventurescence in gemstones is caused by oriented inclusions, and would appear as a sudden intense reflection (box E) that occurs only in certain directions, commonly known as schiller (Colony, 1935).

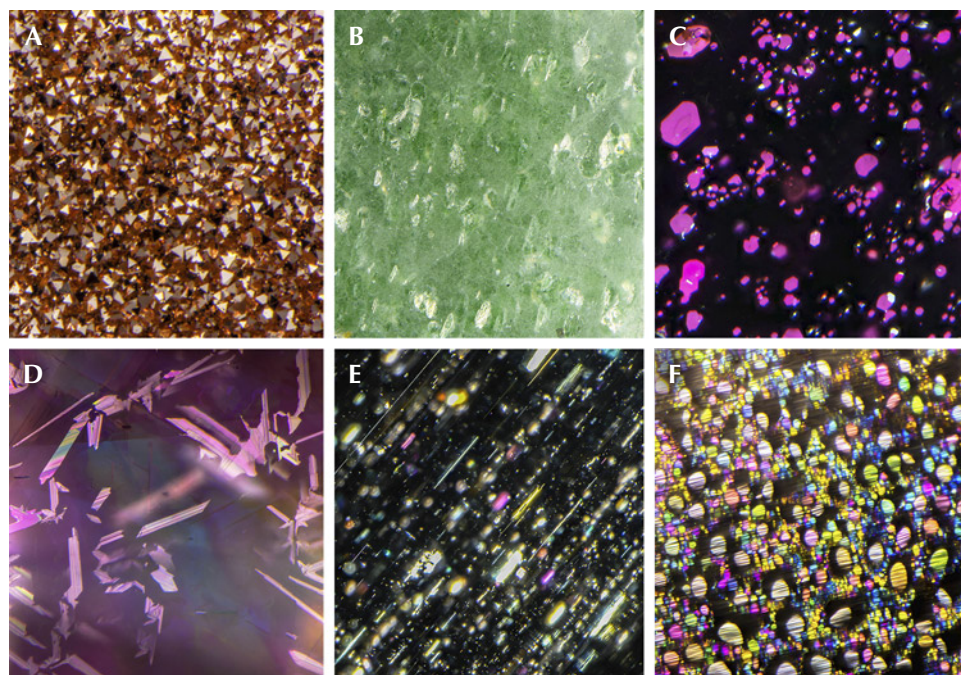


Figure 20. A: Triangular copper particles in goldstone glass. B: Glitters of fuchsite (Cr-muscovite) in aventurine quartz (quartzite). C: Flaky covellite (CuS) inclusions in a quartz crystal showing magenta color under reflected lighting. D: Flaky titanite (sphene) inclusions in a spinel crystal. E: Rectangular and needle inclusions in aventurescent aquamarine. F: Thin-film fluid inclusions in aquamarine. Photomicrographs by Nathan Renfro; fields of view 1.34 mm (A), 5.50 mm (B), 3.15 mm (C), 1.22 mm (D), 5.78 mm (E), and 2.36 mm (F). Courtesy of John I. Koivula.

BOX E: REFLECTION OF LIGHT AND THIN-FILM INTERFERENCE

When light is incident on a smooth interface between two optical media with different RIs, part of its energy reflects off the interface while the rest transmits through the material. The direction of the reflected light follows the law of reflection, with the reflected angle the same as the incident angle. The intensities of the reflected light rays follow the Fresnel equations and are functions of the incident angle, the relative RI between the two media, and the polarization of light. Generally, reflection is stronger with a larger relative RI. For incident light perpendicular to the interface, the reflectivity, or the fraction of energy reflected at the surface, equals:

$$\left(\frac{n_A - n_B}{n_A + n_B} \right)^2 \quad (\text{E-1})$$

in which n_A and n_B are the RIs of the two media. The reflectivity also decreases with increasing glancing angle (angle between the incident light and the reflecting surface) (figure E-1).¹

When two parallel interfaces are very close to each other, with the distance in between less than the wavelength of light, the light rays reflected from them interfere with one another and create colors. This process is commonly known as thin-film interference. The interference conditions depend on the RI of the film

relative to the media around it (figure E-2) because the phase of the reflected light is shifted by 180° when traveling on the side with lower RI, but not when traveling on the side with higher RI. When the thin film is coated on the surface of a medium with higher RI, such as the antireflective coating on eyeglasses and binoculars or the tarnish layer on the surface of ore minerals, the phase change occurs at both surfaces of the thin film (figure E-2, left). Therefore, constructive interference occurs when the light reflected from the bottom surface of a thin film with thickness d travels one (or any integer multiple m) wavelength (λ) farther than the light reflected from the top surface:

$$2n_B d \sin \theta_B = m\lambda \quad (\text{E-2})$$

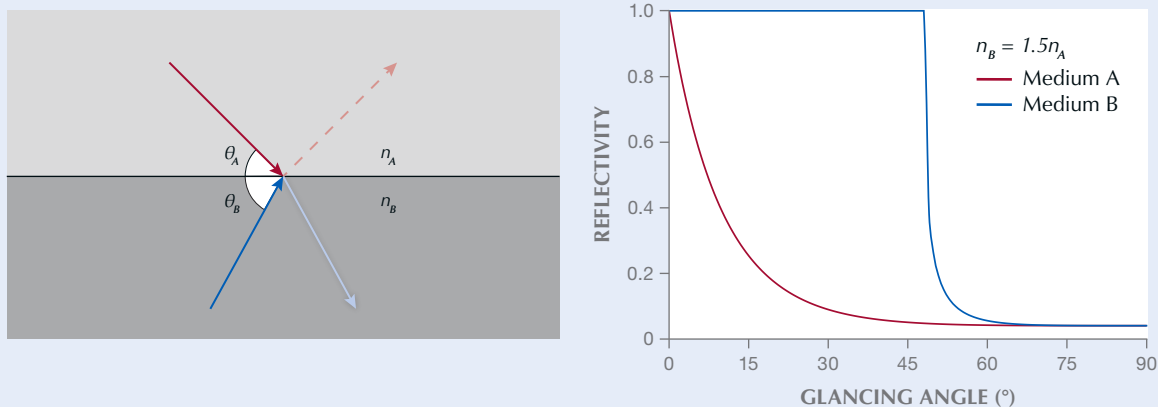
On the other hand, if the thin film is sandwiched between the same medium, such as a soap film or a bubble in air, or film inclusions in transparent minerals, the phase change occurs only at the top surface (or only at the bottom surface if the RI of the film is lower than the surrounding medium) (figure E-2, right). In this case, constructive interference occurs if the optical path difference is half of the wavelength (or any odd integer multiples of the half wavelength):

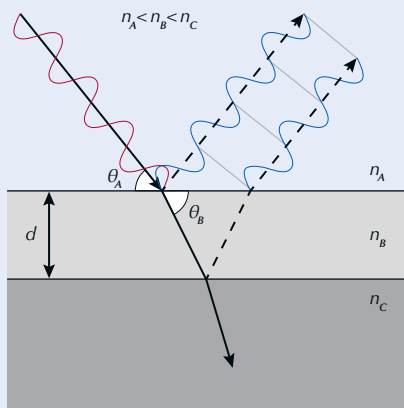
$$2n_B d \sin \theta_B = (m - 1/2)\lambda \quad (\text{E-3})$$

Interference colors also can be created by pairs of thin film layers periodically stacked on top of one another. This is much more complicated than simple thin-film interference because incident light is split at each interface and

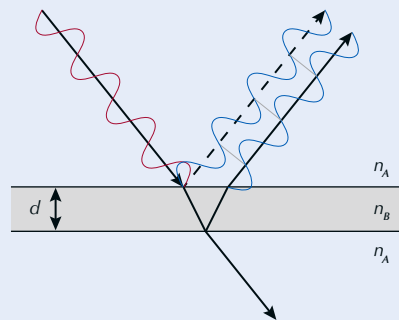
¹Glancing angle instead of incident angle is used in this article to maintain consistency with the other optical processes discussed.

Figure E-1. Schematic drawing of light rays reflecting off a flat interface, with reflectivity plotted as a function of the glancing angle (the angle θ between the incident light and the interface). When light is incident from the side with a smaller RI (red arrows from medium A), only a fraction of the energy reflects back (red curve on the graph), with the rest refracted through the interface. However, from the side with a larger RI (blue arrows from medium B), 100% of the energy reflects back at small glancing angles (total internal reflection, flat section of blue line on the graph) and only refracts through the interface at large glancing angles.





$$2n_B d \sin \theta_B = m\lambda$$



$$2n_B d \sin \theta_B = (m - 1/2)\lambda$$

Figure E-2. Schematic drawing of thin-film interference between light reflected by two adjacent interfaces. Left: When the RI of the film is intermediate between the media above and below it, the light reflected by both interfaces changes its phase by 180° , resulting in a simple interference condition (equation E-2). Right: When the RI of the film is higher or lower than the media both above and below it, the phase change occurs only at one of the interfaces, and the required thickness for interference is halved (equation E-3).

reflected multiple times before exiting the material (figure E-3). This type of texture is known as a one-dimensional photonic crystal (periodic stacking in one direction). Qualitatively, it can be considered the summed effect of multiple thin-film interferences. For each pair of A-B layers, with respective RIs of n_A and n_B , the condition for constructive interference is:

$$2(n_A d_A \sin \theta_A + n_B d_B \sin \theta_B) = m\lambda \quad (\text{E-4})$$

This equation models the interference among all solid (or dashed) reflected rays in figure E-3. At the same time, thin-film interference is generated within individual A (or B) layers (between solid and dashed rays in figure E-3):

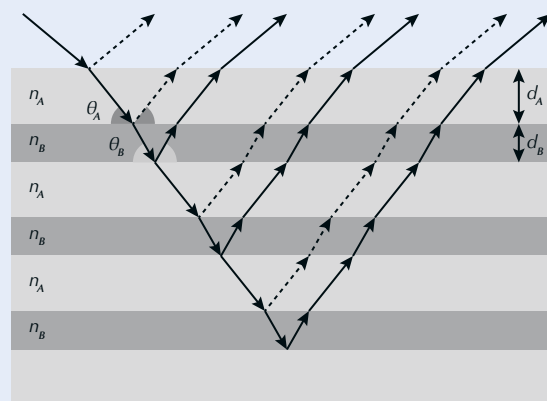
$$2n_A d_A \sin \theta_A = (m' - 1/2)\lambda \quad (\text{E-5})$$

If both equations are satisfied, the reflected intensity is maximized, and the structure is known as an ideal multilayer, whereas if only the first equation (equation E-4 here) is satisfied, the reflected intensity is weaker, and the structure is called a non-ideal multilayer (Kinoshita, 2008).

Note that the interference wavelength (λ) is a function of the film thickness (d), the RI of the film (n_B), and the angle between the refracted light and the film surface (θ_B), which means that in theory the interference color should change with different incident angles. However, the RI of the interfering film is often much higher than that of air or the host mineral, so the range of θ_B is much smaller than θ_A . Moreover, the reflection is only strong enough to be

observable at certain incident angles due to Fresnel's equations (figure E-1), further restraining the possible range of θ_B . This is partly why the interference color from thin films or multilayers in minerals often remains the same with changing viewing angles.

Figure E-3. Schematic drawing of multilayer interference. The interference condition can be approximated by thin-film interference of each periodic layer pair, and also by each individual layer.



It should be noted that although less abundant than needle inclusions, flaky or thin-film inclusions are not uncommon in minerals (e.g., figure 20, C–F). Indeed, inclusions of any shape may have flat facets that reflect light. Almost all needles discussed above have a rectangular cross section with flat surfaces when examined with an electron microscope, which means light will be scattered preferentially perpendicular to the flat surfaces and create a schiller or sheen effect. The straight edges of some film inclusions, on the other hand, can also scatter light more randomly like a needle, creating chatoyancy or asterism in a cabochon-cut stone. It is not unusual for inclusions in a stone to vary in size and shape. As a result, the appearance of a stone, or the phenomenon it displays, depends greatly on how it is cut and polished.

COPPER SUNSTONE

Gem-quality aventurine feldspars are typically known as “sunstones” (Andersen, 1915), with mainly two types of reflective inclusions found in nature: metallic copper and iron oxides. Copper platelet inclusions in feldspars are rare and only have been reported in feldspar phenocrysts in certain basalts, as in the well-known Oregon sunstone. Similar material has also been reported from Ethiopia, but it shows a chemistry distinct from that of Oregon sunstone (Kiefert et al., 2019; Sun et al., 2020). The copper platelets are oriented along the cleavage planes of

feldspar, mostly the (010) plane and less commonly the (001) plane (Farfan and Xu, 2008; Xu et al., 2017). Because the copper platelets are completely opaque, the color of the schiller arises only from the light reflected by the copper particles, which is reddish brown (figure 21). Copper sunstones may contain colloidal copper particles in addition to the platelets, resulting in red or blue-green bodycolors underneath the schiller (again, see figure 1 second from left in bottom row). As mentioned earlier, copper is known to diffuse quickly in feldspar crystals, which may be why the relatively fast cooling in volcanic rocks is necessary for them to precipitate as metallic particles instead of diffusing out of the crystal as the solubility of copper decreases in the feldspar. Nonetheless, the cooling rate of sunstone-bearing basaltic rocks is still much slower than in any experiments in a laboratory. It may take months to years for the basaltic lava to cool down from the melting temperature. This is why copper sunstone showing strong aventurescence has yet to be created in a laboratory, even though red and green colors have been produced relatively easily from copper diffusion (Jin et al., 2023).

HEMATITE SUNSTONE

Hematite sunstones are mostly found in granites or pegmatites and can be generally divided into two categories: orthoclase and sodic plagioclase (oligoclase or albite). They typically can be easily distinguished by

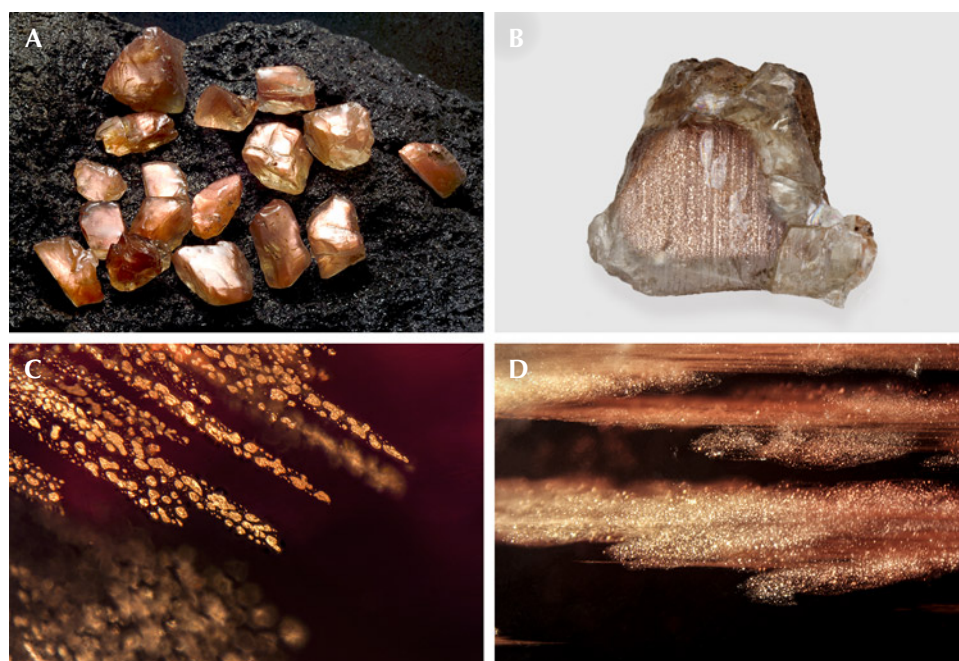


Figure 21. A: Rough Oregon sunstones showing strong schiller from copper platelets. B: A 20 ct rough Oregon sunstone from the Ponderosa mine. C and D: Copper platelets of different sizes and shapes in Oregon sunstone. Photos by Desert Sun Mining & Gems (A), Robert Weldon (B), and Rosie Young (C and D); fields of view 3.57 mm (C) and 5.14 mm (D).

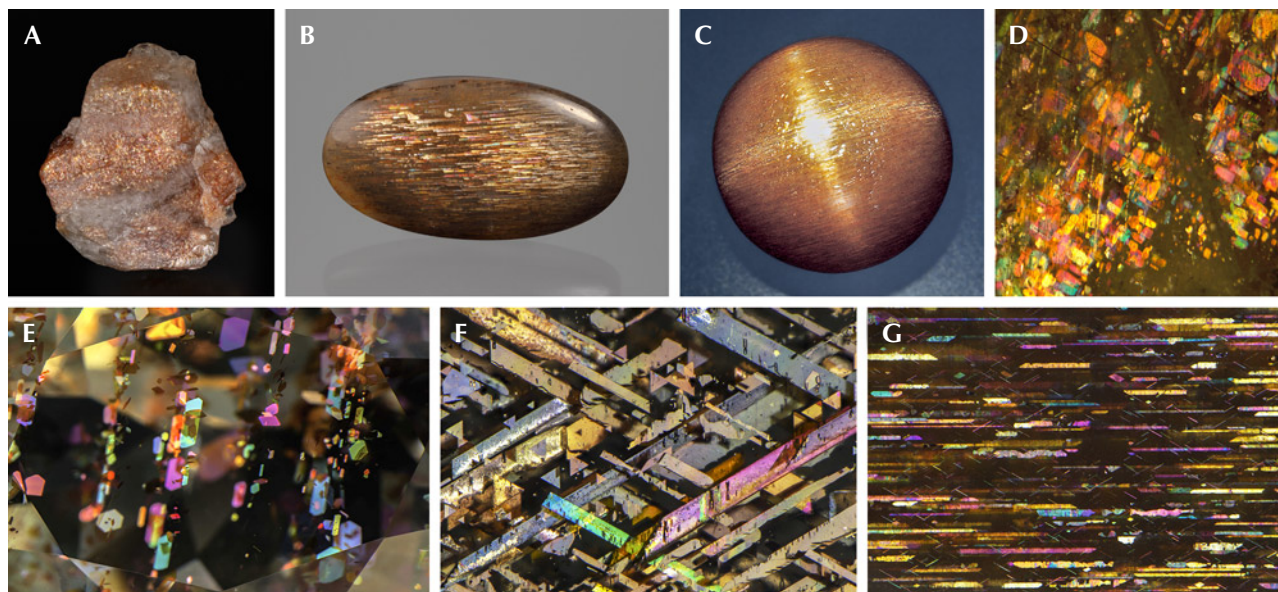


Figure 22. A: A 42.50 ct rough oligoclase sunstone reportedly from Tanzania. B: An 18.40 ct “meteor shower sunstone” cabochon from Tanzania. C: A 14.77 ct round orthoclase sunstone cabochon from Tanzania showing a four-rayed star. D: Iridescent reflection from hematite inclusions in a Canadian labradorite due to thin-film interference. E: Hematite platelets in an oligoclase “confetti sunstone” from Tanzania; courtesy of John I. Koivula. F: Thin-film magnetite and hematite blades elongated along the $\langle 011 \rangle$ directions in an orthoclase rainbow lattice sunstone from Australia. G: Thin-film iridescent hematite blades elongated along the $\langle 010 \rangle$ directions in an orthoclase sunstone from Tanzania, along with some tiny needles along the $\langle 011 \rangle$ directions. Photos by Emily Lane (A), Annie Haynes (B), Maha Tannous (C), Shiyun Jin (D), and Nathan Renfro (E, F, and G); fields of view 2.2 mm (D), 9.56 mm (E), 6.39 mm (F), and 7.20 mm (G).

the shape and orientation of the hematite films. Sodic sunstone, mostly oligoclase, such as the most studied examples from Tvedestrand, Norway (Andersen, 1915; Divljan, 1960; Neumann and Christie, 1962; Kraeft and Saalfeld, 1967; Copley and Gay, 1978, 1979, 1982), contains rectangular and hexagonal hematite plates along the (112) , $(1\bar{1}2)$, (150) , and $(\bar{1}50)$ planes. Due to the triclinic symmetry of plagioclase feldspar, the hematite plates are oriented askew relative to the cleavage planes (figure 22, A, D, and E). Orthoclase sunstones, such as those from Tanzania (Hänni et al., 2003) and Australia (Koivula and Kammerling, 1989), on the other hand, tend to have long hematite blades parallel to the (100) plane and extended along the $[010]$ or $\langle 011 \rangle$ directions of the feldspar (figure 22, B, C, F, and G), which are always symmetrical around the cleavage planes (Jin et al., 2022b). These elongated inclusions often create chatoyancy or asterism when cut into a cabochon (Hyrsl, 2001; Hänni et al., 2003). Smaller hexagonal or triangular flakes parallel to the (100) and (102) planes are also common in lower-quality orthoclase sunstones (Liu et al., 2018; Jin et al., 2022b).

Unlike the metallic black color of large hematite crystals, the hematite film inclusions in sunstones are transparent with orange to deep red colors depending on their thicknesses, yielding what appears to be an orange to red bodycolor. The transparent hematite flakes in sunstones are sometimes misidentified as biotite by those who are not familiar with their transparent appearance (Lee and Parsons, 2015). The thinner hematite inclusions can also create iridescent colors due to thin-film interference (figure 22, D–G), primarily observable only with an optical microscope.

The process that creates the hematite flakes in sunstones takes much longer than the process that creates the copper platelets, as indicated by the different types of rocks they are found in. The mechanism that produces the hematite flakes is still not well understood, with several hypotheses proposed over the past two centuries (Smith and Brown, 1988, pp. 638–639). Simultaneous crystallization was the first to be rejected because hematite flakes are not oriented along the common growth faces of feldspar (Andersen, 1915). Precipitation of iron from the feldspar lattice is the simplest theory, but this

explanation poses the question of why some feldspars with exceptionally high iron content remain hematite-free. Another hypothesis is that reaction with the surrounding fluid introduces iron into the feldspar crystals, but it does not explain how the imported iron is transported and precipitated as hematite flakes inside the feldspar. A recent study of rainbow lattice sunstone from central Australia showed that the hematite films in orthoclase sunstone were originally magnetite (Mag: Fe_3O_4) films that were oxidized at a later stage (Jin et al., 2022b). Rainbow lattice sunstone is a unique sunstone with exceptionally large magnetite and hematite “blades,” creating a rainbow lattice effect resulting from the thin-film interference of light reflected by hematite films (figure 22F). Only the thinner parts of the magnetite films have been oxidized to hematite, showing light yellow to orange colors in transmitted light and pink to blue iridescence under reflected light. The magnetite films, crosscutting the plagioclase lamellae exsolved from the orthoclase matrix, clearly represent precipitation of iron dissolved in the feldspar lattice, likely due to decreasing oxygen fugacity. The orientation of the magnetite films, like the other oriented precipitates in mineral crystals

such as star sapphire, is a result of minimization of the surface energy by finding the interface with the best lattice match. The same mechanism should apply to other orthoclase sunstones, such as those from Tanzania and the United States (North Carolina) (Hänni et al., 2003; Choudhary, 2008; Challener et al., 2017), based on the similar appearance and orientation of the hematite films. The only difference is that all of the precipitated magnetite films in the other orthoclase sunstones have been oxidized to hematite due to their smaller and thinner sizes. However, it is not clear whether this process can be expanded to the sodic plagioclase sunstones, as those hematite flakes are typically thicker (darker red color with less iridescence) with more pristine hexagonal forms.

CLOUDED FELDSPAR

Although only a small proportion of included feldspars qualify as sunstones, crystallographically oriented needle-like iron oxide inclusions are almost ubiquitous in plutonic and metamorphic plagioclase feldspars (e.g., figure 23A). Feldspars containing dense iron oxide needles, also known as clouded feldspars

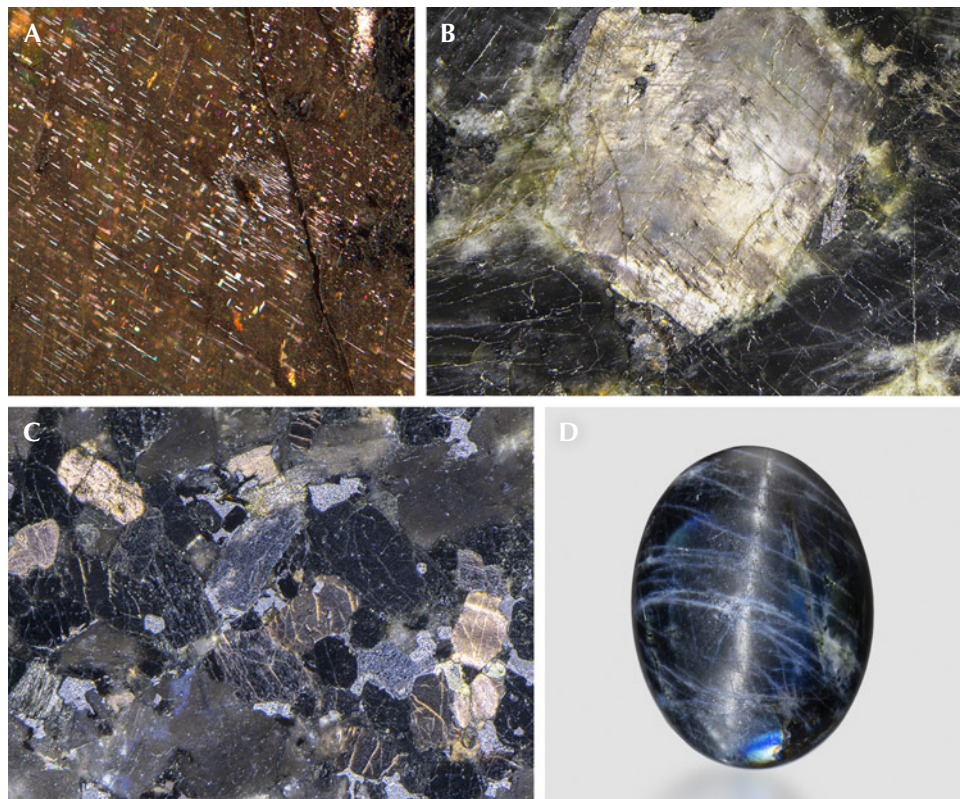


Figure 23. A: Oriented needle inclusions in a labradorite from Ukraine (commercially known as “Volga Blue”). B: A labradorite crystal in a polished anorthosite slab (Volga Blue) showing silver sheen at a different angle from iridescence. C: Labradorite crystals in a gabbro slab from India (commercially known as “black galaxy”) showing golden sheen from oxidized magnetite needles. D: A 14.54 ct labradorite cabochon showing chatoyancy. Photos by Shiyun Jin (A), Nathan Renfro (B and C), and Emily Lane (D); fields of view 4.76 mm (A), 36.5 mm (B), and 9.7 mm (C).

(Smith and Brown, 1988, p. 639), display black, dark gray, or brown colors with an almost opaque appearance. A silver (or less commonly golden) sheen can often be observed on the polished surfaces of these clouded feldspars, which makes their host gabbro or anorthosite rocks popular countertop materials (figure 23, B and C). When cut into cabochons, clouded feldspar can display a cat's-eye (or star) effect as expected (figure 23D). However, cat's-eye (or star) plagioclase feldspars rarely appear in the gem market, mostly because the quality of the chatoyancy or asterism is generally not attractive enough by itself to be worth the cost of careful cutting and polishing.

Due to their geological importance in the study of magmatic and metamorphic processes, as well as the historical evolution of Earth's magnetic field, the needle inclusions in plagioclase feldspar have been studied extensively compared to the other oriented inclusions found in minerals, providing important insights into how they formed. Combining optical microscopy, EBSD, and TEM analysis has revealed multiple types of magnetite needles with different CORs to the host feldspars (Bian et al., 2023 and references therein). Most observations suggest that these needles form by precipitation of iron that was originally dissolved in the feldspar structure, perhaps due to interaction with a reducing fluid (Bian et al., 2021). The crystallographic orientations of the magnetite needles likely resulted from the minimization of both interfacial energy and atomic rearrangement. Interestingly, the needle inclusions seem to appear only in more calcic plagioclase feldspars (andesine, labradorite, bytownite, and anorthite), whereas the thin-film and platy iron oxide inclusions (hematite or magnetite) are primarily found in sodic plagioclase and alkali feldspars (oligoclase, albite, and orthoclase)

(Jin et al., 2022b), although both types of inclusions have been observed in labradorite from Canada (figure 22D) (Jin et al., 2021). Several factors might contribute to this different morphology of iron oxide inclusions, including lattice parameters and crystal structures, anisotropic diffusion of iron, and thermal and redox histories.

GOLDEN SHEEN SAPPHIRE

Another example of gemstones displaying both asterism and aventurescence is gold sheen sapphire (or Zawadi sapphire) reportedly from Kenya (figure 24, left), yet the exact location of the mine is still unclear (Bui et al., 2015; Soonthorntantikul et al., 2016). Although most star sapphires can display a weak shimmer or sheen on a flat polished (001) surface, gold sheen sapphire shows a much stronger aventurescence, comparable to that of sunstone. A facet-grade aventurescent sapphire, with an appearance resembling Oregon sunstone's schiller (figure 24, right; Sripoonjan et al., 2019), was also reported with a Kenyan origin, although it may not be from the same mine as the typical translucent to opaque material. And obviously, gold sheen sapphire also displays very strong asterism in a cabochon cut (Bui et al., 2015; Miura et al., 2018). Most inclusions in gold sheen sapphire are the typical acicular hematite and ilmenite as in most star sapphires but noticeably denser in number (again, see figure 8C). Many of these hematite and ilmenite inclusions also expand into flaky shapes, sometimes with irregular edges, which further enhances their reflectivity. Dark platy magnetite inclusions with triangular or rhombic shapes, like those observed in rainbow lattice sunstone, are also found in gold sheen sapphire (Bui et al., 2015;

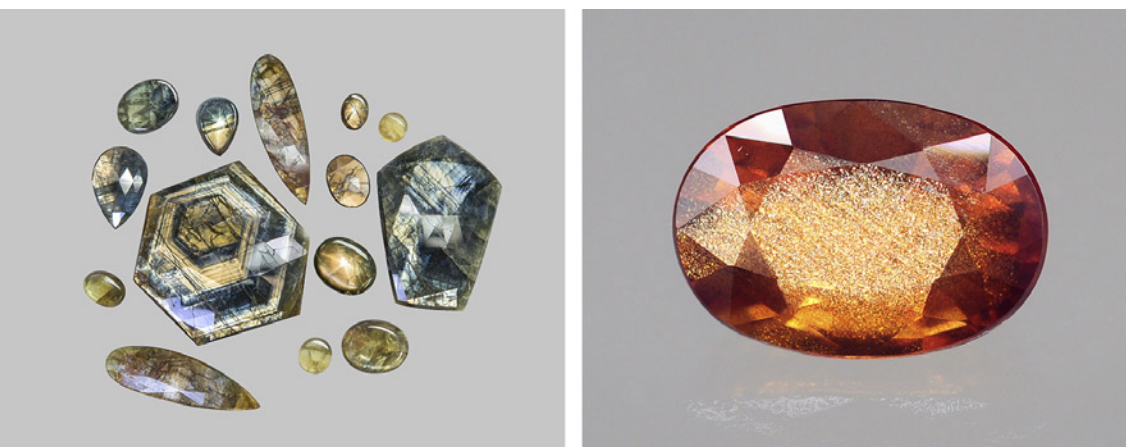


Figure 24. Left: Gold sheen sapphires from eastern Kenya (largest 97.69 ct). Photo by Lhapsin Nillapat. Right: A 4.34 ct faceted transparent orange sapphire showing a golden sheen effect. Photo by Tasnara Sripoonjan; courtesy of the Gem and Jewelry Institute of Thailand.

Narudeesombat et al., 2018) and have not been reported in other star sapphires. The occasional goethite inclusions are likely from late-stage alteration of hematite and magnetite, as much gold sheen sapphire material is severely fractured. Unsurprisingly, the iron concentration in gold sheen sapphire is on the higher end for natural sapphire, but there is nothing unusual about the trace element chemistry of these stones (Miura et al., 2018; Narudeesombat et al., 2018; Sripoonjan et al., 2019). The flaky iron oxide inclusions with irregular edges parallel to the (001) plane strongly suggest solid-state precipitation of oversaturated iron from the corundum lattice instead of epitactic crystallization during crystal growth, because most gold sheen sapphire material shows obvious hexagonal {110} growth zoning parallel to the *c*-axis. These sapphires may have experienced some special thermal and redox histories that promoted the precipitation of iron, and further investigation is warranted. It should be noted that there is most certainly a marketing bias for these heavily included sapphires, because the more common black star sapphires from Thailand, Cambodia, or Australia can also display a strong golden sheen on flat polished surfaces but are never noted for their aventurescence. Nonetheless, since the name *gold sheen*³ is more closely associated with the Kenyan material, perhaps the more general term *golden sheen sapphire* could be used for heavily included sapphires of unclear origins that display a strong golden aventurescence.

SHEEN AND IRIDESCENT OBSIDIAN

Some obsidian glasses display a diffuse sheen due to reflections from aligned inclusions, which sometimes qualify as aventurescence. Depending on the color of the reflection, they are commonly referred to as silver sheen obsidian or gold sheen obsidian (figure 25, A and B; videos 4 and 5). Some obsidian, often called rainbow or fire obsidian, can display a wide range of iridescence (figure 25, C–F; Johnson and Koivula, 1997). Unfortunately, despite the availability of this material, studies of these included volcanic glasses are extremely limited, providing little information on the mechanism creating the optical phenomenon. Obsidian is an amorphous solid formed by rapid

quenching of siliceous melts, an extremely fast process far from equilibrium, and it is therefore more difficult to determine the parageneses of the inclusions in obsidian relative to those for crystalline mineral hosts that are mostly controlled by thermodynamics. Lenticular features filled with gas or glass of a different composition, flattened and aligned due to the flow of the silicic melt, along with oriented pyroxene or feldspar crystals, have been reported in samples of Mexican obsidian, which can contribute to the sheen from internal reflections (Ma et al., 2001). Thin layers measuring 300 to 700 nm thick filled with nano-size magnetite crystals observed in fire obsidian from Glass Buttes, Oregon, may cause thin-film interference and explain the rainbow colors (Ma et al., 2007). A recent study showed that these aligned inclusions in obsidian can not only produce special optical effects but also create complex magnetic properties in these natural glasses (Mameli et al., 2016). Given the dramatically different appearances of sheen obsidians from different locations, multiple mechanisms could be involved in creating these optical phenomena.

IRIDESCENCE IN FELDSPARS

Iridescent feldspars are the most studied phenomenal gemstones, mainly due to their accessibility and geological importance. Prominent physicists Robert Strutt, fourth Baron Rayleigh (son of third Baron Rayleigh, who discovered Rayleigh scattering) and C.V. Raman (who discovered Raman scattering) both investigated these spectacular phenomenal stones during their careers (Strutt, 1923a; Raman, 1950a; Raman and Jayaraman, 1950, 1953a). The amount of research on this subject could easily constitute a separate review article on its own. Only the results of the studies that are most relevant to the gemological and optical properties of iridescent feldspars will be summarized in this section.

Iridescent feldspars generally can be separated into three categories based on their bulk chemical composition: labradorite, peristerite, and moonstone (figure 26), all of which owe their optical phenomena to submicron intergrowth textures resulting from solid-state exsolution (figure 27). Because oriented iron oxide inclusions are so common in feldspars, iridescent feldspars often also display aventurescence at a different orientation (figure 22). In fact, uniform golden aventurescence in some sunstones can appear quite similar to yellow/orange iridescence in labradorite (figure 23).

³At the time of writing, “Gold Sheen” is a refused and abandoned trademark application (#87535320) by the United States Patent and Trademark Office, although it (or its translation) may be a valid trademark in some other markets.

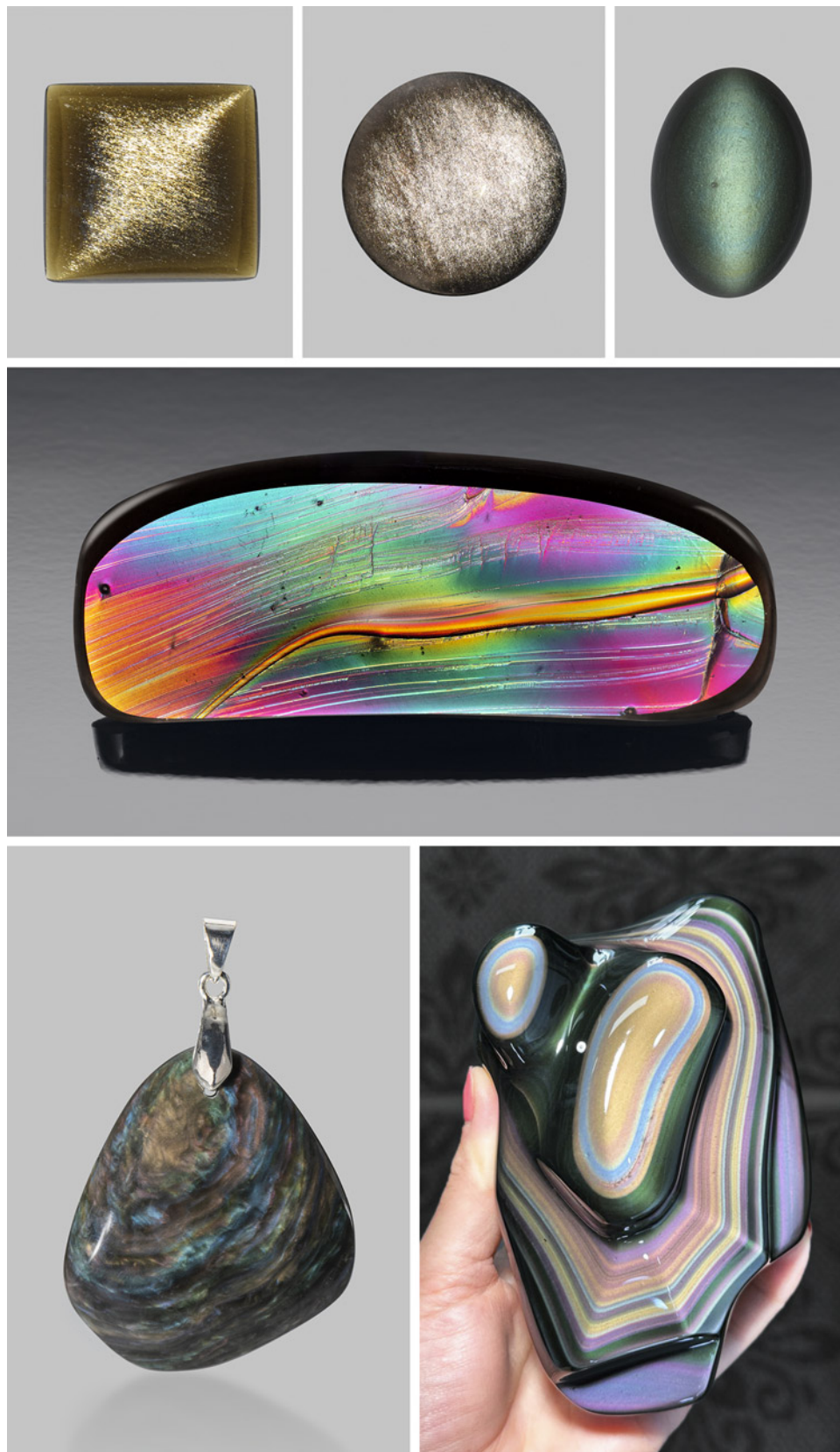


Figure 25. A: A 7.26 ct golden sheen obsidian from Mexico. B: A 6.95 ct silver sheen obsidian from Mexico. C: A 7.69 ct cat's-eye obsidian from Mexico. D: A 54.32 ct fire obsidian fashioned by Tom Dodge. E: A 14.7 g "velvet" obsidian from Mexico. F: A rainbow obsidian showing layers with different iridescent colors. Note that only A and B are considered aventurescent due to the eye-visible reflective inclusions, whereas the sheen in C–F is not created by visually discernible structures. Photos by Annie Haynes (A–C), Robert Weldon (D), and Emily Lane (E). Courtesy of John I. Koivula (A–C) and Rocks for the Spirit (F).

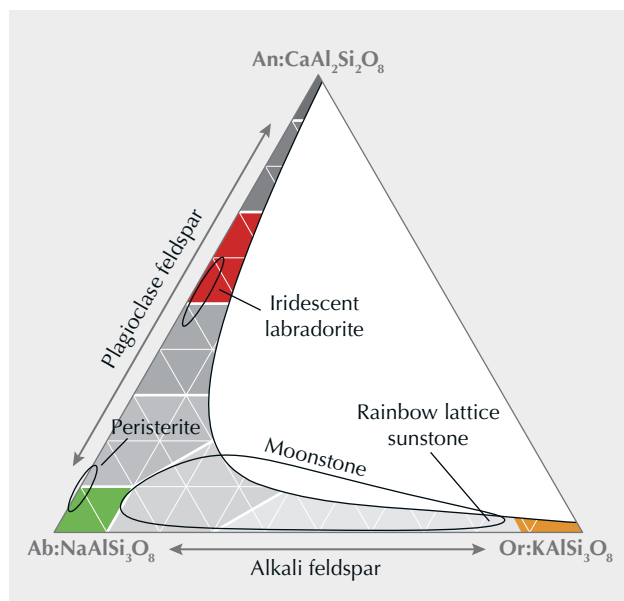


Figure 26. Ternary diagram of the feldspar group minerals, with the composition ranges of three different types of iridescent feldspars circled. The chemical ranges of labradorite s.s. (stricto sensu), albite s.s., and adularia are highlighted in red, green, and orange, respectively.

cence than for aventurescence (e.g., Colony, 1935). In this article, “schiller” is defined as any specular reflection arising from within a crystal, either because of flaky inclusions or exsolution lamellae, as long as it is strongly directional.

Iridescent Labradorite. The term *labradorite*, without any modification, refers to any plagioclase feldspar with a composition between An₅₀ (50 mol.% anorthite and 50 mol.% albite) and An₇₀ (70 mol.% anorthite and 30 mol.% albite) (figure 26). For instance, most Oregon sunstones are labradorites. The name *labradorite* originated from its type locality, Paul’s Island in Labrador, Canada, which produces the most famous iridescent variety. Iridescent labradorites are found around the world in plutonic rocks that experienced extremely slow cooling or high-grade metamorphism, with bulk compositions between An_{46±2} and An_{60±2} (Ribbe, 1983; Smith, 1983). These crystals can grow to exceptionally large sizes, sometimes up to several decimeters. Anorthosite rocks composed of iridescent labradorites

To avoid confusion, Smith and Brown (1988, p. 20) tried to redefine the term *schiller* to be reserved only for reflections from visible inclusions, as in aventurescence. Unfortunately, such an attempt to change the definition of a long-used term is unlikely to be widely adopted, especially since the term has been equally (if not more) commonly used for irides-

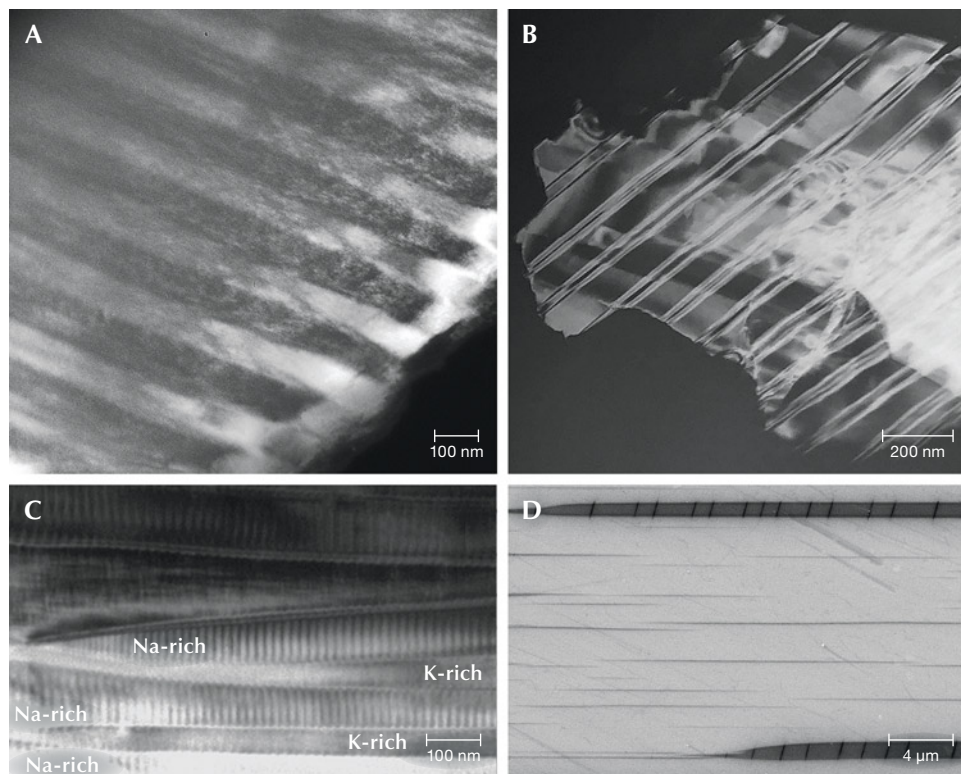


Figure 27. A: Darkfield TEM image of labradorite from Canada with blue iridescent color. B: Darkfield image of peristerite with blue iridescent color from the U.S. state of Virginia. C: Brightfield image of moonstone with greenish yellow iridescence. D: SEM image of the (010) cleavage surface of rainbow lattice sunstone from Australia. Images by Seungyeol Lee (A) and Shiyun Jin (D); images B and C courtesy of Huifang Xu.

are often used as high-end countertop materials. The best-quality iridescent labradorites are found in Canada, Finland, and Madagascar.

The exsolution texture in iridescent labradorite, known as the Bøggild intergrowth, is composed of alternating wider calcic lamellae (~70–200 nm) and thinner sodic lamellae (~50–100 nm), which are mostly oriented parallel to the $(\bar{3} 20 2)$ plane (Bøggild, 1924), making the iridescence observable on the (010) cleavage surface. The iridescent color correlates with the average thickness of the lamellae, such that a total thickness of adjacent calcic and sodic lamellae of ~150 nm yields blue iridescent colors, >250 nm yields red iridescent colors, and a continuous prismatic spectrum is observed in between (Ribbe, 1983). The periodicity of the Bøggild intergrowth is very regular (figure 27A) compared to exsolution textures in other minerals, so the iridescence of labradorite is almost

always intense with high saturation (figure 28). As a result, the iridescent spectrum can be predicted using a relatively simple kinematic theory of light reflection (Bolton et al., 1966), and the appearance rendered by computer modeling of the iridescence is quite realistic with only a few parameters (Weidlich and Wilkie, 2009).

Although labradorites with the same iridescent color from different locations can have different compositions, the iridescent color zones within the same crystal are always directly correlated with the composition, with the red iridescent zone ~2–3 mol. % more calcic than the blue iridescent zone (Jin et al., 2021). Because of this high sensitivity to small chemical variations, the iridescent color zones in labradorite often feature straight, sharp boundaries (figure 28, A–D), which are not observed in other iridescent feldspars. This characteristic is interpreted to reflect the special

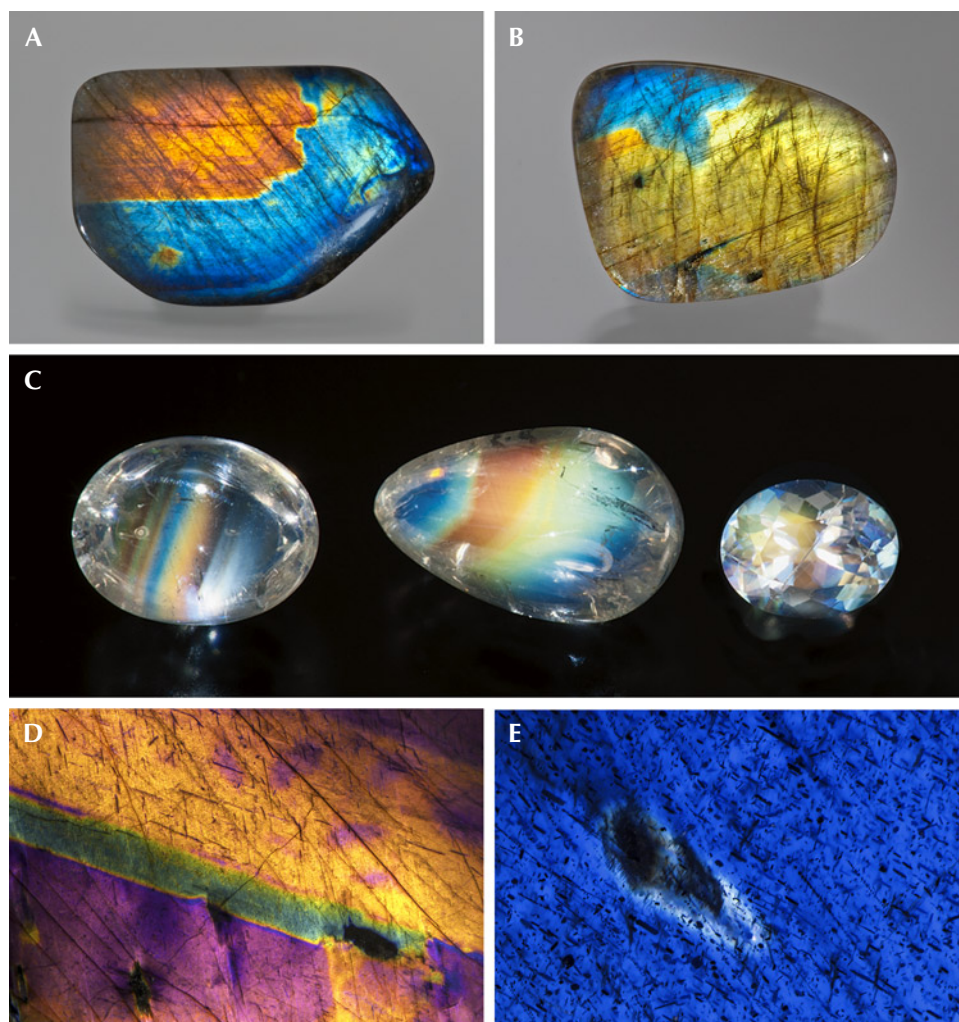


Figure 28. A and B: Labradorite from Finland (28.05 × 42.66 mm) and Madagascar (23 × 35 mm), respectively, showing iridescence close to the surface; courtesy of Black Star Trading Company. C: The iridescence of Zambian “rainbow moonstone” labradorite (largest 2.82 ct) comes from much deeper inside the stone due to its high transparency; gift of Scott Davies. D: Labradorite from Finland is heavily clouded with opaque inclusions that block light from traveling deep into the crystal, so the iridescence appears as a coating on the surface. E: Higher magnification reveals that the opaque inclusions are floating over the blue iridescence, indicating that the interference color always arises from inside the labradorite crystal. Photos by Robert Weldon (A–C) and Nathan Renfro (D and E); fields of view 18.8 mm (D) and 5.05 mm (E).

shape of the miscibility gap creating the Bøggild intergrowth, which is an inclined loop that closes at low temperature (Jin et al., 2021). Nonetheless, the exact shapes or even topologies of the Bøggild intergrowths are still not fully resolved, mainly due to the challenges of accurately analyzing the composition of individual lamellae, as well as the limited numbers of samples studied in detail (Jin et al., 2021).

The bodycolor of iridescent labradorite is mainly determined by the density of iron oxide inclusions, as most calcic plagioclases from plutonic rocks are clouded. The darkness of labradorite can dramatically affect the appearance of iridescence by controlling the depth of the light reflected by the lamellae inside the crystal. Spectrolite from Finland, with a nearly black bodycolor, shows iridescence at the surface of the crystal (figure 28, A and D), whereas “rainbow moonstone” labradorite with almost no iron oxide inclusions (Koivula, 1987; Win and Moe, 2012) shows diffuse iridescence coming from deeper inside the crystal (figure 28C), resulting in an appearance that may be confused with moonstone, as suggested by its name.

Peristerite. Peristerite is the least-known iridescent feldspar, and it is nearly always misidentified as moonstone due to their similar appearances. Technically, peristerites are sodic plagioclases with bulk

compositions between An_2 and An_{16} that have exsolution textures. Only sodic plagioclase from a pegmatite with a composition ranging from An_5 to An_{13} can develop exsolution lamellae coarse enough to cause multilayer interference of visible light and create iridescent colors (Ribbe, 1983). The name *peristerite* comes from *peristera*, Greek for “pigeon,” for its resemblance to the iridescent colors of a pigeon’s neck feathers. The unmixing is driven by the aluminum-silicon ordering in the pure albite structure as it transitions from “high albite” (disordered aluminum-silicon framework) to “low albite” (fully ordered aluminum-silicon framework) below 600°C (Smith, 1983). As a result, pure low albite ($\sim An_0$) is the dominant phase in peristerites, with intergrowths of minor oligoclase ($\sim An_{20}$). The best-known peristerite location is Ontario, Canada. The iridescence of peristerite is mostly light blue, with light yellow and pink iridescence also occasionally observed. The peristerite exsolution lamellae are generally oriented parallel to the (081) plane (Ribbe, 1983), similar to Bøggild intergrowths, with the iridescence also observable on the (010) cleavage surface (figure 29). Although its light bodycolor and desaturated iridescence may resemble moonstone, peristerite can be easily identified by the presence of polysynthetic Albite-twin lamellae, as well as by the orientation of the iridescence.

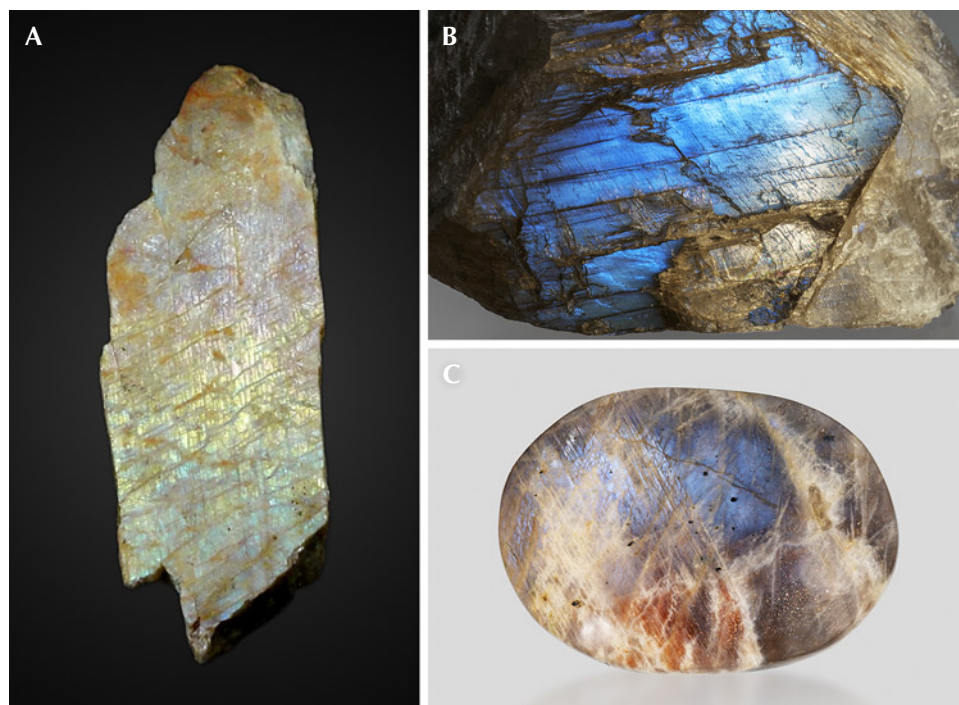


Figure 29. A: A peristerite from Ontario, Canada (7 cm long), showing pink, yellow, and green iridescence; courtesy of GIA Museum, collection no. 32588. B: Clear peristerite from Tanzania (677 g) showing light blue iridescence on the (010) cleavage surface; gift of Lithos Africa. C: A polished peristerite from Tanzania (7.5 cm long) that also displays aventurescence from hematite platelet inclusions; courtesy of Rachelle Turnier. Photos by John Montgomery (A) and Emily Lane (B and C).



Figure 30. A: Moonstone cabochons of various colors from India (113.79 carats total); in memory of Dr. Frederick H. Pough. B: An iridescent anorthoclase in larvikite from Norway (commercially known as “blue pearl”). C: A 2.6 cm long rough moonstone fragment from the U.S. state of Wisconsin, showing strong blue iridescence. D: A rainbow lattice sunstone from Australia showing white iridescence. E: Three cat’s-eye moonstones (left to right: 13.1, 6.36, and 6.08 ct) exhibiting chatoyancies of different sharpness; right stone gift of Beverly J. Bystricky, courtesy of GIA Museum, nos. 22154, 38696, and 39155. F: A four-rayed star moonstone (17.3 ct) from Madagascar; courtesy of GIA Museum, collection no. 19470. Photos by Emily Lane (A, B, and F), Shiyun Jin (C and D), and Orasa Weldon (E).

Moonstone. Moonstone is named after its white or silver iridescent glow that resembles moonlight. Only cryptoperthite, an alkali feldspar with nonperiodic submicron intergrowth textures between albite and orthoclase, can produce such desaturated iridescence and be called “moonstone.” Unfortunately, the name has been haphazardly applied to any light-colored feldspars, such as peristerite or transparent labradorite, that display a diffuse or desaturated iridescence, which has added confusion to an already complicated subject. Although light bodycolors are the most common, a wide range of different colors and shades can be found in moonstones, mostly determined by the types and densities of inclusions (figure 30).

Unlike the multiple discrete miscibility gaps of the plagioclase series between albite and anorthite, the alkali feldspar solid solution between albite and orthoclase has only one large miscibility gap. Despite its simple topology, the wide composition range of this solvus results in more intricate intergrowth textures in alkali feldspars, with lamellar thicknesses ranging from a few nanometers to several millimeters. The lamellar textures are further complicated by the composition-dependent order-disorder phase transitions and the resulting twin structures. Many book chapters and review articles have been dedicated to this subject (Yund, 1983, 1984; Parsons and Brown, 1984, 1991; Parsons et al., 2015). Although the submicroscopic exsolution textures responsible

for the iridescence of moonstone have been extensively studied using electron microscopy, their direct correlations with the iridescent colors have not been carefully investigated.

Depending on the composition and thermal history, a menagerie of widely different textures has been reported in moonstone. Alkali feldspars with intermediate compositions ($\sim\text{Ab}_{80}\text{Or}_{20}$ – $\text{Ab}_{40}\text{Or}_{60}$) start with spinodal decomposition that creates alternating albite and orthoclase lamellae with flat interfaces nearly parallel to the $\{601\}$ plane (figure 27C), which over time can evolve to wavy and zigzag boundaries along the $\{661\}$ planes to minimize the elastic strain at the interface. Further coarsening of the texture may result in isolated domains of albite with lozenge-shaped cross sections (Yund, 1983). These moonstones typically show blue iridescence with various degrees of saturation (e.g., figure 30C), although light yellow iridescence has also been occasionally observed.

Alkali feldspars with more potassic compositions develop a different texture when they exsolve. Because their compositions fall outside the range for spinodal decomposition, it is only possible for them to exsolve through nucleation and growth of albite lamellae from the orthoclase matrix. As a result, the albite lamellae occur as isolated thin films (or thicker “spindles”) parallel to the $\{601\}$ plane (Parsons et al., 2015), which can create iridescence through thin-film interference (Jin et al., 2022b). However, unlike the hematite films in sunstones with parallel faces and constant thickness, the albite films are lens-shaped, thicker in the middle and tapering out at the edges (figure 27D). Therefore, the thickness of the albite films covers a continuous range from zero to a few hundred nanometers, causing thin-film interference over the entire visible spectrum and thereby creating a bright white iridescence (figure 30D). Sodic alkali feldspars may behave similarly to potassic feldspars, except with orthoclase thin films exsolving from an albite matrix. However, high-quality sodic moonstone is relatively rare, partly due to the complications related to the lower symmetry and the more calcic composition.

Because of the wide miscibility gap and faster interdiffusion rate between albite and orthoclase, the individual lamellae or domains in moonstones are always close to the end-member compositions. The larger chemical difference between lamellae means a larger disparity in RIs, creating stronger reflection and scattering at the interfaces (again, see equation C-1 and figure E-1). The more distinct crystal structures also create strong strains at the interface, making

them vulnerable to low-temperature fluid-induced alterations. This is why moonstone almost always has a milky translucent appearance, with the iridescence shallow beneath the surface (figure 30). The most extreme case is the anorthoclase in larvikite (figure 30B), which is often misidentified as labradorite due to its darker bodycolor. Moonstone’s milky appearance often leads to the misconception that its iridescent sheen is caused by Rayleigh or Mie scattering, similar to opalescence (Cartier, 2009), instead of interference of light reflected by lamellar structures. In contrast, with much smaller chemical and RI differences between lamellae, inclusion-free labradorite and peristerite can appear crystal-clear with iridescence coming from much deeper inside the crystal (figures 28C and 29B, respectively).

In gemology, moonstone’s iridescence is called *adularescence*. Unfortunately, this term presents some issues that often lead to confusion. First, it incorrectly implies relevance to *adularia*, a low-temperature variety of almost pure potassic feldspar (defined by a unique rhombic crystal habit; figure 26), which never⁴ displays *adularescence* (e.g., Tutton, 1921). “*Adularescence*” did not appear in any academic mineralogical literature on feldspars until very recently (Jin et al., 2022b), making it impossible to trace its origin. Perhaps “*perthescence*” after perthite would have been a more proper name, following a similar logic as *labradorescence* and *peristerescence*, but feldspar mineralogists have adopted the more general term *iridescence*.

Second, the character of iridescence in moonstone is highly variable, and some more saturated iridescent colors may look similar to peristerite and labradorite (figure 30C). The diverse appearance of moonstone iridescence has misled some to incorrectly associate the name with a light bodycolor instead of the moonlight-like glow. Consequently, “*adularescence*” is often applied to peristerite and light-colored labradorite, likely because “moonstone” is much more marketable than some iridescent plagioclase with an obscure name. This unrestricted and often confusing usage of the name *moonstone* created strange trade names such as

⁴It may be theoretically plausible for a highly sodic *adularia* formed in extremely unusual conditions to develop exsolution textures and become a moonstone, but to the best of the authors’ knowledge at the time of writing, no such material has been reported. This incorrectly implied relevance between moonstone and *adularia* might be the reason for a common misconception that all moonstones are orthoclase feldspars.

TABLE 1. Comparison of the properties of various iridescent feldspars.

	Labradorite	Peristerite	Moonstone
Chemical composition	$\text{Ca}_{0.60-0.46}\text{Na}_{0.38-0.52}\text{K}_{0.02-0.03}\text{Al}_{1.60-1.46}\text{Si}_{2.40-2.54}\text{O}_8$	$\text{Na}_{0.95-0.87}\text{Ca}_{0.05-0.13}\text{K}_{0-0.03}\text{Al}_{1.05-1.13}\text{Si}_{2.95-2.87}\text{O}_8$	$\text{K}_{0.85-0.1}\text{Na}_{0.15-0.9}\text{Ca}_{0-0.1}\text{Al}_{1-1.1}\text{Si}_{3-2.9}\text{O}_8$
Phenomenon	Labradorescence	Peristerescence	Adularescence
RI	1.56–1.57	1.54–1.55	1.52–1.53
Crystal system	Triclinic	Triclinic	Monoclinic/triclinic
Twinning	Polysynthetic Albite twins parallel to (010) always prominent; Pericline twins near (001) cutting through the iridescence also possible		Not observable without magnification except in anorthoclase; complicated patterns may be seen under the microscope
Orientation of iridescence	Best seen on the (010) cleavage, parallel to the Albite twin lamellae		Mostly on fractures or polished surface near (100), intersecting both cleavage planes
Color of iridescence	Any spectral color, from violet to red, always high saturation	Mostly blue, but yellow, pink, and violet also common	Silver, white, light blue, and occasionally light yellow
Zoning of iridescence	Multiple iridescent colors separated by sharp boundaries almost always present in large specimens (figure 28, A–D)	Uncommon; if present, the transition is always smooth and blurry between different zones (figures 29A and 30, B and C)	
Bodycolor and transparency	Mostly dark colored due to opaque inclusions, although materials from certain locations can be transparent and clear (figure 28)	Almost always light colored; transparency may vary depending on inclusions and alteration; mostly transparent to semitransparent	Color varies widely depending on chemistry and inclusions, but light colors are most common; always milky in appearance and translucent to semitranslucent
Other possible phenomena	Silver chatoyancy or asterism due to opaque needle inclusions are common in dark-colored labradorite cabochons (figure 23B); aventurescence also observed in some specimens (figure 22D)	Low-quality aventurescence possible but uncommon (figure 29C)	
		Chatoyancy or asterism (rare) may appear in cabochon-cut stones (figure 30, E and F); aventurescence, if present, usually overwhelms adularescence, and the material would be classified as sunstone before moonstone (e.g., figures 22F and 30D)	

“rainbow moonstone.” If moonstone is named after its resemblance to moonlight, how can something with rainbow colors be called moonstone?

It is certainly unrealistic to hope that the gem trade will always adopt scientifically accurate mineralogical terms and abandon ambiguous trade names such as “rainbow moonstone.” Nonetheless, for gemological researchers and collectors who care about proper usage, the iridescent feldspar terminology certainly needs to be clarified. Although it would not be possible to replace the term *adularescence* due to its long history and wide adoption in gemology, ideally the term should be restricted for the moonlight-like white or silver glow as originally intended. However, since the name *moonstone* now includes any iridescent cryptoperthite (Smith and Brown, 1988, p. 20), it is perhaps inevitable that adularescence would cover the less common blue or yellow iridescence as well. Still, it should be strictly limited to “true moonstones” that are alkali feldspars with intergrown albite and orthoclase. Note

that the general term *iridescence*,⁵ probably for lack of a better word, has been used in the mineralogical literature to describe all optical effects that involve the interference of light, including white and silver adularescence (e.g., Parsons, 2010). The term *iridescent color*, however, should certainly be reserved for spectral interference colors with high saturation (figure B-1). The key distinctions between different iridescent feldspars are twinning, zoning, and iridescence orientation. Bodycolors, inclusions, and iridescent color are certainly useful but not always diagnostic as many would assume. The physical and color properties of various iridescent feldspars are summarized in table 1.

⁵The terms *adularescence*, *labradorescence*, and *peristerescence* are not descriptive terms based on appearance but are directly tied to the gem species moonstone, labradorite, and peristerite, respectively. This means that they are only useful when the gemstone has already been positively identified. Therefore, only the general term *iridescence* should be used when describing an unidentified feldspar gem.

To observe the iridescence of a moonstone, or any other iridescent feldspar, a face near-parallel to the lamellae orientation must be well-polished. On a flat surface, the iridescence can be seen only at certain angles relative to the illumination, which is why it is a schiller effect. As on asteriated or chatoyant stones, a curved surface focuses the reflected light into a smaller area above the stone, allowing the iridescence to be seen over a wider angle. This is why iridescent feldspars are often cut into cabochons or “pebbles.” Moreover, the lamellae in moonstones are not simple two-dimensional structures. The thin films in potassic moonstones are elongated belts along the [106] axis (Jin et al., 2022b). The zigzag lamellae in intermediate or sodic moonstones have parallel ridges, which can evolve further into isolated needle-shaped albite domains parallel to the [106] axis. These linear features in the exsolution textures can create chatoyancy in a cabochon-cut moonstone (figure 30E). It is still unclear what textures cause the rare star effect in moonstones without hematite inclusions (figure 30F), but it might be related to the tweed or crosshatched twinning texture often found in low-temperature orthoclase. The “pull-aparts” along the (001) cleavage planes in the thicker albite spindles (dark near-vertical lines in figure 27D) resulting from the lattice dimension discrepancy between albite and orthoclase (Fitz Gerald et al., 2006) could also be responsible for the extra asterism rays in addition to the common cat’s-eye associated with the linear textures along the [106] axis.

It is worth noting that synthetic colorless spinels showing chatoyancy or asterism, likely due to exsolution lamellae of corundum, have been reported as imitations of moonstone (Breebaart, 1958; Renfro, 2011a; Hodgkinson, 2017).

OTHER IRIDESCENT MINERALS WITH THIN-FILM OR MULTILAYER STRUCTURES

Exsolution textures are common in mineral solid solutions beyond feldspars, which means that iridescent colors due to multilayer interference can be found in other minerals as well. However, with crystal sizes much smaller than feldspars, these other iridescent stones do not draw nearly as much attention as iridescent feldspars. Two notable examples are Nuummite and iridescent garnet.

Nuummite, meaning “derived from Nuuk” in Greenlandic, is the trade name for iridescent amphibole, first found near Nuuk, Greenland (Appel and

Jensen, 1987; Rodgers et al., 1996). Similar material has also been discovered in the Sahara Desert of central Mauritania (Renfro, 2011b) and in the U.S. state of Wyoming (Dietrich et al., 1988). Studies of exsolution textures in orthoamphiboles are very limited compared to those of feldspars. It is confirmed that the iridescence in Nuummite is caused by periodic exsolution lamellae parallel to (010), alternating between anthophyllite (Ath: $\text{Mg}_7\text{Si}_8\text{O}_{22}(\text{OH})_2$) and gedrite (Ged: $\text{Mg}_5\text{Al}_4\text{Si}_6\text{O}_{22}(\text{OH})_2$) (Christie and Olsen, 1974; Champness and Lorimer, 1976; Gittos et al., 1976; Champness and Rodgers, 2000). With iridescent colors from golden yellow to violet-blue, over a dark gray matrix, Nuummite appears very similar to labradorite, except with smaller crystal sizes and elongated blade shapes (figure 31A). Also similar to iridescent feldspars, some Nuummite show zoning in the iridescence (Renfro, 2011b), likely due to slight variations in the chemical composition within the amphibole crystal.

Pink to blue iridescence are also sometimes observed in andradite garnet, known as “iridescent garnet” or “rainbow andradite” (figure 31B). They were first discovered in the Adelaide mining district in the state of Nevada (Ingerson and Barksdale, 1943), and later also found in Sonora, Mexico; Nara, Japan; and Inner Mongolia, China (Badar and Akizuki, 1997; Hainschwang and Notari, 2006; Badar et al., 2010; Nakamura et al., 2017; Yang et al., 2023). Electron microscope images show lamellar textures in these iridescent stones parallel to the {110} crystal face, with alternating layers rich in iron and aluminum (Nakamura et al., 2017). It is not clear whether these lamellae were created by exsolution or crystal growth. Structure refinement shows that the iridescent garnet has a non-cubic symmetry, resulting in anomalous birefringence in the typically isotropic mineral (Nakamura et al., 2017). A recent study discovered an orthorhombic garnet phase in the middle of the andradite-grossular ($\text{Ca}_3\text{Fe}_2\text{Si}_3\text{O}_{12}$ – $\text{Ca}_3\text{Al}_2\text{Si}_3\text{O}_{12}$) solid-solution series with almost complete Fe-Al ordering in the structure, separated by miscibility gaps with the end members (Xu et al., 2023), which might be related to the formation of iridescent garnet. Further studies, particularly of the chemical compositions of the individual lamellae, are necessary to fully understand these rare and mysterious gemstones.

Many ore minerals, such as “peacock ore” (bornite, Bn: Cu_5FeS_4) (Buckley and Woods, 1983; Vaughan et al., 1987), show an iridescent tarnish on the surface due to a submicron oxidation layer that

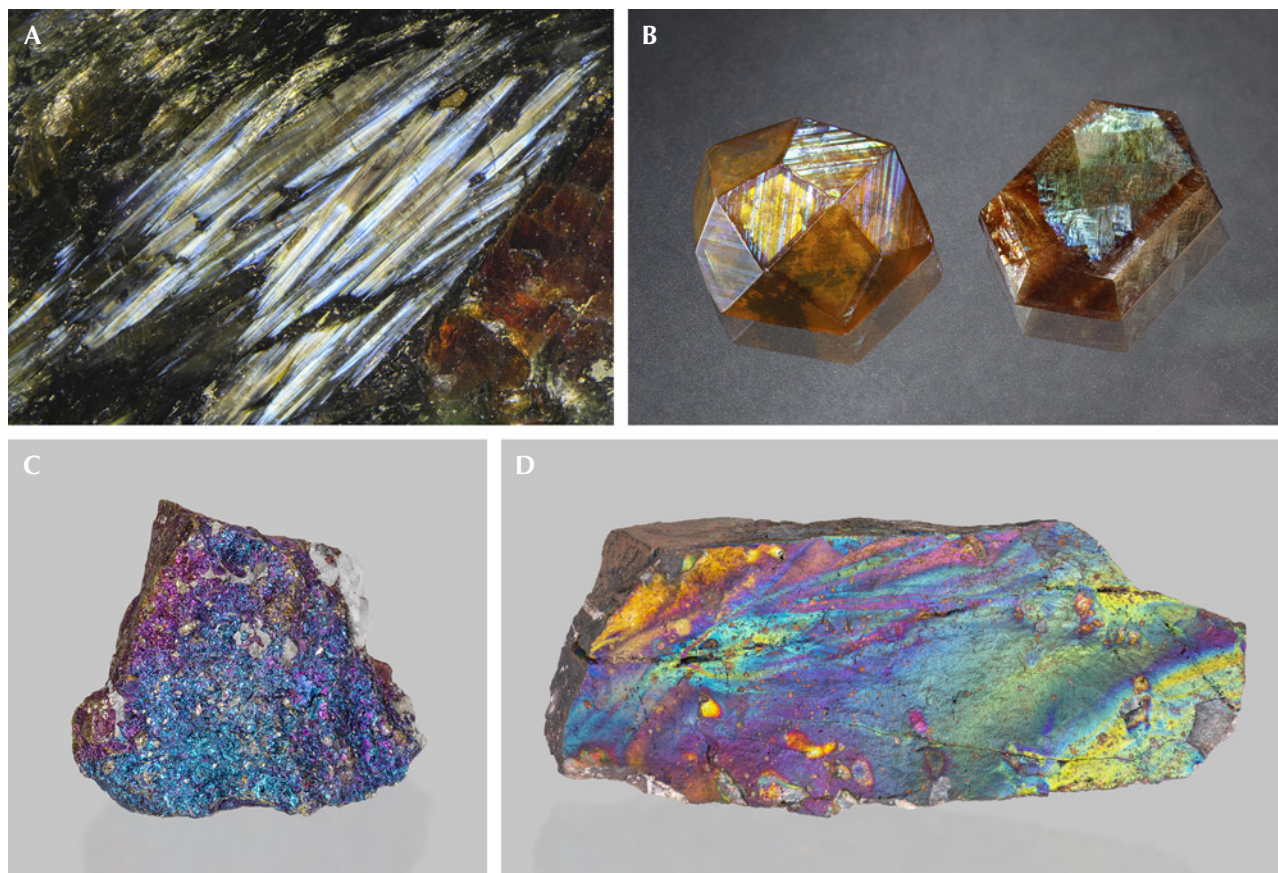


Figure 31. A: Elongated orthoamphibole crystals in Nuummite showing blue and yellow iridescence; field of view 10.29 mm. B: Two polished iridescent andradite crystals from Sonora, Mexico (left, 12 ct; courtesy of GIA's Dr. Edward J. Gübelin collection, no. 33283), and Nara, Japan (right, 11.39 ct; courtesy of Keiko Suehiro, GIA Museum no. 36136). C: Acid-treated chalcopyrite (7 cm wide) showing purple and blue iridescent tarnish on the surface; courtesy of Rachelle Turnier. D: Iridescent goethite (turgite) from Bukit Besi, Malaysia (12 cm long); courtesy of Rachelle Turnier. Photos by Nathan Renfro (A), Annie Haynes (B), and Emily Lane (C and D).

can cause thin-film interference. Most of these minerals are sulfides and native metals, which form in reducing conditions and can be easily oxidized when exposed to an oxidizing atmosphere. This process can be accelerated by acid treatment, which is used to artificially create the iridescent tarnish (e.g., figure 31C). Iridescent goethite, or turgite, which can already be an alteration or weathering product of other iron ore minerals, is a notable exception among iron ores (figure 31D). Electron microscopy analyses reveal quasiperiodic layers of voids near the surface that can cause thin-film or multilayer interference responsible for the striking iridescent colors. It is not clear how these void layers form, but episodic surface poisoning due to cyclical weather conditions is a likely mechanism (Heaney et al., 2018).

IRIDESCENT QUARTZ

Natural iridescent quartz, also known as iris quartz, rainbow quartz, schiller quartz, anandalite, and adularescent quartz, has been recognized since its discovery in the Deccan Traps of India in the nineteenth century (Petrov and Tanaka, 2011). Iridescent quartz has also been reported from the United States (Washington), Uruguay, Brazil, Germany, Turkey, and Morocco (Gübelin and Koivula, 2005; Petrov and Tanaka, 2011; Renfro and Koivula, 2011). Although it was discovered more than a hundred years ago, iridescent quartz mostly escaped scientific investigation, with the exception of a brief study by Raman (1950b). The structure in natural quartz causing the iridescent colors, ranging from red to blue, was not revealed until recently (Lin and Heaney, 2017). The iridescence in quartz is visible only on the minor z {011} faces of

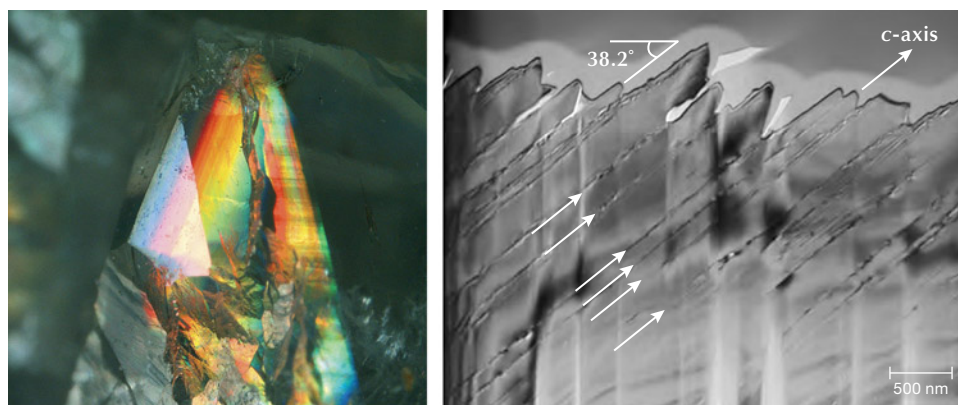


Figure 32. Left: An iridescent quartz crystal from India. Photomicrograph by Nathan Renfro; field of view 6.3 mm. Right: A TEM image showing periodic grooves on the z face of an iridescent quartz; image from Lin and Heaney (2017).

euhrhedral quartz crystals, not on any other crystal faces or broken surfaces (figure 32, left). Upon polishing, the iridescence briefly intensifies before completely disappearing, indicating it comes from a very thin layer near the surface of the crystal. Electron microscope and AFM images reveal periodic groove structures on the iridescent face correlated with polysynthetic Brazil twin lamellae, which can diffract visible light like a diffraction grating (box F) and create iridescence (figure 32, right). The grooves are theorized to form by preferential surface etching along the twin boundaries by invasive fluids.

PRECIOUS OPAL

Opal has been studied extensively due to its broad occurrence and long history as a gemstone, as well as the more recent interest in photonic material design with an opal-like periodic structure (Baryshev et al., 2006; Arnon et al., 2018). However, like with moonstone, most scientific investigations of opal focus on its submicron textures and atomic structures, with few quantifying its optical properties. In gemology, “precious opal” is separated from “common opal” by its play-of-color⁶ (figure 33). Only microscopically ordered opal-AG and opal-CT may show the play-of-color effect (Curtis et al., 2019), and SEM investigations into the iridescence have revealed stacked silica nanospheres (opal-AG) or “lepispheres” (spheres of blades in opal-CT) of the same size (~250 nm), providing the first evidence of 3D photonic crystals (figure 34) (Sanders, 1964; Daragh and Sanders, 1965). Common opal-AG is also composed of nano-size silica spheres, but the latter are not regularly stacked due to their nonspherical shapes and broad size distributions (again, see figure 2). Common opal-CT shows even more variability with respect to nanostructures, ranging from nano-size silica platelets to nanofibers (Gaillou et al., 2008). Some non-iridescent opals also have regular

periodic structures, but the diameters of the silica spheres are too large or too small to diffract visible light. Precious opal can be synthesized through the Stöber process (Stöber et al., 1968), which involves organic solvents that are not present in geological environments where natural opals form. Some XRD analyses show that synthetic opal can be more crystalline than opal-CT, even though they comprise silica nanospheres similar to natural opal-AG, instead of the lepispheres as in natural opal-CT (Hernández-Ortiz et al., 2015). The fragility of synthetic opals is similar to that of natural ones, which is partly why opal simulants made partially or purely of plastic are more common in the market (Renfro and Shigley, 2018; Renfro, 2019).

Sanders (1968) performed a light diffraction experiment on a precious opal using a similar configuration as X-ray crystallography, thereby directly correlating the optical effect and the internal structure of opal for the first time. Quantitative models have also been developed for synthetic opals,⁷ showing an angle dependence for the diffracted color that matches the experimental observations (Baryshev et al., 2003a,b, 2006). Besides the sharp diffraction spots expected for a perfect 3D periodic structure, local planar or linear stacking defects of the nanospheres in opal can also give rise to continuous scattering features, which is why asterism and chatoyancy can be observed in some opals (Sanders, 1976; Soonthorntantikul, 2014) (figure 33, E and F).

⁶Using the term *opalescence* to describe opal’s play-of-color should be discouraged because not all opal displays play-of-color. The milky appearance, however, is a common feature of all opals, which should be what the term is used to describe.

⁷Because opal does not have a well-defined chemistry or crystal structure, it is difficult to define a distinct boundary between synthetic opal and opal simulants (e.g., Schmetzer and Henn, 1987). Therefore, the term *synthetic opal* may not always be used precisely in non-gemological literature.

BOX F: DIFFRACTION OF LIGHT BY PERIODIC STRUCTURES

Light scattered by a periodic structure can interfere and cause diffraction of certain wavelengths along specific directions. The simplest example of this phenomenon is from a diffraction grating, which is a planar optical element with a periodic structure (figure F-1). Diffraction gratings can be further categorized into transmission gratings, with periodic slits that allow light to pass through, and reflective gratings, which have periodic grooves that reflect light. Note that the individual slits or grooves in a diffraction grating may scatter light in multiple directions like the needle inclusions described in box B, although certain directions may be preferred over others depending on the shape of the cross section.

The principle for constructive interference, or the “diffraction” condition, is the same as for thin-film interference, such that the optical path difference between light scattered by different slits (period of d) or grooves is an integral multiple (m) of the wavelength (λ):

$$2d(\cos \theta_i - \cos \theta_s) = m\lambda \quad (\text{F-1})$$

where θ_i and θ_s are the incident angle and the scattering angle relative to the grating plane, respectively. This equation is also known as the Laue equation in X-ray crystallography. It should be noted that the scattering angle in the equation applies to both backscattering (reflection grating) and forward scattering (transmission grating). In fact, a diffraction grating can function as both

a transmission grating and a reflective grating if the surfaces between the slits are reflective.

Note that the equation has two independent angles, which is much less restrictive than the thin-film or multilayer interference that follows the law of reflection and refraction. This means that the diffraction colors from periodic structures can be seen in many different directions, instead of only at one specific orientation. Moreover, the cosine function is more sensitive to changes at the typical viewing angles closer to 90°. As a result, the iridescent color from diffraction dramatically changes with small changes of incident angle, sample orientation, or viewing direction (figure F-2), creating the phenomenon known as play-of-color. In fact, with a large enough diffraction grating, the entire visible spectrum can be seen without any movement, as light diffracted from various parts of the diffraction grating enters the eye at different angles and is seen as different colors (figure F-2).

The periodic diffraction structure can be expanded into two or three dimensions, which creates more complicated diffraction patterns. The basic principle remains the same as in equation F-1, except it would need to be applied to all periodic arrays found in the higher-dimensional structure. The volumetric equivalent of the planar diffraction grating is called a “photonic crystal” because it diffracts visible light similar to the way in which a crystalline solid diffracts X-rays. Depending on the num-

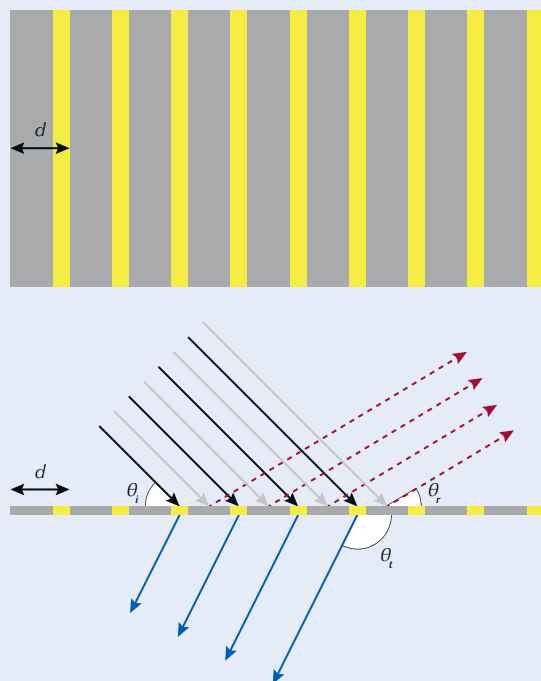


Figure F-1. Schematic drawing of a diffraction grating (top) and its cross section (bottom). Light can be reflected by the periodic grooves or transmitted through the periodic slits in the grating. The light waves scattered by different grooves or slits can constructively interfere with each other depending on the incident and scattering angles.

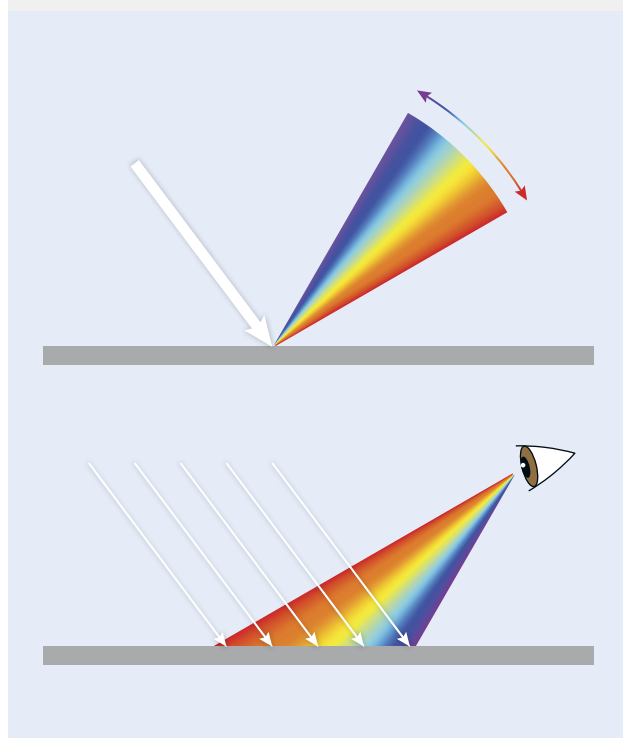


Figure F-2. The interference color created by a diffraction grating is very sensitive to the scattering angle. Dramatic color change can be observed with a small tilt (top), and the entire color spectrum may be seen over a wider area (bottom). This is why iridescence created by diffraction is often called *play-of-color*.

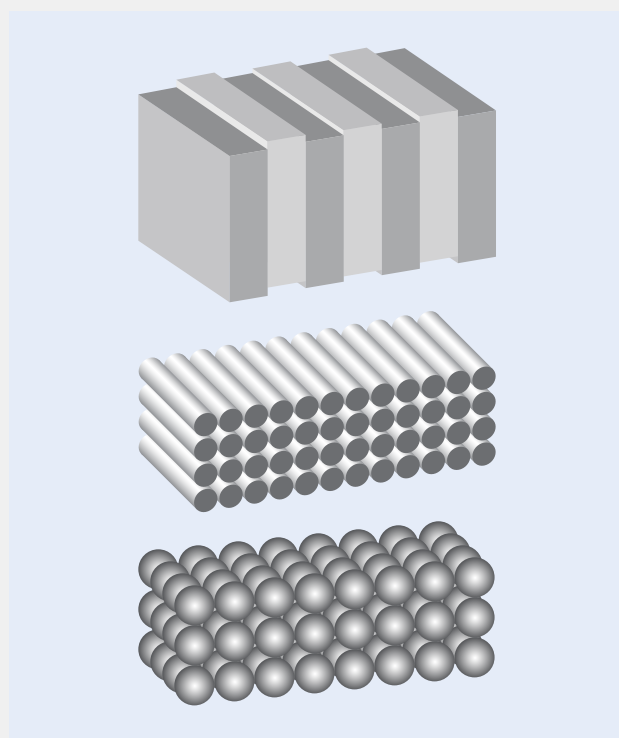


Figure F-3. Schematic drawing of 1D (top), 2D (middle), and 3D (bottom) photonic crystals, as defined by the number of dimensions in which they are periodic. The periodic units in photonic crystals are typically at a scale of ~100–200 nm.

ber of periodic directions, they can be further divided into 1D, 2D, and 3D photonic crystals (figure F-3). The layered structures of iridescent feldspars and garnets discussed above are examples of 1D photonic crystals, which is why the multilayer interference condition is sometimes described as Bragg's law following the terminology of crystallography. By a similar analogy, the disordered structures that scatter light randomly, as in common opal, milky sapphire, and fancy white diamond, can be considered photonic glasses. Compared to the particles, needles, and films discussed in previous sections, the periodic structures of diffraction gratings and photonic crystals are much more intricate and require more complicated processes to form, so they are typically less common in minerals. The formation mechanisms of the gemstones discussed in this section are also generally not well understood.

Colors created by the scattering, interference, or diffraction of light are often known as structural colors (or less commonly "physical" colors), as they are produced by the physical structures in the material. Unlike pig-

mented (chemical) colors created by the selective absorption of wavelengths within the visible light spectrum due to electron transfer or excitation, which thus are determined only by chemistry, structural colors are often considered "not real" and referred to as "pseudochromatic" colors in older literature references (e.g., Ostwald, 1965; Nassau, 1978), partly because they may change dramatically with the viewing angle. However, the difference between structural color and pigmented color may not be as distinct as most would assume. For instance, the colors of metal colloids, such as the red and green colors of Oregon sunstones, are certainly structural as they depend strongly on the sizes and shapes of the metallic nanoparticles, although their appearances are often indistinguishable from chemical pigments. Compared to pigmented colors, structural colors are typically brighter, easier to tune, more durable, and more economical and environmentally friendly, which might be why they are so prominent in the biological world, most commonly found in butterfly wings and bird feathers (Kinoshita, 2008).

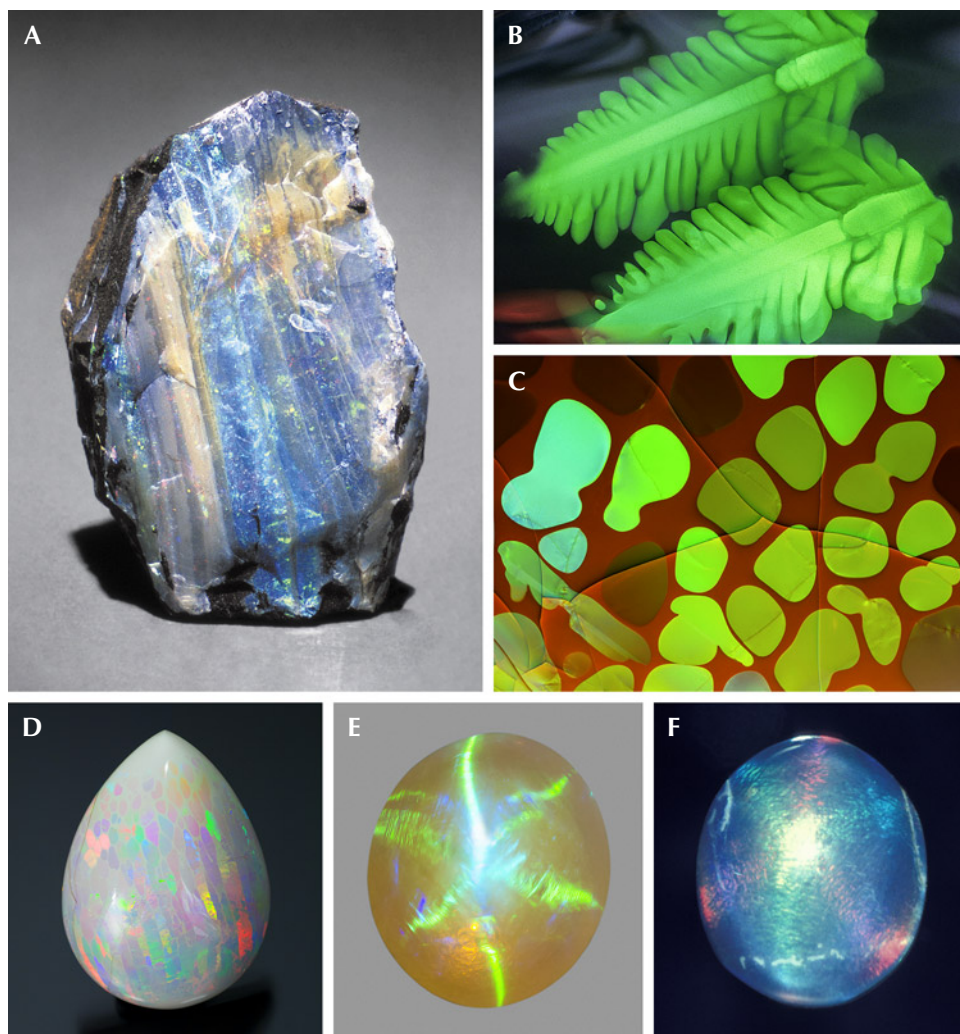


Figure 33. A: A rough opal showing play-of-color in a layered structure. B: Opal from the U.S. state of Nevada, showing two fern-shaped holographic play-of-color patterns. C: Play-of-color in a cell structure; courtesy of John I. Koivula. D: Ethiopian opal showing play-of-color in a digit pattern; courtesy of Opalinda and EyaOpal. E: A 2.39 ct opal showing a six-rayed star with play-of-color. F: Another star opal with different play-rays on the opposing rays. Photos by GIA staff (A, E, and F), John I. Koivula (B), Nathan Renfro (C), and Robert Weldon (D); fields of view 13.5 mm (B) and 11.28 mm (C).

IRIS AGATE AND FIRE AGATE

Agate is a banded variety of chalcedony, which is a fibrous cryptocrystalline variety of silica mostly composed of polysynthetic Brazil-twinned α -quartz intergrown with mogánite (Mog: SiO_2), a silica polymorph. Agates form mostly in the cavities of acidic or basic volcanic rocks, although they are also occasionally found in hydrothermal veins or sedimentary

rocks. The characteristic banding of even unpigmented agates with respect to darkness and clarity reflects variations in the relative proportions of quartz and mogánite and their crystal sizes and habits, as well as the presence of porosity and micro-inclusions (Götze et al., 2020). The chalcedony fibers in agate are mostly “length-fast,” meaning they are elongated perpendicular to the *c*-axis of quartz,

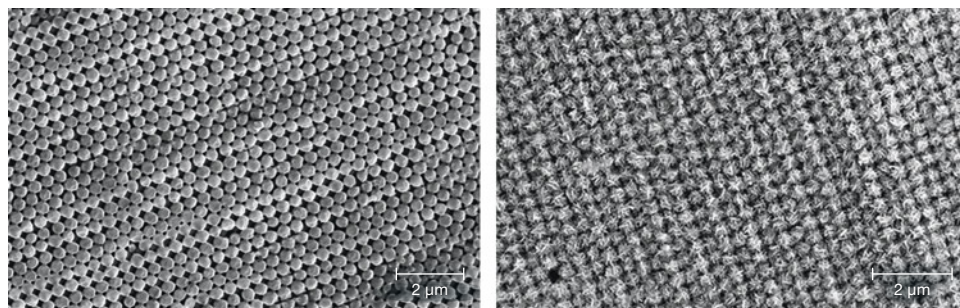


Figure 34. Left: SEM image of a precious opal-AG from California. Right: SEM image of a precious opal-CT from Mexico showing lepis-spheric structures. Images from Gaillou (2015).

instead of parallel to that axis like prismatic quartz crystals. Pervasive screw dislocations torque the optical axis of the silica crystallites in agate to twist around the fiber axis (Heaney, 1993), creating a unique banded pattern in cross-polarized light known as *Runzelbänderung* (figure 35A; Bernauer, 1927). The more vibrant colors of agate arise mainly from pigmentation by iron (hydr)oxides or manganese oxide compounds. The formation mechanism of agate is still mostly enigmatic, and no attempts at synthesis have been successful in reproducing the nanoscale textures of agate (Götze et al., 2020; Moxon and Palyanova, 2020; Heaney, 2021).

Some agate, when cut into doubly polished thin slabs, show iridescence under transmitted light and therefore are called “iris agate” (figure 35, B–D). The iridescence of most iris agate is diffuse, with low color saturation, although brilliant play-of-color can occasionally be observed in specimens of the best quality. The special optical property of iris agate was first described by Brewster (1813 and 1843) who observed a periodic texture parallel to the agate banding that functions as a transmission grating, which was first captured photographically by Jones (1952). Raman and Jayaraman (Jayaraman, 1953; Raman and Jayaraman, 1953b, 1955) correctly pre-

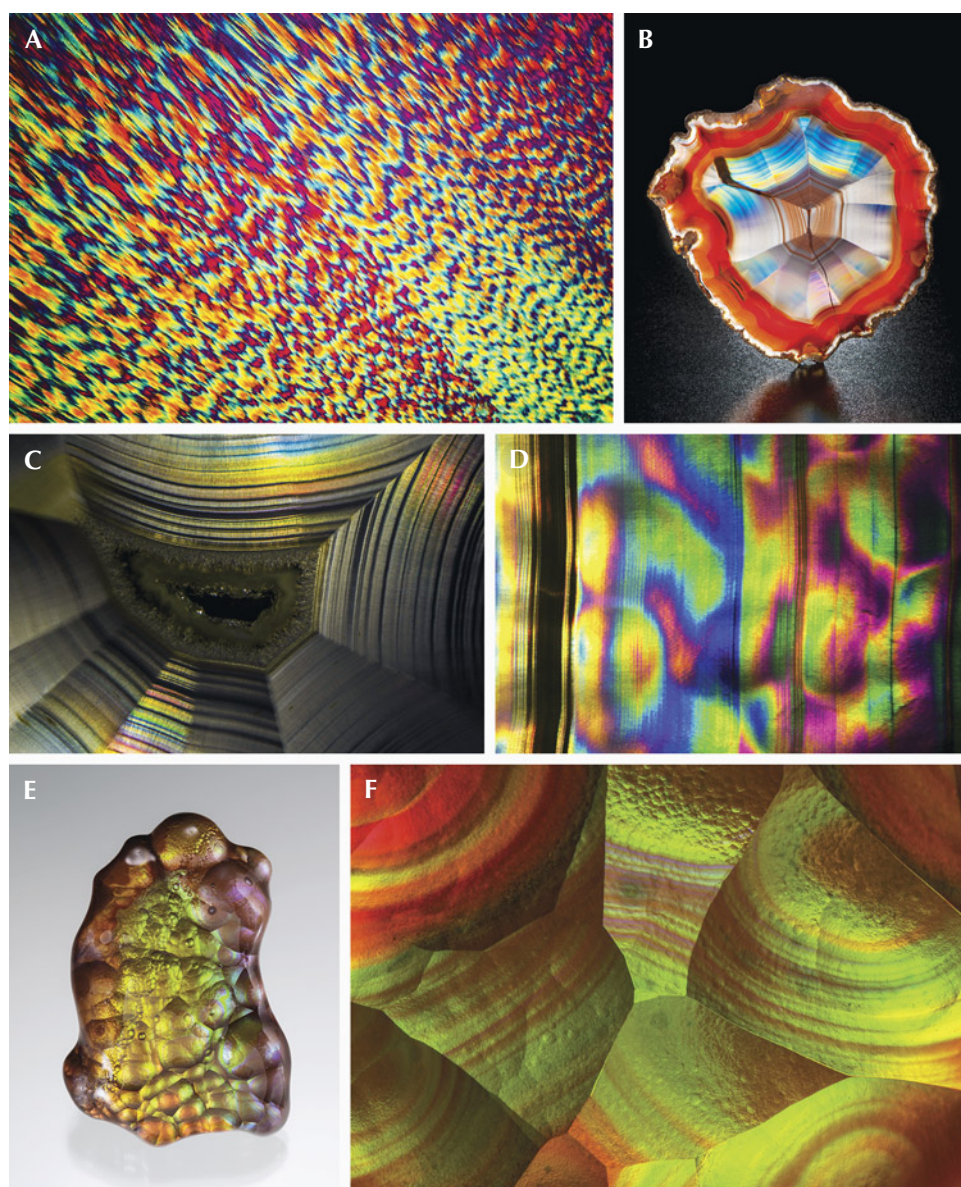


Figure 35. A: A thin section of iris agate under cross-polarized light (lambda plate inserted) showing a *Runzelbänderung* pattern. B: An iris agate slice from Mexico; courtesy of Si and Ann Frazier. C: Iris agate banding. D: Iris agate banding with patchy play-of-color. E: A 48.04 ct botryoidal fire agate from the U.S. state of Arizona; courtesy of Larry Woods, GIA Museum no. 37742. F: Iridescent surface of a botryoidal fire agate showing concentric patterns. Photos by Nathan Renfro (A, C, D, and F) and Robert Weldon (B and E); fields of view 32 mm (C), 15.67 mm (D), and 6.87 mm (F).

dicted the optical orientation of the quartz crystallites based on the polarization of the transmitted light. Electron and optical microscopy studies have revealed hierarchical fractal textures in agate, which show intricate intergrowth relations among mogánite, Brazil-twinned quartz, and untwinned quartz at scales ranging from nanometers to centimeters (Heaney, 2021). Unfortunately, no study has been published that couples TEM analyses with laser light diffraction experiments to clarify the relation between the iridescence quality and the periodicity of the intergrowth texture.

Fire agate is another variety of iridescent chalcedony that typically has a botryoidal form. It displays primarily green to orange iridescence over a predominantly brown bodycolor (figure 35, E and F). The iridescence, or “fire,” of fire agate is observed on the unpolished natural surface under reflected light, and it does not change dramatically at different angles. Studies on fire agates are terribly limited, and thus, without any careful high-resolution electron microscopy investigation, the cause of the iridescence is still undetermined. Thin-film interference from layers of iron (hydr)oxide, which is also responsible for the dark brown bodycolor, is the most probable cause

of the iridescence in fire agate (McMackin, 1974; Schumann, 2009; Newman, 2014).

It should be noted that fire agate is often not considered real agate because identification is based on its iridescence rather than the characteristic banding. Nonetheless, a recent study revealed typical agate banding in the cross section of a fire agate from the U.S. state of Arizona (Natkaniec-Nowak et al., 2020), although it is not clear if the banding is necessary to create the fire effect, or if they are even related at all. More careful microscopic studies over a broader selection of samples are needed to confirm (or disprove) the relation between the fire effect and the agate banding.

“RAINBOW” HEMATITE

Metamorphic hematite schist in a banded-iron formation from the Andrade iron ore deposit in Minas Gerais, Brazil, shows sparkling iridescent colors ranging from purple, blue, and green to yellow and orange (figure 36A). SEM and AFM images show orderly stacked spindle-shaped hematite nanorods arranged in a triangular pattern (figure 36, B and C). The hematite nanocrystals are ~200–300 nm long and

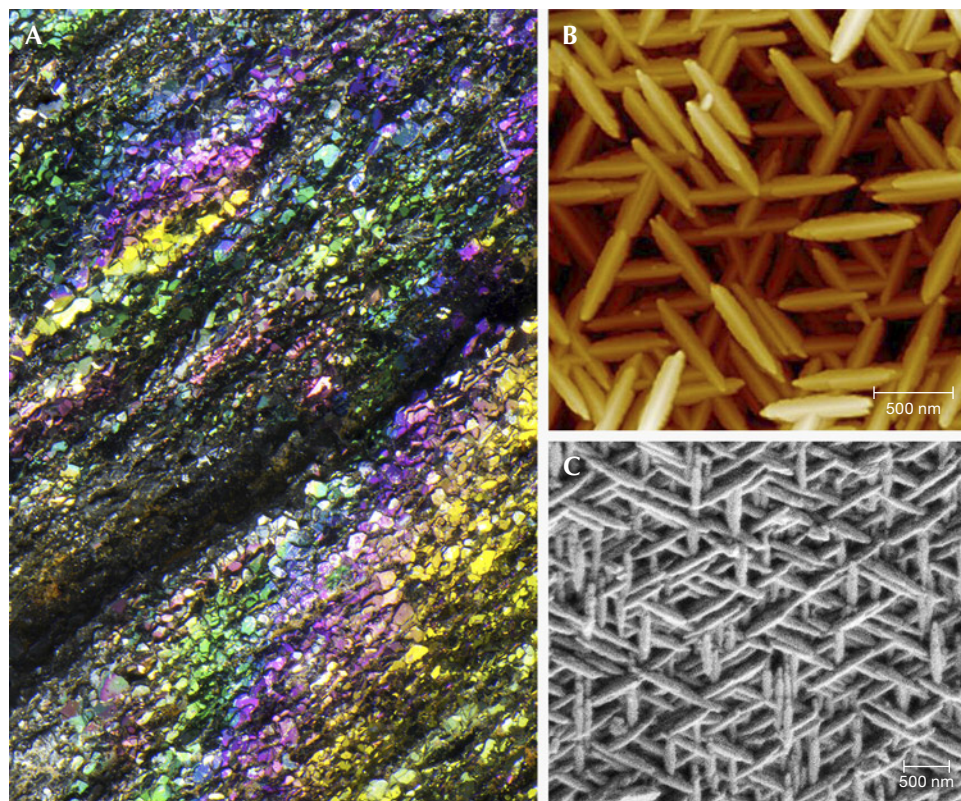


Figure 36. A: “Rainbow” hematite specimen showing different iridescent colors; courtesy of Rhonda Wilson. Photomicrograph by Nathan Renfro; field of view 4.07 mm. B and C: AFM and SEM images of the surface of “rainbow” hematite; images from Lin et al. (2018).

~50–60 nm wide, with the spacing in between on the scale of 280–400 nm, which makes “rainbow” hematite a 3D photonic crystal like precious opal (Lin et al., 2018). Nonetheless, the iridescence appears to be a surface effect in light of hematite’s high absorptivity and reflectivity. Hematite’s high RI further constrains the diffraction angle, resulting in iridescent colors that do not change noticeably with changing angles, instead of the play-of-color effect observed in precious opal.

EDS analyses and structural refinement from XRD reveal high concentrations of aluminum and trace phosphorus impurities in “rainbow” hematite, which may be the reason for the unusual shape of the nanocrystals. Phosphorus is known to preferentially attach to the prismatic {100} and {110} faces, which promotes spindle-shaped crystals over the typical rhombohedral form. The orderly stacked texture of “rainbow” hematite is theorized to have resulted from oriented aggregation, due to spontaneous alignment of the crystal lattices of independently crystallized hematite nanorods (Lin et al., 2018).

The nanorod structure was believed to be pervasive throughout the entire specimen because the iridescence can also be observed on freshly fractured surfaces (Lin et al., 2018). However, because strongly foliated hematite schist is composed of iridescent flakes at the scale of ~100 µm (figure 36A), the “freshly fractured” surface could be mostly separated boundaries between flakes, instead of revealing the interior of individual flakes. A recent study showed that some flakes contain non-iridescent patches,

which are exposed areas of bulk hematite crystals (free of aluminum or phosphorus in the EDS spectrum) under a “coating” of stacked nanorods (Rossman and Ma, 2025). Somewhat similar nanorod structures associated with the enrichment of aluminum and phosphorus (or arsenic) have also been observed on the surface of several non-foliated hematite specimens from Mexico and the United States (Oregon and Alaska), although their nature could not be confirmed by XRD or EBSD due to the limited size (Rossman and Ma, 2025).

RAINBOW SCAPOLITE

Some included scapolite (Scp: $\text{Ca}_4\text{Al}_6\text{Si}_6\text{O}_{24}\text{CO}_3$ – $\text{Na}_4\text{Al}_3\text{Si}_9\text{O}_{24}\text{Cl}$ solid solution) crystals, reportedly from India, Tanzania, and Mozambique (Choudhary, 2013; Ye et al., 2021), display striking iridescent colors under reflected light (figure 37), hence called rainbow scapolite. The iridescence derives from thin brown lamellar inclusions decorated by darker dots, which are identified as magnetite using Raman spectroscopy and XRD (Sun et al., 2015; Ye et al., 2021), presumably formed by solid-state precipitation.

Different from the iron oxide inclusions in rainbow lattice sunstone, the iridescence from the magnetite inclusions in scapolite changes color dramatically when observed at different angles (video 6), making it a play-of-color effect like that in precious opal. The transparent appearance of the typically opaque magnetite lamellae also indicates that the iridescence of rainbow scapolite is created

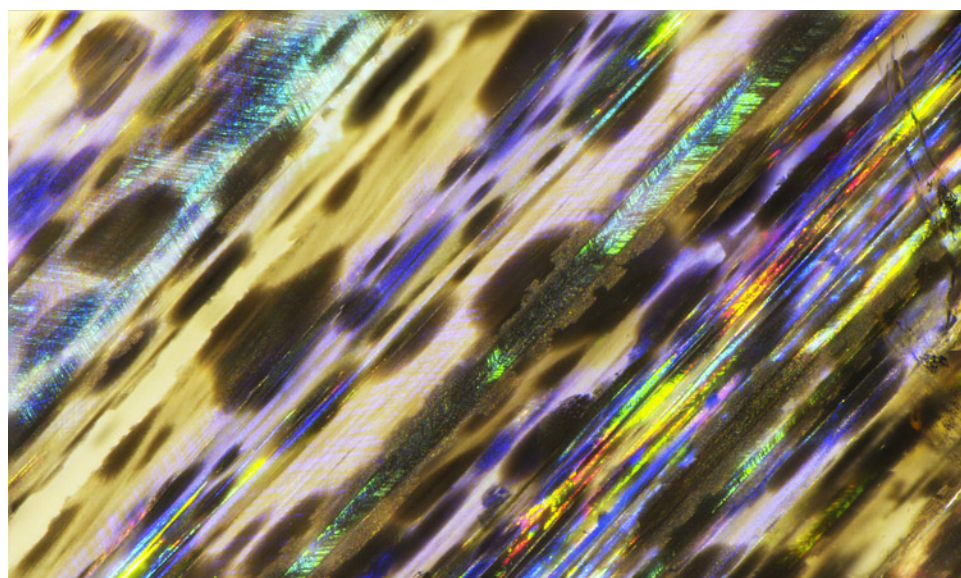


Figure 37. Magnetite inclusions in rainbow scapolite showing iridescence under reflected light. The iridescent color is observed only at certain angles due to diffraction. Photomicrograph by Nathan Renfro; field of view 4.8 mm.

by a diffraction grating instead of thin-film interference (Ye et al., 2021). Scapolite is a unique mineral that can contain the diffracting crystals inside rather than on the surface, so it can be faceted without affecting the play-of-color. Further electron microscopic investigation is needed to understand the mechanism that creates such an intricate structure inside an otherwise homogeneous crystal.

IRIDESCENCE OF SHELL AND PEARL

Structural colors are much more common in the biological world than in the mineral world because living creatures are better at creating minute and regular structures at the optical scale. Butterfly wings, bird feathers, beetle shells, fish scales, and even fern leaves can all display brilliant iridescent colors from submicron structures that have been perfected by natural selection over millions of years (Kinoshita, 2008). With shells and pearls, mineralogy and biology intersect through the process known as biomineralization.

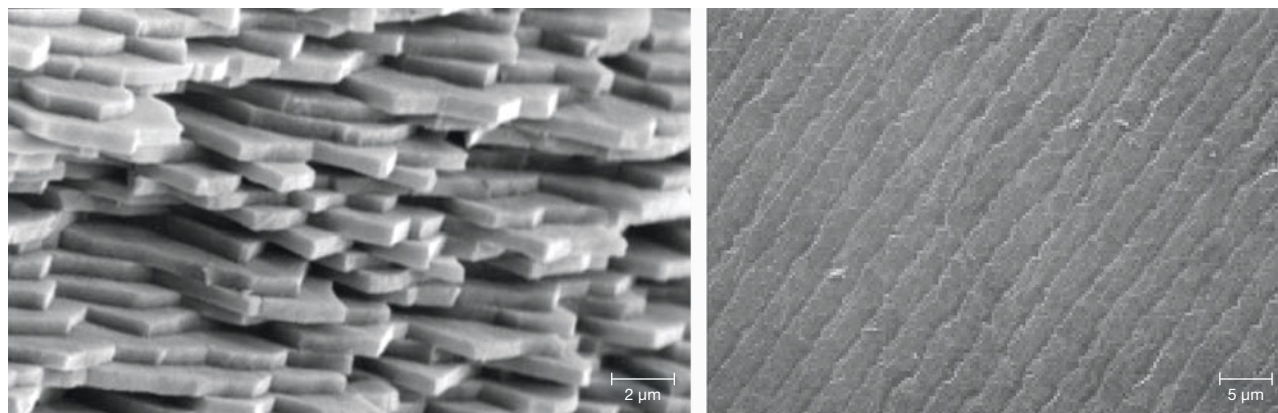
Most pearls and the inner surfaces of shells of pearl-producing mollusks are constructed of nacre, or mother-of-pearl, a composite material consisting of closely packed single-crystal aragonite (Arg: CaCO_3) platelets bonded together by thin films of conchiolin (an insoluble protein), forming a “brick-and-mortar” structure (figure 38, left). The aragonite platelets range from ~300–600 nm in thickness (Snow et al., 2004), with the degree of variation depending on the species and growth conditions. Surprisingly, despite the seemingly straightforward lamellar texture reminiscent of that of iridescent

labradorite, the origin of iridescence in nacre is not as simple as many would assume.

Most studies of iridescent nacre have been performed on shells instead of pearls (Raman, 1935; Ball, 1982; Liu et al., 1999, 2003; Brink et al., 2002; Tan et al., 2004; Snow and Pring, 2005), mainly because iridescence is more prominent in the former (Snow et al., 2004) (figure 39), although the lower prices and larger sizes of shells certainly also influence sample selection. The nacre of a pearl is believed to be identical to the shell it is extracted from, as they form through the same mineralization process. However, it should not be assumed that the cause of iridescence is also the same for pearls and shells, because surface textures could play an important role.

Much evidence suggests that the iridescence of nacre is caused by a diffraction grating on its surface. Early studies showed that some iridescent colors of nacre can be “communicated” or transferred to beeswax (Brewster, 1833; Pfund, 1917; Strutt, 1923b). More recent studies of shells have both documented the periodic grooves on the shell surface using SEM and measured the optical backscatter diffraction pattern with a laser (Liu et al., 1999, 2003; Tan et al., 2004). The periodic steps observed in these studies are created by the shell surface intersecting the stacked aragonite layers at a small angle (figure 38, right). Interestingly, as Raman (1935) first pointed out, the internal multilayer interference effect coincides with a section of the surficial diffraction spectrum along the same direction, because the diffraction grating on the surface arises from the layered structure inside the nacre. Several recent computational studies have simulated the appearance of

Figure 38. Left: SEM image of the cross section of a broken pearl showing packed aragonite platelets. Image from Snow et al. (2004). Right: SEM image of the surface of an iridescent shell showing periodic grooves that act as a reflection grating. Image from Liu et al. (1999).



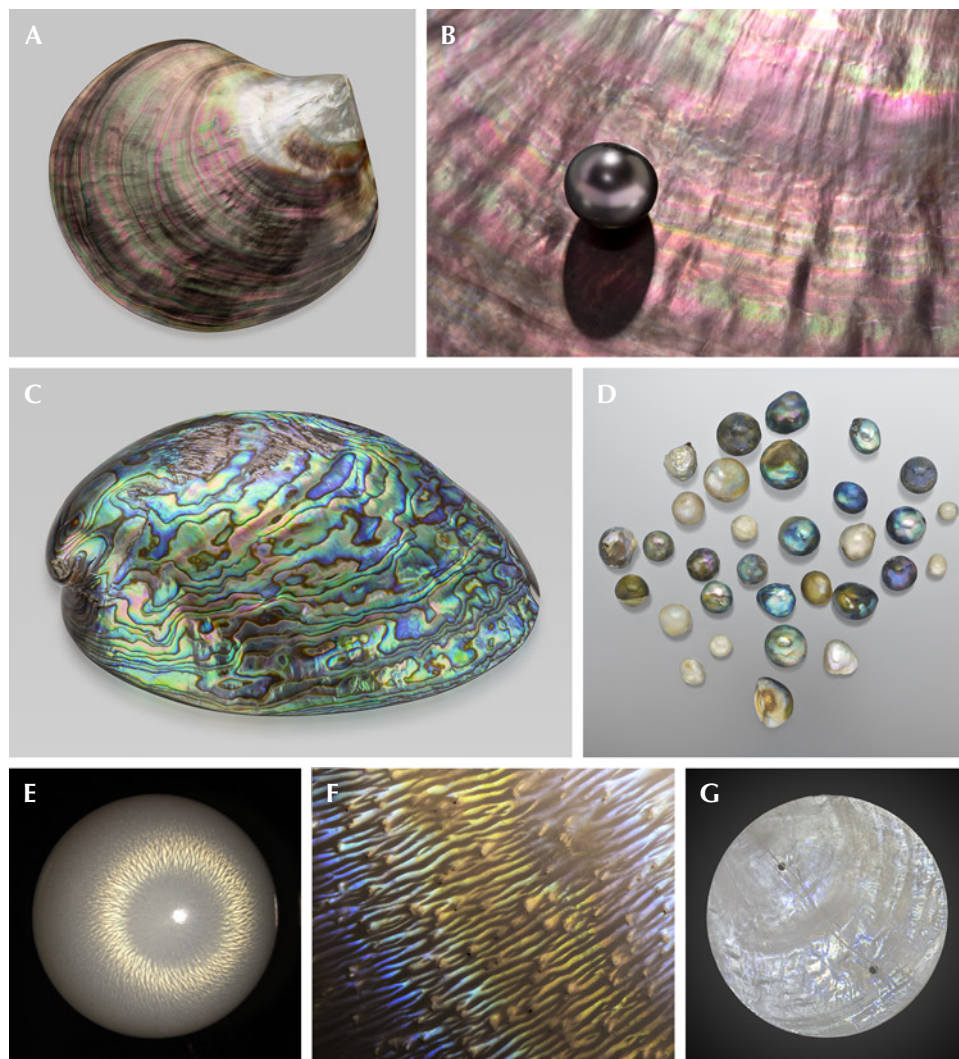


Figure 39. A: A polished *Pinctada margaritifera* shell (110.9 g) from Tahiti showing strong iridescent colors; courtesy of GIA Museum, collection no. 23105. B: A Tahitian cultured pearl with pink iridescent overtone on top of an iridescent shell. C: An 87.90 g polished abalone shell; courtesy of GIA Museum, collection no. 36706. D: Semi-round abalone pearls, the largest measuring 10.93 mm and the smallest 4.46 mm; courtesy of KCB Natural Pearls. E: Iridescent flame structure on a 9.80 mm non-nacreous *Tridacna* pearl under fiber-optic illumination resembles a chatoyant effect. F: Flame structure of a *Spondylus* pearl showing yellow and blue iridescent colors; field of view 2.34 mm. G: Circularly cut windowpane oyster (*Placuna placenta*) shell (50 mm in diameter) showing faint iridescence. Photos by Emily Lane (A, C, and G), Robert Weldon (B), and Artitaya Homkraj (E and F).

pearls quite accurately using the multilayer interference model (Fan et al., 2021; Ozaki et al., 2021).

The most striking iridescent nacre is found in the shells of abalone (figure 39C), which as a sea snail (Gastropoda), belongs to a different class of shellfish than oysters, clams, and scallops (Bivalvia). Abalone is also known for producing irregularly shaped pearls with strong iridescence (figure 39D). The nacre produced by gastropods is columnar, comprising aragonite platelets that are thinner and more uniform than the sheet nacre found in bivalve shells (Snow and Pring, 2005), perhaps accounting for the stronger iridescence. The columnar nacre also contains isolated “stacks” on the surface (Guo, 2010), although it is not clear whether they contribute to the iridescent colors of abalone shells and pearls.

It is often assumed that the iridescence in shell and pearl is exclusive to the nacreous surface. However, recent studies have found a tilted lamellar structure under the non-nacreous outer surface of limpet shells, creating polarization-dependent green iridescent colors (Brink et al., 2002; Brink and van der Berg, 2005). Iridescence has also been observed in the flame structure of some non-nacreous pearls (figure 39, E and F), the underlying submicron structures of which have not yet been studied. A pearl consisting of calcite (Cal: CaCO_3) instead of aragonite with a “nacreous” appearance has also been discovered (Au, 2022). And a study on the windowpane oyster shell, which can display faint iridescence (figure 39G), revealed a calcite-dominant composition as well (Li and Ortiz, 2013).

IRIDESCENT AMMONITE

Ammonite is another shell-making mollusk closely related to squid and octopus, all of which belong to the class Cephalopoda. Ammonites are discussed separately in this section because they went extinct along with non-avian dinosaurs ~66 million years ago; therefore, they can be found only as fossils in sedimentary rocks. Ammonite fossils have been studied extensively by paleontologists, as they are considered important index fossils for the Devonian through the Cretaceous periods due to their broad geographic distribution and rapid evolutionary trends.

Some ammonite fossils from Madagascar, Canada, and Russia display iridescence with various colors, making them desirable not only to rock and fossil collectors but also in the gem market (figure 40). The best-quality material with the brightest iridescence is found in the marine shales of the Bearpaw Formation in southern Alberta, Canada, which was trademarked by the mining company Korite as “Ammolite,” a term that is now in the public domain and can be applied to any iridescent ammonite (Mychaluk et al., 2001; Mychaluk, 2009). The iridescent ammonite recently discovered in Krasnoyarsk Krai, Russia, appears to be of comparable quality to Canadian ammolite, but in much smaller quantities (Radko et al., 2021). Most iridescent ammonites are in fractured pieces, which are extremely fragile and require special stabilization and manufacturing processes (e.g., stabilization with epoxy or made into doublets or triplets backed and

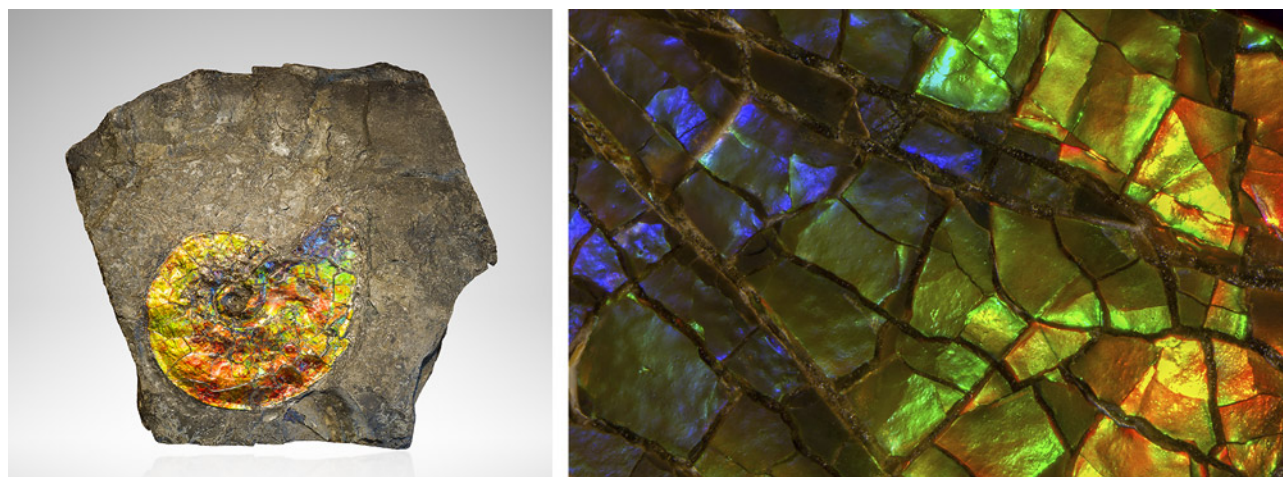
covered by tougher materials) before they can be used for jewelry (Mychaluk et al., 2001; Shen and Liao, 2017).

The iridescence of ammolite is among the brightest of all iridescence in gem materials, yet studies of its optical properties and internal structures are very limited, partly due to its relatively recent discovery (Mychaluk et al., 2001). Iridescent ammonite is comprised of mostly aragonite, with small amounts of apatite, pyrite, siderite, and calcite (Shen and Liao, 2017; Radko et al., 2021). The few SEM images of iridescent ammonite reveal layers of aragonite platelets similar to the nacre in modern shells and pearls (Mychaluk et al., 2001; Shen and Liao, 2017; Radko et al., 2021). It is not clear how the fossilization process has altered the internal structures of the shells and affected the iridescent colors. The breakdown and replacement of the organic films in the original nacre would change the reflective properties of ammonite and may enhance the iridescent color.

SUMMARY

The range of different optical phenomena in the gem world is quite astonishing. The diversity of different optical phenomena in gemstones reflects the extreme ranges of thermodynamic conditions exhibited by geological processes. Most of the light-diffracting structures in phenomenal gemstones are secondary and form long after the original crystal-

Figure 40. Left: Iridescent ammonite fossil in its shale host rock (45 cm wide) from Alberta, Canada; gift of Korite International, GIA Museum no. 30195. Right: An ammonite fossil from Alberta, Canada, showing a full spectrum of color; courtesy of John I. Koivula. Photos by Kevin Schumacher (left) and Nathan Renfro; field of view 13.09 mm (right).



lization through precipitation, exsolution, or chemical alteration. Crystals formed in equilibrium are normally homogeneous without any internal texture. Cooling, decompression, and changing oxygen fugacity can push a homogeneous crystal out of equilibrium to start unmixing or reacting with its surroundings. These diffusion-controlled solid-state reactions are typically very slow, which restricts the scale of the inclusions and exsolution textures to sizes small enough to scatter or diffract visible light.

The primary heterogeneities in gemstones typically form directly through nonequilibrium processes. Low-temperature mineralization (e.g., agate and opal) is often disequilibrated by kinetic barriers, with the extreme case being biomineralization at ambient temperature (i.e., shells and pearls). Nonequilibrium processes can also occur at higher temperatures due to drastically changing temperature, pressure, or chemistry. For instance, rapid crystal growth can create linear defects such as growth tubes in pegmatite minerals, and rapid quenching of flowing lava can form flattened gas bubbles in sheen obsidian.

The degree of disequilibration strongly affects the form of optical phenomena in gemstones. Phenomenal gemstones that formed slowly at high temperatures, through magmatism or metamorphism, typically have a more pervasive and uniform appearance, such as asteriated corundum and iridescent feldspars. On the other hand, those formed at lower temperatures, or rapidly within a short period of time, are often more heterogeneous and disorganized, such as iris agate and fire obsidian. Perhaps the most enigmatic aspect of the phenomenal gemstone formation is the fine line between order and randomness. For instance, how do opal and agate textures switch rapidly back and forth between vibrant play-of-color and dull milky scattering within the same specimen? Why do pearls and shells from the same species display such different iridescent colors?

All optical phenomena in gemstones can be described as diffraction of light by their submicron inclusions or textures with broadly variable sizes and shapes. The diffraction pattern is the reciprocal of the light-diffracting particle, meaning the more extended the particle is in a certain dimension, the more confined the diffracted light is in that direction. The nanoparticles in fancy white diamonds and milky sapphires are zero-dimensional particles, which scatter light evenly in every direction in three-dimensional space. The one-dimensional nee-

dles in chatoyant and asteriated gemstones diffract light into a two-dimensional cone. The two-dimensional plates and layers in aventurescent and schillerized gemstones reflect light in a fixed direction, with one remaining degree of freedom (the incident angle can still change). The diffraction condition of the three-dimensional photonic crystals is restricted to zero dimension (to use the terminology of X-ray crystallography, the reciprocal space of a 3D periodic structure consists of arrays of discrete zero-dimensional spots, meaning that the diffracted beam can only be observed when the incident angle, diffraction angle, and wavelength satisfy a very specific condition with zero degrees of freedom).

The optical effects of phenomenal gemstones are described only qualitatively in this article. However, just as crystal structures can be determined and refined from XRD patterns, the optical properties can quantitatively reveal the submicron structures and textures of minerals. For instance, the iridescence spectrum can be used to calculate the lamellae thickness distribution in labradorite and peristerite, and the particle size and density in milky sapphires or copper feldspars can be quantified by measuring the scattering intensity in different directions. Unfortunately, despite the immense research focus on biomimetic photonic materials, there have been few attempts to quantify the submicron structures in minerals using their optical properties. Admittedly, such measurements can be quite challenging due to the heterogeneity and irregular shapes commonly found in natural materials. Nonetheless, as powerful as modern electron microscopes are, they can provide only two-dimensional information for surfaces and cross sections, whereas optical diffraction and spectroscopy can characterize the textures in three dimensions. Hopefully the studies of optical phenomena in gemstones can inspire new analytical techniques for characterizing three-dimensional structures and textures of both synthetic and natural nanomaterials.

For videos of phenomenal gemstones, visit:
gia.edu/gems-gemology/summer-2025-phenomenal-gemstones



ABOUT THE AUTHORS

Dr. Shiyun Jin is a senior research scientist, Nathan D. Renfro is senior manager of colored stone identification, Dr. Aaron C. Palke is senior manager of research, and Dr. James E. Shigley is a distinguished research fellow, at GIA in Carlsbad, California.

ACKNOWLEDGMENTS

The authors thank Peter Heaney and an anonymous reviewer for many constructive comments and suggestions. The authors are deeply grateful to everyone who contributed the photographs and images used in this article. Special thanks to John I. Koivula, Rachelle Turnier, and McKenzie Santimer for providing many of the specimens from personal and museum collections, and to Emily Lane and Annie Haynes for their photography and photo editing. We would also like to thank Artitaya Homkrajai for sharing her expertise in pearls and shells, which helped clarify some of the terminology for these organic gems.

REFERENCES

- Abduriyim A. (2009) The characteristics of red andesine from the Himalaya Highland, Tibet. *Journal of Gemmology*, Vol. 31, No. 5–8, pp. 283–298.
- Abduriyim A., McClure S.F., Rossman G.R., Leelawatanasuk T., Hughes R.W., Laurs B.M., Lu R., Isatelle F., Scarratt K., Dubinsky E.V., Douthit T.R., Emmett J.L. (2011) Research on gem feldspar from the Shigatse Region of Tibet. *G&G*, Vol. 47, No. 2, pp. 167–180.
- Ague J.J., Eckert J.O. (2012) Precipitation of rutile and ilmenite needles in garnet: Implications for extreme metamorphic conditions in the Acadian Orogen, U.S.A. *American Mineralogist*, Vol. 97, No. 5–6, pp. 840–855, <http://dx.doi.org/10.2138/am.2012.4015>
- Andersen O. (1915) On aventurine feldspar. *American Journal of Science*, Vol. s4-40, No. 238, pp. 351–399, <http://dx.doi.org/10.2475/ajs.s4-40.238.351>
- Appel P.W.U., Jensen A. (1987) A new gem material from Greenland: Iridescent orthoamphibole. *G&G*, Vol. 23, No. 1, pp. 36–42, <http://dx.doi.org/10.5741/GEMS.23.1.36>
- Applin K.R., Hicks B.D. (1987) Fibers of dumortierite in quartz. *American Mineralogist*, Vol. 72, No. 1–2, pp. 170–172.
- Arnon Z.A., Pinotsi D., Schmidt M., Gilead S., Guterman T., Sadhanala A., Ahmad S., Levin A., Walther P., Kaminski C.F., Fändrich M., Kaminski Schierle G.S., Adler-Abramovich L., Shimon L.J.W., Gazit E. (2018) Opal-like multicolor appearance of self-assembled photonic array. *ACS Applied Materials & Interfaces*, Vol. 10, No. 24, pp. 20783–20789, <http://dx.doi.org/10.1021/acsami.8b04912>
- Au C.Y.W. (2022) Lab Notes: Calcite found on the surface of a salt-water “nacreous” pearl. *G&G*, Vol. 58, No. 4, pp. 477–478.
- Axler J.A., Ague J.J. (2015) Oriented multiphase needles in garnet from ultrahigh-temperature granulites, Connecticut, U.S.A. *American Mineralogist*, Vol. 100, No. 10, pp. 2254–2271, <http://dx.doi.org/10.2138/am-2015-5018>
- Badar M.A., Akizuki M. (1997) Iridescent andradite garnet from the Sierra Madre Mountains, Sonora, Mexico. *Neues Jahrbuch für Mineralogie - Monatshefte*, Vol. 1997, No. 12, pp. 529–539, <http://dx.doi.org/10.1127/njmm/1997/1997/529>
- Badar M.A., Akizuki M., Hussain S. (2010) Optical anomaly in iridescent andradite from the Sierra Madre Mountains, Sonora, Mexico. *Canadian Mineralogist*, Vol. 48, No. 5, pp. 1195–1203, <http://dx.doi.org/10.3749/canmin.48.5.1195>
- Bailey S.W. (1977) Report of the I.M.A.-I.U.Cr. Joint Committee on Nomenclature. *American Mineralogist*, Vol. 62, No. 5–6, pp. 411–415.
- Baldwin L.C., Tomaschek F., Ballhaus C., Gerdes A., Fonseca R.O.C., Wirth R., Geisler T., Nagel T. (2017) Petrogenesis of alkaline basalt-hosted sapphire megacrysts. Petrological and geochemical investigations of in situ sapphire occurrences from the Siebengebirge Volcanic Field, Germany. *Contributions to Mineralogy and Petrology*, Vol. 172, No. 6, article no. 43, <http://dx.doi.org/10.1007/s00410-017-1362-0>
- Ball R.A. (1982) Further studies on iridescence of marine shells. *Australian Gemmologist*, Vol. 14, No. 10, pp. 266–271.
- Barry J.C., Bursill L.A., Hutchison J.L., Lang A.R., Rackham G.M., Sumida N. (1987) On voidites: A high-resolution transmission electron microscopic study of faceted void-like defects in natural diamonds. *Philosophical Transactions of the Royal Society of London. Series A, Mathematical and Physical Sciences*, Vol. 321, No. 1560, pp. 361–401, <http://dx.doi.org/10.1098/rsta.1987.0018>
- Baryshev A.V., Kaplyanskii A.A., Kosobukin V.A., Limonov M.F., Samusev K.B., Usvyat D.E. (2003a) Bragg diffraction of light in high-quality synthetic opals. *Physica E: Low-dimensional Systems and Nanostructures*, Vol. 17, pp. 426–428, [http://dx.doi.org/10.1016/S1386-9477\(02\)00905-0](http://dx.doi.org/10.1016/S1386-9477(02)00905-0)
- (2003b) Bragg diffraction of light in synthetic opals. *Physics of the Solid State*, Vol. 45, No. 3, pp. 459–471, <http://dx.doi.org/10.1134/1.1562231>
- Baryshev A.V., Kosobukin V.A., Samusev K.B., Usvyat D.E., Limonov M.F. (2006) Light diffraction from opal-based photonic crystals with growth-induced disorder: Experiment and theory. *Physical Review B*, Vol. 73, No. 20, article no. 205118, <http://dx.doi.org/10.1103/PhysRevB.73.205118>
- Bernauer F. (1927) Über zickzackbänderung (Runzelbänderung) und verwandte polarisationerscheinungen an kristallen und kristallaggregation. *Neues Jahrbuch für Mineralogie, Geologie und Palaeontologie, Beilageband*, Vol. 55, pp. 92–143.
- Bian G., Ageeva O., Rečnik A., Habler G., Abart R. (2021) Formation pathways of oriented magnetite micro-inclusions in plagioclase from oceanic gabbro. *Contributions to Mineralogy and Petrology*, Vol. 176, No. 12, article no. 104, <http://dx.doi.org/10.1007/s00410-021-01864-8>
- Bian G., Ageeva O., Roddatis V., Habler G., Schreiber A., Abart R. (2023) Oriented secondary magnetite micro-inclusions in plagioclase from oceanic gabbro. *American Mineralogist*, Vol. 108, No. 9, pp. 1642–1657, <http://dx.doi.org/10.2138/am-2022-8784>
- Bøggild O.B. (1924) On the labradorization of the feldspars. *Mathematisk-Fysiske Meddelelser*, Vol. 6, pp. 1–79.
- Bohren C.F., Huffman D.R. (1998) *Absorption and Scattering of Light by Small Particles*. John Wiley & Sons, Ltd, Mörlenbach, Germany.
- Bolton H.C., Bursill L.A., McLaren A.C., Turner R.G. (1966) On the origin of the colour of labradorite. *Physica Status Solidi (B)*, Vol. 18, No. 1, pp. 221–230, <http://dx.doi.org/10.1002/pssb.19660180123>
- Boyd S.R., Kiflawi I., Woods G.S. (1995) Infrared absorption by the B nitrogen aggregate in diamond. *Philosophical Magazine B*, Vol. 72, No. 3, pp. 351–361, <http://dx.doi.org/10.1080/13642819508239089>
- Breebaart A.J. (1958) Synthetic moonstone—Coloured spinel. *Journal of Gemmology*, Vol. 6, No. 5, pp. 213–214.
- Brewster D. (1813) XIII. On some properties of light. *Philosophical*

- Transactions of the Royal Society of London*, Vol. 103, pp. 101–109, <http://dx.doi.org/10.1098/rstl.1813.0016>
- (1833) *A Treatise on Optics*. Carey, Lea, & Blanchard, Philadelphia.
- (1843) On the cause of the colour in iris agate. *Philosophical Magazine*, Vol. 22, pp. 434–435.
- Brink D.J., van der Berg N.G. (2005) An investigation of green iridescence on the mollusc *Patella granatina*. *Journal of Physics D: Applied Physics*, Vol. 38, No. 2, article no. 338, <http://dx.doi.org/10.1088/0022-3727/38/2/019>
- Brink D.J., van der Berg N.G., Botha A.J. (2002) Iridescent colors on seashells: An optical and structural investigation of *Helcion pruinosus*. *Applied Optics*, Vol. 41, No. 4, pp. 717–722, <http://dx.doi.org/10.1364/AO.41.000717>
- Brown L.D. (2005) Characterisation of Australian Opals. PhD thesis, University of Technology Sydney, Ultimo, Australia.
- Buckley A.N., Woods R. (1983) X-ray photoelectron spectroscopic investigation of the tarnishing of bornite. *Australian Journal of Chemistry*, Vol. 36, No. 9, pp. 1793–1804, <http://dx.doi.org/10.1071/ch9831793>
- Bui T.N., Deliousi K., Malik T.K., De Corte K. (2015) From exsolution to ‘gold sheen’: A new variety of corundum. *Journal of Gemmology*, Vol. 34, No. 8, pp. 678–691.
- Bui T.N., Entremont P., Gauthier J.-P. (2017) Large 12-rayed black star sapphire from Sri Lanka with asterism caused by ilmenite inclusions. *Journal of Gemmology*, Vol. 35, No. 5, pp. 430–435.
- Bui T.N., Entremont P., Mazzero F., Gauthier J.-P. (2020) Stereoscopia in asteriated gemstones revisited. *Journal of Gemmology*, Vol. 37, No. 3, pp. 298–305.
- Cartier R. (2009) Optical phenomena in gemstones. *Australian Gemmologist*, Vol. 23, No. 10, pp. 447–449.
- Challener S., Renfro N.D., Sun Z. (2017) Micro-World: New phenomenal feldspar from North Carolina with iridescent inclusions. *G&G*, Vol. 53, No. 4, p. 467.
- Champness P.E., Lorimer G.W. (1976) Exsolution in silicates. In H.-R. Wenk, Ed., *Electron Microscopy in Mineralogy*. Springer, Berlin, Heidelberg, pp. 174–204, http://dx.doi.org/10.1007/978-3-642-66196-9_9
- Champness P.E., Rodgers K.A. (2000) The origin of iridescence in anthophyllite-gedrite from Simiutatt, Nuuk district, southern West Greenland. *Mineralogical Magazine*, Vol. 64, No. 5, pp. 885–889, <http://dx.doi.org/10.1180/002646100549715>
- Choudhary G. (2008) Aventurine K-feldspar. *Journal of Gems & Gemmology*, Vol. 10, No. 3, pp. 20–22.
- (2011) Gem News International: Pink cat’s-eye quartz, with color and chatoyancy caused by tourmaline needles. *G&G*, Vol. 47, No. 3, pp. 245–246.
- (2013) Gem News International: Zoned scapolite from India. *G&G*, Vol. 49, No. 1, pp. 58–59.
- Choudhary G., Vyas M.B. (2009) “Multiphenomenal” quartz from India. *Gems & Jewellery*, Vol. 18, No. 1, pp. 10–12.
- Christie O.H.J., Olsen A. (1974) Spinodal precipitation in minerals. Review and some new observations. *Bulletin de Minéralogie*, Vol. 97, No. 2, pp. 202–205, <http://dx.doi.org/10.3406/bulmi.1974.6879>
- Colony R.J. (1935) Schiller structure. *American Mineralogist*, Vol. 20, No. 12, pp. 828–837.
- Copley P.A., Gay P. (1978) A scanning electron microscope investigation of some Norwegian aventurine feldspars. *Norsk Geologisk Tidsskrift*, Vol. 58, No. 1, pp. 93–95.
- (1979) Crystallographic studies of some Norwegian aventurinized feldspars by optical, X-ray, and electron optical methods. *Norsk Geologisk Tidsskrift*, Vol. 59, No. 3, pp. 229–237.
- (1982) The heat treatment of some Norwegian aventurinized feldspars. *Mineralogical Magazine*, Vol. 45, No. 337, pp. 107–110, <http://dx.doi.org/10.1180/minmag.1982.045.337.12>
- Curtis N.J., Gascooke J.R., Johnston M.R., Pring A. (2019) A review of the classification of opal with reference to recent new localities. *Minerals*, Vol. 9, No. 5, article no. 299, <http://dx.doi.org/10.3390/min9050299>
- Darragh P.J., Sanders J.V. (1965) Origin of colour in opal based on electron microscopy. *Australian Gemmologist*, Vol. 7, pp. 9–12.
- Dietrich R.V., White J.S., Nelen J.E., Chyi K.-L. (1988) A gem-quality iridescent orthoamphibole from Wyoming. *G&G*, Vol. 24, No. 3, pp. 161–164, <http://dx.doi.org/10.5741/GEMS.24.3.161>
- Divljan S. (1960) The results of field and laboratory studies of aventurine plagioclases from some Norwegian pegmatites. In: *Proceedings of the 21st International Geological Congress, Norden*. pp. 94–101.
- Drev S., Komelj M., Mazaj M., Daneu N., Rečnik A. (2015) Structural investigation of (130) twins and rutile precipitates in chrysoberyl crystals from Rio das Pratinhas in Bahia (Brazil). *American Mineralogist*, Vol. 100, No. 4, pp. 861–871, <http://dx.doi.org/10.2138/am-2015-5120>
- Durán A., Fernández Navarro J.M., García Solé J., Agulló-López F. (1984) Study of the colouring process in copper ruby glasses by optical and EPR spectroscopy. *Journal of Materials Science*, Vol. 19, No. 5, pp. 1468–1475, <http://dx.doi.org/10.1007/BF00563041>
- Eaton-Magaña S., Ardon T., Breeding C.M., Shigley J.E. (2019) Natural-color fancy white and fancy black diamonds: Where color and clarity converge. *G&G*, Vol. 55, No. 3, pp. 320–337, <http://dx.doi.org/10.5741/GEMS.55.3.320>
- Ediriweera R.N., Perera S.I., Phil M. (1989) Heat treatment of Gauda stones – Spectral investigation. *Journal of Gemmology*, Vol. 21, No. 7, pp. 403–404.
- Emmett J.L., Douthit T.R. (2009) *Copper Diffusion in Plagioclase*. GIA News from Research, <https://www.gia.edu/doc/Cu-diffusion-Emmett.pdf>
- Emori K., Oto S., Igami Y., Uzuhashi J., Ohkubo T., Kitawaki H., Miyake A. (2024) Nano-inclusions associated with beryllium in untreated blue sapphires from Diego Suarez, Madagascar. *Journal of Gemmology*, Vol. 39, No. 4, pp. 364–372.
- Eppler W.F. (1958) Notes on asterism in corundum, rose quartz and almandine garnet, and chatoyancy in beryl. *Journal of Gemmology*, Vol. 6, No. 5, pp. 195–212.
- Evans T., Kiflawi I., Luyten W., van Tendeloo G., Woods G.S. (1995) Conversion of platelets into dislocation loops and voidite formation in type IaB diamonds. *Proceedings of the Royal Society of London. Series A: Mathematical and Physical Sciences*, Vol. 449, No. 1936, pp. 295–313, <http://dx.doi.org/10.1098/rspa.1995.0045>
- Fan N., Zhou C., Myagkaya E. (2021) Investigation of nacre nanostructure by analyzing its structural color pattern. *Scientific Reports*, Vol. 11, No. 1, article no. 19686, <http://dx.doi.org/10.1038/s41598-021-99327-4>
- Farfan G., Xu H. (2008) Pleochroism in calcic labradorite from Oregon: Effects from size and orientation of nano- and micro-precipitates of copper and pyroxene. *Geochimica et Cosmochimica Acta*, Vol. 72, No. 12, p. A256. Presented at the Goldschmidt Conference, Vancouver, British Columbia, Canada.
- Fitz Gerald J.D., Parsons I., Cayzer N. (2006) Nanotunnels and pull-aparts: Defects of exsolution lamellae in alkali feldspars. *American Mineralogist*, Vol. 91, No. 5-6, pp. 772–783, <http://dx.doi.org/10.2138/am.2006.2029>
- Freestone I. (1987) Composition and microstructure of early opaque red glass. In M. Bimson and I. Freestone, Eds., *Early Vitreous Materials British Museum Occasional Paper 56*, British Museum, London, pp. 173–191.
- Freestone I., Meeks N., Sax M., Higgitt C. (2007) The Lycurgus Cup—A Roman nanotechnology. *Gold Bulletin*, Vol. 40, No. 4, pp. 270–277, <http://dx.doi.org/10.1007/BF03215599>
- Fronde C. (1954) Commercial synthesis of star sapphires and star rubies. *Transactions of the American Institute of Mining and*

- Metallurgical Engineers*, Vol. 199, No. 1, pp. 78–80.
- Gaillou E. (2015) An overview of gem opals: From the geology to color and microstructure. In *Thirteenth Annual Sinkankas Symposium—Opal*, Pala International, Inc., pp. 10–19.
- Gaillou E., Fritsch E., Aguilar-Reyes B., Rondeau B., Post J., Barreau A., Ostroumov M. (2008) Common gem opal: An investigation of micro- to nano-structure. *American Mineralogist*, Vol. 93, No. 11–12, pp. 1865–1873, <http://dx.doi.org/10.2138/am.2008.2518>
- Gao Y., Merkle K.L., Chang H.L., Zhang T.J., Lam D.J. (1992) Study of defects and interfaces on the atomic scale in epitaxial TiO₂ thin films on sapphire. *Philosophical Magazine A*, Vol. 65, No. 5, pp. 1103–1125, <http://dx.doi.org/10.1080/01418619208201499>
- Gauthier J.-P., Fritsch E., Bui T.N., Fereire J. (2023) Clues to understanding the enigma of the unusual asterism in “Mercedes-star” quartz. *Journal of Gemmology*, Vol. 38, No. 7, pp. 678–695.
- Gittos M.F., Lorimer G.W., Champness P.E. (1976) The phase distributions in some exsolved amphiboles. In H.-R. Wenk, Ed., *Electron Microscopy in Mineralogy*. Springer, Berlin, Heidelberg, pp. 238–247, http://dx.doi.org/10.1007/978-3-642-66196-9_16
- Giuliani G., Ohnenstetter D., Fallick A.E., Groat L., Fagan A.J. (2014) Chapter 2: The Geology and Genesis of Gem Corundum Deposits. In L.A. Groat, Ed., *Geology of Gem Deposits, Second Edition*. Mineralogical Association of Canada, pp. 29–112, <http://dx.doi.org/10.3749/9780921294696.ch02>
- Goreva J.S., Ma C., Rossman G.R. (2001) Fibrous nanoinclusions in massive rose quartz: The origin of rose coloration. *American Mineralogist*, Vol. 86, No. 4, pp. 466–472, <http://dx.doi.org/10.2138/am-2001-0410>
- Götze J., Möckel R., Pan Y. (2020) Mineralogy, geochemistry and genesis of agate—A review. *Minerals*, Vol. 10, No. 11, article no. 1037, <http://dx.doi.org/10.3390/min10111037>
- Gouzy S., Rondeau B., Vinogradoff V., Chauviré B., Coulet M.-V., Grauby O., Terrisse H., Carter J. (2024) Opal synthesis: Toward geologically relevant conditions. *Minerals*, Vol. 14, No. 10, article no. 969, <https://dx.doi.org/10.3390/min14100969>
- Griffiths T.A., Habler G., Abart R. (2020) Determining the origin of inclusions in garnet: Challenges and new diagnostic criteria. *American Journal of Science*, Vol. 320, No. 9, pp. 753–789, <http://dx.doi.org/10.2475/11.2020.01>
- Gu T., Ohfuji H., Wang W. (2019) Origin of milky optical features in type IaB diamonds: Dislocations, nano-inclusions, and polycrystalline diamond. *American Mineralogist*, Vol. 104, No. 5, pp. 652–658, <http://dx.doi.org/10.2138/am-2019-6699>
- Gu T., Wang W. (2018) Optical defects in milky type IaB diamonds. *Diamond and Related Materials*, Vol. 89, pp. 322–329, <http://dx.doi.org/10.1016/j.diamond.2018.09.010>
- Gübelin E.J., Koivula J.I. (2005) *Photoatlas of Inclusions in Gemstones*, Vol. 2, Opinio Verlag, Basel, Switzerland.
- Guinél M.J.-F., Norton M.G. (2006) The origin of asterism in almandine-pyropes garnets from Idaho. *Journal of Materials Science*, Vol. 41, No. 3, pp. 719–725, <http://dx.doi.org/10.1007/s10853-006-6500-4>
- Gunaratne H.S. (1981) Geuda sapphires – Their colouring elements and their reaction to heat. *Journal of Gemmology*, Vol. 17, No. 5, pp. 292–300.
- Guo D.-J. (2010) Microstructure and crystallography of abalone shells. Masters thesis, University of Glasgow, Glasgow, Scotland.
- Hainschwang T., Notari F. (2006) The cause of iridescence in rainbow andradite from Nara, Japan. *G&G*, Vol. 42, No. 4, pp. 248–258, <http://dx.doi.org/10.5741/GEMS.42.4.248>
- Hänni H.A., Koivula J.I., Tannous M. (2003) Gem News International: Star sunstone from Tanzania. *G&G*, Vol. 39, No. 3, pp. 235–236.
- He J. (2006) Precipitation in titanium-doped sapphire. PhD thesis, Case Western Reserve University, Cleveland, OH, USA.
- He J., Lagerlof K.P.D., Heuer A.H. (2011) Structural evolution of TiO₂ precipitates in Ti-doped sapphire (α -Al₂O₃). *Journal of the American Ceramic Society*, Vol. 94, No. 4, pp. 1272–1280, <http://dx.doi.org/10.1111/j.1551-2916.2010.04217.x>
- Heaney P.J. (1993) A proposed mechanism for the growth of chalcidony. *Contributions to Mineralogy and Petrology*, Vol. 115, No. 1, pp. 66–74, <http://dx.doi.org/10.1007/BF00712979>
- (2021) Iris agates and cantor dusts: The textural complexity of agates. *Seventeenth Annual Sinkankas Symposium—Agate and Chalcedony*. Pala International, Inc., pp. 29–39.
- Heaney P.J., Fisher D.M. (2003) New interpretation of the origin of tiger’s-eye. *Geology*, Vol. 31, No. 4, pp. 323–326, [http://dx.doi.org/10.1130/0091-7613\(2003\)031<0323:NIOTOO>2.0.CO;2](http://dx.doi.org/10.1130/0091-7613(2003)031<0323:NIOTOO>2.0.CO;2)
- Heaney P.J., Post J.E., Chen S.A., Clark T., Wenzel T., Jacucci G., Vignolini S. (2018) Painting a rainbow with ochre: Iridescence in botryoidal goethite. Presented at the GSA Annual Meeting, GSA, Indianapolis, Indiana, USA, <http://dx.doi.org/10.1130/abs/2018AM-318614>
- Hernández-Ortiz M., Hernández-Padrón G., Bernal R., Cruz-Vázquez C., Castaño V. (2015) Nanocrystalline mimetic opals: Synthesis and comparative characterization vs. natural stones. *International Journal of Basic and Applied Sciences*, Vol. 4, No. 2, pp. 238–243, <http://dx.doi.org/10.14419/ijbas.v4i2.4174>
- Hodgkinson A. (2017) Moonstone mystery. *Journal of Gemmology*, Vol. 35, No. 5, pp. 378–380.
- Hofmeister A.M., Rossman G.R. (1983) Color in feldspars. In P.H. Ribbe, Ed., *Feldspar Mineralogy*. Mineralogical Society of America, Washington, D.C., pp. 271–280, <http://dx.doi.org/10.1515/9781501508547-016>
- Hu K., Heaney P.J. (2010) A microstructural study of pietersite from Namibia and China. *G&G*, Vol. 46, No. 4, pp. 280–286, <http://dx.doi.org/10.5741/GEMS.46.4.280>
- Hughes E.B. (2018) Micro-World: Star spinel with four and six rays. *G&G*, Vol. 54, No. 2, p. 230.
- Hwang S.-L., Shen P., Chu H.-T., Yui T.F., Iizuka Y. (2013) A TEM study of the oriented orthopyroxene and forsterite inclusions in garnet from Otrøy garnet peridotite, WGR, Norway: New insights on crystallographic characteristics and growth energetics of exsolved pyroxene in relict majoritic garnet. *Journal of Metamorphic Geology*, Vol. 31, No. 2, pp. 113–130, <http://dx.doi.org/10.1111/jmg.12002>
- (2015) Origin of rutile needles in star garnet and implications for interpretation of inclusion textures in ultrahigh-pressure metamorphic rocks. *Journal of Metamorphic Geology*, Vol. 33, No. 3, pp. 249–272, <http://dx.doi.org/10.1111/jmg.12119>
- Hwang S.-L., Shen P., Yui T.-F., Chu H.-T. (2010) On the coherency-controlled growth habit of precipitates in minerals. *Journal of Applied Crystallography*, Vol. 43, No. 3, pp. 417–428, <http://dx.doi.org/10.1107/S0021889810007454>
- Hyršl J. (2001) Some new unusual cat’s-eyes and star stones. *Journal of Gemmology*, Vol. 27, No. 8, pp. 456–460.
- Ignatov S.I., Platonov A.N., Sedenko V.S., Taran M.N. (1990) Pozheve zavravlennya kvarcu, zvyazane z mikrovklyucheniyami dumortyeritu. *Dopovidi Akademii nauk Ukrainskoi RSR, Seriya B: Heolohichni, khimichni ta biolohichni nauky*, Vol. 7, pp. 23–26.
- Ingerson E., Barksdale J.D. (1943) Iridescent garnet from the Adelaide Mining District, Nevada. *American Mineralogist*, Vol. 28, No. 5, pp. 303–312.
- Izokh A.E., Smirnov S.Z., Egorova V.V., Anh T.T., Kovyazin S.V., Phuong N.T., Kalinina V.V. (2010) The conditions of formation of sapphire and zircon in the areas of alkali-basaltoid volcanism in Central Vietnam. *Russian Geology and Geophysics*, Vol. 51, No. 7, pp. 719–733, <http://dx.doi.org/10.1016/j.rgg.2010.06.001>
- Jayaram V. (1988) The precipitation of alpha-TiO₂ from supersaturated solutions of Ti in alumina crystal structure and morphology. *Philosophical Magazine A*, Vol. 57, No. 3, pp.

- 525–542, <http://dx.doi.org/10.1080/01418618808204683>
- Jayaraman A. (1953) The structure and optical behaviour of chalcedony. *Proceedings of the Indian Academy of Sciences – Section A*, Vol. 38, No. 6, pp. 441–449, <http://dx.doi.org/10.1007/BF03045262>
- Jin S., Palke A.C., Renfro N.D., Sun Z. (2023) Special colors and optical effects of Oregon sunstone: Absorption, scattering, pleochroism, and color zoning. *G&G*, Vol. 59, No. 3, pp. 298–322, <http://dx.doi.org/10.5741/GEMS.59.3.298>
- Jin S., Saxey D.W., Quadir Z., Reddy S.M., Rickard W.D.A., Fougere D., Sun X., Palke A.C. (2024) Nanoparticles in natural beryllium-bearing sapphire: Incorporation and exsolution of high field strength elements in corundum. *Contributions to Mineralogy and Petrology*, Vol. 179, No. 12, article no. 110, <http://dx.doi.org/10.1007/s00410-024-02189-y>
- Jin S., Sun Z., Palke A.C. (2022a) Color effects of Cu nanoparticles in Cu-bearing plagioclase feldspars. *American Mineralogist*, Vol. 107, No. 12, pp. 2188–2200, <http://dx.doi.org/10.2138/am-2022-8325>
- (2022b) Iron oxide inclusions and exsolution textures of rainbow lattice sunstone. *European Journal of Mineralogy*, Vol. 34, No. 2, pp. 183–200, <http://dx.doi.org/10.5194/ejm-34-183-2022>
- Jin S., Xu H., Lee S. (2021) Revisiting the Bøggild intergrowth in iridescent labradorite feldspars: Ordering, kinetics, and phase equilibria. *Minerals*, Vol. 11, No. 7, article no. 727, <http://dx.doi.org/10.3390/min11070727>
- Johnson M.L., Koivula J.I. (1997) Gem News: “Rainbow” obsidian hearts. *G&G*, Vol. 33, No. 1, p. 63.
- (1999) Gem News: Twelve-rayed star quartz from Sri Lanka. *G&G*, Vol. 35, No. 1, pp. 54–55.
- Johnson M.L., McClure S.F. (1997) Lab Notes: Quartz: Cat’s-eye effect caused by large rutile needles. *G&G*, Vol. 33, No. 1, p. 59.
- Jones F.T. (1952) Iris agate. *American Mineralogist*, Vol. 37, No. 7–8, pp. 578–587.
- Keller D.S., Ague J.J. (2019) Crystallographic and textural evidence for precipitation of rutile, ilmenite, corundum, and apatite lamellae from garnet. *American Mineralogist*, Vol. 104, No. 7, pp. 980–995, <http://dx.doi.org/10.2138/am-2019-6849>
- (2020) Quartz, mica, and amphibole exsolution from majoritic garnet reveals ultra-deep sediment subduction, Appalachian orogen. *Science Advances*, Vol. 6, No. 11, article no. eaay5178, <http://dx.doi.org/10.1126/sciadv.aay5178>
- (2022) Predicting and explaining crystallographic orientation relationships of exsolved precipitates in garnet using the edge-to-edge matching model. *Journal of Metamorphic Geology*, Vol. 40, No. 7, pp. 1189–1218, <http://dx.doi.org/10.1111/jmg.12662>
- Khamloet P., Pisutha-Arnond V., Sutthirath C. (2014) Mineral inclusions in sapphire from the basalt-related deposit in Bo Phloi, Kanchanaburi, western Thailand: Indication of their genesis. *Russian Geology and Geophysics*, Vol. 55, No. 9, pp. 1087–1102, <http://dx.doi.org/10.1016/j.rgg.2014.08.004>
- Kiefert L., Wang C., Sintayehu T., Link K. (2019) Gem Notes: Sunstone labradorite-bytownite from Ethiopia. *Journal of Gemmology*, Vol. 36, No. 8, pp. 694–695.
- Kiflawi I., Bruley J. (2000) The nitrogen aggregation sequence and the formation of voids in diamond. *Diamond and Related Materials*, Vol. 9, No. 1, pp. 87–93, [http://dx.doi.org/10.1016/S0925-9635\(99\)00265-4](http://dx.doi.org/10.1016/S0925-9635(99)00265-4)
- Killingback H. (2005) Stereoscopic effect in asterism and chatoyancy. *Journal of Gemmology*, Vol. 29, No. 5–6, pp. 312–315.
- (2006) Diasterism in rose quartz. *Gems & Jewellery*, Vol. 15, No. 3, p. 64.
- (2015) The “coffee-and-cream” effect in chatoyant cabochons. *Journal of Gemmology*, Vol. 34, No. 6, pp. 524–530.
- Kinoshita S. (2008) *Structural Colors in the Realm of Nature*. World Scientific Publishing, Singapore.
- Koivula J.I. (1987) Gem News: “Rainbow moonstones” are labradorite. *G&G*, Vol. 23, No. 3, p. 175.
- Koivula J.I., Kammerling R.C. (1989a) Gem News: A beautiful new form of orthoclase. *G&G*, Vol. 25, No. 1, p. 47.
- Koivula J.I., Kammerling R.C., Fritsch E. (1993) Two interesting “double star” sapphires. *Australian Gemmologist*, Vol. 18, No. 7, pp. 235–236.
- Kraeft U., Saalfeld H. (1967) Über die aventurin-oligoklase von Tvedestrand und Bjordam (Norwegen). *Swiss Mineralogical and Petrographic Bulletin*, Vol. 47, pp. 247–256, <http://doi.org/10.5169/seals-36949>
- Kumaratilake W.L.D.R.A. (1997) Gems of Sri Lanka: A list of cat’s-eyes and stars. *Journal of Gemmology*, Vol. 25, No. 7, pp. 474–482.
- (1998) Spinel and garnet star networks: An interesting asterism in gems from Sri Lanka. *Journal of Gemmology*, Vol. 26, No. 1, pp. 24–28.
- Lee M.R., Parsons I. (2015) Diffusion-controlled and replacement microtextures in alkali feldspars from two pegmatites: Perth, Ontario and Keystone, South Dakota. *Mineralogical Magazine*, Vol. 79, No. 7, pp. 1711–1735, <http://dx.doi.org/10.1180/minmag.2015.079.7.21>
- Li L., Ortiz C. (2013) Biological design for simultaneous optical transparency and mechanical robustness in the shell of *Placuna placenta*. *Advanced Materials*, Vol. 25, No. 16, pp. 2344–2350, <http://dx.doi.org/10.1002/adma.201204589>
- Lin X., Heaney P.J. (2017) Causes of iridescence in natural quartz. *G&G*, Vol. 53, No. 1, pp. 68–81, <http://dx.doi.org/10.5741/GEMS.53.1.68>
- Lin X., Heaney P.J., Post J.E. (2018) Iridescence in metamorphic “rainbow” hematite. *G&G*, Vol. 54, No. 1, pp. 28–39, <http://dx.doi.org/10.5741/GEMS.54.1.28>
- Liu J., Cao S., Zhou D., Li X., Wu Y., Wang H., Li W. (2022) Characteristics and formation of corundum within syenite in the Yushishan rare metal deposits in the northeastern Tibetan Plateau. *American Mineralogist*, Vol. 107, No. 12, pp. 2291–2306, <http://dx.doi.org/10.2138/am-2022-8223>
- Liu J., Shen A.H., Zhang Z., Wang C., Shao T. (2018) Revisiting rainbow lattice sunstone from the Harts Range, Australia. *Journal of Gemmology*, Vol. 36, No. 1, pp. 44–52.
- Liu Y., Hurwit K.N., Tian L. (2003) Relationship between the groove density of the grating structure and the strength of iridescence in mollusk shells. *Australian Gemmologist*, Vol. 21, No. 10, pp. 405–407.
- Liu Y., Shigley J.E., Hurwit K.N. (1999) Iridescence color of a shell of the mollusk *Pinctada Margaritifera* caused by diffraction. *Optics Express*, Vol. 4, No. 5, pp. 177–182, <http://dx.doi.org/10.1364/OE.4.000177>
- Ma C., Goreva J.S., Rossman G.R. (2002) Fibrous nanoinclusions in massive rose quartz: HRTEM and AEM investigations. *American Mineralogist*, Vol. 87, No. 2–3, pp. 269–276, <http://dx.doi.org/10.2138/am-2002-2-308>
- Ma C., Gresh J., Rossman G.R., Ulmer G.C., Vicenzi E.P. (2001) Micro-analytical study of the optical properties of rainbow and sheen obsidians. *Canadian Mineralogist*, Vol. 39, No. 1, pp. 57–71, <http://dx.doi.org/10.2113/gscanmin.39.1.57>
- Ma C., Rossman G.R., Miller J.A. (2007) The origin of color in “fire” obsidian. *Canadian Mineralogist*, Vol. 45, No. 3, pp. 551–557, <http://dx.doi.org/10.2113/gscanmin.45.3.551>
- Mameli V., Musinu A., Niznansky D., Peddis D., Ennas G., Ardu A., Lugliè C., Cannas C. (2016) Much more than a glass: The complex magnetic and microstructural properties of obsidian. *Journal of Physical Chemistry C*, Vol. 120, No. 48, pp. 27635–27645, <http://dx.doi.org/10.1021/acs.jpcc.6b08387>
- Mayeron W. (2001) Lab Notes: Sapphires with diffusion-induced stars. *G&G*, Vol. 37, No. 4, pp. 324–325.
- McClure S.F. (1998) Lab Notes: Ruby, with a true double star. *G&G*, Vol. 34, No. 3, p. 217.
- McMackin C.E. (1974) Fire agate – The rising star of the West. *Rocks & Minerals*, Vol. 49, No. 9, pp. 566–568, <http://dx.doi.org/10.1080/00357529.1974.11762304>

- Mie G. (1908) Beiträge zur optik trüber medien, speziell kolloidaler metallösungen. *Annalen der Physik*, Vol. 330, No. 3, pp. 377–445, <http://dx.doi.org/10.1002/andp.19083300302>
- Miura M., Katsurada Y., Saruwatari K. (2018) Gem News International: Update on trace-element chemical characteristics of golden sheen sapphire. *G&G*, Vol. 54, No. 2, pp. 238–241.
- Moon A.R., Phillips M.R. (1984a) The physics of asterism in sapphire. *Swiss Mineralogical and Petrographic Bulletin*, Vol. 64, No. 3, pp. 329–334, <http://dx.doi.org/10.5169/SEALS-49548>
- (1984b) An electron microscopy study of exsolved phases in natural black Australian sapphire. *Micron and Microscopica Acta*, Vol. 15, No. 3, pp. 143–146, [http://dx.doi.org/10.1016/0739-6260\(84\)90044-3](http://dx.doi.org/10.1016/0739-6260(84)90044-3)
- (1985) Asterism—No mystery: A response to “Asterism—the Great Enigma.” *Australian Gemmologist*, Vol. 15, No. 11, pp. 395–399.
- (1991) Titania precipitation in sapphire containing iron and titanium. *Physics and Chemistry of Minerals*, Vol. 18, No. 4, pp. 251–258, <http://dx.doi.org/10.1007/BF00202577>
- Moretti C., Gratuze B., Hreglich S. (2013) Goldstone of aventurine glass: History, recipes, analyses and manufacture. *Archeo-Sciences. Revue d'archéométrie*, No. 37, pp. 135–154, <http://dx.doi.org/10.4000/archeosciences.4033>
- Moxon T., Palyanova G. (2020) Agate genesis: A continuing enigma. *Minerals*, Vol. 10, No. 11, article no. 953, <http://dx.doi.org/10.3390/min10110953>
- Mychaluk K.A. (2009) Update on Ammolite production from Southern Alberta, Canada. *G&G*, Vol. 45, No. 3, pp. 192–196, <http://dx.doi.org/10.5741/GEMS.45.3.192>
- Mychaluk K.A., Levinson A.A., Hall R.L. (2001) Ammolite: Iridescent fossilized Ammonite from Southern Alberta, Canada. *G&G*, Vol. 37, No. 1, pp. 4–25, <http://dx.doi.org/10.5741/GEMS.37.1.4>
- Nakamura Y., Kuribayashi T., Nagase T., Imai H. (2017) Cation ordering in iridescent garnet from Tenkawa village, Nara prefecture, Japan. *Journal of Mineralogical and Petrological Sciences*, Vol. 112, No. 2, pp. 97–101, <http://dx.doi.org/10.2465/jmps.161114a>
- Narudesombat N., Saengbuanglam S., Lhuaamporn T., Leelawatanasuk T. (2018) Golden sheen and non-sheen sapphires from Kenya. *Gem Quality Standards & Gem Optics and Color Science*, pp. 282–288.
- Nassau K. (1968) On the cause of asterism in star corundum. *American Mineralogist*, Vol. 53, No. 1–2, pp. 300–305.
- (1978) The origins of color in minerals. *American Mineralogist*, Vol. 63, No. 3–4, pp. 219–229.
- Natkaniec-Nowak L., Dumańska-Słowik M., Gawel A., Łatkiewicz A., Kowalczyk-Szpyt J., Wolska A., Milovská S., Luptáková J., Ladoň J. (2020) Fire agate from the Deer Creek deposit (Arizona, USA) – New insights into structure and mineralogy. *Mineralogical Magazine*, Vol. 84, No. 2, pp. 343–354, <http://dx.doi.org/10.1180/mgm.2020.8>
- Navon O., Wirth R., Schmidt C., Jablon B.M., Schreiber A., Emmanuel S. (2017) Solid molecular nitrogen (δ -N₂) inclusions in Juina diamonds: Exsolution at the base of the transition zone. *Earth and Planetary Science Letters*, Vol. 464, pp. 237–247, <http://dx.doi.org/10.1016/j.epsl.2017.01.035>
- Neumann H., Christie O.H.J. (1962) Observations on plagioclase aventurines from southern Norway. *Norsk Geologisk Tidsskrift*, Vol. 42, No. 2, pp. 389–393.
- Newman R. (2014) *Exotic Gems, Volume 3: How to Identify, Evaluate, Select and Care for Matrix Opal, Fire Agate, Blue Chalcedony, Rubellite, Indicolite, Paraiba and Other Tourmalines*. International Jewelry Publications, Los Angeles, California.
- Olsen J.S., Gerward L., Jiang J.Z. (1999) On the rutile/ α -PbO₂-type phase boundary of TiO₂. *Journal of Physics and Chemistry of Solids*, Vol. 60, No. 2, pp. 229–233, [http://dx.doi.org/10.1016/S0022-3697\(98\)00274-1](http://dx.doi.org/10.1016/S0022-3697(98)00274-1)
- Ostwald J. (1965) Schiller and pseudochromatism in minerals and gemstones. *Journal of Gemmology*, Vol. 9, No. 9, pp. 309–324.
- Ozaki R., Kikumoto K., Takagaki M., Kadowaki K., Odawara K. (2021) Structural colors of pearls. *Scientific Reports*, Vol. 11, No. 1, article no. 15224, <http://dx.doi.org/10.1038/s41598-021-94737-w>
- Palke A.C., Breeding C.M. (2017) The origin of needle-like rutile inclusions in natural gem corundum: A combined EPMA, LA-ICP-MS, and nanoSIMS investigation. *American Mineralogist*, Vol. 102, No. 7, pp. 1451–1461, <http://dx.doi.org/10.2138/am-2017-5965>
- Palke A.C., Saeseaw S., Renfro N.D., Sun Z., McClure S.F. (2019a) Geographic origin determination of blue sapphire. *G&G*, Vol. 55, No. 4, pp. 536–579, <http://dx.doi.org/10.5741/GEMS.55.4.536>
- (2019b) Geographic origin determination of ruby. *G&G*, Vol. 55, No. 4, pp. 580–613, <http://dx.doi.org/10.5741/GEMS.55.4.580>
- Parsons I. (2010) Feldspars defined and described: A pair of posters published by the Mineralogical Society. Sources and supporting information. *Mineralogical Magazine*, Vol. 74, No. 3, pp. 529–551, <http://dx.doi.org/10.1180/minmag.2010.074.3.529>
- Parsons I., Brown W.L. (1984) Feldspars and the thermal history of igneous rocks. In W.L. Brown, Ed., *Feldspars and Feldspathoids: Structures, Properties and Occurrences*, NATO ASI Series. Springer Netherlands, Dordrecht, pp. 317–371, http://dx.doi.org/10.1007/978-94-015-6929-3_9
- (1991) Mechanisms and kinetics of exsolution—Structural control of diffusion and phase behavior in alkali feldspars. In J. Ganguly, Ed., *Diffusion, Atomic Ordering, and Mass Transport*, Advances in Physical Geochemistry. Springer-Verlag New York, pp. 304–344, http://dx.doi.org/10.1007/978-1-4613-9019-0_10
- Parsons I., Fitz Gerald J.D., Lee M.R. (2015) Routine characterization and interpretation of complex alkali feldspar intergrowths. *American Mineralogist*, Vol. 100, No. 5–6, pp. 1277–1303, <http://dx.doi.org/10.2138/am-2015-5094>
- Perera S.I., Phil M., Pannila A.S., Gunasekera H.P.N.J., Ediriweera R.N. (1991) Anomalous behaviour of certain geuda corundums during heat treatment. *Journal of Gemmology*, Vol. 22, No. 7, pp. 405–407.
- Petrov A., Tanaka Y. (2011) Iris Quartz. [mindat.org](http://mindat.org/article.php/1335/Iris+Quartz), <https://mindat.org/article.php/1335/Iris+Quartz>, December 2023.
- Pfund A.H. (1917) The colors of mother-of-pearl. *Journal of the Franklin Institute*, Vol. 183, No. 4, pp. 453–464, [http://dx.doi.org/10.1016/S0016-0032\(17\)91045-2](http://dx.doi.org/10.1016/S0016-0032(17)91045-2)
- Phillips D.S., Heuer A.H., Mitchell T.E. (1980) Precipitation in star sapphire I. Identification of the precipitate. *Philosophical Magazine A*, Vol. 42, No. 3, pp. 385–404, <http://dx.doi.org/10.1080/01418618008239365>
- Promwongnan S., Ounorn P., Maneekrajangsaeng M., Leelawatanasuk T. (2017) Gem Notes: An unusual blue synthetic star spinel. *Journal of Gemmology*, Vol. 35, No. 6, pp. 500–502.
- Proyer A., Habler G., Abart R., Wirth R., Krenn K., Hoinkes G. (2013) TiO₂ exsolution from garnet by open-system precipitation: Evidence from crystallographic and shape preferred orientation of rutile inclusions. *Contributions to Mineralogy and Petrology*, Vol. 166, No. 1, pp. 211–234, <http://dx.doi.org/10.1007/s00410-013-0872-7>
- Radko V.A., Ananyev S.A., Petrochenkov D.A., Bondina S.S. (2021) Iridescent ammonite fossil shell material from Norilsk, Krasnoyarsk Krai, Russia. *Journal of Gemmology*, Vol. 37, No. 6, pp. 608–617.
- Raman C.V. (1935) On iridescent shells: Part II. Colours of laminar diffraction. *Proceedings of the Indian Academy of Sciences – Section A*, Vol. 1, No. 9, pp. 574–589, <http://dx.doi.org/10.1007/BF03035610>
- (1950a) The iridescent feldspars. *Current Science*, Vol. 19, No. 10, pp. 301–305.

- (1950b) Crystals of quartz with iridescent faces. *Proceedings of the Indian Academy of Sciences – Section A*, Vol. 31, No. 5, pp. 275–279, <http://dx.doi.org/10.1007/BF03050101>
- Raman C.V., Jayaraman A. (1950) The structure of labradorite and the origin of its iridescence. *Proceedings of the Indian Academy of Sciences – Section A*, Vol. 32, No. 1, article no. 1, <http://dx.doi.org/10.1007/BF03172469>
- (1953a) The diffusion haloes of the iridescent feldspars. *Proceedings of the Indian Academy of Sciences – Section A*, Vol. 37, No. 1, pp. 1–10, <http://dx.doi.org/10.1007/BF03052851>
- (1953b) The structure and optical behaviour of iridescent agate. *Proceedings of the Indian Academy of Sciences – Section A*, Vol. 38, No. 3, pp. 199–206, <http://dx.doi.org/10.1007/BF03045221>
- (1955) On the optical behaviour of crypto-crystalline quartz. *Proceedings of the Indian Academy of Sciences – Section A*, Vol. 41, No. 1, pp. 1–6, <http://dx.doi.org/10.1007/BF03050587>
- Renfro N.D. (2011a) Lab Notes: Synthetic star spinel imitation of moonstone. *G&G*, Vol. 47, No. 1, pp. 54–55.
- (2011b) Gem News International: Nuummite from Mauritania. *G&G*, Vol. 47, No. 3, pp. 242–243.
- (2019) Gem News International: Imitation opal with interesting play-of-color pattern. *G&G*, Vol. 55, No. 3, pp. 446–447.
- Renfro N.D., Koivula J.I. (2011) Gem News International: Spectral interference in quartz from India. *G&G*, Vol. 47, No. 1, pp. 58–59.
- Renfro N.D., Shigley J.E. (2018) Lab Notes: New plastic imitation opal from Kyocera. *G&G*, Vol. 54, No. 1, pp. 60–62.
- Ribbe P.H. (1983) Exsolution textures in ternary and plagioclase feldspars; interference colors. In P.H. Ribbe, Ed., *Feldspar Mineralogy*. Mineralogical Society of America, Washington, D.C., pp. 241–270, <http://dx.doi.org/10.1515/9781501508547-015>
- Rodgers K.A., Kinny P.D., McGregor V.R., Clark G.R., Henderson G.S. (1996) Iridescent anthophyllite-gedrite from Simiutatt, Nuuk district, southern West Greenland composition, exsolution, age. *Mineralogical Magazine*, Vol. 60, No. 403, pp. 937–947, <http://dx.doi.org/10.1180/minmag.1996.060.403.08>
- Rossmann G.R. (2011) The Chinese red feldspar controversy: Chronology of research through July 2009. *G&G*, Vol. 47, No. 1, pp. 16–30, <http://dx.doi.org/10.5741/GEMS.47.1.16>
- Rossmann G.R., Ma C. (2025) Iridescent iron oxides. *Minerals*, Vol. 15, No. 2, article no. 108, <http://dx.doi.org/10.3390/min15020108>
- Saminpanya S. (2001) Ti-Fe mineral inclusions in star sapphires from Thailand. *Australian Gemmologist*, Vol. 21, No. 3, pp. 125–128.
- Sanders J.V. (1964) Colour of precious opal. *Nature*, Vol. 204, pp. 1151–1153.
- (1968) Diffraction of light by opals. *Acta Crystallographica Section A*, Vol. 24, No. 4, pp. 427–434, <http://dx.doi.org/10.1107/S0567739468000860>
- (1976) The structure of star opals. *Acta Crystallographica Section A*, Vol. 32, No. 2, pp. 334–338, <http://dx.doi.org/10.1107/S0567739476000727>
- Schmetzer K. (1988) Orientated lath-like inclusions of a new type in spinel. *Journal of Gemmology*, Vol. 21, No. 2, pp. 69–72.
- Schmetzer K., Bernhardt H.-J. (2002) Star garnets from Ilakaka, Madagascar. *Australian Gemmologist*, Vol. 21, No. 5, pp. 202–206.
- Schmetzer K., Bernhardt H.-J., Gilg H.A. (2016) Characterization of oriented inclusions in cat's-eye, star and other chrysoberyls. *Journal of Gemmology*, Vol. 35, No. 1, pp. 28–54.
- Schmetzer K., Bernhardt H.-J., Hainschwang T. (2013) Titanium-bearing synthetic alexandrite and chrysoberyl. *Journal of Gemmology*, Vol. 33, No. 5–6, pp. 131–142.
- Schmetzer K., Bernhardt H.-J., Kiefert L. (2002) Star garnets and star garnet cat's-eyes from Ambatondrazaka, Madagascar. *Journal of Gemmology*, Vol. 28, No. 1, pp. 13–24.
- Schmetzer K., Glas M. (2003) Multi-star quartzes from Sri Lanka. *Journal of Gemmology*, Vol. 28, No. 6, pp. 321–332.
- Schmetzer K., Gübelin E., Bernhardt H.-J., Kiefert L. (2000) Oriented inclusions in spinels from Madagascar. *Journal of Gemmology*, Vol. 27, No. 4, pp. 229–232.
- Schmetzer K., Henn U. (1987) Synthetic or imitation? An investigation of the products of Kyocera Corporation that show play-of-color. *G&G*, Vol. 23, No. 3, pp. 148–151, <http://dx.doi.org/10.5741/GEMS.23.3.148>
- Schmetzer K., Hodgkinson A. (2011) Synthetic star alexandrite. *Gems & Jewellery*, Vol. 20, No. 3, pp. 9–11.
- Schmetzer K., Steinbach M.P. (2022) Gem Notes: Asteriated quartz sphere with sagenitic rutile inclusions. *Journal of Gemmology*, Vol. 38, No. 4, pp. 314–315.
- (2023) Gem Notes: Three-rayed asterism in quartz: A multi-star network. *Journal of Gemmology*, Vol. 38, No. 6, pp. 552–553.
- Schmetzer K., Steinbach M.P., Gilg H.A., Blake A.R. (2015) Dual-color double stars in ruby, sapphire, and quartz: Cause and historical account. *G&G*, Vol. 51, No. 2, pp. 112–143, <http://dx.doi.org/10.5741/GEMS.51.2.112>
- Schumann W. (2009) *Gemmstones of the World*. Sterling Publishing Company, Inc., New York.
- Shen A.H. (2011) The nature of the Be-Nb-Ta containing cloud in natural Madagascar blue sapphire – An FIB/HRTEM study. GIA News from Research, <https://www.gia.edu/gia-news-research/nano-inclusions-natural-sapphire>
- Shen A.H., Wirth R. (2012) Gem News International: Beryllium-bearing nano-inclusions identified in untreated Madagascar sapphire. *G&G*, Vol. 48, No. 2, pp. 150–151.
- Shen C., Liao J. (2017) A study of gemological characteristics of ammolite. *Acta Petrologica Et Mineralogica*, Vol. 35, No. S1, pp. 111–118.
- Shipley R.M. (1945) *Dictionary of Gems and Gemology*. Gemological Institute of America, Los Angeles, CA.
- Shiryaev A.A., Chesnokov Y., Vasiliev A.L., Hainschwang T. (2023) Exsolution of oxygen impurity from diamond lattice and formation of pressurized CO₂-I precipitates. *Carbon Trends*, Vol. 11, article no. 100270, <http://dx.doi.org/10.1016/j.cartre.2023.100270>
- Smith J.V. (1983) Phase equilibria of plagioclase. In P.H. Ribbe, Ed., *Feldspar Mineralogy*. Mineralogical Society of America, Washington, D.C., pp. 223–239, <http://dx.doi.org/10.1515/9781501508547-014>
- Smith J.V., Brown W.L. (1988) *Feldspar Minerals: Crystal Structures, Physical, Chemical, and Microtextural Properties*, Vol. 1. Springer-Verlag, Berlin, Heidelberg.
- Snow M.R., Pring A. (2005) The mineralogical microstructure of shells: Part 2.1 The iridescence colors of abalone shells. *American Mineralogist*, Vol. 90, No. 11–12, pp. 1705–1711, <http://dx.doi.org/10.2138/am.2005.1788>
- Snow M.R., Pring A., Self P., Losic D., Shapter J. (2004) The origin of the color of pearls in iridescence from nano-composite structures of the nacre. *American Mineralogist*, Vol. 89, No. 10, pp. 1353–1358, <http://dx.doi.org/10.2138/am-2004-1001>
- Sobolev N.V., Logvinova A.M., Tomilenko A.A., Wirth R., Bul'bak T.A., Luk'yanova L.I., Fedorova E.N., Reutsky V.N., Efimova E.S. (2019) Mineral and fluid inclusions in diamonds from the Urals placers, Russia: Evidence for solid molecular N₂ and hydrocarbons in fluid inclusions. *Geochimica et Cosmochimica Acta*, Vol. 266, pp. 197–219, <http://dx.doi.org/10.1016/j.gca.2019.08.028>
- Soonthorntantikul W. (2014) Lab Notes: Star opal. *G&G*, Vol. 50, No. 2, pp. 152–153.
- Soonthorntantikul W., Atikarnsakul U., Weeramongkhonlert V. (2016) Lab Notes: Update on spectroscopy of “gold sheen” sapphires. *G&G*, Vol. 52, No. 4, pp. 413–414.
- Soonthorntantikul W., Vertriebt W., Raynaud-Flattot V.L., Sangsawong S., Atikarnsakul U., Khawpong C., Weeramongkhonlert

- V., Pardieu V. (2017) An in-depth gemological study of blue sapphires from the Baw Mar Mine (Mogok, Myanmar). *GIA News from Research*, <https://www.gia.edu/gia-news-research/blue-sapphires-baw-mar-mine-mogok-myanmar>
- Sorokina E.S., Karampelas S., Nishanbaev T.P., Nikandrov S.N., Semiannikov B.S. (2017) Sapphire megacrysts in syenite pegmatites from the Ilmen Mountains, South Urals, Russia: New mineralogical data. *Canadian Mineralogist*, Vol. 55, No. 5, pp. 823–843, <http://dx.doi.org/10.3749/canmin.1700016>
- Speich L., Kohn S.C., Wirth R., Bulanova G.P., Smith C.B. (2017) The relationship between platelet size and the B' infrared peak of natural diamonds revisited. *Lithos*, Vol. 278–281, pp. 419–426, <http://dx.doi.org/10.1016/j.lithos.2017.02.010>
- Sripoonjan T., Saengbuanglam S., Maneekrajangsaeng M. (2019) Gem News International: Unique orange sapphire with golden sheen effect reportedly from Kenya. *G&G*, Vol. 55, No. 1, pp. 152–155.
- Steinbach M.P. (2016) *Asterism: Gems with a Star*. MPS Publishing and Media, Idar-Oberstein, Germany.
- (2018) An overview of asteriated gems: From common star sapphire to rare star aquamarine to one-of-a-kind star zircon. *G&G*, Vol. 54, No. 3, pp. 258–259.
- Stöber W., Fink A., Bohn E. (1968) Controlled growth of monodisperse silica spheres in the micron size range. *Journal of Colloid and Interface Science*, Vol. 26, No. 1, pp. 62–69, [http://dx.doi.org/10.1016/0021-9797\(68\)90272-5](http://dx.doi.org/10.1016/0021-9797(68)90272-5)
- Strutt R.J. (1923a) Studies of iridescent colour, and the structure producing it. III.—The colours of labrador felspar. *Proceedings of the Royal Society of London Series A*, Vol. 103, No. 720, pp. 34–45, <http://dx.doi.org/10.1098/rspa.1923.0037>
- (1923b) Studies of iridescent colour, and the structure producing it.—II. Mother-of-pearl. *Proceedings of the Royal Society of London. Series A, Containing Papers of a Mathematical and Physical Character*, Vol. 102, No. 719, pp. 674–677, <http://dx.doi.org/10.1098/rspa.1923.0025>
- Sun Z., Renfro N.D., Palke A.C. (2015) Gem News International: Iridescent scapolite. *G&G*, Vol. 51, No. 1, pp. 104–106.
- Sun Z., Renfro N.D., Palke A.C., Breitzmann H., Muyal J., Hand D., Hain M., McClure S.F., Katsurada Y., Miura M., Rossman G.R. (2020) Gem News International: Sunstone plagioclase feldspar from Ethiopia. *G&G*, Vol. 56, No. 1, pp. 184–188.
- Tan T.L., Wong D., Lee P. (2004) Iridescence of a shell of mollusk *Haliotis Glabra*. *Optics Express*, Vol. 12, No. 20, pp. 4847–4854, <http://dx.doi.org/10.1364/OPEX.12.004847>
- Tschauner O., Ma C., Lanzirotti A., Newville M.G. (2020) Riesite, a new high pressure polymorph of TiO₂ from the Ries impact structure. *Minerals*, Vol. 10, No. 1, article no. 78, <http://dx.doi.org/10.3390/min10010078>
- Tschauner O., Navon O., Schmidt C. (2022) Deltanitrogen, IMA 2019-067b. In *CNMNC Newsletter 69, European Journal of Mineralogy*, Vol. 34, No. 5, p. 467, <http://dx.doi.org/10.5194/Ejm-34-463-2022>
- Tutton A.E.H. (1921) The structure of adularia and moonstone. *Nature*, Vol. 108, No. 2715, pp. 352–353, <http://dx.doi.org/10.1038/108352a0>
- van Roermund H.L.M., Drury M.R., Barnhoorn A., De Ronde A. (2000) Non-silicate inclusions in garnet from an ultra-deep orogenic peridotite. *Geological Journal*, Vol. 35, No. 3–4, pp. 209–229, <http://dx.doi.org/10.1002/gj.858>
- Vaughan D.J., Tossell J.A., Stanley C.J. (1987) The surface properties of bornite. *Mineralogical Magazine*, Vol. 51, No. 360, pp. 285–293, <http://dx.doi.org/10.1180/minmag.1987.051.360.11>
- Vertriest W., Bruce-Lockhart S. (2018) Gem News International: Twelve-rayed star sapphire from Thailand. *G&G*, Vol. 54, No. 2, p. 238.
- Viti C., Ferrari M. (2006) The nature of Ti-rich inclusions responsible for asterism in Verneuil-grown corundums. *European Journal of Mineralogy*, Vol. 18, No. 6, pp. 823–834, <http://dx.doi.org/10.1127/0935-1221/2006/0018-0823>
- von Vultée J. (1955) Über die orientierten Verwachsungen von Rutil in Quarz. *Neues Jahrbuch für Mineralogie Abhandlungen*, Vol. 87, No. 3, pp. 389–415.
- (1956) Die Verwachsungsgesetze der orientierten Einlagerungen von Rutil in Quarz. *Zeitschrift für Kristallographie*, Vol. 107, No. 1–2, pp. 1–17, <http://dx.doi.org/10.1524/zkri.1956.107.1-2.1>
- Walcott A.J. (1937) Asterism in garnet, spinel, quartz and sapphire. *Geological Series of Field Museum of Natural History*, Vol. 7, No. 3, pp. 39–57.
- Wang C., Shen A.H., Heaney P.J., Palke A., Wang K., Wang H., Kiefert L. (2025) Cu nanoparticle geometry as the key to bicolor behavior in Oregon sunstones: An application of LSPR theory in nanomineralogy. *American Mineralogist*, Vol. 110, No. 2, pp. 293–305, <http://dx.doi.org/10.2138/am-2023-9141>
- Wang C.-M., Thevuthasan S., Gao F., McCready D.E., Chambers S.A. (2002) The characteristics of interface misfit dislocations for epitaxial α -Fe₂O₃ on α -Al₂O₃(0001). *Thin Solid Films*, Vol. 414, No. 1, pp. 31–38, [http://dx.doi.org/10.1016/S0040-6090\(02\)00452-2](http://dx.doi.org/10.1016/S0040-6090(02)00452-2)
- Watts E.A. (2021) Lab Notes: Asterism in natural diamond cabochons. *G&G*, Vol. 57, No. 1, pp. 52–53.
- Weibel M., Wessicken R. (1981) Haemetit als Einschluss im schwarzen Sternsaphir. *Gemmologie: Zeitschrift der Deutschen Gemmologischen Gesellschaft*, Vol. 30, No. 3–4, pp. 170–176.
- Weibel M., Wessicken R., Woensdregt C.F., Wüthrich A. (1980) Sternsaphir und sternquarz. *Schweizerische Mineralogische und Petrographische Mitteilungen*, Vol. 60, No. 2–3, pp. 133–136, <http://dx.doi.org/10.5169/seals-46663>
- Weidlich A., Wilkie A. (2009) Rendering the effect of labradorescence. In *Proceedings of Graphics Interface 2009*, Canadian Information Processing Society, pp. 79–85.
- White J.S. (2015) Mineral mysteries: Star rose quartz. *Rocks & Minerals*, Vol. 90, No. 3, pp. 282–284, <http://dx.doi.org/10.1080/00357529.2015.1012960>
- Wibel F. (1873) Der faserquarz vom Cap - Eine pseudomorphose nach krokydolith. *Neues Jahrbuch für Mineralogie, Geologie und Palaeontologie*, pp. 367–380.
- Win W.L., Moe K.S. (2012) Gem News International: Rainbow moonstone from Zambia. *G&G*, Vol. 48, No. 2, pp. 146–147.
- Woensdregt C.F., Weibel M., Wessicken R. (1980) Star quartz asterism caused by sillimanite. *Schweizerische Mineralogische und Petrographische Mitteilungen*, Vol. 60, No. 2–3, pp. 129–132, <http://dx.doi.org/10.5169/SEALS-46662>
- Wüthrich A., Weibel M. (1981) Optical theory of asterism. *Physics and Chemistry of Minerals*, Vol. 7, No. 1, pp. 53–54, <http://dx.doi.org/10.1007/BF00308202>
- Wüthrich A., Weibel M., Gübelin E.J. (1983) Elucidating the optical theory of chatoyancy and asterism. *Australian Gemmologist*, Vol. 15, No. 1, pp. 3–6.
- Xiao S.Q., Dahmen U., Heuer A.H. (1997) Phase transformation of TiO₂ precipitates in sapphire (α -Al₂O₃) induced by the loss of coherency. *Philosophical Magazine A*, Vol. 75, No. 1, pp. 221–238, <http://dx.doi.org/10.1080/01418619708210292>
- Xu H., Hill T.R., Konishi H., Farfan G. (2017) Protoenstatite: A new mineral in Oregon sunstones with “watermelon” colors. *American Mineralogist*, Vol. 102, No. 10, pp. 2146–2149, <http://dx.doi.org/10.2138/am-2017-6186>
- Xu H., Jin S., Lee S., Brown P.E. (2023) Cation ordering, twinning, and pseudo-symmetry in silicate garnet: The study of a birefringent garnet with orthorhombic structure. *American Mineralogist*, Vol. 108, No. 3, pp. 572–583, <http://dx.doi.org/10.2138/am-2022-8455>
- Xu H.J., Wu Y. (2017) Oriented inclusions of pyroxene, amphibole and rutile in garnet from the Lüliangshan garnet peridotite massif, North Qaidam UHPM belt, NW China: An electron backscatter diffraction study. *Journal of Metamorphic Geology*, Vol. 35, No. 1, pp. 1–17, <http://dx.doi.org/10.1111/jmg.12208>
- Yang J., Chen Q., Xu F., Li Y., Liu X. (2023) Gem News Interna-

- tional: A newly discovered iridescent andradite from Inner Mongolia, China. *G&G*, Vol. 59, No. 3, pp. 391–394.
- Ye X., Qiu Z., Chen C., Zhang Y. (2021) Nondestructive identification of mineral inclusions by Raman mapping: Micro-magnetite inclusions in iridescent scapolite as example. *Spectroscopy and Spectral Analysis*, Vol. 41, No. 7, pp. 2105–2109.
- Yund R.A. (1983) Microstructure, kinetics and mechanisms of alkali feldspar exsolution. In P.H. Ribbe, Ed., *Feldspar Mineralogy*. Mineralogical Society of America, Washington, D.C., pp. 177–202, <http://dx.doi.org/10.1515/9781501508547-012>
- (1984) Alkali feldspar exsolution: Kinetics and dependence on alkali interdiffusion. In W.L. Brown, Ed., *Feldspars and Feldspathoids: Structures, Properties and Occurrences*, NATO ASI Series. Springer Netherlands, Dordrecht, pp. 281–315, http://dx.doi.org/10.1007/978-94-015-6929-3_8
- Zhang J.F., Xu H.J., Liu Q., Green II H.W., Dobrzhinetskaya L.F. (2011) Pyroxene exsolution topotaxy in majoritic garnet from 250 to 300 km depth. *Journal of Metamorphic Geology*, Vol. 29, No. 7, pp. 741–751, <http://dx.doi.org/10.1111/j.1525-1314.2011.00939.x>
- Zhao Q., Zhao S., Xu C. (2022) Hematite exsolutions in corundum from Cenozoic basalts in Changle, Shandong Province, China: Crystallographic orientation relationships and interface characters. *Crystals*, Vol. 12, No. 7, article no. 905, <http://dx.doi.org/10.3390/cryst12070905>
- Zhou Q., Wang C., Shen A.H. (2021) Copper nanoparticles embedded in natural plagioclase mineral crystals: In situ formation and third-order nonlinearity. *Journal of Physical Chemistry C*, Vol. 126, No. 1, pp. 387–395, <http://dx.doi.org/10.1021/acs.jpcc.1c09145>
- Zhou Q., Wang C., Shen A.-H. (2022) Application of high-temperature copper diffusion in surface recoloring of faceted labradorites. *Minerals*, Vol. 12, No. 8, article no. 920, <http://dx.doi.org/10.3390/min12080920>

For online access to all issues of GEMS & GEMOLOGY from 1934 to the present, visit:

gia.edu/gems-gemology



Trusted Innovation, Backed by Science.



GIA®

**Science and
innovation
meet modern
design to
provide the
technology
you need to
safeguard your
customers and
business.**



GIA® Gemolite® NXT
Introducing GIA® Gemolite®
NXT, where form meets
function. Ergonomic
design ensures comfort,
while advanced proprietary
LED lighting and clarity of
optics provide unparalleled
precision. GIA sets the new
standard in gemological
instruments.

Learn More



GIA.edu/gemolite

©2025 Gemological Institute
of America, Inc. (GIA). All
trademarks are registered
trademarks owned by GIA.
GIA is a nonprofit 501(c)(3)
organization. All rights reserved.

Lab Notes

Editors

Thomas M. Moses | Shane F. McClure
Sally Eaton-Magaña | Artitaya Homkrajae

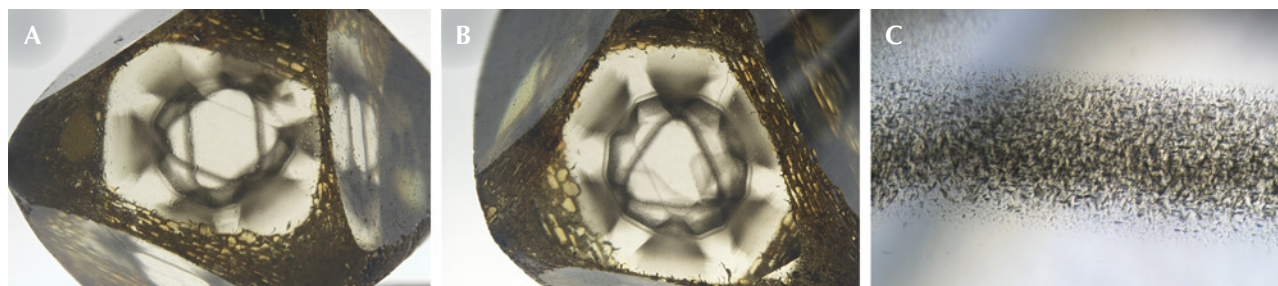
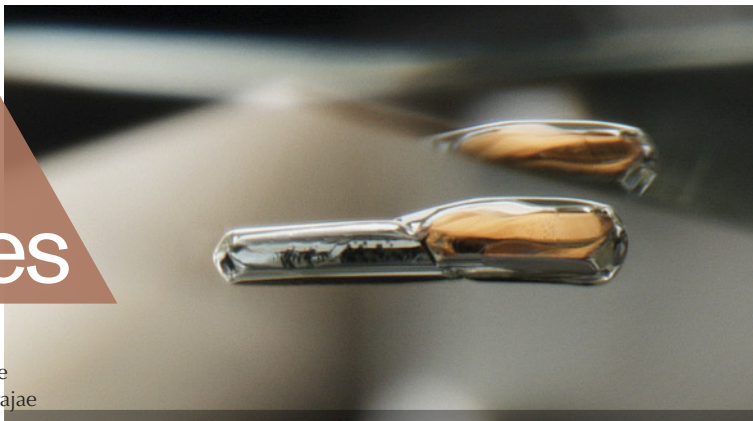


Figure 1. This 3.45 ct natural diamond was partially faceted to highlight the unusual clouds composed of dark micro-inclusions (A and B). At higher magnifications, the distinct micro-inclusions can be observed (C). Photomicrographs by Taryn Linzmeyer; fields of view 7.19 mm (A and B) and 0.72 mm (C).

Unusual Patterns in DIAMONDS Composed of Dark Micro-Inclusions

Recently, at the Carlsbad laboratory, the authors studied two diamonds, submitted separately for scientific examination, with interesting appearances due to the presence of dark micro-inclusions.

The first stone, a 3.45 ct diamond reportedly from Zimbabwe, was partially faceted with rough surfaces preserved along the edges (figure 1A). The stone had six-lobed asteriated inclusion sectors, with a six-sided star pattern visible in the center. When tilted to view through a different facet, some of the star's points were fainter, making the pattern appear as a triangle (figure 1B). These patterns were formed by dark micro-inclusions (figure 1C), concluded as graphite from visual examination.

The visible/near-infrared (Vis-NIR) absorption spectra showed the nitrogen-related features N3 and H3, the radiation-related feature GR1, and a hydrogen-related band at 835 nm. Pronounced brown radiation staining was observed on the unpolished surfaces. The infrared (IR) absorption spectrum confirmed the diamond as type Ia with

high amounts of nitrogen and hydrogen, consistent with other diamonds exhibiting similar inclusion scenes (Fall 2019 Lab Notes, p. 417; Fall 2021 *G&G Micro-World*, pp. 269–270; Summer 2024 Lab Notes, pp. 212–214). The inclusion patterns formed in such natural diamonds are often symmetrical and can appear as various configurations of lobed “stars” or triangles when viewed through the polished windows. This diamond was unusual as it showed the graphitic clouds radiating outward starting from the central figure—a pattern not previously seen by the authors.

The second natural diamond was faceted and displayed dark clouds of micro-inclusions with clear openings in the center of the main facets (figure 2). IR absorption spectroscopy indicated that the 13.89 ct stone was also type Ia with hydrogen-related defects. Photoluminescence (PL) mapping using 455 nm laser excitation revealed that the dark cloud inclusion sectors correlated with high concentrations of the S3 defect (figure 3A). This nickel-related peak (A.M. Zaitsev, *Optical Properties of Diamond: A Data Handbook*, Springer-Verlag, Berlin, 2001) caused the clouds to fluoresce green when exposed to long-wave UV, such as in the cloud-inclusion sectors observed in asteriated diamonds (e.g., Fall 2019 Lab Notes, p. 417; Summer 2024 Lab Notes, pp. 212–214). PL spectra within the cloud sector using 532 nm excitation also showed another potentially nickel-related feature at ~694.3 nm.

The stone also contained etch channels passing through clear openings of the clouds. Within the etch chan-

Editors' note: All items were written by staff members of GIA laboratories.

GEMS & GEMOLOGY, Vol. 61, No. 2, pp. 172–182.

© 2025 Gemological Institute of America

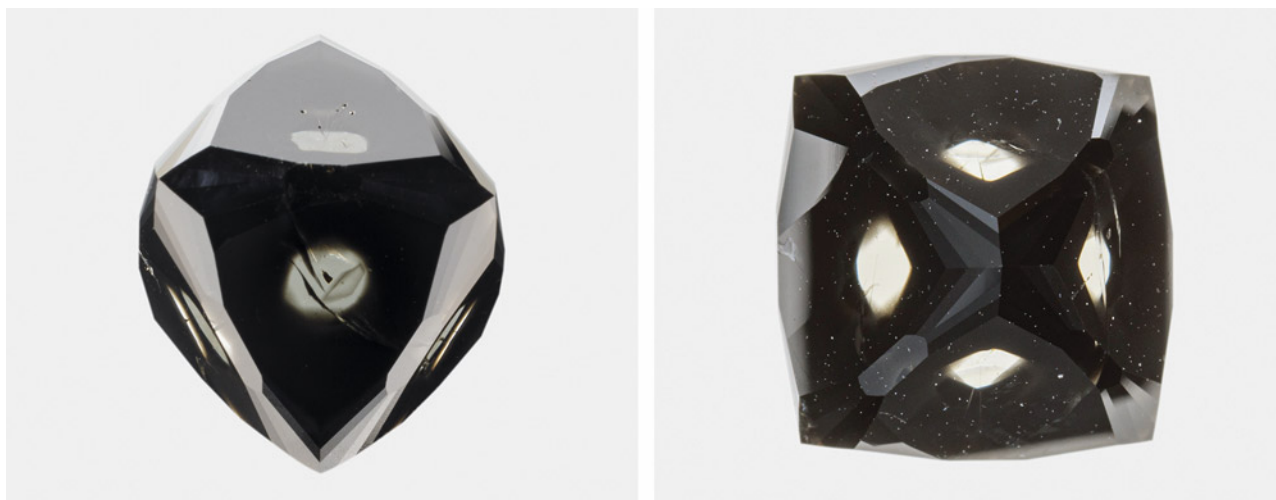


Figure 2. As seen from each main facet, this 13.89 ct natural diamond displays black cloud inclusion sectors with clear openings in the center. Photos by Annie Hayes.

nels, brown radiation stains and a high concentration of PL features were detected, such as NV⁻ (figure 3, B and C), GR1, and a peak at 588.6 nm. These defects may have been produced by radioactive fluids entering the etch channel while in the earth, creating the resulting stains; subsequent annealing could then create higher concentrations of several vacancy-related centers such as NV⁻.

Although both of these diamonds have similar infrared spectra, radiation staining, and the presence of dark micro-inclusions, the diamonds manifest these characteristics in different ways. They provide another example that all natural diamonds have their own journey and origin story.

Taryn Linzmeyer and Sally Eaton-Magaña

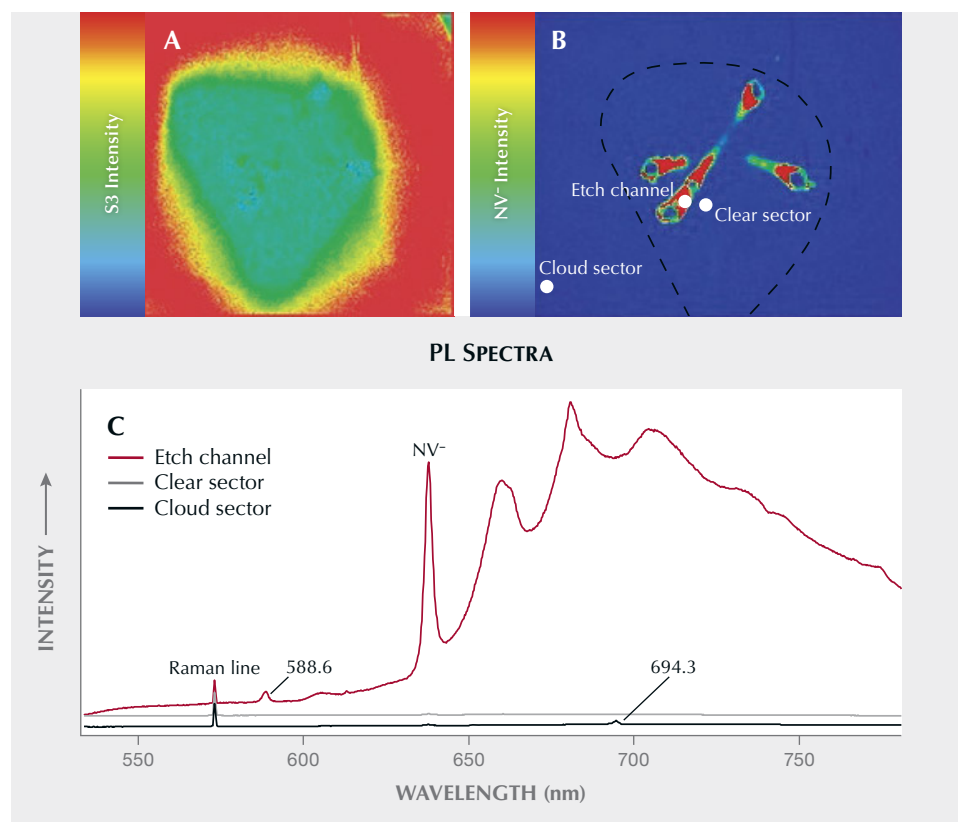


Figure 3. A: False-color 455 nm PL map of one of the 13.89 ct diamond's faces showing a high concentration of the nickel-related S3 center in the dark clouds of micro-inclusions, compared with the clear opening in the center. B: The false-color 532 nm PL map indicates that a high concentration of NV⁻ defect exists within the etch channels; the dashed line indicates the boundary of the clear opening in the cloud inclusions. Spots of the extracted PL spectra plotted in C are marked with white dots. C: PL spectra collected from the etch channel, clear sector, and cloud sector of the stone are overlaid with Raman lines scaled to equal intensities.

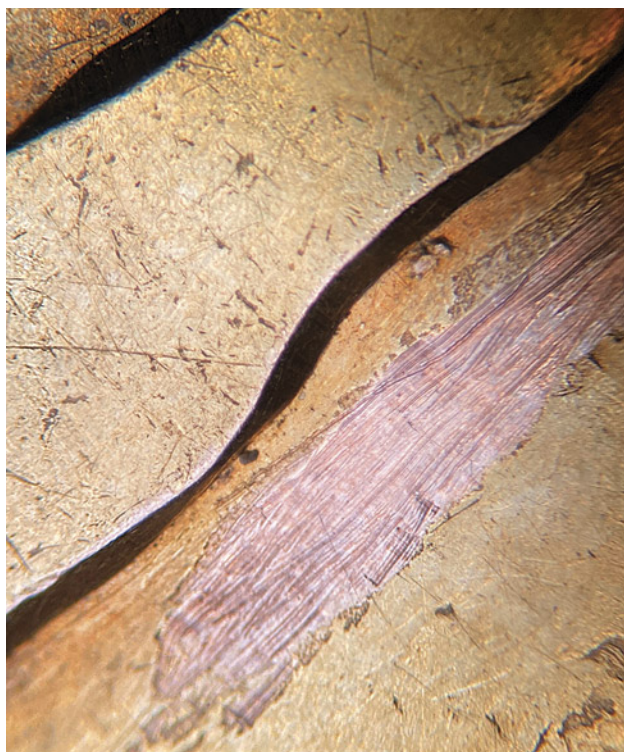


Figure 4. In this gold-plated rose gold item submitted as 14K, the rose gold base tested 9K and the yellow gold layer tested 13.5K. Photo by Carlos Bautista.

Gold-Plated GOLD

GIA's new jewelry verification service examines hundreds of jewelry pieces each day to determine the identity of the metals and mounted gemstones. Recently, the Carlsbad laboratory identified a method that might be used to deceive customers. Adding a layer of gold plating to a gold

alloy affects the X-ray fluorescence (XRF) results, and depending on the thickness of the plating, false results can be obtained. XRF metal testing is one of the most reliable ways to analyze metal composition in the jewelry industry, and it can also detect thin plating when the top metal layer differs from the base layer. This method is unreliable, however, when a piece of metal is coated with the same element; therefore, visual observation under a microscope is essential to check for metal discoloration, plating damage, or previous destructive testing that exposes the base material.

We have seen an abundance of gold items plated with gold. This practice is used to change the color of a rose or white gold piece to yellow (figure 4) or to revive the luster in a dull piece of thin yellow gold. Application of plating can be deceitful, as the practice can cause the XRF to determine an inaccurately high gold purity for a piece. For example, coating 10K gold with a precise amount of gold plating can alter the XRF results, identifying the alloy as 14K or 18K gold without detecting any of the plating (figure 5). This is particularly harmful to the consumer if the seller does not disclose this practice and sells alloys with a lower gold content than stated, especially with gold prices reaching all-time highs.

Carlos Bautista

LABORATORY-GROWN DIAMONDS

CVD-Grown Diamond with Unusual Cause of Greenish Color

Recently, the Carlsbad laboratory received a fancy-color diamond grown by chemical vapor deposition (CVD) for a grading report. The 3.07 ct oval brilliant received a color grade of Fancy Light brownish greenish yellow (figure 6)



Figure 5. In this gold-plated pendant submitted as 18K solid gold, the base layer tested 10K and the top layer tested 18K. Arrows show where the gold plating has rubbed off due to use. Photo by Diego Sanchez.



Figure 6. This 3.07 ct HPHT-treated CVD-grown diamond received a color grade of brownish greenish yellow, with the causes of color including isolated nitrogen and SiV⁻ centers. Photo by Diego Sanchez.

and a clarity grade of VS₁ due to the presence of some graphitic pinpoints. The photoluminescence (PL) spectra and DiamondView fluorescence imaging confirmed a CVD origin and post-growth high-pressure, high-temperature (HPHT) treatment.

The CVD-grown diamond's infrared absorption spectrum showed a weak 1344 cm⁻¹ peak with an isolated nitrogen concentration of ~2 ppm. The visible/near-infrared (Vis-NIR) absorption spectrum shows a featureless absorption rise within the blue wavelengths due to the isolated nitrogen (figure 7, left). This is the primary cause of the yellow color. The CVD-grown diamond had been HPHT-treated, which is often used with the intention of removing brownish coloration; nevertheless, the color

grade does include a brownish modifier. Although we do not know the color of the CVD diamond before HPHT processing, this treatment can enhance yellow coloration in natural diamonds by increasing the single substitutional nitrogen concentration (D. Fisher and R.A. Spits, "Spectroscopic evidence of GE POL HPHT-treated natural type IIa diamonds," Spring 2000 *G&G*, pp. 42–49). Interestingly, this diamond also contains a greenish modifier which is ascribed as likely due to the absorption of SiV⁻ centers at 737 nm. This absorption within the red portion of the visible spectrum and flanked by nitrogen-related absorption in the blue region created a transmission window within the green that, while subtle, was sufficient to create a detectable greenish color component. PL mapping using 633 nm excitation (figure 7, right) shows a very strong intensity of SiV⁻ on the majority of the table facet area.

Previously, green color contributions in CVD-grown diamonds have been due to post-growth irradiation to form the GR1 center with its zero-phonon line at 741.2 nm (e.g., Summer 2018 Lab Notes, pp. 215–216). GIA has examined CVD-grown diamonds colored by much stronger absorption of SiV⁻ centers, but those samples lacked isolated nitrogen absorption and often resulted in colors from pink to brown (S. Eaton-Magaña et al., "Laboratory-grown diamonds: An update on identification and products evaluated at GIA," Summer 2024 *G&G*, pp. 146–167). An internal GIA database search indicated that this was likely the first submitted CVD-grown diamond in which a green color contribution could be attributed to SiV⁻ at 737 nm instead of GR1 at 741.2 nm.

Sally Eaton-Magaña

Figure 7. Left: Vis-NIR absorption spectrum collected at liquid nitrogen temperature for the 3.07 ct CVD-grown diamond. Right: False-color PL map of the table facet collected with 633 nm excitation. The peak area of the SiV⁻ color center at 737 nm is normalized by the unsaturated diamond Raman peak area.

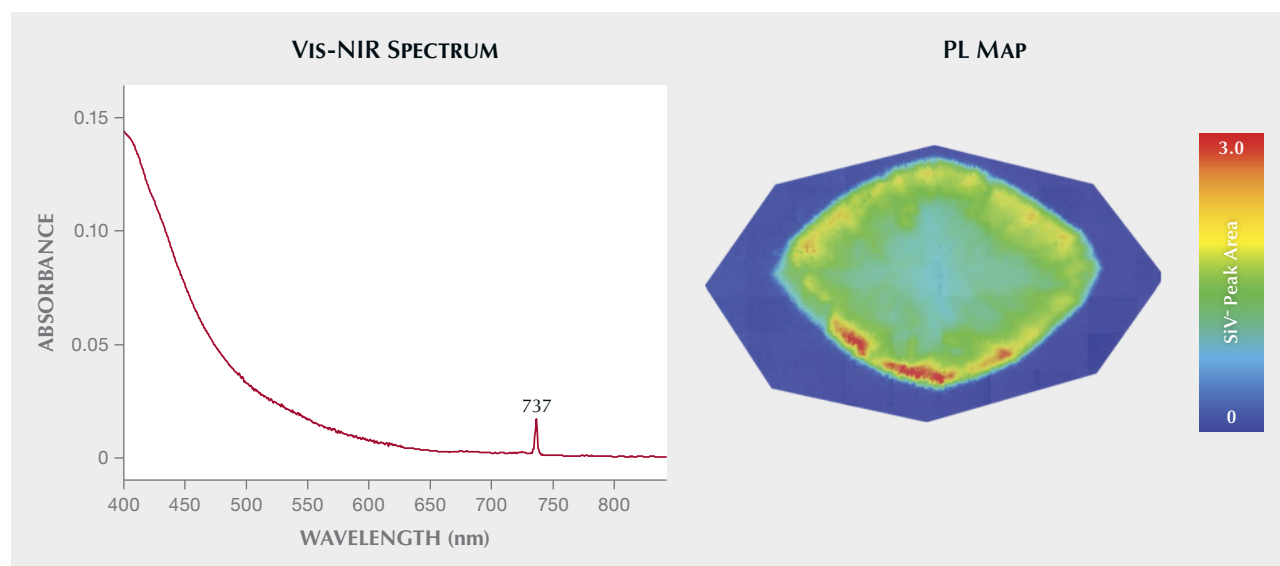


TABLE 1. Comparison of characteristics of submissions with counterfeit inscriptions and their accompanying GIA grading reports.

Samples	Weight (ct)	Measurements (mm)	Color	Clarity	Cut	Polish	Symmetry	Noted inclusions
1 Fraudulent	1.07	6.52–6.56 × 4.04	E	VS1	EX	EX	EX	Feather, internal graining
Original	1.07	6.51–6.55 × 4.04	E	VVS1	EX	EX	EX	Cloud, pinpoint, feather
2 Fraudulent	1.11	6.63–6.67 × 4.07	E	VVS1	EX	EX	EX	Chip, feather
Original	1.11	6.61–6.65 × 4.07	E	VVS1	EX	EX	EX	Pinpoint
3 Fraudulent	2.02	8.49–8.53 × 5.09	D	VVS2	EX	EX	VG	Pinpoint
Original	2.02	8.48–8.54 × 5.10	E	VVS2	EX	EX	EX	Cloud, pinpoint
4 Fraudulent	1.00	6.39–6.45 × 3.93	G	VVS2	VG	VG	EX	Pinpoint, needle
Original	1.00	6.41–6.46 × 3.92	G	VVS2	EX	EX	EX	Needle, cloud, pinpoint, feather, indented natural, natural

HPHT-Processed Natural and Laboratory-Grown Diamonds with Counterfeit Inscriptions

Recently, the Dubai laboratory encountered four stones submitted for update services inscribed with fraudulent GIA report numbers. Inconsistent font styles and placement indicated the numbers were not authentic GIA inscriptions.

A careful comparison of their quality characteristics confirmed that these were not the same diamonds as described in their accompanying reports. Although the diamonds were carefully selected to closely match the features listed on the original reports, several subtle differences in their color grades, measurements, and other characteristics were identified (table 1). Even more obvious were the spectral differences between the fraudulent and original stones. The difference in the one-phonon region of the Fourier-transform infrared absorption spectroscopy clearly revealed a discrepancy in the diamond types. The diamonds from the original reports were type Ia with aggregated nitrogen impurities, while these submitted stones were all type IIa, confirming they were, in fact, different stones.

On fraudulent diamonds 1 and 2, photoluminescence (PL) spectra produced by 514 nm laser excitation at liquid-nitrogen temperature showed that 637 nm peaks were greater than 575 nm peaks. The 575 and 637 nm peaks are emissions from the nitrogen vacancy center in its neutral [NV]⁰ and negative [NV]⁻ charge states, respectively. The 575:637 nm emission ratio of intensities of less than 1 (D. Fisher and R.A. Spits, “Spectroscopic evidence of GE POL HPHT-treated natural type IIa diamonds,” Spring 2000

G&G, pp. 42–49), along with other PL features, indicated that fraudulent diamonds 1 and 2 with the counterfeit inscriptions were natural diamonds that had undergone high-pressure, high-temperature (HPHT) treatment for color improvements.

The visible/near-infrared (Vis-NIR) absorption spectrum for fraudulent diamond 3, on the other hand, showed a 737 nm peak, which corresponds to the unresolved silicon vacancy [SiV]⁻ defect at 736.6/736.9 nm commonly seen in laboratory-grown diamonds using the chemical vapor deposition (CVD) growth method (P. Martineau et al., “Identification of synthetic diamond grown using chemical vapor deposition (CVD),” Spring 2004 *G&G*, pp. 2–25). The observation of such features led to the determination that this stone was CVD-grown and subjected to post-grown HPHT processing.

Further PL spectroscopy analysis on fraudulent diamonds 3 and 4 using 633 nm excitation confirmed the presence of the SiV⁻ doublet feature on both diamonds. In alignment with the Vis-NIR and PL spectra, DiamondView images of these two fraudulent stones displayed clear striations with interruption layers indicative of CVD growth (figure 8). These patterns are consistent with the step-flow growth structure of CVD-grown diamond, which was also visible under the microscope using crossed polarizers and further supported their laboratory-grown origins. The other two fraudulent diamonds (1 and 2), however, showed a lack of such patterns and demonstrated natural-looking features, which confirmed them as HPHT-processed natural diamonds.

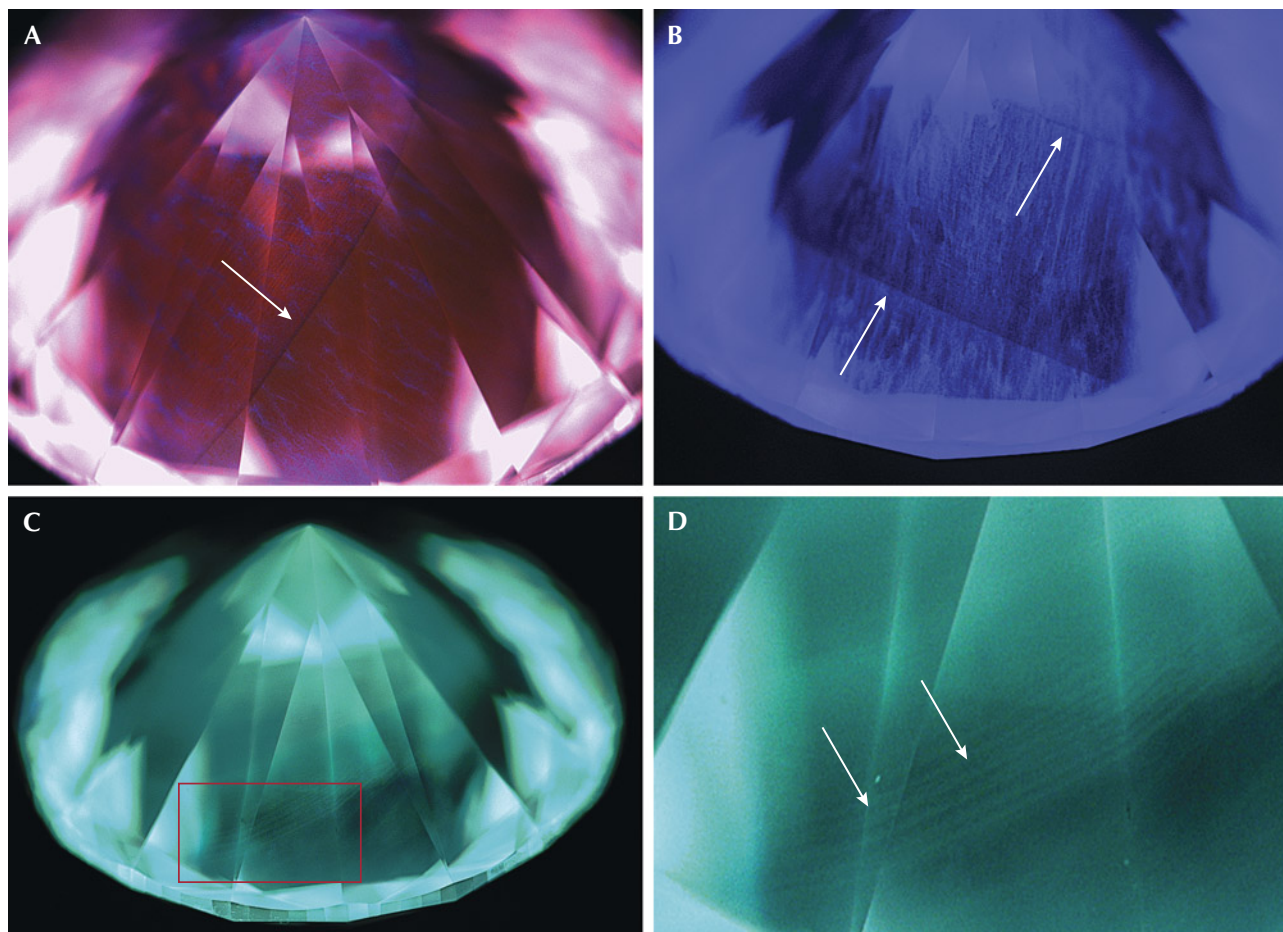


Figure 8. A and B: DiamondView imaging shows clear interruption planes resulting from start-stop environment change during the CVD growth of fraudulent diamond 3. A band pass filter centered at 390 nm shows even clearer interruption layers (indicated by arrows). C and D: Fraudulent diamond 4 shows subtle striations (indicated by arrows) on the pavilion view, but a closer look reveals the layered patterns indicative of CVD-grown diamonds. Images by Nick “Ka Chun” Chan.

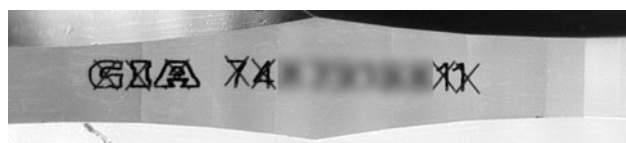
Considering all evidence, we concluded that two of the four stones were laboratory-grown diamonds, and the other two were HPHT-processed natural diamonds. All four diamonds were not the same natural diamonds as described in their accompanying GIA grading reports. In accordance with GIA procedures, the counterfeit inscriptions were crossed out (figure 9) and new report numbers were assigned. In addition, GIA inscribes “TREATED COLOR” on natural diamonds with post-

treatment history and “LABORATORY-GROWN” along with a GIA report number and distinct GIA LG logo on laboratory-grown diamonds.

Deceptive practices have occurred previously in the trade; similar instances of diamonds with fraudulent inscriptions have been reported by GIA (e.g., Summer 2021 Lab Notes, pp. 150–152; Fall 2021 Lab Notes, pp. 258–259). Additionally, non-diamond materials, such as synthetic moissanite, with fraudulent GIA inscriptions have been submitted as diamonds to GIA (Fall 2020 Lab Notes, pp. 424–425; Fall 2022 Lab Notes, pp. 360–361). These cases highlight the importance of verifying inscription authenticity because a fraudulent inscription could be overlooked by simple visual examination. One possible solution is GIA’s Match iD, a device that compares a diamond’s inscription with its grading report in the GIA database.

Nick “Ka Chun” Chan and Satyaprasad Pradhan

Figure 9. GIA’s standard procedure is to cross out the counterfeit inscription. Image by GIA staff.



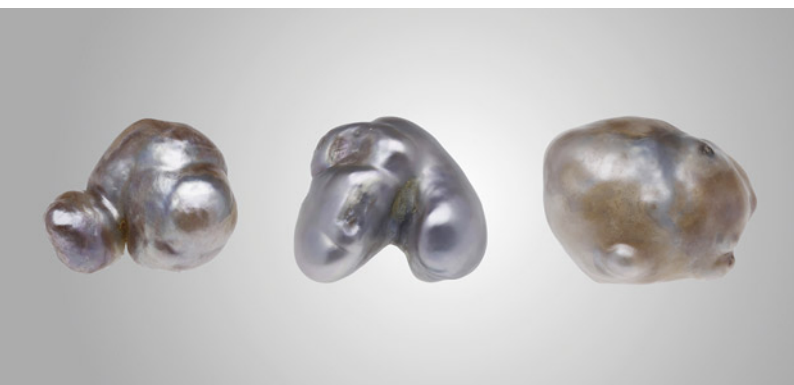


Figure 10. Three large, reportedly natural pearls with hollow interiors from the *Pinctada radiata* species from Bahrain, weighing 1.97, 3.92, and 6.13 ct, respectively. Photo by Gaurav Bera.

PEARLS

Three Large Natural Hollow *Pinctada radiata* Pearls

Recently, three large baroque natural hollow pearls reportedly from the *Pinctada radiata* species were submitted for scientific examination at GIA's Mumbai laboratory. According to the owner, the pearls were obtained from Bahraini divers more than a decade ago. Weighing 1.97, 3.92, and 6.13 ct, and measuring $10.09 \times 8.40 \times 6.32$ mm, $12.78 \times 11.12 \times 9.45$ mm, and $16.00 \times$

13.94×11.60 mm, respectively, these pearls had surprisingly low heft for their sizes (figure 10). Their purplish gray bodycolor, with varying tones of orient, displayed brown patches of different intensities.

Under high magnification, the gray areas exhibited a fine striated nacre growth pattern of overlapping platelets typical of nacreous pearls from *Pinctada* species. Small areas on pearls 1 and 2 displayed a distinctive spiral platy structure, with the translucent outer nacre revealing layers of resinous organic-rich material. In addition, dull brownish patches with a crackled surface texture and a bumpy botryoidal appearance were observed in pearls 1 and 3, surrounded by minor surface blemishes. All three pearls exhibited an inert reaction when subjected to X-ray fluorescence. Energy-dispersive X-ray fluorescence spectrometry showed no traces of manganese and higher strontium levels of 853, 973, and 1013 ppm, respectively, indicative of a saltwater environment. When viewed under long-wave ultraviolet radiation, the pearls showed a moderate bluish green reaction (figure 11) and a similar weaker reaction under short-wave ultraviolet radiation.

Real-time X-ray microradiography (RTX) imaging of all the pearls revealed large voids and organic-rich material of varying opacities extending to the pearls' edges. X-ray computed microtomography (μ -CT) imaging further emphasized the distinct features within these hollow pearls. The large voids consistently followed the outline of

Sample details	RTX image	μ -CT image	LWUV
Pearl 1 1.97 ct			
Pearl 2 3.92 ct			
Pearl 3 6.13 ct			

Figure 11. RTX and μ -CT images and long-wave ultraviolet reaction of the three natural hollow pearls. The dark organic-rich voids are marked with red arrows, the white walls are marked with yellow arrows, and the aggregates in pearl 3 are marked with blue arrows. Photos by Gaurav Bera.



Figure 12. The white imitation pearl measuring approximately 1.70×1.12 mm and weighing 0.01 ct. Photo by Gaurav Bera.

the pearls and were surrounded by fine growth arcs unlike the typical irregular voids found in non-bead cultured (NBC) pearls, which mostly lack natural growth arcs in the outer nacre ("The microradiographic structures of non-bead cultured pearls," *GIA Research News*, November 20, 2009). In addition, they contained organic-rich material enclosed by white walls that seamlessly followed each pearl's shape. Interestingly, pearl 3 also displayed intriguing concentric aggregates within the void area.

Upon analysis and comparison with reference samples in GIA's research database, it was evident that these specimens closely resembled natural hollow pearls observed in *Pinctada* species. The radiopacity and shape of the voids within them differed from voids typical of saltwater NBC pearls, which tend to be darker, irregular, and more elongated ("Non-bead-cultured pearls from *Pinctada margaritifera*," *GIA Research News*, April 27, 2018). In contrast, the voids in natural hollow pearls exhibit varying degrees of radiopacity. Furthermore, hollow pearls are distinguished by their large, enclosed

cavities (*The Pearl Blue Book*, CIBJO, 2023), which sets them apart from solid core pearls.

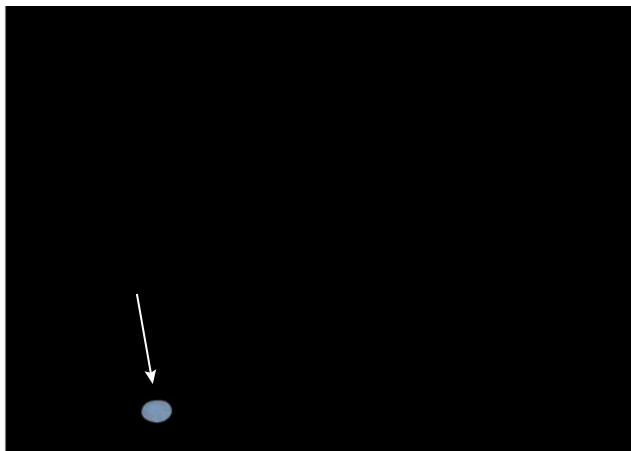
Notably, many antique pearl jewelry pieces dating before the twentieth century, prior to the start of pearl cultivation, feature large hollow natural pearls. These hollow natural pearls were often too fragile to set on jewelry and were frequently filled with metal fragments to increase both their durability and weight. Despite their significant size, hollow pearls are deceptively light. It is quite common for natural pearls to exhibit a hollow structure. The exploration of such pearls has consistently captivated gemologists, as their intricate and complex internal structures pose challenges in drawing definitive conclusions, with similar voids occasionally observed in NBC pearls. The study of such specimens provides valuable insights and significantly contributes to our understanding of the formation processes associated with natural hollow pearls.

Prasad Mane, Roxane Bhot Jain, and Abeer Al-Alawi

Imitation Seed Pearl with Blue X-Ray Fluorescence

GIA's Mumbai laboratory recently received a submission of 18 strands of pearls for identification, consisting of approximately 9,360 white to light cream pearls weighing a total of 706.79 carats. When subjected to X-ray fluorescence, most of the pearls were inert, indicating a saltwater origin, while a few exhibited the strong yellowish green fluorescence of freshwater pearls. Notably, one white oval "pearl," measuring approximately 1.70×1.12 mm and weighing 0.01 ct (figure 12), displayed a unique moderate blue reaction upon X-ray exposure (figure 13)—an effect not previously observed in saltwater or freshwater pearls. The "pearl" was visually similar to the other submitted pearls, but its extremely large drill

Figure 13. Left: The imitation pearl (marked with arrow) in the strand appearing similar to other pearls. Right: When exposed to X-ray fluorescence, it exhibits a blue reaction, while the remaining pearls are inert. Images by Karan Rajguru.



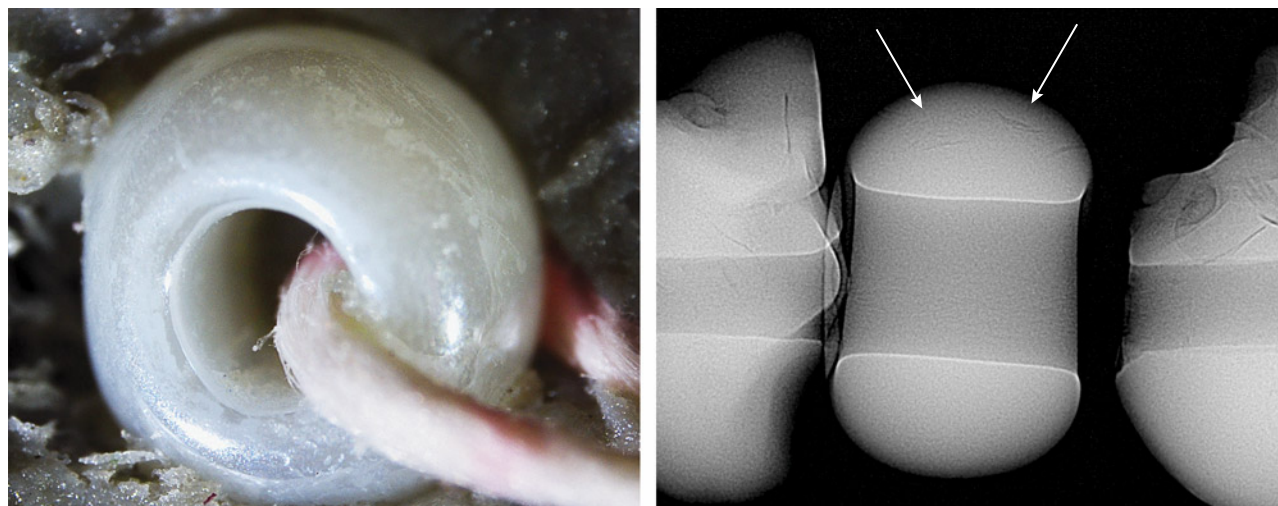


Figure 14. Left: Extremely large drill hole and surface showing liquid-like remnants; field of view 1.6 mm. Right: RTX image revealing arcs in the imitation pearl (indicated by arrows) similar to those of two adjacent natural pearls. Images by Karan Rajguru.

hole raised suspicion (figure 14, left). Under higher magnification, its smooth surface lacked characteristic nacreous overlapping aragonite platelets, displaying a unique liquid-like surface residue instead. This “pearl” appeared inert under long-wave ultraviolet light, while other pearls were greenish yellow. Additionally, it exhibited a light yellow reaction under the deep-UV wavelength (<225 nm) of the DiamondView, unlike the typical blue reactions observed in pearls. Raman spectroscopy with different laser excitations did not reveal any distinctive features indicative of calcium carbonate polymorphs typically found in pearls. Based on these findings, it was concluded that the material in question was not a pearl but rather an imitation. Real-time X-ray microradiography (RTX) indicated that, with the exception of the one imitation, the 18 strands contained a mixture of natural and non-bead cultured pearls. Interestingly, the imitation displayed a similar radiopacity to the other pearls. A few arcs were present at the outer edges, comparable to growth arcs observed in the adjacent natural pearls strung in the strand (figure 14, right).

Common pearl imitations often utilize material such as solid or hollow glass, plastic, or shell bead coated with a “pearl essence” substance that simulates nacre’s iridescence (J. Hanano et al., “Majorica imitation pearls,” Fall 1990 *G&G*, pp. 178–188). These imitations lack the usual nacreous platelets, mosaic patterns, and cellular structures observed in pearls, and often present a glittery surface appearance of coating material and occasional “molded” drill holes. Such imitations may show variations in RTX results depending on the composition of the substance and the coating.

Distinguishing imitations when mixed with large quantities of pearls in an item can be a challenge. Due to their similarity in appearance, these materials are occasionally mixed with pearl strands and jewelry. Fur-

thermore, the presence of arcs in the examined imitation sample may have been misleading, potentially going unnoticed without the aid of the blue fluorescence under X-ray exposure during routine testing. The utilization of X-ray fluorescence screening has proven useful in the identification of certain types of imitation materials, particularly in the case of smaller pearls strung in strands. While encountering such imitation materials is not frequent in routine testing, it remains essential to accurately distinguish and identify them to maintain the authenticity of pearl collections.

Karan Rajguru, Anukul Belanke, and Abeer Al-Alawi

PEZZOTTAITE with Multiple Cat’s-Eyes

An 11.23 ct purplish pink cabochon exhibiting multiple cat’s-eye phenomena was recently submitted to the Tokyo laboratory for identification (figure 15, left). Standard gemological testing results included a spot refractive index of 1.59, a specific gravity of 3.11, dichroism, and an inert reaction under both long-wave (365 nm) and short-wave (254 nm) UV radiation. Microscopic observation revealed several inclusions: iridescent parallel growth tubes or elongated thin films, trichite-like iridescent fingerprints, and transparent colorless crystals. The Raman spectrum was consistent with pezzottaite ($\text{CsLiBe}_2\text{Al}_2\text{Si}_6\text{O}_{18}$).

Pezzottaite was discovered in Madagascar in 2002 and approved as a new mineral by the International Mineralogical Association in 2004. While it belongs to the beryl mineral group, pezzottaite has a trigonal crystal system, differing from beryl’s hexagonal crystal system, and can be described as having imperfect cleavage parallel to the basal {001} planes, which are perpendicular to the *c*-axis (i.e., the optical axis; F.C. Hawthorne et al., “Pezzottaite $\text{Cs}(\text{Be}_2\text{Li})\text{Al}_2\text{Si}_6\text{O}_{18}$: A spectacular new beryl-group mineral

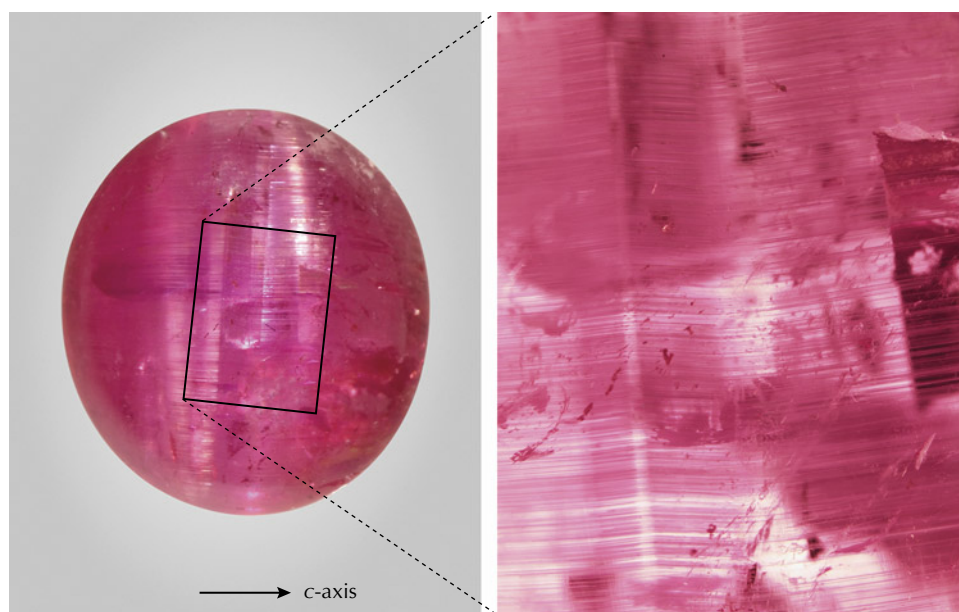


Figure 15. Left: An 11.23 ct purplish pink pezzottaite cabochon, measuring $14.43 \times 13.10 \times 7.39$ mm, displaying multiple cat's-eyes. The arrow indicates the c-axis (i.e., the optical axis). Photo by Shunsuke Nagai. Right: These cat's-eyes are produced by growth tubes likely bent by imperfect {001} cleavage planes. Photomicrograph by Taku Okada; field of view 4.80 mm.

from the Sakavalana pegmatite, Fianarantsoa province, Madagascar," *Mineralogical Record*, Vol. 35, No. 5, 2004, pp. 369–378).

In the submitted stone, the growth tubes or elongated thin films were oriented nearly parallel to the c-axis and displayed multiple bends possibly resulting from imperfect {001} cleavage planes, producing multiple cat's-eyes perpendicular to them, or almost perpendicular to the c-axis (figure 15, right). Though it is unknown how the bending of these inclusions happened, they work together to produce the highly exceptional and impressive phenomenon of multiple cat's-eyes.

Taku Okada and Kazuko Saruwatari

QUARTZ Assemblage Imitating Emerald

Gemstone assemblages, composed of two or more materials fused or bonded together, have long been used to imitate a variety of natural gemstones. These composite constructs are regularly encountered in gemological laboratories, where they are identified by their component parts and may be referred to as imitations of various natural stones. Assembled stones designed to mimic emeralds have historically been constructed using colorless spinel with colored cement, layered glass, or beryl doublets/triplets. One of the most widely encountered assembled emerald imitations is the *soudé emerald*, which entered mass production in the early twentieth century. Over time, its construction evolved from the use of rock crystal to colorless synthetic spinel, and later to colorless beryl or pale aquamarine.

GIA's New York laboratory recently examined a green stone mounted in a necklace with a total weight of 7.84 grams (figure 16). While the deep green color of this stone suggested it may be an emerald, a spot refractive index measurement yielded a value of 1.54, indicating the stone was

likely quartz. Under both long- and short-wave ultraviolet radiation, the assemblage exhibited a whitish fluorescence, which was confined to an internal layer within the stone. Raman spectroscopy using a 514 nm laser further confirmed the identification of the material as quartz.

Initial microscopic examination of the green stone revealed a separation plane near the carved top, along with

Figure 16. A pendant necklace featuring a green stone measuring $13.35 \times 12.20 \times 12.20$ mm that was identified as a quartz assemblage. Photo by Michele Wong.





Figure 17. The assemblage appears as two carved pieces attached to the setting with a green cement. Colorless gas bubbles can be observed, an indication that this piece is not what it seems. Photomicrograph by Ezgi Kiyak; field of view 21.2 mm.

numerous gas bubbles, and some large air-filled voids that blocked the cement, creating colorless zones (figure 17). These colorless voids reinforced the observation that the green color appeared to be confined to the cement layer (figure 18). Further inspection under the microscope revealed natural fluid inclusions, supporting the identification of natural rock crystal quartz.

This detailed examination of the green stone exposed three sections of colorless natural quartz in various

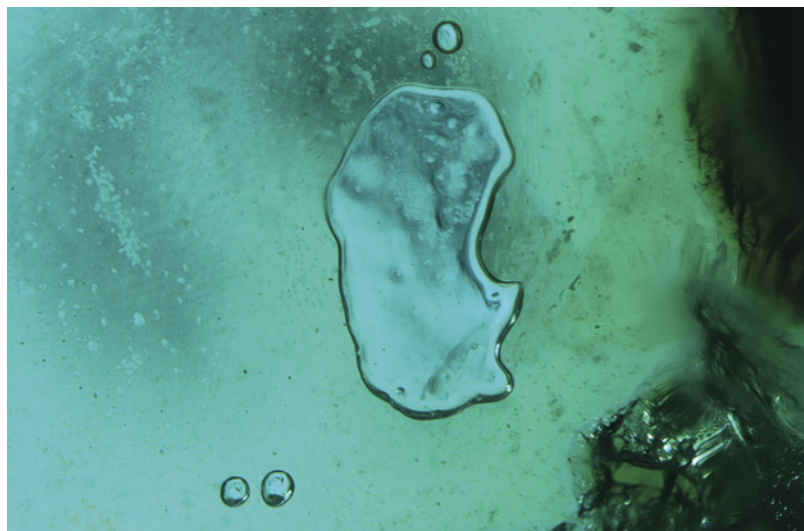
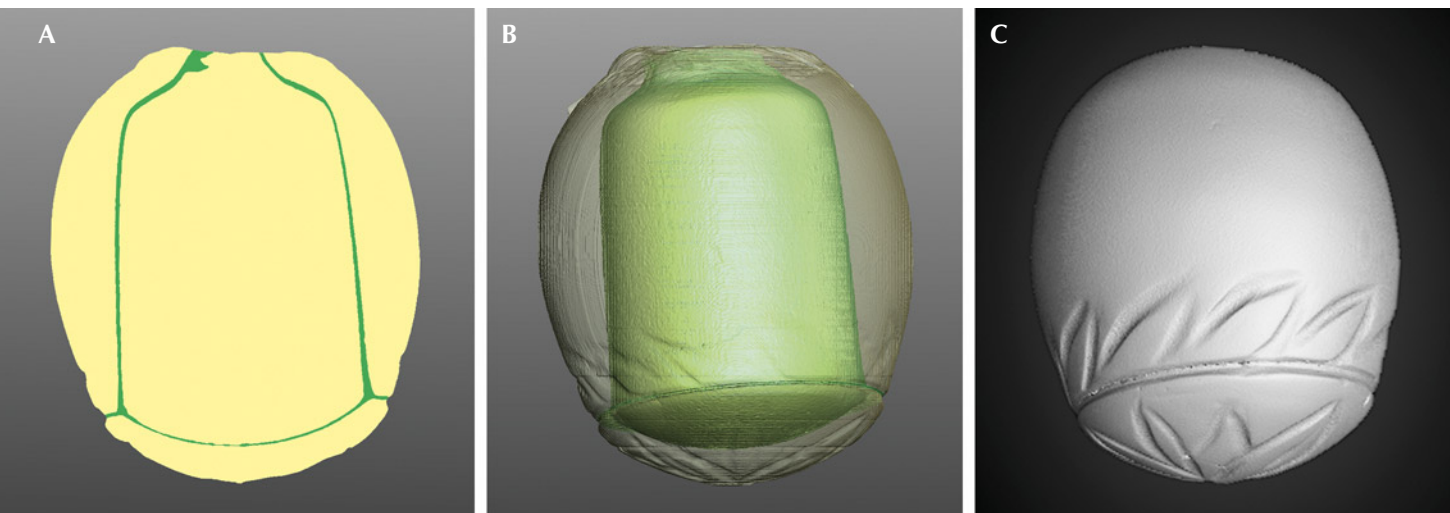


Figure 18. Tabular bubbles in the bluish green cement demarcate the boundary between the quartz segments. Photomicrograph by Hannah Wiggins; field of view 7.19 mm.

thicknesses joined with a green-colored cement, prompting the authors to collect X-ray tomography images to investigate how the green stone was assembled. The X-ray computed tomography showed three distinct quartz components connected by a cement layer with an average thickness of 0.20 mm along a clearly defined interface (figure 19). The exceptionally precise machining of the parts of this assemblage makes this piece a particularly sophisticated assembled stone.

Hannah Wiggins and Ezgi Kiyak

Figure 19. A and B: 3D scanned images indicating the colored cement layer between the carved parts. C: The carving details from the outside. Images by Emiko Yazawa and W. Henry Towbin.



Introducing Jewelry Services

Our legacy of trust,
now available for jewelry.



GIA®

New GIA Jewelry Services

For generations, the world has trusted GIA to provide accurate reports for loose gems.

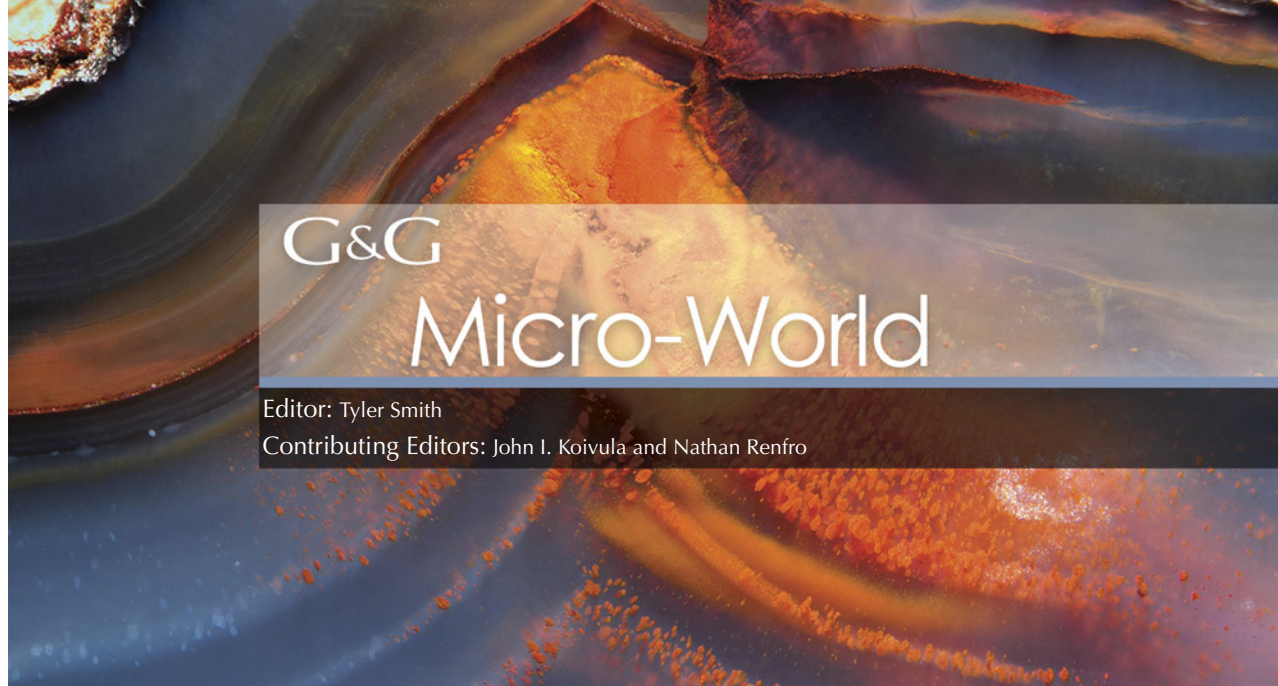
Now, we're bringing our global leadership to new horizons by providing jewelry services.

Expect the same rigorous GIA standards, deep expertise, and advanced technology to add confidence and credibility to every jewelry report.



[GIA.edu/jewelryservices](https://www.gia.edu/jewelryservices)

Jewelry provided courtesy
of The ClearCut.



G&G

Micro-World

Editor: Tyler Smith

Contributing Editors: John I. Koivula and Nathan Renfro

Anatase “Dandelion” in Agate

Rutile is a common inclusion in quartz, but its polymorphs, such as anatase and brookite, are much rarer to find. Recently, a spherical conglomeration of acicular anatase crystals (identified by Raman spectroscopy) resembling the seed-head phase of a dandelion was seen as an inclusion within an agate slice (figure 1). Nearby, orangy yellow iron staining was also observed in a dendritic growth pattern.

Anatase and rutile are both tetragonal crystallizations of titanium dioxide (TiO_2). Rutile, with its more compact crystal structure, is more stable and therefore more common. Brookite and anatase will convert to rutile under

specific heat and pressure conditions. Anatase typically manifests as reddish brown to brownish yellow tabular or pyramidal crystals. Anatase inclusions are rare, but this inclusion with an acicular crystal habit is an exceptionally unusual occurrence.

*Britni LeCroy
GIA, Carlsbad*

Diamond Within a Diamond Within a Diamond

Recently, the authors examined a 2.57 ct natural type Ia diamond with some interesting inclusion features. This

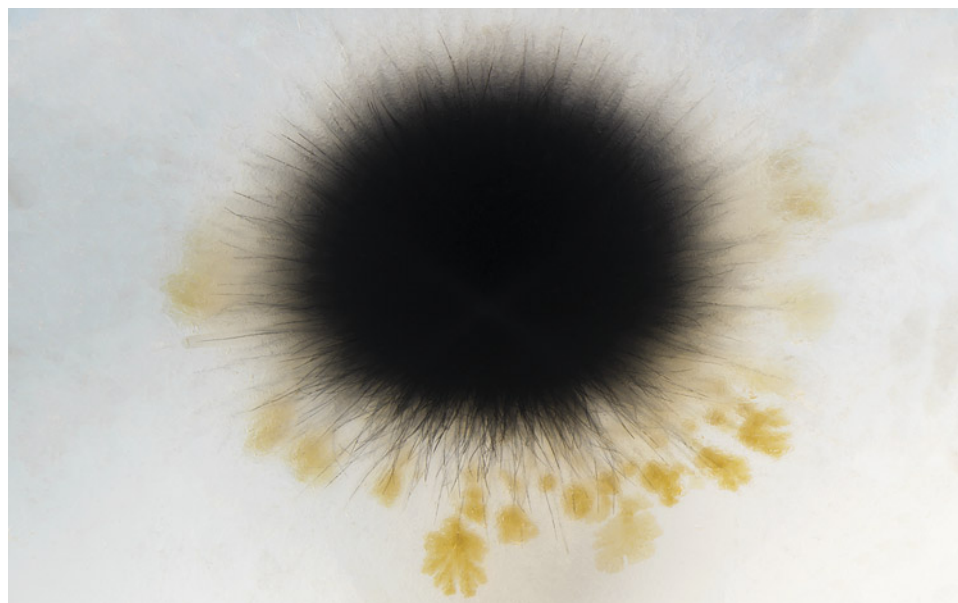


Figure 1. An acicular cluster of anatase crystals within agate resembling a dandelion seed head. Photomicrograph by Britni LeCroy; field of view 4.79 mm.

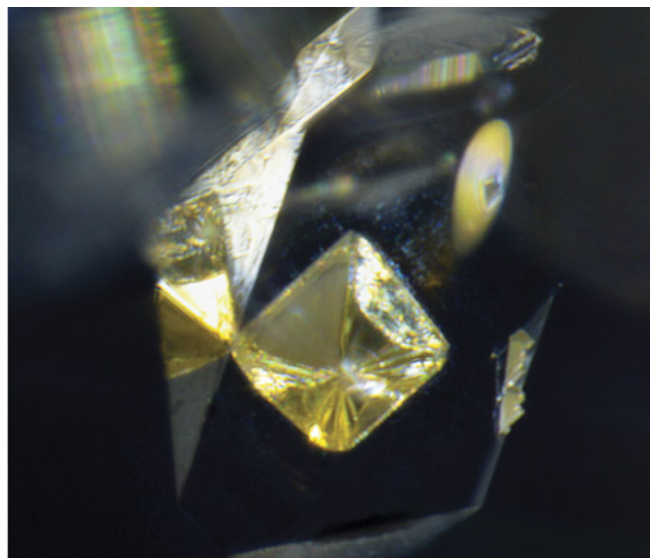


Figure 2. Left: Viewed from the pavilion of the 2.57 ct diamond, this transparent crystal inclusion with mirror image reflection resembles the profile of a faceted diamond under darkfield lighting. Image captured in monochrome; field of view 0.88 mm. Right: Using fiber-optic lighting, the crystal inclusion that appears opaque in the left image is displayed as a yellow octahedron; field of view 0.40 mm. Photomicrographs by Yagnesh Vyas (left) and Hemal Trivedi (right).

round brilliant stone with I-color and I₁ clarity contained interesting transparent and yellow crystal inclusions (figure 2). The transparent crystal resembled the profile view of a faceted round brilliant diamond. Within the “crown” of this ghostly faceted transparent crystal, a yellow crystal was also observed. Although the crystal’s identity was unconfirmed, it showed a morphology resembling that of an octahedral rough diamond. Similar inclusions have been documented previously (Summer 2022 *G&G Micro-World*, pp. 227–228; Spring 2024 *G&G Micro-World*, pp. 81–82). No obvious strain was observed when the diamond was examined through crossed polarizing filters. These unusual inclusions—resembling a miniature faceted diamond and a yellow octahedral rough diamond—are “knot” commonly observed in the laboratory.

Ravikumar Sharma and Krishna Sagar
GIA, Mumbai

Sally Eaton-Magaña
GIA, Carlsbad

About the banner: This laguna agate from Chihuahua, Mexico, shows peaked bands of orange iron oxide concretions. The shape of these bands is dictated by the morphology of the vug within which the agate formed. Photomicrograph by Tyler Smith; field of view 4.79 mm.

GEMS & GEMOLOGY, VOL. 61, NO. 2, PP. 184–191.

© 2025 Gemological Institute of America

“Goose Bumps” on South Sea Pearl

Pearls occasionally develop marks on their surface during formation. Recently, when examining a strand of cultured golden South Sea pearls approximately 12 mm in diameter, we discovered a pearl covered with innumerable pinpoints resembling a dotted pattern similar to that of goose bumps when viewed under the gemological microscope (figure 3). When present, pinpoints such as these usually only occur sporadically on the surface of South Sea and Tahitian pearls, but the densely covered surface in this pearl is

Figure 3. “Goose bumps” on the surface of a 12 mm golden South Sea pearl. Photomicrograph by Le Ngoc Nang; field of view 5 mm.



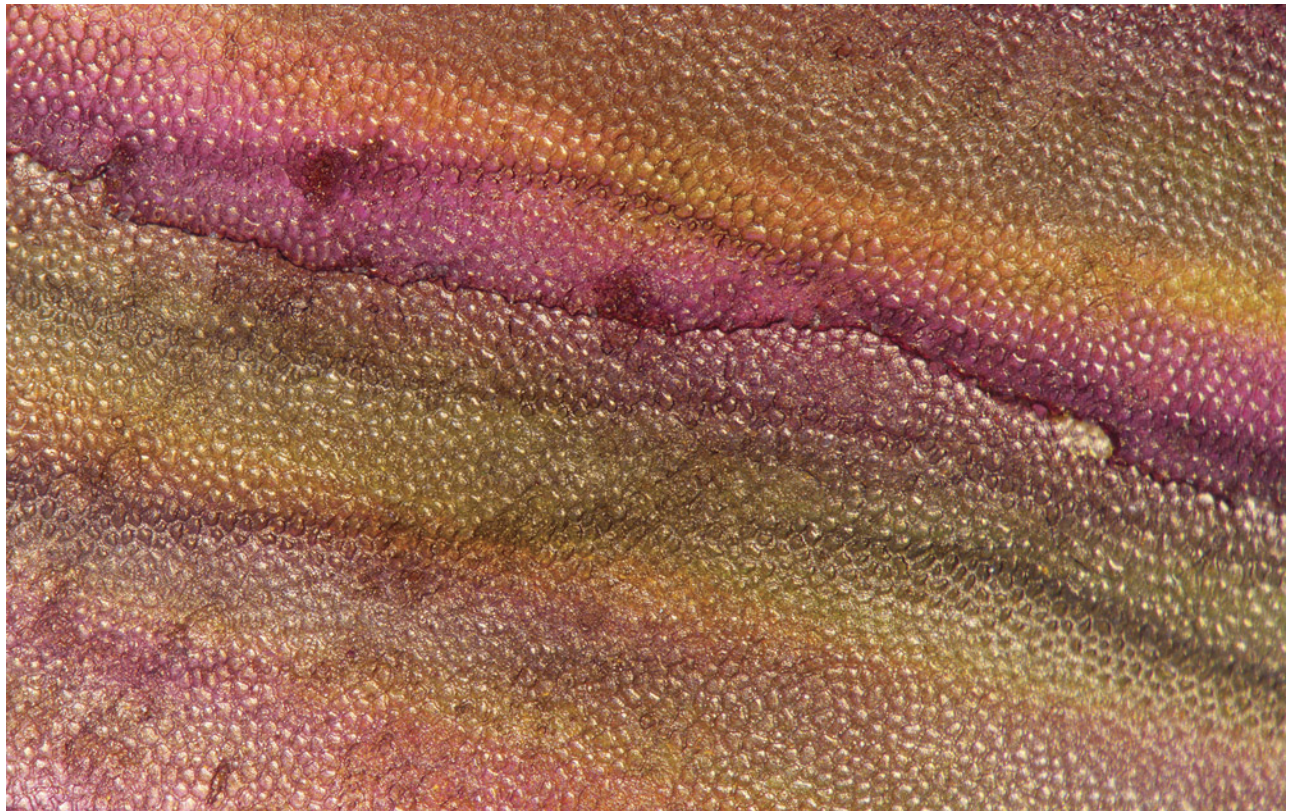


Figure 4. A thin layer of iridescent aragonite overlays the prismatic calcite of a Pinnidae shell, creating a captivating iridescent effect. Photomicrograph by Ravenya Atchalak; field of view 2.88 mm.

extremely rare. Interestingly, despite their high density, these inclusions had little effect on the luster and quality of the pearl when viewed without magnification, allowing the pearl to maintain its beauty and high value.

Le Ngoc Nang
Liu Gemological Research and Application Center
Ho Chi Minh City

Iridescent Pen Shell

The thin, wedge-shaped shell of the Pinnidae family (pen) mollusk is made of calcium carbonate in the forms of calcite and aragonite. The outer (posterior) surface is composed of non-nacreous calcite prisms covering the entire shell, while the inner (anterior) surface is composed of both calcite and aragonite. The nacreous aragonite

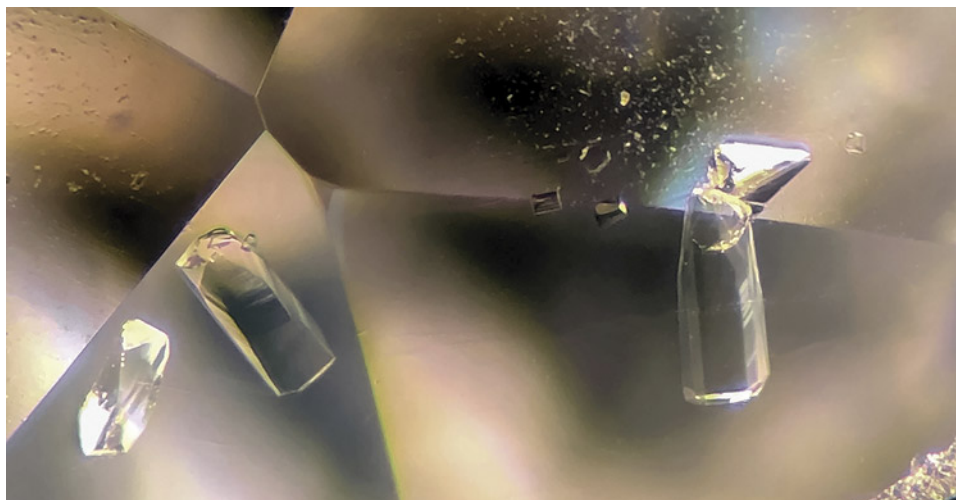


Figure 5. Transparent danburite crystals in phenakite from Momeik, Myanmar, shown in a combination of dark-field and oblique illumination. Photomicrograph by Kyaw Thu; field of view 2 mm.



Figure 6. This orange inclusion in quartz (left) with a striated bipyramidal structure was identified as lithiophilite (right). Photos by Wingtak Lui (left) and Liyan He; field of view 13.0 mm (right).

tablets are deposited over the calcite and restricted to a section of the shell at the tapered end. Figure 4 shows the calcite covered by a thin, iridescent layer of aragonite. The interplay between the two crystalline forms highlights the intricate structural complexity of the shell.

Ravenya Atchalak
GIA, Bangkok

Colorless Danburite Crystals in Phenakite from Myanmar

Phenakite (Be_2SiO_4), also known as phenacite, is a rare beryllium silicate mineral characterized primarily by its colorless appearance, although it may also exhibit shades of yellow, pink, or brown. Phenakite is typically found in granitic pegmatite deposits and is recognized from many localities worldwide.

A 4.68 ct colorless faceted oval specimen measuring $10.37 \times 9.25 \times 7.52$ mm sourced from Khetchel, near Momeik in Myanmar, was recently examined by the authors. Based on its physical and optical properties, such as a refractive index of 1.653–1.670 and a specific gravity of 2.97, the mineral was identified as phenakite. Microscopic observation revealed the presence of well-formed prismatic crystal inclusions (figure 5). These transparent crystals were identified through Raman microanalysis as danburite ($\text{CaB}_2(\text{SiO}_4)_2$). Unusual inclusions, such as perettiite-(Y) and tusionite, have been documented in phenakite from Khetchel (Summer 2018 *G&G Micro-World*, p. 228). To the authors' knowledge,

however, this is the first documented case of danburite inclusions in phenakite.

Sai Gon Khay and Kyaw Thu
S Gemmological Institute (SGI)
Yangon, Myanmar

Lithiophilite in Quartz

The 52.52 ct transparent colorless quartz in figure 6 displayed a large orange crystal near the surface with a well-formed bipyramidal habit. The crystal surface showed growth features and had weak pleochroism.

Raman microanalysis identified the inclusion as lithiophilite. Lithiophilite ($\text{LiMn}^{2+}\text{PO}_4$) is a member of the triphylite group and quite rare as an inclusion in quartz, especially in such a well-crystallized form. Lithiophilite generally forms in granitic pegmatites, mostly in environments rich in lithium and phosphorus. This unique inclusion in quartz is one of the best well-crystallized examples of lithiophilite that the authors have observed.

Liyan He
Guangdong Gemstones & Precious Metals Testing Center
Guangzhou, China

Wingtak Lui and Wang Zhang
Min De Minerals & Gem Research Co., Ltd.
Nanjing, China

Monazite in Quartz

Recently, several platy orange-yellow inclusions were observed within a highly transparent colorless quartz crystal



Figure 7. Left: Numerous orange-yellow to orange solid inclusions are visible within the transparent colorless quartz. Right: Closer observation reveals bright orange wedge-shaped crystals. Photomicrographs by Wingtak Lui; fields of view 5.1 mm (left) and 3.2 mm (right).

(figure 7, left). These inclusions exhibited an orange-yellow to orange color, a smooth surface, and a glassy luster, with a euhedral or subhedral appearance. Closer inspection revealed that some crystals displayed the typical wedge shape of monoclinic crystals (figure 7, right). This distinct crystal morphology and vibrant color prompted further investigation into their composition.

Raman spectroscopy identified the inclusions as monazite, a phosphate mineral $[(\text{Ce}, \text{La}, \text{Nd}, \text{Th})\text{PO}_4]$. Further analysis using X-ray fluorescence confirmed a high concentration of cerium, classifying the inclusions specifically as monazite-(Ce).

Rui Rui Xing, Wingtak Lui, and Tsu Wei Chang
Min De Minerals @ Gem Research Co., Ltd.
Nanjing, China

Mystery Pebbles in Quartz

Sometimes strange specimens come to us for examination and publication in the *Micro-World* column. The transparent to opaque, partially polished crystal of doubly terminated rock crystal quartz shown in figure 8 is one such example.

The crystal weighed 150.97 ct and measured $55.52 \times 24.59 \times 19.13$ mm. Raman analysis revealed that the pebbles embedded in the quartz were composed of a mineral in the amphibole supergroup, though the exact type of amphibole remains unknown.

Thought to have come from the Fengjiashan mine in Daye County, Hubei Province, China, the crystal contained numerous opaque light gray to white and yellowish fibrous rounded pebbles with a felted texture, in various



Figure 8. This 150.97 ct quartz crystal hosts pebbles of an amphibole, stacked like rocks in a stone wall. Photo by Annie Haynes.



Figure 9. The fibrous felted texture of the amphibole pebbles was revealed under magnification. Photomicrograph by Nathan Renfro; field of view 20.57 mm.

sizes up to 12 mm, as shown in figure 9. Overall, the inclusion scene had the appearance of rocks stacked in a stone wall. How the inclusions formed in this way is a gemological mystery, but they certainly provided us with a very photogenic specimen.

*John I. Koivula, Nathan Renfro, and Maxwell Hain
GIA, Carlsbad*

Well-Formed Rutile Star in Quartz

Rutile, one of the five forms of titanium dioxide, can be found in many gemstones as inclusions. In this colorless cabochon, acicular crystals of rutile formed around a

hematite core as a protogenetic mineral to the quartz host. A large quantity of rutile needles intersects and radiates outward to form a six-rayed “star” inclusion (figure 10). While rutilated quartz is not uncommon, this attractive inclusion provided a striking contrast to the colorless quartz backdrop.

*Isabelle Corvin
Olympia, Washington*

“Sugar Plum” in Titanium-Diffused Blue Sapphire

A recently examined 4.20 ct blue sapphire included a frosted cluster surrounded by a rimmed bubbly discoidal



Figure 10. Intersecting needles of rutile form a “star” inclusion in this colorless quartz. Photomicrograph by Isabelle Corvin; field of view 2.2 mm.

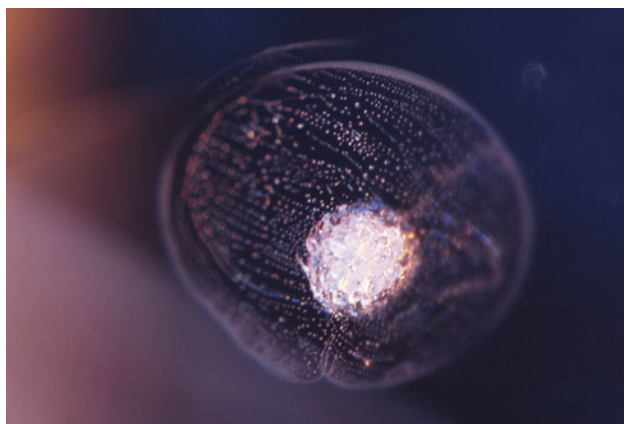


Figure 11. A sugar plum-like frosted zircon cluster in blue sapphire. Photomicrograph by Taku Okada; field of view 1.05 mm.

fingerprint, resembling a sugar plum, Portuguese *confeito*, or Japanese *konpeito* (figure 11). The inclusion appeared to be a former zircon (ZrSiO_4) cluster, which is a common inclusion in sapphire and decomposes after heat treatment above about 1400°C (W. Wang et al., “The effects of heat treatment on zircon inclusions in Madagascar sapphires,” Summer 2006 *G&G*, pp. 134–150). When viewed with diffused white light, the stone displayed concentrations of blue color at the facet edges of the pavilion, indicating titanium diffusion treatment, which usually happens around $1675\text{--}1750^\circ\text{C}$ for 96–150 hours (R.W. Hughes et al., *Ruby & Sapphire: A Gemologist’s Guide*, RWH Publishing/Lotus Publishing, Bangkok, 2017). At such high temperatures, the aluminum oxide (Al_2O_3) component of the surrounding corundum decreases the melting point of the decomposing zircon and causes partial melting, especially through interaction with the SiO_2 component of the zircon inclusion (W. Wang et al., 2006). High-temperature heat treatment sometimes creates such sugar plum-like frosted zircon inclusions as seen in this sapphire.

Taku Okada
GIA, Tokyo

“Soap Bubbles” in Yellow Sphe

Sphene, better known to mineralogists as titanite (CaTiSiO_5), is typically yellow, green, orange, or brown in color and is known for its incredible fire resulting from high dispersion. Recently, the author examined a 6.28 ct yellow cushion-cut stone displaying fire and strong eye-visible doubling. Its over-the-limit refractive index reading and visual appearance, as well as Raman spectroscopy, identified the specimen as sphene. Internal growth features, healed fissures, and a cloud of reflective particles were observed. Interestingly, the reflection of light from minute particles within the doubly-refractive sphene resulted in the appearance of a cloud of soap bubble-like inclusions, displaying interference colors in

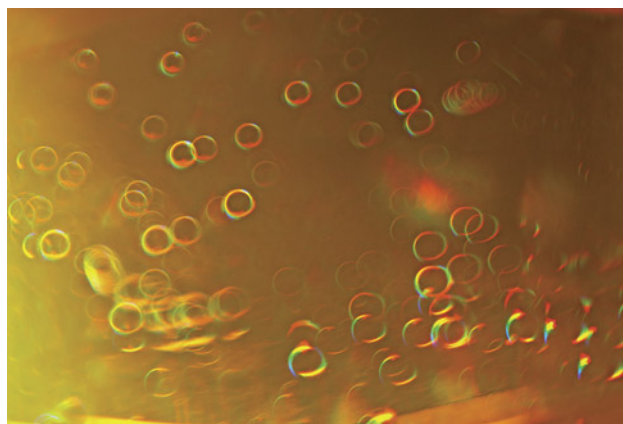


Figure 12. A 6.28 ct faceted yellow sphene exhibited interference “soap bubbles.” Photomicrograph by Ungkhana Atikarnsakul; field of view 3.6 mm.

some crown facets (figure 12). The inclusions were best viewed with oblique fiber-optic lighting, creating a fantastic scene in this yellow sphene.

Ungkhana Atikarnsakul
GIA, Bangkok

Figure 13. Weighing 2.22 ct and measuring 8.26 mm in the largest dimension, this unique diamond octahedron contains a high-relief, three-dimensional phantom visible through all eight octahedral faces. Photo by Diego Sanchez.



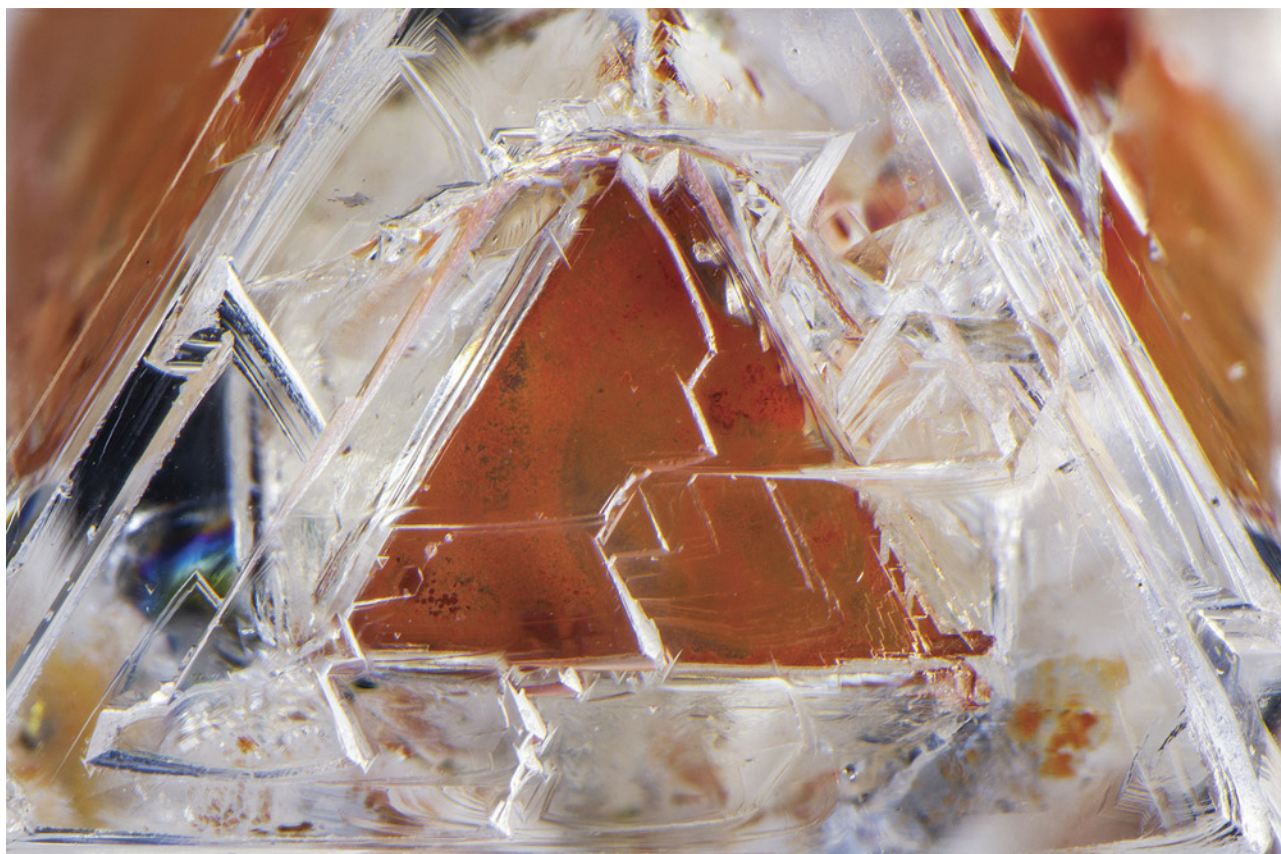


Figure 14. One of eight triangular limonitic faces in the 2.22 ct diamond crystal containing a phantom. Photomicrograph by Nathan Renfro; field of view 4.78 mm.

Quarterly Crystal: Unique Phantom in Diamond

When we think about phantoms as inclusions, quartz typically comes to mind. However, this Quarterly Crystal is a bit different, in that the phantom examined resides in a well-formed, transparent octahedral diamond crystal reportedly from the De Beers mine in the Republic of South Africa (figure 13). The colorless diamond host measures $8.26 \times 6.20 \times 5.37$ mm, weighs 2.22 ct, and was purchased from David New in 1989 in Tucson, Arizona.

As shown in figure 14, the phantom is a most unusual octahedral orangy red-brown limonitic crystal formation showing trigons and dark green radiation

stains on its inner surfaces. The triangular faces of the phantom were likely once composed of an iron sulfide, such as pyrrhotite, which was subsequently altered epigenetically to limonite, a rusty mixture of hematite and goethite.

The complete phantom is visible through each of the eight octahedral faces of the diamond host. We have never encountered anything like this unique diamond crystal, nor does the literature on diamonds contain any such descriptions of similar phantoms.

*John I. Koivula and Nathan Renfro
GIA, Carlsbad*



Gem Granitic Pegmatites

Granitic pegmatites have long attracted attention as important sources of valuable minerals and gems (table 1), while also representing somewhat of a conundrum for geoscientists trying to understand their geological origin. Occurring in various parts of the world, they are significant producers of gem tourmaline, beryl, spodumene, topaz, and garnet (figure 1; Simmons et al., 2012) along with mineral specimens. They are also valuable sources of bulk industrial products such as quartz, feldspar, mica, and columbite-tantalite ores (e.g., coltan). For more than a century, pegmatites have been the focus of scientific studies to better understand the geological conditions of their formation and the reasons for their diverse mineralogy, rock texture, and overall structure.

The renowned French mineralogist René-Just Haüy (1823, p. 536) defined the word *pegmatite* as “*feldspath*

laminaire avec cristaux de quartz enclaves” (laminar feldspar with enclosed quartz crystals), using it as a rock textural term and as a synonym to describe igneous rocks that displayed a pronounced intergrowth of tabular or skeletal quartz crystals in a feldspar host—rocks that up until then were often referred to as “graphic granite.”

According to London (2008, p. 4), the name *pegmatite* comes from the Homeric Greek word *πήγνυμι* (*pēgnymi*), which means “to bind or to fasten together.” Again its use was related to describing graphic granite, where the pattern of darker glassy quartz crystals embedded in a lighter perthitic feldspar host could vaguely resemble ancient written characters.

Austrian mineralogist Wilhelm Karl von Haidinger (1845, p. 585) first used the term *pegmatite* in its present

TABLE 1. Common and less common granitic pegmatite minerals, as well as those mined industrially as bulk products.

Common	Less common		Industrial
Amblygonite-montebrazite	Amazonite	Jeremejevite	Beryl
Apatite	Bertrandite	Kyanite	Cassiterite
Beryl	Beryllonite	Lithiophilite-triphyllite	Clay
Chrysoberyl	Brazilianite	Monazite	Columbite-tantalite
Feldspar	Columbite-tantalite	Petalite	Feldspar
Garnet	Danburite	Pezzottaite	Mica
Quartz	Epidote	Phenakite	Monazite
Spodumene	Euclase	Pollucite	Pollucite
Topaz	Eudialyte	Rhodizite	Quartz
Tourmaline	Fluorite	Scapolite	Spodumene
Zircon	Hambergite	Sodalite	
	Herderite	Sphene	



Figure 2. Exposed cross section of a zoned pegmatite dike consisting of large tan K-feldspar crystals below a central white quartz core; a mixture of Na-feldspar, quartz, and tourmaline grains above the core; and banded fine-grained minerals (known as “line rock”) along the base. This photo was captured in 1979 at the San Diego mine near Mesa Grande in San Diego County, California. Courtesy of David London.



Figure 4. A large sapphire crystal in a syenitic pegmatite host rock from Pegmatite 298 in the Ilmen Mountains mineralogical reserve, Ural Mountains, Russia. Photo by Peter Lyckberg; courtesy of the Ilmen Mineralogical Museum.

common minerals (mainly quartz, alkali feldspar, and mica; see figures 2 and 3) that are sometimes accompanied by rare element-bearing minerals. Their bulk chemical compositions correspond closely to those of familiar non-pegmatitic plutonic igneous rocks. Within pegmatite bodies, the constituent minerals can span several orders of magnitude in size from small grains to large individual crystals (a much greater range of grain size than would be encountered in an ordinary granite). Pegmatites are note-

worthy for having produced some of the largest-known crystals—in particular microcline, quartz, mica, spodumene, and beryl—that have reportedly reached up to

Figure 3. A granitic pegmatite vein measuring 70 cm wide in the cogenetic Bohus granite at Lysekil in Bohuslän County, Sweden. The vein consists of quartz, feldspars, muscovite, and accessory garnet. Photos by Peter Lyckberg.





Figure 5. The light-colored rock is the outcrop exposure of a cross section of the westward-dipping Stewart pegmatite dike, located north of the small town of Pala in northern San Diego County, California. Photo by James E. Shigley.

10 meters or more in length (Rickwood, 1981). As implied by the early definitions of nineteenth-century scientists, one of the most unique textural features of granitic pegmatites is the intergrowth of quartz and feldspar crystals mentioned above as “graphic granite.”

Basic, intermediate, and alkaline igneous rocks can sometimes also display similar pegmatitic textures. They include pegmatitic gabbro, syenite, and nepheline syenite, all of which are composed of minerals such as pyroxene, plagioclase feldspar, mica, olivine, hornblende, and nepheline. Figure 4 illustrates a large corundum (sapphire) crystal embedded in a syenitic pegmatite from the Ilmen Mountains in Russia.

Structure. Pegmatites exhibit a diverse variety of shapes, sizes, and internal structures. They can occur as narrow dikes (figure 5), sills, veins, or more oval-shaped bodies found within larger parental intrusive igneous host rocks.

They can also extend outward as veins within other surrounding metamorphic or igneous host rocks. Often minor in size compared to the enclosing rocks, they are centimeters to meters or more across and less than a meter up to a kilometer or more in length (figure 6). The pegmatite edges are often marked by distinct boundaries. Multiple pegmatite dikes may occur within the same host rock.

In terms of internal structure, they fall into two categories. The majority are referred to as simple pegmatites, which are more homogeneous in mineralogy—they lack any internal mineral zoning and are composed of the same common minerals found in other silica-rich igneous rocks like granites. Their main difference from the host rocks is their coarser grain size.

Complex pegmatites are composed of these same minerals, often along with rare and unusual minerals (such as beryl, tourmaline, and many others). They display an inhomogeneous texture with several layered, vertical, or



Figure 6. Underground exposure of the Dada pegmatite at the Pederneira mine near Governador Valadares, Minas Gerais, Brazil, showing black crystals of schorl tourmaline along with other minerals. Photo by Andrea Dini; courtesy of Federico Pezzotta.



Figure 7. Open pockets along the core zone of the Havey pegmatite near Poland, Androscoggin County, Maine, in June 2017. Courtesy of William (Skip) Simmons.

concentric internal zones of different minerals and mineral grain sizes, and central zones that may contain open crystal-filled cavities (figure 7). Grain size generally increases inward from the margins toward the center of the pegmatite body. Concentric zoning is typical in an oval-shaped body, while internal zoning in a horizontal dike can be more asymmetric (figure 8). Distinct zonation is typically better developed and more evident in larger pegmatites because of the opportunity for greater differentiation of the residual magma and fluids during magma crystallization. Again, internal zones form from the outer edge inward, with the core being the final zone to solidify from the magmatic fluid.

In a complex pegmatite, internal zones can often be recognized by increasing mineral grain size, but they can vary in thickness and mineral composition. From the outside inward, the zones follow this sequence:

- A thin border zone where the pegmatite magma came into contact with the preexisting host rock
- A thicker wall zone consisting of feldspar and quartz
- An intermediate zone that is richer in feldspar and contains occasional crystal-lined cavities
- A core zone consisting of massive quartz and occasional crystal-lined cavities

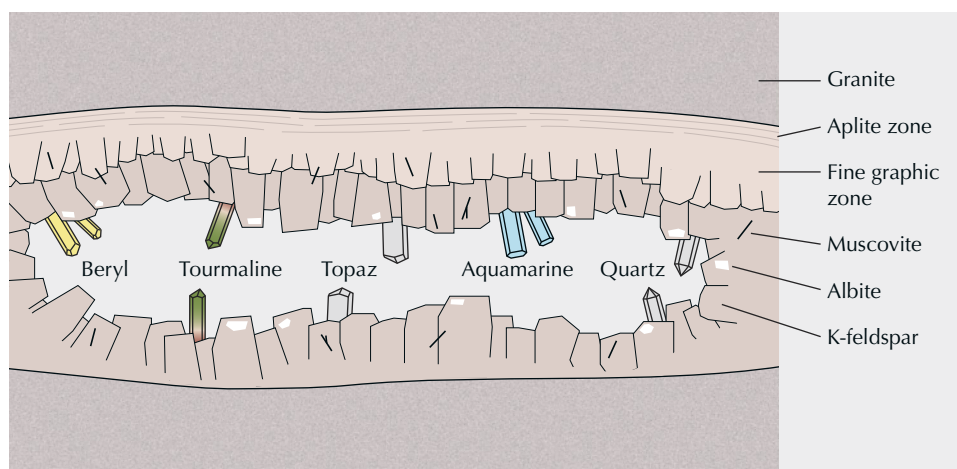


Figure 8. Simplified diagram of an internally zoned pegmatite dike.

Pegmatite Formation

The occurrence, mineralogy, texture, and structure of pegmatites have long attracted the attention of geoscientists, who have shared various theories of origin (Jahns, 1955). While scientific discussions of pegmatites date from the late 1800s, modern studies originated from several past interrelated trends:

- The laboratory studies of fractional crystallization in igneous magmas pioneered by Bowen at the Geophysical Laboratory of the Carnegie Institution of Science in Washington, DC, from 1912 to 1937. His 1928 book entitled *The Evolution of the Igneous Rocks* provided the geochemical and geophysical foundation for the petrological study of igneous rocks and minerals and their conditions of formation. London (1992 and 2008) summarized past ideas and more recent experimental work on granitic pegmatite formation by his group and other researchers.
- The wealth of valuable minerals found in pegmatites in Madagascar that were described in detail by Lacroix based on his visit to the island in 1911 (Lacroix, 1922a,b, 1923).
- The description of the extensive occurrences of nepheline syenite pegmatites in southern Norway by Brögger (1890; also Müller et al., 2017).
- The field studies of pegmatite occurrences in Brazil, the United States, and elsewhere undertaken in the 1940s and 1950s to document the occurrence of rare elements such as tantalum in demand for industrial use during and after World War II (Johnston, 1945; Hanley et al., 1950; Page et al., 1953; Cameron et al., 1954; Jahns, 1955).

Most granitic pegmatites form relatively close to the earth's surface, and they occur either within or near the upper portions of a genetically related larger body of igneous parent rock called a pluton. The magmas that might eventually produce pegmatite bodies were generated by the melting of crustal rocks and pluton formation in two different geological settings. The first—referred to as orogenic magmas—formed during the compressive collision of crustal plates, which created mountain chains along the collision boundaries. The magmas formed along the collision zone produced granitic rocks that comprise a large proportion of the currently exposed crustal surface. The second—called anorogenic magmas—formed during the stretching and thinning of crustal plates that are being pulled apart. The shallow underlying presence of a volume of heated mantle causes melting and magma formation within the extended overlying portion of the plate. The variety of igneous rocks produced by these anorogenic magmas are more restricted in occurrence as sources of gem-bearing pegmatites. Some so-called anatectic pegmatites appear to have formed by the melting of metamorphic parent rocks since they have no obvious connection to an igneous pluton.

Based on field observations and experimental studies, granitic pegmatites are believed to have crystallized in the continental crust from relatively small volumes of a separate residual hydrous- and volatile-rich magmatic fluid fraction that remained during the solidification of a larger granitic magma body. During the final stages of pegmatite formation, this magmatic fluid is thought to have coexisted in small volumes with the residual pegmatitic magma. Pegmatite evolution and final crystallization involves a series of processes including fractional crystallization of minerals, immiscibility within the residual melt, the increasing influence on mineral formation of alkali and halogen contents and enrichment of so-called incompatible elements (i.e., rare earth elements (REE), tantalum, niobium, lithium, and beryllium), and the exsolution of a hydrothermal aqueous fluid phase (Pauly et al., 2021).

The bulk compositions of pegmatites are similar to the compositions of the magmas from which they form. Whether or not a particular granitic magma will generate pegmatites depends in large part on the needed presence of chemical components such as boron, phosphorus, and fluorine as well as excess amounts of water in the magma (Černý et al., 2012). The model of granitic pegmatite formation described by Jahns and Burnham (1969) envisioned the transition from granite to pegmatite formation being marked by the exsolution of an aqueous fluid from the silicate melt and the partitioning of chemical components between these two phases. Subsequent experimental work on pegmatite mineral systems and studies of the compositions of fluid inclusions in late-stage pegmatite minerals have brought some concepts of this genesis model into question.

When this residual hydrous magmatic fluid forms within the cooling granitic pluton itself or is injected into fractures in the surrounding country rock, minerals begin to crystallize within the pegmatite body as temperatures decrease from the outside inward in a relatively static geological environment. The rapid cooling combined with the low residual heat content results in limited chemical interactions between the magmatic fluid and the surrounding host rocks (Černý et al., 2012).

Within the host granite, simple internally homogeneous pegmatites form from a trapped volume of the residual magma with a similar mineralogy, but they can display large variations in texture and mineral grain size. These rock bodies are often composed of approximately 65% alkali feldspar, 25% quartz, 5–10% mica, and about 5% other accessory minerals (Glover et al., 2012). They often lack rare ore minerals, but they are significant sources of common minerals such as feldspar. They are thought to represent a transition stage of magma crystallization between granites and rare-element pegmatites.

In contrast, complex pegmatites crystallize with the same bulk minerals but a more complicated internal structure and a more varied chemical and mineral composition. They crystallize from the outside contacts inward in the form of concentric or layered zones that often have different

mineral assemblages and/or textures, sometimes ending with an almost monomineralic central quartz core (Norton, 1983). As crystallization proceeds, the chemical composition of this fluid fraction progressively evolves as solidifying minerals remove certain elements from, and other elements are concentrated in, the decreasing remaining fluid, which then allows new minerals to form.

These evolving residual magmatic fluids become enriched in volatile components and trace elements (water as hydroxyl (OH⁻)) and rare elements (such as lithium, beryllium, boron, fluorine, phosphorus, rubidium, zirconium, niobium, cesium, and tantalum) that are not incorporated for the most part in common minerals such as feldspar and quartz in earlier-forming igneous rocks. This rare-element fractionation and chemical enrichment result in the formation of a host of uncommon minerals in these complex pegmatites which are rarely, if ever, found in such abundance in other geological settings (thought to be more than 500 mineral species; Menzies and Scovil, 2022). The diversity has long attracted the attention of both geoscientists and mineral collectors.

In comparison to the initial silica-rich granitic magma, the residual mineralized aqueous fluid within the pegmatite body has a lower viscosity and melting point due to the increased presence of fluxing agents. At the lower temperatures of this stage of pegmatite formation, geologists believe that the rate of nucleation of tiny new crystals is slower than the rate of crystal growth, which tends to favor the growth of fewer but larger crystals. When trapped within the central core zone of a crystallizing pegmatite, isolated volumes of this increasingly water-rich fluid allow for the formation of one or more generations of well-formed, larger-size gem-quality crystals within open

crystal-lined spaces or cavities as the final stage of crystallization. Recent work suggests that during this stage, crystal growth rates could have accelerated dramatically from millimeters to a meter or more per day (Phelps et al., 2020). Subsequent alteration and weathering of pegmatite feldspars and micas resulted in the formation of secondary clays, which often completely fill any remaining open space in the cavities and coat any crystals. These so-called miarolitic pegmatites occur within or near magmatic plutons that intruded to shallow depths in the crust; occasionally, they can also be found in migmatite terrain in anatectic pegmatites (Webber et al., 2019).

This diversity of size, occurrence, internal structure, rock texture, and mineralogy found in pegmatites presents challenges for geoscientists trying to unravel the story of these fascinating igneous rocks. The variety of pegmatite occurrences suggests that other geological processes may on occasion be involved in their formation beyond the volatile-rich magma crystallization model summarized above.

Pegmatite Classification

The diversity of the more complex granitic pegmatites observed in the field has led geologists to propose various schemes to classify them based on features such as mineralogy, geochemistry, texture, shape, size, and/or relationship to host rocks. The trace element signatures of most rare-element pegmatites (containing elements such as lithium, beryllium, boron, niobium, yttrium, fluorine, and others) allow them to be grouped into two distinctive families, with occurrences of so-called lithium-cesium-tantalum (LCT) granitic pegmatites greatly outnumbering those of the niobium-yttrium-fluorine

TABLE 2. Examples of pegmatites mined for bulk industrial minerals.

Mine	Location	Ore minerals	References
Harding	New Mexico, United States	Lepidolite, microlite, spodumene, tantalite-columbite	Jahns and Ewing (1977)
Black Hills area	South Dakota, United States	Beryl, feldspar, mica, spodumene	Page et al. (1953)
Tanco	Manitoba, Canada	Pollucite, spodumene, tantalite-columbite	Crouse and Černý (1972)
Kolmozero	Kola Peninsula, Russia	Rare earth minerals, spodumene	Propachkin et al. (2022)
Greenbushes	Western Australia, Australia	Cassiterite, spodumene, tantalite-columbite	Partington et al. (1995)
Koktokay area	Xinjiang, China	Beryl, lepidolite, pollucite, spodumene, tantalite-columbite	Zhou et al. (2015)



Figure 9. Large microcline crystal with smoky quartz, albite feldspar, and tourmaline from the Oceanview mine near Pala in San Diego County, California. The specimen measures $46 \times 30 \times 30$ cm and the microcline crystal $25 \times 25 \times 13$ cm. Photo by Mimi Travis.

(NYF) family. For further discussion, see Černý and Ercit, 2005, and Černý et al., 2012. This classification scheme reflects the increasing complexity of internal zones and the chemical evolution of the pegmatite-forming magmas with distance from their source (London, 2008).

Economic Importance

Industrial Minerals. Although of lesser volumetric importance than other crustal igneous rocks, pegmatite bodies and dikes are major sources of both common and rare minerals. Hence, they are the focus of mineral collecting, as well as mining activities on both small and large scales, in various parts of the world.

Most pegmatites have a simple granitic composition and mineralogy, and their mining focuses on recovering feldspar, quartz, mica, beryl, and spodumene as well as certain high-value ore minerals (Glover et al., 2012). The overall chemical purity of these minerals and the very high percentage of mineable rock at a deposit make granitic pegmatites important mining targets. Several examples of localities mined for industrial minerals and for gem crystals are listed in tables 2 and 3, respectively.

Industrial minerals such as feldspar and quartz are mined in very large quantities. Once excavated and transported, the crushed ore is washed and then separated into specific minerals by various physical, electrical, magnetic, or flotation techniques. These mineral concentrates can then be further processed into particular chemical compounds depending on the final applications for the material, such as Li_2O from bulk spodumene or petalite (Pripachkin et al., 2022; Kundu et al., 2023; Roy et al., 2023) and Ta_2O_3 from tantalite (Melcher et al., 2017a,b). These bulk materials have important industrial uses, such as in the glass and ceramic industries in the case of feldspar (figure 9).

Gems and Mineral Specimens. The conditions of granitic pegmatite formation result in several chemical elements occurring at much higher concentrations than in most other igneous rocks. In some situations, these concentrations are sufficient to allow these rare elements to occur as major constituents in distinct minerals (e.g., pollucite, a cesium aluminosilicate zeolite).

Some of the finest gem crystals and specimens from the mineral kingdom originate mainly and sometimes solely from complex, internally zoned pegmatites (Simmons et al., 2012). These gem minerals occur most often in open

Figure 10. Underground exposure of a subhorizontal pegmatite dike at the San Diego mine near Mesa Grande in San Diego County, California, in 1986. Several open pockets, from which the contents have been removed, extend along the central portion of the dike, which is about 2 meters across from top to bottom. Courtesy of David London.



TABLE 3. Pegmatite areas mined for gem minerals.

Country	Area (province, state, or region)	Gem minerals
Afghanistan	Kunar, Nuristan	Beryl, garnet, spodumene, topaz, tourmaline
Brazil	Minas Gerais	Amblygonite, beryl, brazilianite, chrysoberyl, euclase, quartz, spodumene, topaz, tourmaline
Brazil	Paraíba, Rio Grande do Norte	Beryl, euclase, garnet, quartz, tourmaline
China	Xinjiang Uygur	Beryl, tourmaline
China	Yunnan	Beryl, garnet, tourmaline
Democratic Republic of the Congo	Katanga, North Kivu	Tourmaline
Finland	South Karelia	Beryl, tourmaline
India	Tamil Nadu	Beryl
Italy	Elba	Pollucite, tourmaline
Kenya	Coast	Tourmaline
Madagascar	Antananarivo, Fianarantsoa, Toamasina	Beryl, danburite, feldspar, garnet, phenakite, spodumene, tourmaline
Mozambique	Nampula, Tete, Zambezia	Beryl, garnet, quartz, spodumene, topaz, tourmaline
Myanmar (Burma)	Mogok, Momeik	Petalite, phenakite, pollucite, tourmaline
Namibia	Erongo	Beryl, topaz, tourmaline
Nigeria	Edo, Kaduna, Kwara, Nasarawa, Oyo, Plateau	Beryl, chrysoberyl, garnet, phenakite, spodumene, topaz, tourmaline
Pakistan	Gilgit-Baltistan	Beryl, garnet, spodumene, topaz, tourmaline
Russia	Ural Mountains	Beryl, chrysoberyl, topaz
Russia	Transbaikalia	Beryl, danburite, garnet, pollucite, topaz, tourmaline
Tanzania	Arusha, Morogoro, Tanga	Garnet, tourmaline
Ukraine	Zhytomyr	Beryl, topaz
Vietnam	Yen Bai	Feldspar, tourmaline
United States	California	Beryl, garnet, spodumene, topaz, tourmaline
United States	Colorado	Beryl, feldspar, quartz, phenakite
United States	Connecticut, Maine, New Hampshire	Beryl, pollucite, tourmaline
Zambia	Central, Eastern	Beryl, garnet, tourmaline
Zimbabwe	Mashonaland West	Beryl, topaz, tourmaline

References: Agheem et al. (2014), Bowersox and Chamberlin (1995), Cassedanne and Philipoo (2015), Clifford et al. (2011), Cornejo and Bartorelli (2010), de Brito-Barreto and Bretas-Bittar (2010), Falster et al. (2002), Groat et al. (2007), London (2008), Menzies (1995), Menzies and Scovil (2022), Pezzotta (2001), Shigley et al. (2010)



Figure 11. Colored tourmaline crystals embedded in secondary clay minerals in a pocket at the Havey pegmatite near Poland, Androscoggin County, Maine, in July 2018. Courtesy of William (Skip) Simmons.



Figure 12. Daron Fisler in 2010 with a spodumene (kunzite) crystal he extracted from the Big Kahuna pocket at the Oceanview mine, Pala District, San Diego County, California. Photo by Mark Mauthner.

(or clay-filled) pockets in the core and central zones of the pegmatite body (figure 10). With diameters typically from centimeters to a meter or more, these pockets are more easily located in a thinner pegmatite dike but can be difficult to find in a thicker one.

Although pockets are normally encountered in the central zones of a pegmatite, their occurrence within that zone is often random and highly variable. Blasting, drilling, or breaking up the pegmatite body risks damaging valuable gem crystals, which influences the mining techniques used. Miners often look for minerals or rock textures as indicators of a nearby gem pocket. For example, one good indicator is the presence of lepidolite mica (many others are discussed by Menzies and

Scovil, 2022). Miners have noted that pockets tend to occur where pegmatite dikes increase in thickness, change direction, or intersect. Such locations may have facilitated the formation of residual aqueous fluids. Nearby pockets can contain similar or very different gem minerals. Several stages of mineral formation may also be evident, and the distribution of mineral contents within pockets can be nonuniform. Some gem crystals show evidence of corrosion, partial dissolution, and mineral replacement.

These pockets are often filled partially or completely with secondary clays (figure 11), so miners use a pointed hand tool such as a screwdriver to gently probe the clay to detect if crystals are present (figures 12 and 13). Once a

Figure 13. A 1.437 kg (7,185 ct) gem beryl crystal in situ in albite inside a giant heliodor pocket of Pegmatite 521. The crystal was found at a depth of 96 m in one of the Volyn chamber pegmatites in the Korosten Pluton near Volodarsk (now Khoroshiv), Zhytomyr Oblast, Ukraine. Photos by Peter Lyckberg.



pocket is located, the contents are carefully removed by hand, and the clay-coated crystals are washed—only then does the miner know what exactly has been found. Crystals may still be attached to the pocket walls or lie as broken pieces on the pocket floor. Besides recovering individual gem crystals, efforts are made to extract attractive rock matrix specimens with the crystals still attached. Careful trimming and cleaning of matrix pocket specimens are often required.

Field-tested remote sensing techniques, such as ground-penetrating radar, can sometimes reveal the presence of an open cavity in a pegmatite body (Patterson and Cook, 2002; Cardoso-Fernandes et al., 2019). The article by Steiner (2019) discusses useful techniques for locating gem pegmatites. Pegmatite mining techniques vary in scale and sophistica-

tion depending on the type of occurrence, with work in many countries carried out by artisanal mining operations.

Summary

Despite their typical small volumetric size, granitic pegmatites represent one of the most important producers of gem crystals along with both common and rare minerals (figure 14). Their varied mineralogy, external shape and internal texture, and widespread occurrence continue to attract the attention of geoscientists seeking to understand the geologic conditions of their formation. They continue to be found and mined wherever granite bodies are exposed at the earth's surface, and they remain a major source of a number of valuable gem minerals.

Figure 14. The “King of Kashmir” aquamarine crystal group, measuring 45 cm tall and 80 cm wide, was collected in 2019 from a miarolitic pegmatite dike in the remote Nyet Bruk region of the Skardu District in northern Pakistan (Trinchillo, 2020). It is considered by many to be one of the most significant gem mineral specimens found in the modern era. Photo by James Elliott/Fine Minerals International; courtesy of Daniel Trinchillo.



ACKNOWLEDGMENTS

The authors thank David London, Peter Lyckberg, Mark Mauthner, Federica Pezzotta, William (Skip) Simmons, Daniel Trinchillo, and Michael Wise for providing photographs for possible use in this article.

REFERENCES

- Agheem M.H., Shah M.T., Khan T., Murata M., Arif M., Dars H. (2014) Shigar Valley gemstones, their chemical composition and origin, Skardu, Gilgit-Baltistan, Pakistan. *Arabian Journal of Geosciences*, Vol. 7, No. 9, pp. 3801–3814, <http://dx.doi.org/10.1007/s12517-013-1045-8>
- Bowen N.L. (1928) *The Evolution of the Igneous Rocks*. Princeton University Press, Princeton, New Jersey, 334 pp.
- Bowersox G.W., Chamberlin B.E. (1995) *Gemstones of Afghanistan*. Geoscience Press, Totnes, United Kingdom, 220 pp.
- Brögger W.C. (1890) Die Mineralien der Syenitpegmatitgänge der süd-norwegischen Augit-und Nephelinsyenite. *Zeitschrift für Kristallographie und Mineralogie*, Vol. 16, pp. 1–658.
- Cameron E.N., Jahns R.H., McNair A.H., Page L.R. (1949) Internal Structure of Granitic Pegmatites. *Economic Geology Monograph Series*, No. 2, Society of Economic Geologists, Urbana, Illinois, 115 pp., <http://dx.doi.org/10.5382/Mono.02>
- Cameron E.N., Larrabee D.M., McNair A.H., Page J.J., Stewart G.W., Shainin V.E. (1954) Pegmatite Investigations 1942–45 New England. United States Geological Survey Professional Paper No. 255, 352 pp., <http://dx.doi.org/10.3133/pp255>
- Cardoso-Fernandes J., Teodoro A.C., Lima A. (2019) Remote sensing data in lithium (Li) exploration: A new approach for the detection of Li-bearing pegmatites. *International Journal of Applied Earth Observation and Geoinformation*, Vol. 76, pp. 10–25, <https://doi.org/10.1016/j.jag.2018.11.001>
- Cassedanne J., Philipoo S. (2015) *Mineral and Gem Deposits of the Eastern Brazilian Pegmatites*, Musée National d'Histoire Naturelle, Luxembourg, 671 pp.
- Černý P. (1982) *Short Course in Granitic Pegmatites in Science and Industry*. Mineralogical Association of Canada, No. 8, 555 pp.
- Černý P., Ercit T.S. (2005) The classification of granitic pegmatites revisited. *Canadian Mineralogist*, Vol. 43, No. 6, pp. 2005–2026, <http://dx.doi.org/10.2113/gscanmin.43.6.2005>
- Černý P., London D., Novák M. (2012) Granitic pegmatites as reflections of their sources. *Elements*, Vol. 8, No. 4, pp. 289–294, <http://dx.doi.org/10.2113/gselements.8.4.289>
- Clifford J., Falster A.U., Hanson S., Liebetrau S., Neumeier G., Staebler G., Eds. (2011) *Topaz: Perfect Cleavage*. extraLapis English No. 14, Lithographie LLC, Denver, Colorado, 104 pp.
- Cornejo C., Bartorelli A. (2010) *Minerals and Precious Stones of Brazil*. Solaris Cultural Publications, São Paulo, Brazil, 704 pp.
- Crouse R.A., Černý P. (1972) The Tanco pegmatite at Bernic Lake, Manitoba; I. Geology and paragenesis. *Canadian Mineralogist*, Vol. 11, No. 3, pp. 591–608.
- de Brito Barreto S., Bretas Bittar S.M. (2010) The gemstone deposits of Brazil: Occurrences, production, and economic impact. *Boletín de la Sociedad Geológica Mexicana*, Vol. 62, No. 1, pp. 123–140.
- Dill H.G. (2015) Pegmatites and aplites: Their genetic and applied ore geology. *Ore Geology Reviews*, Vol. 69, pp. 417–561, <http://dx.doi.org/10.1016/j.oregeorev.2015.02.022>
- (2016) The CMS classification scheme (chemical composition – mineral assemblage – structural geology) - linking geology to mineralogy of pegmatitic and aplitic rocks. *Neues Jahrbuch für Mineralogie Abhandlungen*, Vol. 193, No. 3, pp. 231–263, <http://dx.doi.org/10.1127/njma/2016/0304>
- Falster A.U., Jarnot M.D., Neumeier G.A., Simmons W., Staebler G.A., Eds. (2002) *Tourmaline: The Gemstone Spectrum*. extraLapis English No. 3, Lapis International, Denver, Colorado, 106 pp.
- Glover A.S., Rogers W.Z., Barton J.E. (2012) Granitic pegmatites: Storehouses of industrial minerals. *Elements*, Vol. 8, No. 4, pp. 269–273, <http://dx.doi.org/10.2113/gselements.8.4.269>
- Groat L.A., Ed. (2007) *Geology of Gem Deposits*. Mineralogical Association of Canada, Short Course Volume 37, 288 pp.
- Hanley J.B., Heinrich E.W.M., Page L.R. (1950) Pegmatite investigations in Colorado, Wyoming and Utah, 1942–1944. United States Geological Survey Professional Paper, No. 227, 134 pp.
- Haüy R-J. (1823) *Traite de Minéralogie*, 2nd Edition, Vol. 4, Librairie Bachelier, Quai des Grands-Augustins, Paris, France, 604 pp.
- Jahns R.H. (1955) The study of pegmatites deposits. *Economic Geology, Fiftieth Anniversary Volume*, pp. 1026–1130, <http://dx.doi.org/10.5382/AV50.25>
- Jahns R.H., Burnham C.W. (1969) Experimental studies of pegmatite genesis; I, A model for the derivation and crystallization of granitic pegmatites. *Economic Geology*, Vol. 64, No. 8, pp. 843–864, <http://dx.doi.org/10.2113/gsecongeo.64.8.843>
- Jahns R.H., Ewing R.C. (1977) The Harding mine, Taos County, New Mexico. *Mineralogical Record*, Vol. 8, No. 2, pp. 115–126.
- Johnston W.D. (1945) Beryl-tantalite pegmatites of northeastern Brazil. *Geological Society of America Bulletin*, Vol. 56, No. 11, pp. 1015–1070, [http://dx.doi.org/10.1130/0016-7606\(1945\)56\[1015:BPONB\]2.0.CO;2](http://dx.doi.org/10.1130/0016-7606(1945)56[1015:BPONB]2.0.CO;2)
- Kundu T., Rath S.S., Das S.K., Parhi P.K., Angadi S.I. (2023) Recovery of lithium from spodumene-bearing pegmatites: A comprehensive review on geological reserves, beneficiation, and extraction. *Powder Technology*, Vol. 415, article no. 118142, <http://dx.doi.org/10.1016/j.powtec.2022.118142>
- Lacroix A. (1922a) *Minéralogie de Madagascar*, Vol. 1. A. Challengel, Paris, 624 pp.
- (1922b) *Minéralogie de Madagascar*, Vol. 2. A. Challengel, Paris, 694 pp.
- (1923) *Minéralogie de Madagascar*, Vol. 3. A. Challengel, Paris, 450 pp.
- Landes K.K. (1933) Origin and classification of pegmatites. *American Mineralogist*, Vol. 18, No. 2-3, pp. 33–56 and 95–103.
- London D. (1992) The application of experimental petrology to the genesis and crystallization of granitic pegmatites. *Canadian Mineralogist*, Vol. 30, No. 3, pp. 499–540.
- (2008) *Pegmatites*. Canadian Mineralogist, Special Publication No. 10, Mineralogical Association of Canada, Quebec, 347 pp.
- Melcher F., Graupner T., Oberthür T., Schütte P. (2017a) Tantalum-(niobium-tin) mineralisation in pegmatites and rare-metal granites of Africa. *South African Journal of Geology*, Vol. 120, No. 1, pp. 77–100, <http://dx.doi.org/10.25131/gssaig.120.1.77>
- Melcher F., Graupner T., Gäbler H-E., Sitnikova M., Oberthür T., Gerdes A., Badanina E., Chudy T. (2017b) Mineralogical and chemical evolution of tantalum-(niobium-tin) mineralisation in pegmatites and granites. Part 2: Worldwide examples (excluding Africa) and an overview of global metallogenetic patterns. *Ore Geology Reviews*, Vol. 89, pp. 946–987, <http://dx.doi.org/10.1016/j.oregeorev.2016.03.014>
- Menzies M.A. (1995) The mineralogy, geology, and occurrence of topaz. *Mineralogical Record*, Vol. 26, No. 1, pp. 5–53.
- Menzies M., Scovil J. (2022) *Pegmatites and Their Gem Minerals*, Canadian Mineralogist, Special Publication No. 15, Mineralogical Association of Canada, Quebec, 616 pp.
- Müller A., Romer R.L., Pedersen R-B. (2017) The Sveconorwegian pegmatite province – Thousands of pegmatites without

- parental granites. *Canadian Mineralogist*, Vol. 55, No. 2, pp. 283–315, <http://dx.doi.org/10.3749/canmin.1600075>
- Norton J.J. (1983) Sequence of mineral assemblages in differentiated granitic pegmatites. *Economic Geology*, Vol. 78, No. 5, pp. 854–874, <http://dx.doi.org/10.2113/gsecongeo.78.5.854>
- Page L.R. et al. (1953) *Pegmatite Investigations 1942–1945 Black Hills, South Dakota*. United States Geological Survey Professional Paper, No. 247, 237 pp.
- Partington G.A., McNaughton N.J., Williams I.S. (1995) A review of the geology, mineralogy and geochronology of the Greenbushes pegmatite, Western Australia. *Economic Geology*, Vol. 90, No. 3, pp. 616–635, <http://dx.doi.org/10.2113/gsecongeo.90.3.616>
- Patterson J.E., Cook F.A. (2002) Successful application of ground-penetrating radar in the exploration of gem tourmaline pegmatites of Southern California. *Geophysical Prospecting*, Vol. 50, No. 2, pp. 107–117, <http://dx.doi.org/10.1046/j.1365-2478.2002.00312.x>
- Pauly C., Gysi A.P., Pfaff K., Merkel I. (2021) Beryl as an indicator of metasomatic processes in the California Blue Mine topaz-beryl pegmatite and associated miarolitic pockets. *Lithos*, Vol. 404–405, article no. 106485, <http://dx.doi.org/10.1016/j.lithos.2021.106485>
- Pezzotta F. (2001) *Madagascar: A Mineral and Gemstone Paradise*. extraLapis English No. 1, Lithographie LLC, Denver, Colorado, 98 pp.
- Phelps P.R., Lee C.T.A., Morton D.M. (2020) Episodes of fast crystal growth in pegmatites. *Nature Communications*, Vol. 11, article no. 4986.
- Pripachkin P.V., Kudryashov N.M., Rundkvist T.V., Morozova L.N. (2022) Lithium in pegmatites of the Fennoscandian Shield and operation prospects for the Kolmozero deposit on the Kola Peninsula (Russia). *Applied Earth Science*, Vol. 131, No. 4, pp. 179–192, <http://dx.doi.org/10.1080/25726838.2022.2089966>
- Rickwood P.C. (1981) The largest crystals. *American Mineralogist*, Vol. 66, No. 9–10, pp. 885–907.
- Roy T., Plante B., Benzaazoua M., Demers I. (2023) Geochemistry and mineralogy of a spodumene-pegmatite lithium ore at various mineral beneficiation stages. *Minerals Engineering*, Vol. 202, article no. 108312, <http://dx.doi.org/10.1016/j.mineng.2023.108312>
- Shigley J.E., Laurs B.M., Janse A.J.A., Elen S., Dirlam D. (2010) Gem Localities of the 2000s. *G&G*, Vol. 46, No. 3, pp. 188–216, <http://dx.doi.org/10.5741/GEMS.46.3.188>
- Simmons W.B., Pezzotta F., Shigley J.E., Beurlen H. (2012) Granitic pegmatites as sources of colored gemstones. *Elements*, Vol. 8, No. 4, pp. 281–287, <http://dx.doi.org/10.2113/gselements.8.4.281>
- Simmons W.B., Webber K.L. (2008) Pegmatite genesis: State of the art. *European Journal of Mineralogy*, Vol. 20, No. 4, pp. 421–438, <http://dx.doi.org/10.1127/0935-1221/2008/0020-1833>
- Simmons W.B., Webber K.L., Falster A.U., Roda-Robles E., Dallaire D.A. (2022) *Pegmatology: Pegmatite Mineralogy, Petrology and Petrogenesis*, Second Edition. Rubellite Press, Cana, Virginia, 287 pp.
- Steiner B.M. (2019) Tools and workflows for grassroots Li-Cs-Ta (LCT) pegmatite exploration. *Minerals*, Vol. 9, No. 8, article no. 499, <http://dx.doi.org/10.3390/min9080499>
- Trinchillo D. (2020) Collecting the King of Kashmir aquamarine. *Mineralogical Record*, Vol. 51, No. 6, pp. 755–779.
- von Haidinger W.K. (1845) *Handbuch der Bestimmenden Mineralogie*. Braumüller & Seidel Publishers, Vienna, Austria, 630 pp.
- Webber K.L., Simmons W.B., Falster A.U., Hanson S.L. (2019) Anatectic pegmatites of the Oxford County pegmatite field, Maine, USA. *Canadian Mineralogist*, Vol. 57, No. 5, pp. 811–815, <http://dx.doi.org/10.3749/canmin.AB00028>
- Zhou Q.F., Qin K.H., Tang D.M., Wang C.L., Tian Y., Sakyi P.A. (2015) Mineralogy of the Koktokay No. 3 pegmatite, Altai, NW China: Implications for evolution and melt–fluid processes of rare-metal pegmatites. *European Journal of Mineralogy*, Vol. 27, No. 3, pp. 433–457, <http://dx.doi.org/10.1127/ejm/2015/0027-2443>

For online access to all issues of GEMS & GEMOLOGY from 1934 to the present, visit:

gia.edu/gems-gemology



The Cutting Edge of Diamond Reporting.



GIA®

The most trusted diamond report, available in print or the GIA App.



Secure

An encrypted database protects your information.

Efficient

Worldwide access to diamond grading reports.

Trusted

The global standard for diamond grading, now at your fingertips.



©2025 Gemological Institute of America, Inc. (GIA). All trademarks are registered trademarks owned by GIA. GIA is a nonprofit 501(c)(3) organization. All rights reserved.



Contributing Editors

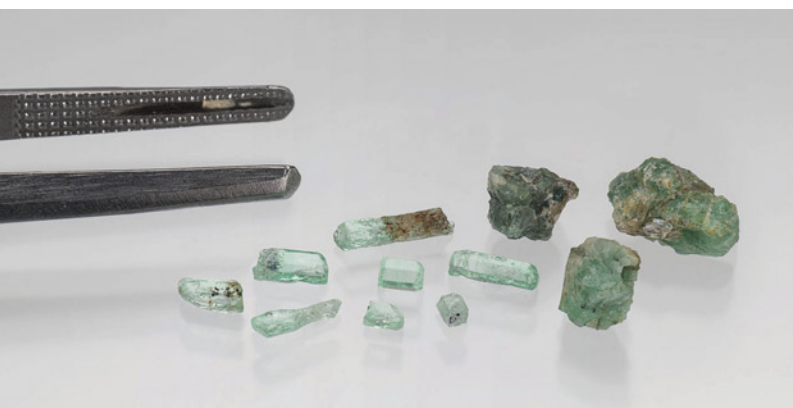
Gagan Choudhary, *IIGJ-Research & Laboratories Centre, Jaipur, India* (gagan.choudhary@iigjrlc.org)

Guanghai Shi, *School of Gemmology, China University of Geosciences, Beijing* (shigh@cugb.edu.cn)

COLORLED STONES AND ORGANIC MATERIALS

Emeralds and beryl from Kazakhstan and Ukraine. A set of emeralds and beryl from Kazakhstan and Ukraine were analyzed at GIA's Carlsbad laboratory as part of an ongoing beryl characterization research project. These stones were generously provided by Dr. Gerhard Franz of Technical University Berlin, and Dr. Oleksii Vyshnevskiy of Institute of Geochemistry, Mineralogy and Ore Formation, Ukraine.

Figure 1. Eight Kazakhstani emeralds (left) and three Ukrainian beryl and emerald samples (right), with gemological tweezers shown for scale. The leftmost Ukrainian emerald has a chemistry between that of aquamarine and emerald. Photo by Emily Lane; courtesy of Gerhard Franz and Oleksii Vyshnevskiy.



Editors' note: Interested contributors should contact gandgeditorial@gia.edu.

GEMS & GEMOLOGY, VOL. 61, No. 2, pp. 206–223.

© 2025 Gemological Institute of America

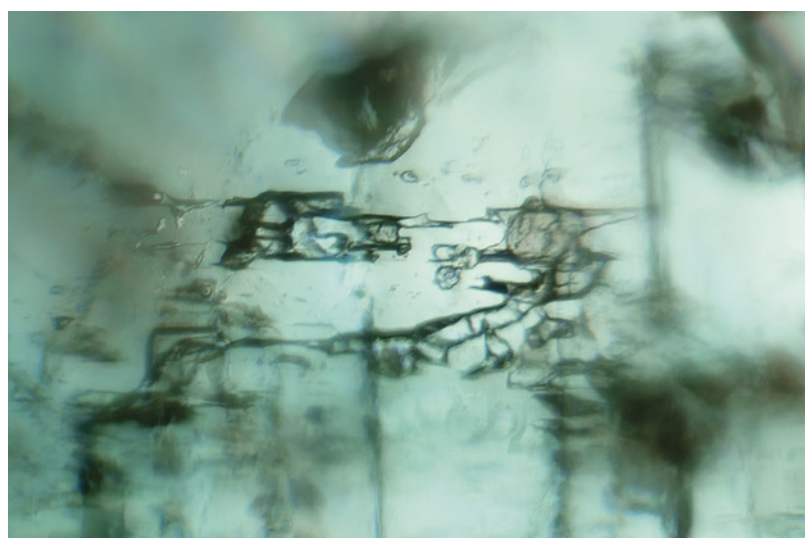


Figure 2. Fluid and two-phase jagged inclusions in a Kazakhstani emerald. Photomicrograph by Rhiana Elizabeth Henry; field of view 1.44 mm.

The study included eight euhedral samples of emerald from the Delbegetey locality in eastern Kazakhstan, and three anhedral beryl and emerald samples from Kruta Balka in southeast Ukraine (figure 1). The Kazakhstani emeralds were light green and had high clarity; they were nearly eye-clean, with small colorless or weakly colored fluid and two-phase inclusions (figure 2). Several had etching and stained surfaces at the base. Due to their high clarity and lively color, they were of gem quality, despite being quite small (only several millimeters in length). The Ukrainian emerald and beryl specimens were bright green and blue-green intergrown anhedral crystals with associated mica, appearing opaque as hand samples.

Chemical analysis by laser ablation–inductively coupled plasma–mass spectrometry (LA-ICP-MS; table 1) revealed distinct compositions based upon a few trace ele-

TABLE 1. Concentrations (in ppm) of significant trace elements in Kazakhstani and Ukrainian emerald and beryl, collected by LA-ICP-MS.

Locality	Mg	Fe	Li	Na	Cs	Cr	V
Kazakhstan	147–302	862–2060	28.7–92.5	316–659	28.7–355	260–716	128–1330
Ukraine	2000–4560	1080–2310	2950–4250	11400–13800	4240–8040	13.5–2000 ^a	4.26–26.2
Detection limits (in ppm)	0.05	2	0.04	2	0.03	0.4	0.02

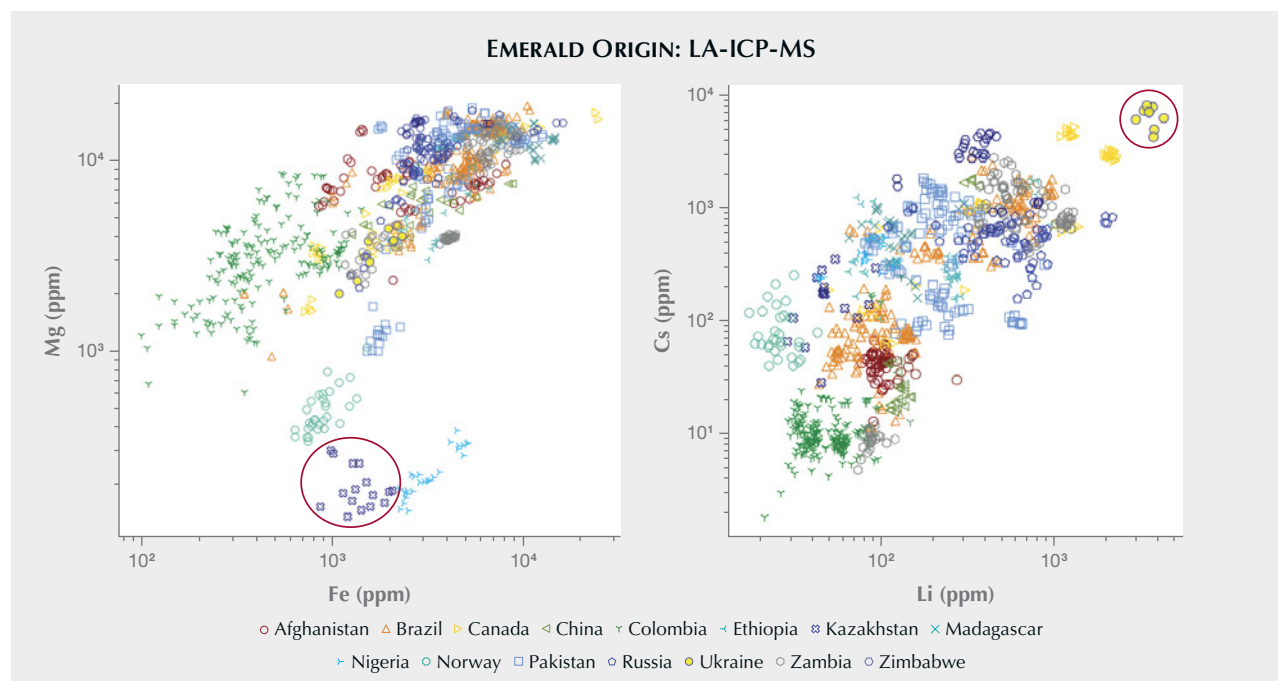
^aThe chromium concentration of Ukrainian emerald is 631–2000 ppm; the almost-aquamarine has a lower concentration range from 13.5–127 ppm.

ments, setting them apart from commercially significant deposits. The data also revealed insights into the geological environment in which they formed.

The Kazakhstani emeralds had some of the lowest documented magnesium, iron, and sodium concentrations for emerald, forming a unique data cluster adjacent to that of emeralds from Norway and Nigeria when comparing magnesium and iron (figure 3, left). The Kazakhstani samples were also among the few emeralds with more iron than magnesium, an indicator of their origin at the greisen intersection of the Delbegetey granitic pluton and a Carboniferous sandstone (E.V. Gavrilenko et al., “Emeralds from the Delbegetey deposit (Kazakhstan): Mineralogical characteristics and fluid-inclusion study,” *Mineralogical Magazine*, Vol. 70, No. 2, 2006, pp. 159–173), neither of

which have significant magnesium to contribute to beryl. While the source of their chromium and vanadium (which contribute to their emerald-green hue in similar proportions) is unknown, some researchers have suggested other regional sedimentary layers as a potential source. Their exceptionally low ratio of magnesium to iron and low but variable cesium to sodium ratio (up to ~0.125 Cs/Na, based on atoms per formula unit) are consistent with formation in a mildly differentiated granite (C. Liu et al., “Continuous Be mineralization from two-mica granite to pegmatite: Critical element enrichment processes in a Himalayan leucogranite pluton,” *American Mineralogist*, Vol. 108, No. 2, 2023, pp. 31–41). This formation environment, which is uncommon in emeralds, most closely matches Nigerian emeralds, which have a similar mint green hue.

Figure 3. Chemical comparison of emeralds from economically significant localities, as well as Kazakhstan and Ukraine. Data collected by LA-ICP-MS. Left: The Kazakhstani emeralds (circled) form a distinct cluster at the lower center of the plot. Right: The Ukrainian emeralds (circled) form a distinct cluster at the upper right of the plot.



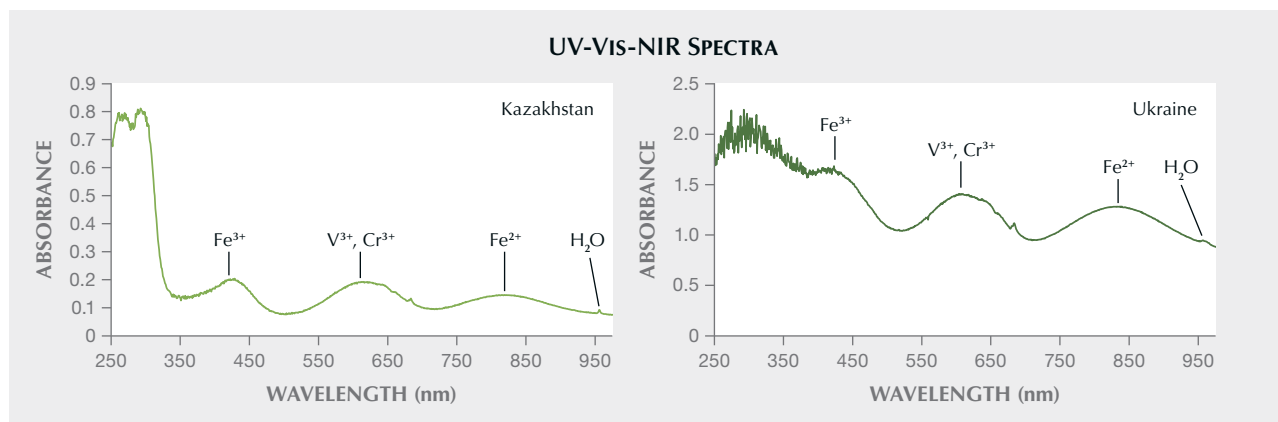


Figure 4. UV-Vis-NIR absorption spectra of a Kazakhstani emerald (left) and a Ukrainian emerald (right). The pale hue is demonstrated by the low absorbance, but the bands clearly show the dominant chromophores and the presence of H_2O , similar to other emeralds.

It is possible that the small size of these emeralds contributes to the perception of paleness, as they have sufficient chromium and vanadium content to provide a distinct green hue that would classify them as emeralds. The ultraviolet/visible/near-infrared (UV-Vis-NIR) spectrum in figure 4 (left) confirms the contribution of these two chromophores.

The Ukrainian beryl and emerald samples are the product of a chemically evolved pegmatite intersecting with an ultramafic host rock, consistent with recent research findings (G. Franz et al., "A new emerald occurrence from Kruta Balka, Western Peri-Azovian region, Ukraine: Implications for understanding the crystal chemistry of emerald," *American Mineralogist*, Vol. 105. No. 2, 2020, pp. 162–181). They had high cesium and lithium (figure 3, right)—higher than what this author recently reported for similar emeralds from Newfoundland, Canada, which form in a similar geological setting (Spring 2024 GNI, pp. 123–125). Only one emerald sample known to the author has had higher cesium content, though it was of uncertain origin, while emeralds from Hiddenite, North Carolina, are rumored to have higher lithium content. The elevated cesium and lithium together are strong indicators of a pegmatitic origin.

The Ukrainian emerald samples had an elevated Cs/Na ratio compared to their Mg/Fe ratio, setting them apart from most other emeralds, though a similar relationship between the two ratios exists in emeralds from Newfoundland, Curlew in Western Australia, and to some extent, Zimbabwe. The green hue of these specimens is attributed more to chromium than vanadium, with a slight influence from iron. The three Ukrainian emeralds also had high zinc compared to other studied emeralds. One had more of a blue hue with lower chromium and vanadium, placing it chemically between an aquamarine and an emerald, but the other two specimens were distinctly emerald based on their significant chromium content and green hue. The UV-Vis-NIR absorption spectrum of one of the green specimens (figure 4, right) confirmed the role of chromium and

vanadium in the hue, though the sample's poor transparency contributed to elevated absorbance.

These specimens expand our understanding of emerald beyond the traditional commercial deposits. With their unique characteristics, these two groups push the boundaries of emerald as a beryl variety. Following the present research project, these rare emerald and beryl specimens will join the GIA Museum collection.

*Rhiana Elizabeth Henry
GIA, Carlsbad*

Unique trapiche grossular from China. Grossular is known in the gem market for its popular varieties, such as tsavorite, hessonite, and rosolite. However, the occurrence of trapiche grossular has rarely been reported. Recently, some previously collected grossular crystals from Hangzhou, Zhejiang Province, China, were found to exhibit a distinct trapiche structure after being cut along specific orientations.

The term *trapiche* refers to a rare growth pattern characterized by radial sector zoning, forming a spoke-like or wheel-shaped appearance. This phenomenon is most commonly observed in emerald, corundum, and tourmaline but has rarely been reported in garnet.

The grossular crystals were collected from a skarn outcrop in southwestern Hangzhou. The formation of skarn is the result of contact metamorphism between granite and limestone. The grossular crystals (figure 5, left) were in the form of rhombic dodecahedrons and appeared black due to a coating of graphite and pyrite. When cut into slices (figure 5, right), they exhibited a colorless and highly transparent appearance. Scanning electron microscopy with energy-dispersive spectroscopy (SEM-EDS) and laser ablation-inductively coupled plasma-mass spectrometry (LA-ICP-MS) analyses indicated their compositions were close to the grossular endmember, with trace amounts of magnesium, titanium, vanadium, chromium, manganese, and iron.



Figure 5. Left: Grossular crystals weighing 0.63 to 4.63 ct from Hangzhou, China. Right: Slices, cut perpendicular to the tetrad axis (top row) and the triad axis (middle and bottom rows). Photos by Hongtao Shen (left) and Tsang Ho Yin (right).

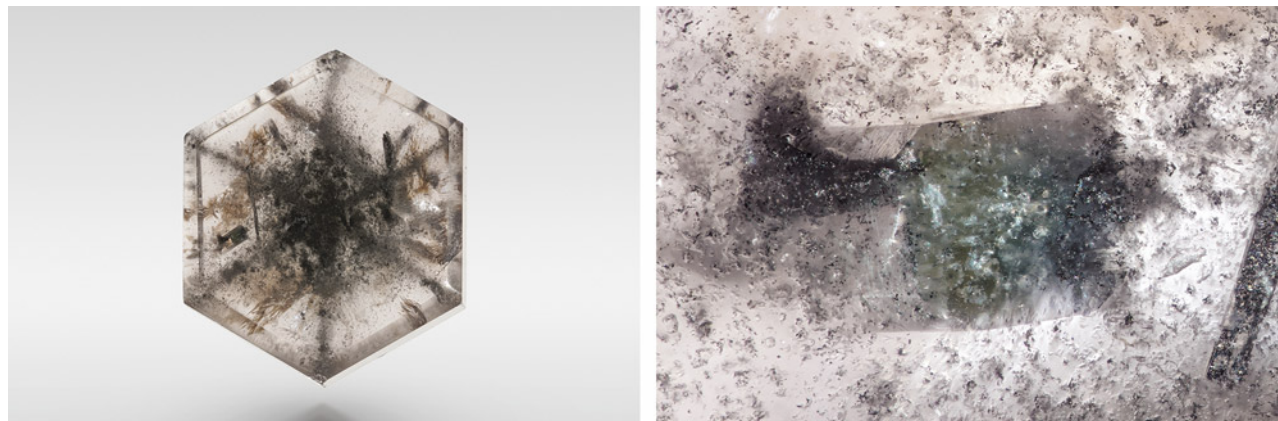
Based on the Raman spectrum and SEM-EDS analyses, the black arms were mainly composed of graphite and possibly other carbonaceous matter (such as bitumen or other amorphous phases). Diopside, fluorapatite, and quartz were also enriched in the arms, which corresponded to boundaries between {110} growth sectors. Furthermore, inclusions were preferentially concentrated along the tetrad and triad axes of the crystals.

The crystals were also fluorescent, showing orangish red under long-wave UV and yellowish orange under short-wave UV. Two main fluorescence centers were identified using 3D fluorescence mapping (not shown). The strongest fluorescence was at ~590 nm in the emission spectra, which is attributed to Mn^{2+} . The weaker fluorescence center in the orange-red region exhibited three sharp peaks centered at 689, 703, and 718 nm, which are usually attributed to Cr^{3+} .

Pyrite, calcite, and zircon were present in almost every sample. Additionally, two rare mineral inclusions, troilite (FeS) and hellandite-Ce, were identified. Troilite was confirmed with SEM-EDS and Raman spectroscopy on

polished thin sections; the Fe/S atomic percentage ratio consistently ranged from 0.93 to 0.96. Electron probe microanalysis–wavelength dispersive spectroscopy (EPMA-WDS) analysis was used to identify hellandite-Ce; one calculated chemical formula was $(Ca_{3.66}Y_{0.34})_{\Sigma 4.00}(Ce_{0.71}Nd_{0.37}Y_{0.37}La_{0.30}Sm_{0.07}Pr_{0.07}Gd_{0.05}Dy_{0.05}Eu_{0.04}Tm_{0.02}Er_{0.02}Yb_{0.02}Ho_{0.01})_{\Sigma 2.12}(Al_{0.94}Ti_{0.06})_{\Sigma 1.00}Si_{4.00}B_{4.00}O_{22}(OH)_{1.74}F_{0.03}$. Troilite occurred as particles up to ~800 μm , while hellandite formed druses ranging from 50 to 195 μm . These inclusions occurred randomly within the slices, without a clear association with growth sectors. In some slices, large columnar inclusions were also observed (figure 6), up to 4 mm in length, identified as marialite ($Na_4Al_3Si_9O_{24}Cl$) by Raman and SEM-EDS analyses. Some marialite crystals were partially or completely replaced by a series of common minerals including calcite, diopside, albite, K-feldspar, cel-sian, prehnite, titanite, and fluorapatite. Celsian ($Ba(Al_2Si_2O_8)$) was also found in some grossular slices and was often associated with K-feldspar with zoning structure resulting from isomorphism. Occasionally, baryte ($BaSO_4$) and alstonite ($BaCa(CO_3)_2$) inclusions could also be detected.

Figure 6. Columnar marialite inclusions in a grossular slice. Photos by Tsang Ho Yin; field of view 0.86 mm (right).



These materials present a new occurrence of a mineral species with a trapiche structure and reflect the unique geological environment of the region as well. The presence of troilite indicates extremely low oxygen fugacity, which suggests a highly reducing environment (X. Li et al., "Thermally induced phase transition of troilite during micro-Raman spectroscopy analysis," *Icarus*, Vol. 390, 2023, article no. 115299). The marialite suggests these grossular garnets may have crystallized from high-salinity hydrothermal fluids (J. Hammerli et al., "Exchange experiments for chlorine and bromine partitioning in scapolite at variable fluid salinities, pressures, and temperatures: Implications for tracing crustal fluid sources via Cl/Br ratios in scapolite," *Contributions to Mineralogy and Petrology*, Vol. 179, 2024, article no. 92). Celsian and some other barium-bearing minerals serve as indicators of an unusual barium-rich environment. Further study of these special inclusions may provide insights into the formation mechanisms of these grossular garnets with fine trapiche textures.

Yinuo Wu, Xingtong Li, and Qian Zhang
Gemological Institute,
China University of Geosciences, Wuhan
Hongtao Shen
State Key Laboratory of Geological Processes and
Mineral Resources
China University of Geosciences, Wuhan
Ningyue Sun
Science Research Institute,
China University of Geosciences, Beijing

Zhi Qu
Qingdao Institute of Measurement Technology,
Shandong, Qingdao, China

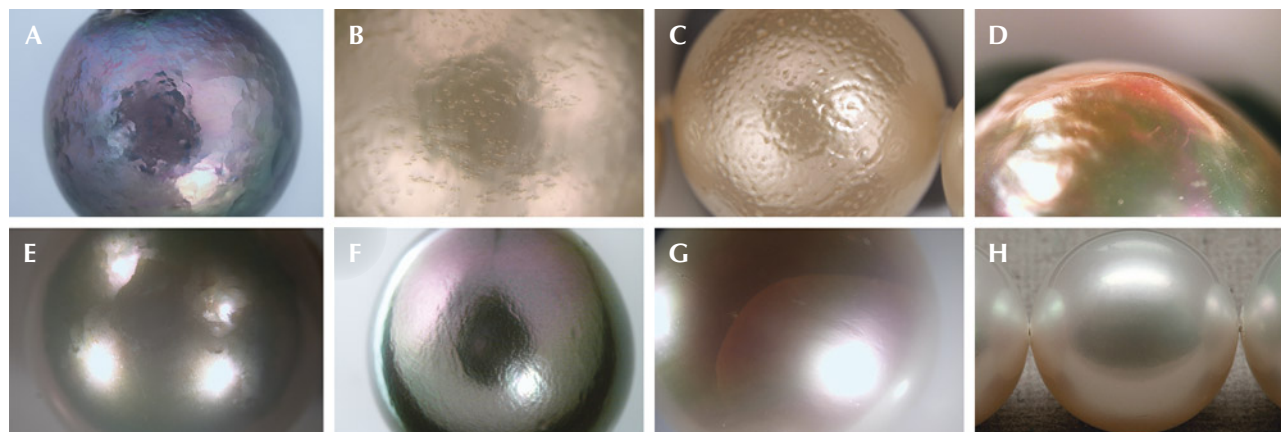
Ho Yin Tsang
Bedside Mineral Studio, Hong Kong SAR, China

Xiang Pi
Meticulous Minerals, Xiamen, China

GIA 7 Pearl Value Factors: An update on nacre classification. Pearls, both natural and cultured, form in a wide variety of sizes, shapes, and colors. This diversity created the need to distinguish their various appearances, characteristics, and a host of other complex factors that contribute to determining quality, desirability, and ultimately, value. Researching and studying pearls since the 1930s, GIA developed the GIA 7 Pearl Value Factors classification system, a systematic approach to evaluate a pearl's various quality factors through consistent methodology and common terminology (J.W.Y. Ho and S.C. Shih, "Pearl classification: The GIA 7 Pearl Value Factors," Summer 2021 *G&G*, pp. 135–137). The system, which has been widely adopted in the pearl industry, classifies pearls according to size, shape, color, luster, surface, nacre, and matching.

Nacre formation plays a critical role in pearl growth, as its structure influences other value factors such as size, shape, luster, and surface quality. Nacre thickness and continuity also affect a pearl's durability. Prior to this update, a grade of Acceptable denoted expected commercial quality standards, while Unacceptable indicated poor-quality nacre that may impact durability. Prompted by trade requests and feedback, an expansion of the nacre designation for the

Figure 7. Some examples of surface and sub-surface nacre features that impact GIA's new nacre classification scale. A: Near- or sub-surface "hammering." B: "Bubble" appearance shown on the nacre surface. C: Shallow pits or channel depressions giving an "orange peel" effect. D: "Seam" found on a baroque pearl where surface planes meet or change direction and create a peaked ridge. E: "Planar edges" showing subtle angular lines spaced apart across the pearl's surface. F: "Striae" features appearing as flame structures on a nacreous pearl. G: "Sub-surface crack" that may pose a threat to the durability of the pearl. H: An example of a pearl showing both a clean surface and excellent nacre (lacks any visible surface or sub-surface characteristics) based on the GIA 7 Pearl Value Factors. Photos by Emiko Yazawa (A–G) and Eric Welch (H); fields of view 19.27 mm (A and F), 7.19 mm (B), 14.52 mm (C, E, and G), and 9.61 mm (D).



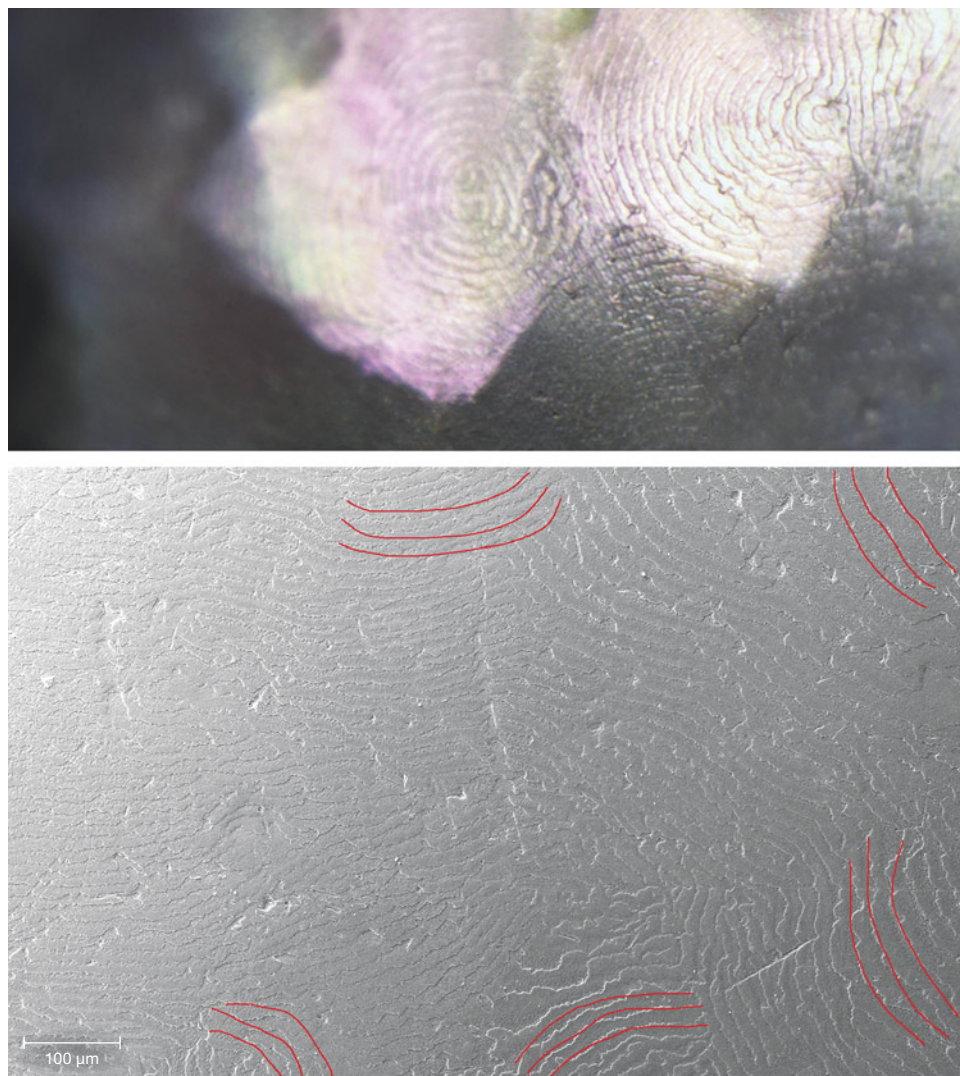


Figure 8. Conventional microscopic (top) and scanning electron microscopic (bottom) observations on the “hammered” surface showed concentric nacre platelet growth patterns on each planar surface. Nacre growth patterns are highlighted in red in the bottom image. Photomicrograph by Chunhui Zhou; field of view 1.40 mm (top).

GIA 7 Pearl Value Factors classification system recently led to the establishment of a new nacre scale more aligned with other quality factors. To implement this change, a detailed investigation was conducted using a variety of pearl samples with surface and sub-surface features indicating various levels of nacre continuity throughout their growth history. As a result, the new nacre scale contains the following five classification ranges: Excellent, Very Good, Good, Fair, and Poor, based on the evaluation of structural or textural nacre features (sometimes referred to as “movement”) found either on the surface or sub-surface levels of the pearls. Figure 7 shows some examples of these features and an example free of such features for comparison. Most of the photomicrographs shown in figure 7 magnify the surface features for illustration purposes. The actual classification of pearls is performed by visual observation without magnification under suitable lighting conditions. While “hammering” is a widely known and used term in the industry, GIA has internally assigned specific descriptive names and definitions to other movement types for consistency of identification.

Hammering, named due to its hammered metal appearance (or faceted appearance), exhibits distinct shallow dents or flats that are often seen on baroque pearls but can be present on any shape. This feature can make luster appear softer than it is due to the dispersion of reflections. As a near-surface or sub-surface feature, hammering can often be visible without magnification. Under both conventional microscopic and scanning electron microscopic observations, interesting aragonite nacre platelet structural patterns have been observed in which the nacre on each large planar surface grew concentrically toward its own center (figure 8), as opposed to more integrated and random overlapping nacre platelet structures found on non-hammered pearls. This surface feature is commonly associated with very rapid pearl growth, instead of a growth rate that can provide consistent regular crystal formation for a smooth nacre deposition throughout the whole growth period (J. Taylor and E. Strack, “Pearl production,” in P.C. Southgate and J.S. Lucas, Eds., *The Pearl Oyster*, Elsevier, 2008, pp. 273–302).

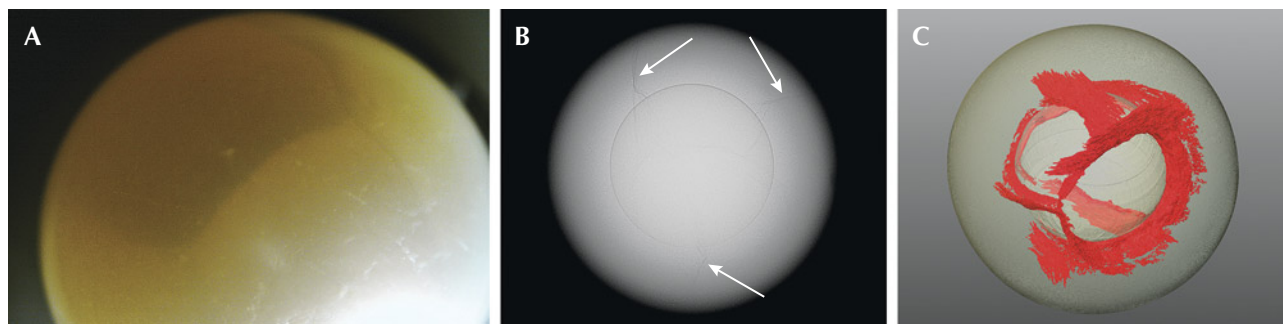


Figure 9. A: A South Sea bead cultured pearl displaying multiple “tideline” features under the surface. Photomicrograph by Emiko Yazawa; field of view 14.52 mm. B: X-ray microradiograph of the pearl showing the cracks (indicated by arrows) extending from the bead nucleus toward the surface. C: 3D reconstruction using X-ray computed microtomography data generated an overall 3D representation of the distribution of the internal cracks (in red).

Another feature commonly seen on some pearls is the internal fissures or cracks not far below the nacre surface that can be observed under strong lighting conditions (sometimes referred to as “tidelines”). Figure 9 presents a good example of such a feature: a South Sea bead cultured pearl containing multiple internal cracks beneath the nacre surface. Under X-ray radiographic examination, these internal cracks can extend toward different directions between the bead nucleus and the nacre surface. 3D reconstruction of the X-ray computed microtomography data showed the extent of these cracks radiating from the bead nucleus, providing a better visualization of how these internal fissures are distributed and interconnected with each other (see video at <https://www.gia.edu/gems-gemology/summer-2025-gemnews-gia-7-pearl-value-factors-update-nacre-classification>). While drilling may occasionally cause internal cracks, undrilled pearls such as this example could also display these growth disruptions within their nacre layers, which may pose durability issues. The exact cause of this feature on undrilled pearls remains unknown.

In summary, the new nacre continuity classification range characterizes the degree of surface or sub-surface nacre disruption, with the baseline being a perfectly smooth, uninterrupted (i.e., Excellent) nacre. Additionally, each cultured pearl type has a minimum parameter for nacre thickness. Based on our observations, most cultured pearls of commercial grade fall into the Good nacre quality range, as opposed to the previous grade of Acceptable, while pearls of higher quality may reach Very Good or Excellent. This update on the nacre quality scale provides improvement to the existing nacre quality description for the GIA 7 Pearl Value Factors classification system.

Akira Hyatt, Emiko Yazawa, and Chunhui Zhou
GIA, New York

Exceptional nacre thickness of hybrid akoya bead cultured pearls. Akoya pearl farming was established in Japan more than a century ago and subsequently expanded to other countries such as China, Vietnam, and Australia. The akoya pearl oyster includes members of mollusks that

Figure 10. Group of 81 hybrid akoya bead cultured pearls ranging from 4.00×3.93 mm to 6.44×6.28 mm. Photo by Nuttapol Kitdee.



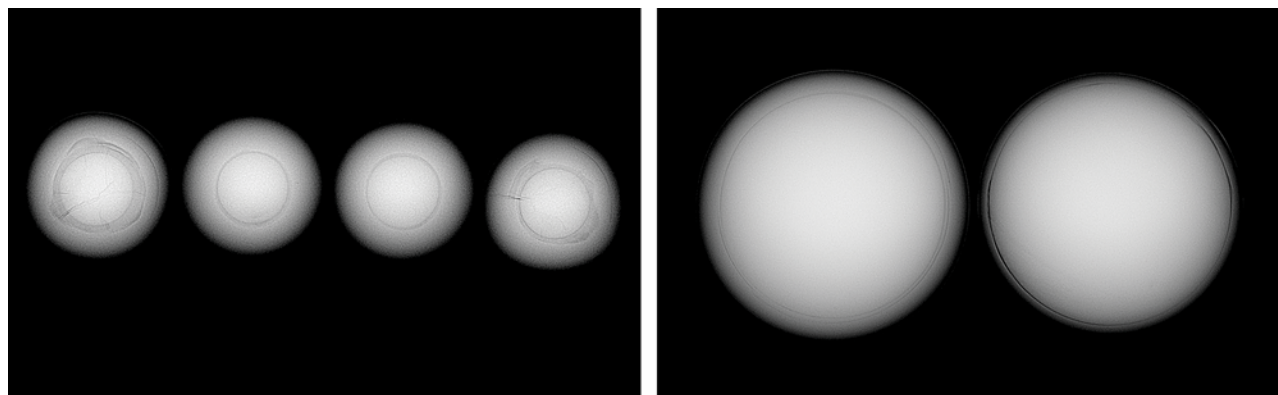


Figure 11. Left: RTX images of the four 6 mm pearls show round bead nuclei and dark gray areas around the beads associated with organic-rich material. Nacre thickness of each pearl from left to right: 1.67, 1.68, 1.62, and 1.64 mm, respectively. Right: The nacre overgrowths are significantly thicker than those of typical akoya pearls, such as the two shown here.

belong to the *Pinctada fucata*, *martensii*, *radiata*, and *imbricata* species complex (K.T. Wada and I. Tëmkin, "Taxonomy and phylogeny," in P.C. Southgate and J.S. Lucas, Eds., *The Pearl Oyster*, Elsevier, Oxford, 2008, pp. 37–75). The *P. fucata* (*martensii*) is the most widely used species to produce akoya cultured pearls.

Akoya bead cultured (BC) pearls are characterized by their round shapes and high luster. The growth period typically ranges from 10 to 14 months, which is shorter than that of South Sea (*P. maxima*) and Tahitian (*P. margaritifera*) BC pearls. A longer growth time can possibly impact the roundness of the pearls. Akoya mollusks can produce high-quality nacre when the water temperature is between 15° to 20°C, as cool water slows the rate of nacre deposition. Due to the shorter growth period and lower temperature growth conditions, akoya BC pearls are generally known to have a thinner nacre overgrowth than South Sea and Tahitian BC pearls. This also implies that a uniform white shell bead with no discoloration must be used during the nucleation process since low-quality beads can affect the quality of the final pearls (N. Sturman et al., "Vietnam: Shell nuclei, pearl hatcheries, and pearl farming," Fall 2020 *G&G*, pp. 402–415). Very thin nacre can impact the durability and luster of pearls. As a result, many pearl farmers continually refine their techniques to achieve the highest quality with respect to shape, luster, and nacre thickness on their final products while balancing culturing time and cost.

GIA's Bangkok laboratory received 91 hybrid akoya bead cultured pearls for study, weighing a total of 53.54 carats and ranging from 4.00 × 3.93 mm to 6.44 × 6.28 mm in diameter, from Orient Pearl (Bangkok) Ltd (figure 10). Reportedly produced at a pearl farm in Nha Trang, Vietnam, the pearls were harvested in April 2023 from hybrid mollusks that were crossbred between *P. fucata* (*martensii*) and *P. radiata* species. These akoya pearls are said to have a thicker nacre than typical akoya BC pearls produced from pure *P. fucata* (*martensii*) species, as the hybrid mollusks are more tolerant of warmer water, and therefore the nacre

of their pearls can grow faster. However, only a very small percentage (around 0.5%) of the total production of these hybrid mollusks yields pearls with nacre significantly thicker than those from pure *P. fucata* mollusks. Traditional American freshwater shell beads were used to grow the pearls, with a cultivation period of only 5 months for the 4 mm pearls and about a year for the 6 mm pearls.

Most of the samples (87 out of 91) were about 4 mm in diameter, and the other four samples were 6 mm. All pearls were round with predominantly cream color, most having noticeable orient and pink and green overtone. They all had fine nacre, with no evidence of processing or color enhancement on their surfaces. The pearls fluoresced a very weak to moderate yellowish green under long-wave UV light. Short-wave UV fluorescence spectroscopy with 275 nm LED excitation resulted in counts of high intensity for these pearls, indicating that they were naturally colored and lacked the processing routinely applied for akoya pearls (Spring 2020 Lab Notes, p. 136). Ultraviolet/visible spectroscopy revealed absorption features around 435 and 460 nm in some of the pearls, which are characteristic features reportedly found on *P. radiata* pearls (A. Al-Alawi et al., "Saltwater cultured pearls from *Pinctada radiata* in Abu Dhabi (United Arab Emirates)," *Journal of Gemmology*, Vol. 37, No. 2, 2020, pp. 164–179).

Real-time X-ray microradiography (RTX) analysis revealed that each pearl showed a thick nacre layer with a round bead nucleus in the center. Some of the beads were surrounded by an organic-rich material, as evidenced by dark gray areas with RTX. X-ray radiography was used to obtain the measurements. The four 6 mm pearls had a nacre thickness between 1.62 to 1.68 mm (figure 11, left), significantly thicker than the typical nacre range of 0.15 to 0.50 mm in traditional akoya pearls (figure 11, right). Nacre thickness of the 4 mm pearls ranged from 1.11 to 1.46 mm.

The degree of X-ray fluorescence (XRF) reaction observed in saltwater BC pearls is dependent on nacre thickness. Freshwater shell beads exhibit a high intensity of greenish

TABLE 1. Measurements of nacre thickness and diameter of the pearl and bead obtained by RTX analysis. Volume ratios of the bead and nacre to the total volume of the pearl can be calculated based on the equations presented.

Pearl	Nacre thickness (mm)	Diameter (mm)		Volume ratio	
		Pearl (<i>D</i>)	Bead (<i>d</i>)	Bead ($(d/D)^3$)	Nacre ($1 - \text{Bead volume ratio}$)
1	1.67	6.30	2.97	0.11	0.89
2	1.68	6.33	2.89	0.10	0.90
3	1.62	6.25	2.93	0.10	0.90
4	1.64	6.14	2.86	0.10	0.90

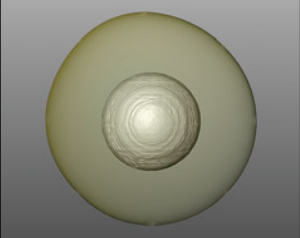
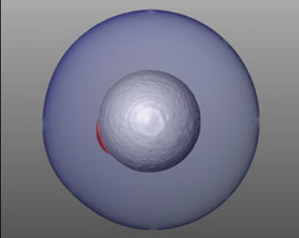
yellow fluorescence due to trace amounts of manganese, while nacre produced in saltwater is generally inert. Thin nacre often allows a bead's fluorescence to pass through, resulting in the pearl displaying noticeable fluorescence. Due to their thick nacre, the four hybrid akoya pearls either exhibited weak fluorescence or were inert to XRF.

Additionally, the diameters of the pearl (*D*) and bead (*d*) can be used to calculate the ratios of both nacre volume and bead volume to total pearl volume, as illustrated in table 1. From the calculation, all four 6 mm pearls have a high percent nacre volume of around 90% of the total pearl volume. Therefore, the bead nucleus only occupies around 10% of the total pearl volume. The nacre volume of all 4 mm pearls ranged from 90–94% of the total pearl volume.

For additional study, two of the 6 mm pearls were selected for X-ray computed microtomography (μ -CT) analysis. Specialized software to render the μ -CT scan images was used to generate three-dimensional models and measure nacre thickness and volume percentage of the pearl nacre and the bead. The results obtained were consistent with the calculation results from RTX analyses (table 2).

This study demonstrated that the hybrid mollusk species of *P. fucata (martensii)* and *P. radiata* can produce BC pearls with a thick nacre layer with the nacre accounting for approximately 90% of the total pearl volume. Furthermore, according to the GIA 7 Pearl Value Factors classification system, the hybrid pearls studied displayed Excellent and Very Good lusters. Therefore, the

TABLE 2. Results from μ -CT and RTX analyses comparing nacre thickness, bead and nacre volumes, and their percent of total pearl volumes for the two 6 mm pearls.

Pearl	μ -CT 3D model	Nacre thickness (mm)		Bead volume		Nacre volume	
		RTX	μ -CT	RTX	μ -CT	RTX	μ -CT
1		1.67	1.67	13.814 mm ³ 11%	12.986 mm ³ 10%	116.690 mm ³ 89%	113.218 mm ³ 90%
2		1.68	1.68	12.730 mm ³ 10%	11.956 mm ³ 10%	119.047 mm ³ 90%	106.530 mm ³ 90%

thick and fine quality of the nacre resulted in high luster. A sufficient nacre layer can enhance durability, which is an essential characteristic that contributes to the value and beauty of akoya BC pearls.

Kwanreun Lawanwong and Ravenya Atchalak
GIA, Bangkok

Emiko Yazawa
GIA, New York

Iridescent gems cut from hinge ligament of South Sea pearl oyster (*Pinctada maxima*). Pearl oysters of the *Pinctada* genus are known to produce beautiful nacreous pearls (*The Pearl Blue Book*, CIBJO, 2022). The iridescent nacre of their shells, known as mother-of-pearl, is often used as a gem material. Another part of the oyster—the hinge ligament—also can be used as a gem material. The hinge ligament is a mineralized tissue that connects the two shells of a bivalve mollusk.

Shoji Naito, a Tokyo-based lapidary with more than forty years of experience in gemstone cutting, had a large South Sea pearl oyster (*Pinctada maxima*) shell that he kept for at least 37 years. The cross section of the shell's thick hinge ligament displayed iridescence. To enhance this attractive phenomenon, the hinge ligament was cut and polished into cabochons, a practice that has remained unknown in the gem industry. Author YK recently purchased one of these cabochons: a 0.72 ct black opaque specimen.

Due to the item's appearance, particularly its greasy luster and iridescence, the cabochon can be confused with other iridescent materials such as opal imitations. Since this unique material has yet to be studied in detail, Naito

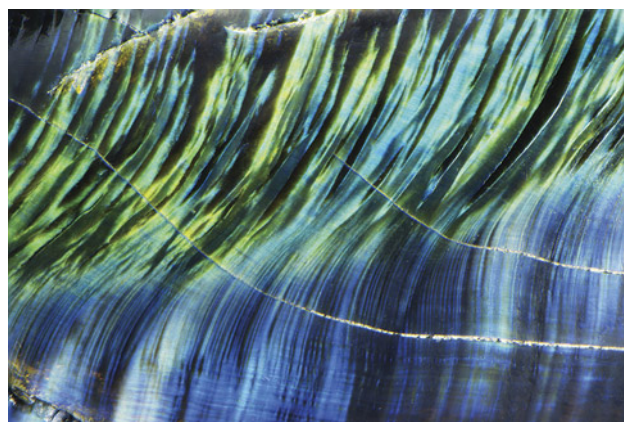


Figure 13. An iridescence on the cross-section surfaces of a hinge ligament fragment from the South Sea pearl oyster. Photomicrograph by Nathan Renfro; field of view 3.60 mm.

loaned rough and polished cabochon ligaments as well as the shell (figure 12) to GIA for gemological examination.

The 0.72 ct cabochon had a refractive index of 1.560 (spot reading) and a hydrostatic specific gravity (SG) of 1.18. The very low SG of this cabochon compared to pearls or shells, which are generally above 2.60, indicated that it contained a higher percentage of organic material. Microscopic observation revealed fibrous structures with iridescent reflections. The fibrous structures displayed a wavy pattern of blue/green-dominant iridescence against the black opaque matrix. Rough fragments showed the same patterns at the cross sections (figure 13).

In addition to standard gemological testing and observations, more advanced testing methods were applied to



Figure 12. Polished and unpolished hinge ligaments with a *Pinctada maxima* shell. Photo by Annie Haynes.

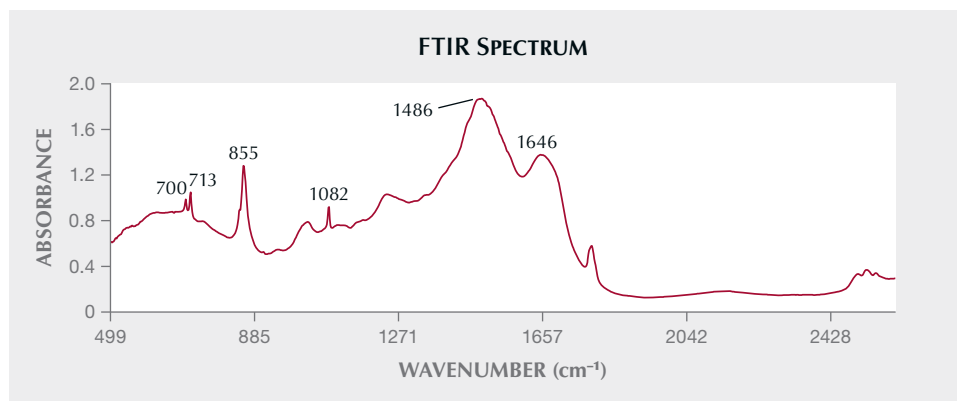


Figure 14. The FTIR spectrum revealed aragonite peaks at 1486, 1082, 855, 713, and 700 cm^{-1} , together with an amide I peak that is associated with conchiolin at 1646 cm^{-1} .

the fragment and polished samples at GIA's laboratory in Carlsbad. Raman spectroscopy with 830 nm laser excitation clearly detected aragonite peaks (1086, a doublet at 702 and 706, 206, and 152 cm^{-1}). The ultraviolet/visible/near-infrared (UV-Vis-NIR) reflectance spectra showed an absorption at 280 nm associated with conchiolin. For collecting Fourier-transform infrared (FTIR) spectra, two KBr pellets were prepared with powders collected from ligament fragments. The FTIR spectra (figure 14) showed aragonite peaks (1486, 1082, 855, 713, and 700 cm^{-1}) and an amide I peak at 1646 cm^{-1} related to conchiolin, which are identical to the spectrum reported for the ligament of the akoya pearl oyster (*P. fucata*) (M. Suzuki et al., "A unique methionine-rich protein-aragonite crystal complex: Structure and mechanical functions of *Pinctada fucata* bivalve hinge ligament," *Acta Biomaterialia*, Vol. 100, 2019, pp. 1–9).

Energy-dispersive X-ray fluorescence (EDXRF) spectroscopy showed very high calcium (397300 ± 1600 ppm), low levels of manganese (110 ± 42 ppm), and high strontium (3077 ± 89 ppm) contents for the 0.72 ct cabochon, confirming calcium carbonate material of saltwater origin. The results for the fragments also showed the same trend. Laser ablation-inductively coupled plasma-mass spectroscopy (LA-ICP-MS) analysis confirmed the EDXRF results. Furthermore, most trace elements exhibited concentrations comparable to previously reported nacreous *P. maxima* pearls (e.g., K. Scarratt et al., "Natural pearls from Australian *Pinctada maxima*," Winter 2012 *G&G*, pp. 236–261; N. Sturman et al., "Bead-cultured and non-bead-cultured pearls from Lombok, Indonesia," Fall 2016 *G&G*, pp. 288–297). The magnesium level was significantly higher, however, which is likely related to the organic-rich nature of the material.

Real-time X-ray microradiography (RTX) revealed that both the cabochons and fragments exhibited a similar banded structure alternating between light gray and dark gray stripes. The light gray areas appeared to be dense aragonite material that was generally more radiopaque than the dark gray areas of protein-rich materials (figure 15). Cracks were presented as darker gray lines across the structure. The internal banded structure corresponds to the arrangement of the fibers creating the iridescent effect.

The hinge ligaments of Tahitian pearl oyster (*P. margaritifera*) shells from GIA's research collection were also tested for comparison. Due to the smaller size of the *P. margaritifera* shell, the hinge ligaments are thinner and display less iridescence than the *P. maxima* sample studied. However, the testing results were consistent.

This study showed that FTIR (KBr pellet) analysis can be used, in addition to standard gemological testing and microscopic observations, to verify the characteristic aragonite and amide I peaks of the hinge ligament. However, KBr pellet analysis is destructive—Raman and UV-Vis-NIR reflectance spectroscopies and RTX analysis should be attempted first.

This unique biogenic material from pearl oysters can potentially produce a new eye-catching blue-green iridescent gem material.

Yusuke Katsurada
GIA, Tokyo

Artitaya Homkrajae and Amiroh Steen
GIA, Carlsbad

Figure 15. The 0.72 ct cabochon showed an internal banded structure alternating between light gray stripes of aragonite and dark gray stripes of protein-rich material in the RTX image. Image by Amiroh Steen.

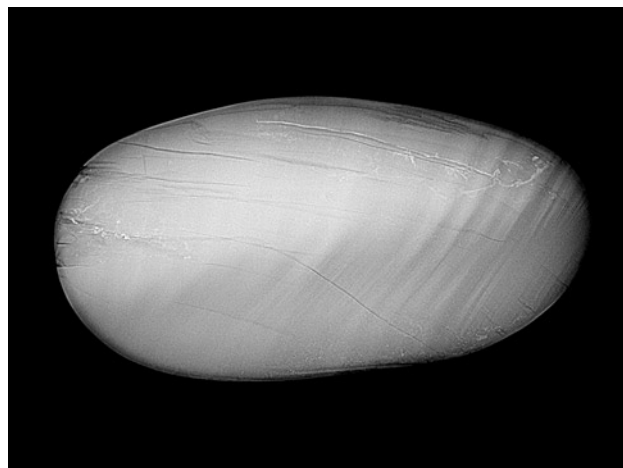




Figure 16. This 0.20 ct faceted transparent, colorless poudretteite measures 3.48×4.06 mm. Photo by Jianxing Wang.

Neptunite inclusions in rare poudretteite. The authors recently found a 0.20 ct faceted transparent, colorless poudretteite (figure 16) resembling colorless spinel or taaffeite at a jewelry market in China's Yunnan Province. Poudretteite is a rare hexagonal silicate gemstone variety with the chemical formula $\text{KNa}_2(\text{B}_3\text{Si}_{12})\text{O}_{30}$ (J.D. Grice et al., "Poudretteite, $\text{KNa}_2(\text{B}_3\text{Si}_{12})\text{O}_{30}$, a new member of the osumilite group from Mont Saint-Hilaire, Quebec, and its crystal structure," *Canadian Mineralogist*, Vol. 25, No. 4, 1987, pp. 763–766). It is found primarily in the Quebec province of Canada and in Mogok, Myanmar (C.P. Smith et al., "Poudretteite: A rare gem species from the Mogok Valley," Spring 2003 *G&G*, pp. 24–31). Northern Myanmar, which borders China's Yunnan Province, is perhaps the most likely origin of this sample. Standard gemological

Figure 17. One of the reddish brown neptunite inclusions in the poudretteite. Photomicrograph by Jianxing Wang; field of view 1.50 mm.

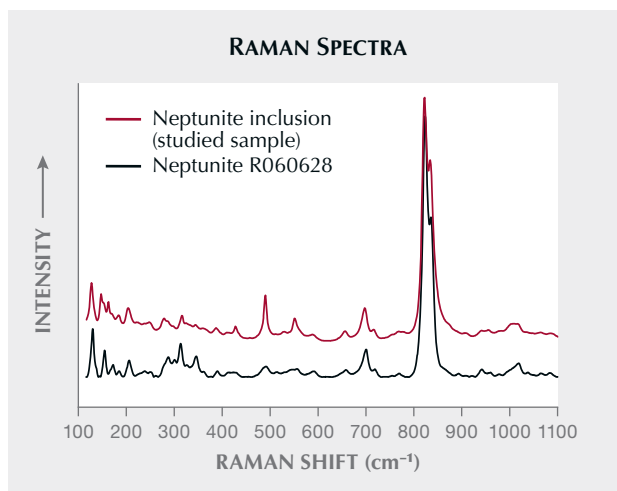


Figure 18. Raman spectrum of the neptunite inclusion in the poudretteite compared to that of a RRUFF reference spectrum. Spectra are offset vertically for clarity.

testing revealed a refractive index of 1.513–1.533 and a hydrostatic specific gravity of 2.51. The stone was uniaxial positive, and its ultraviolet fluorescence was inert. Raman spectroscopy confirmed the sample was poudretteite.

Three reddish brown crystal inclusions were observed within the stone (figure 17). Raman spectroscopy identified them as the rare mineral neptunite ($\text{KNa}_2\text{Li}(\text{Fe}^{2+}, \text{Mn})_2\text{Ti}_2\text{Si}_8\text{O}_{24}$) (figure 18; B. Lafuente et al., 2015, <https://rruff.info/about/downloads/HMC1-30.pdf>), which has been found in Greenland, Canada, and the United States (Summer 2021 *G&G* Micro-World, pp. 160–161). To the best of our knowledge, this is the first recorded occurrence of neptunite inclusions in poudretteite.

Jianxing Wang
Jewelry Testing Center,
Shenzhen Polytechnic University, China
Kong Gao
College of Jewelry,
Guangzhou Panyu Polytechnic, China

New väryrynenite production from Nigeria. Väryrynenite was officially described as a mineral in 1954, based on samples from the Viitaniemi pegmatite field in central Finland. The rare phosphate mineral ($\text{BeMn}^{2+}(\text{PO}_4)(\text{OH})$) was named after professor H.A. Väryrynen. Nearly all the material was initially found as opaque, fine-grained aggregates, lacking any euhedral crystal formation.

It wasn't until the 1970s that the mineral gained popularity with the discovery of well-formed crystals in the Chitral area of Pakistan. Initially, most of the interest was in mineral specimens. Occasionally, material suitable for faceting was recovered, but it was often included and limited to sizes under 1 carat, making väryrynenite a true collector's stone. Some small faceted material was recently reported from Afghanistan as well (Spring 2025 GNI, p. 102).

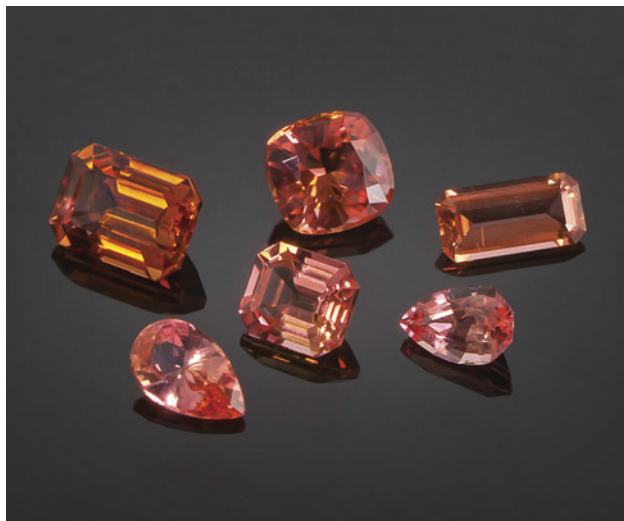


Figure 19. Nigerian väyrynenite vary from orange to orangy pink colors and occur in high clarity. These stones range from 0.72 to 2.45 ct. Photo by Nuttapol Kitdee; courtesy of Thai Lanka Trading.

Since fall 2024, larger stones have been seen in the trade, including multiple clean faceted gems over 10 ct. These are reportedly from Nasarawa State in Nigeria, near the village of Angwan Doka, roughly 20 km southeast of the city of Keffi. The area around Keffi is well known for pegmatite-related gems, especially pink, green, and bicolor tourmalines. In mid-2024, at a site previously mined for tourmaline, artisanal miners struck a pocket of unknown orange to orangy pink material later identified as väyrynenite. Väyrynenite occurs as an alteration product in certain types of pegmatites.

GIA recently studied a set of stones, weighing 0.72 to 2.45 ct, from the new Nigerian source loaned from Mark Smith of Thai Lanka Trading in Bangkok (figure 19). All properties matched previously known väyrynenite: refractive index of 1.639–1.676 with a birefringence ranging from 0.025–0.027, biaxial optical figure, and a density of 3.22–3.25. Its orangy pink color sometimes ranged into a pure orange. Using a dichroscope, the stones showed trichroism (pinkish orange–pure pink–yellowish orange). None of the stones showed fluorescence under long-wave (365 nm) or short-wave (254 nm) UV. Raman spectroscopy confirmed their identity as well.

All stones were eye-clean but showed strong doubling of the pavilion facets under 10× magnification. Inclusions were limited to healed fractures with two-phase fluid inclusions.

While its mineral properties and colors are similar to those of the Pakistani material, the new material from Nigeria exhibits larger crystal sizes and higher clarities. This is exciting news for the gem world, where väyrynenite is becoming more accessible in higher qualities.

Wim Vertriest
GIA, Bangkok



Figure 20. Deep-UV imaging of the 0.07 ct multilayered laboratory-grown diamond ($4.20 \times 2.26 \times 1.27$ mm) showing fluorescence of a thin blue-green layer between two pink-orange CVD layers. Image by Sean O'Neal.

DIAMONDS

Multilayered laboratory-grown diamond. A marquise-shaped laboratory-grown diamond weighing 0.07 ct and measuring $4.20 \times 2.26 \times 1.27$ mm was recently submitted to Stuller's gemological laboratory for testing. The near-colorless (G–H color range) and very slightly included (VVS₂–VS₁) stone provided some unusual results.

Deep-UV excitation (<225 nm) of the laboratory-grown diamond produced a multicolored pink-orange fluorescence accented by the dislocation bundles' vein-like

Figure 21. Short-wave UV imaging of the multilayered laboratory-grown diamond showed the thin layer phosphorescing while the rest of the diamond remained inert. Image by Guy Borenstein.



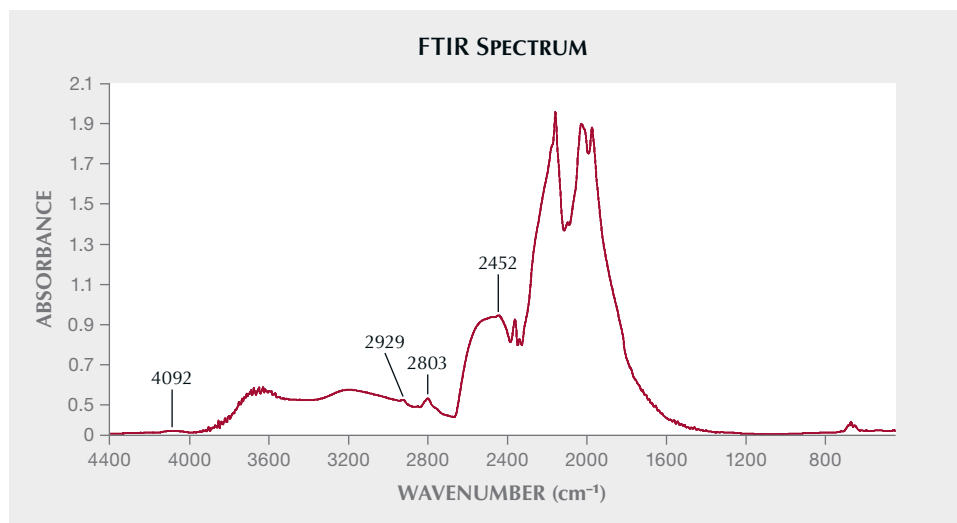


Figure 22. FTIR spectrum of the laboratory-grown diamond showing uncompensated boron at 4092, 2929, 2803, and 2452 cm^{-1} .

pattern toward the long pointed edges and a thin ($<50\ \mu\text{m}$) greenish blue layer crossing the center of the stone vertically from the table facet to the pavilion (figure 20). Viewed separately using broad-range pulsed xenon (120–2000 nm) and short-wave UV (254 nm) imaging, it exhibited a persistent ($>5\ \text{s}$) zone of greenish blue phosphorescence in the same location as the previously mentioned greenish blue fluorescent layer (figure 21).

When viewed with crossed polarizing filters, a strain in columnar and cross-hatched patterns was easily observed, though a thin layer of dark solid color was also observed. The section with the solid strain was once again consistent with the area of fluorescence and phosphorescence. Infrared spectroscopy revealed indications of uncompensated boron at 4092, 2929, 2803, and 2452 cm^{-1} , and no nitrogen was detected (figure 22). Photoluminescence (PL) spectroscopy under liquid nitrogen (77K, -196°C), using 532 nm laser excitation, showed differences between areas within the stone. When the laser was

focused on the long edges, sharp peaks at 575 and 637 nm (the NV^0 and NV^- centers, respectively) were observed, with the former being stronger. The NV^0 and NV^- centers are shown in figure 23, labeled “side A” and “side B,” respectively. Also, weak SiV^- lines at 737 nm were detected on both edges. When the laser was focused on the thin layer labeled “center” in figure 23, the NV^0 and NV^- zero-phonon lines were significantly reduced and no SiV^- was detected.

The distinctive fluorescence and phosphorescence patterns observed under deep-UV, short-wave UV, and xenon imaging, as well as the presence of zonal dislocation bundles, strain characteristics, and PL spectra differences, suggest a complex growth process involving multiple layers.

NV^0 causes orange-red fluorescence in deep UV, a typical property of diamonds grown by chemical vapor deposition (CVD) without post-growth high-pressure, high-temperature (HPHT) treatment (P.M. Martineau et al.,

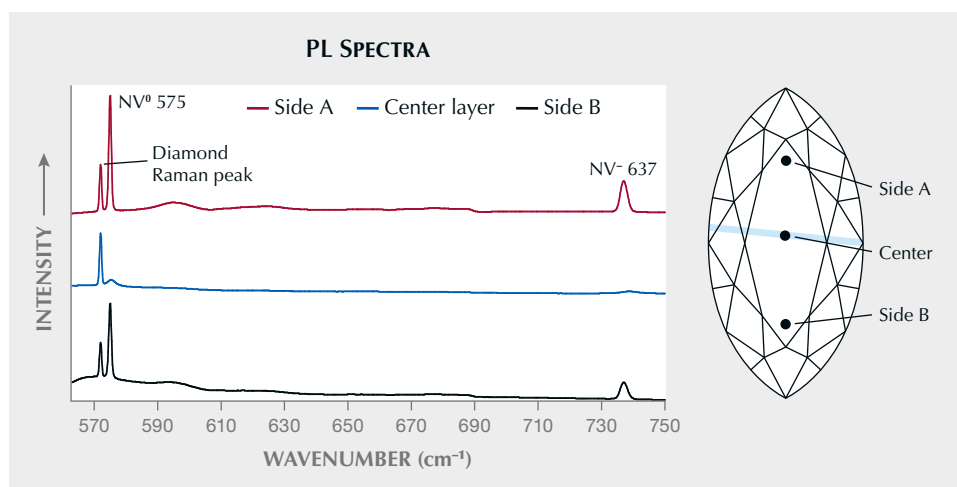


Figure 23. PL spectra of three areas within the laboratory-grown diamond. Sides A and B display a similar pattern with strong NV^0 and NV^- peaks at 575 and 637 nm, respectively. The center layer ($<50\ \mu\text{m}$) shows a different response, with much lower intensities. Spectra are offset vertically for clarity.

"Identification of synthetic diamond grown using chemical vapor deposition," Spring 2004 *G&G*, pp. 2–25). The green-blue fluorescence and long-term phosphorescence reaction to deep UV is associated with both HPHT-grown and CVD-grown diamonds, while the infrared spectrum and long-term phosphorescence under short-wave UV are associated with boron impurities. These features are typical properties of HPHT-grown diamonds (C.M. Welbourn et al., "De Beers natural versus synthetic diamond verification instruments," Fall 1996 *G&G*, pp. 156–169; K. Watanabe et al., "Phosphorescence in high-pressure synthetic diamond," *Diamond and Related Materials*, Vol. 6, No. 1, 1997, pp. 99–106), but can also point to the phosphorescence seen in boron-incorporated type IIb CVD-grown products and interfaces between CVD growth layers (S. Eaton-Magaña et al., "Observations on HPHT-grown synthetic diamonds: A review," Fall 2017 *G&G*, pp. 262–284; S. Eaton-Magaña, "Summary of CVD lab-grown diamonds seen at the GIA laboratory," Fall 2018 *G&G*, pp. 269–270; S. Eaton-Magaña et al., "Laboratory-grown diamonds: An update on identification and products evaluated at GIA," Summer 2024 *G&G*, pp. 146–167).

The strain shown in two patterns on each side of the stone was consistent with CVD growth (E. Fritsch et al., "Birefringence' in diamond: A useful tool to separate natural from synthetic diamond," *32nd International Gemmological Conference IGC*, Interlaken, Switzerland, July 13–17, 2011, pp. 71–72). However, the pattern difference indicates that each layer was created separately. In addition, the thin layer in the center showed a dark solid strain. This layer's dark appearance could be due to an elastic strain applied to the neighboring layers, possibly masking a thin, strain-free area commonly observed in HPHT-grown diamonds.

Infrared spectroscopy using the DRIFT technique confirmed a type IIb diamond structure, mostly typical of colorless to near-colorless HPHT-grown diamonds (Eaton-Magaña et al., 2017) or boron-incorporated type IIb CVD-grown diamond (Eaton-Magaña et al., 2024). Also, the nitrogen vacancies' peak changes between layers, observed using PL, could be the result of an HPHT process in the center thin layer or different growth conditions in the CVD feed gas during start-stop cycles (Eaton-Magaña, 2018). Considering the relatively high boron detected, contamination due to HPHT annealing seems unlikely. Hence, the center layer was either grown using an HPHT method or formed as a boron-rich CVD layer during a multi-stage growth.

These results highlight the stone's heterogeneous composition. The findings suggest a multilayered synthetic diamond, with either three distinctly different CVD growth layers or two CVD layers on both ends of the stone and a thin HPHT layer between them. This case highlights the challenges of discerning the intricacies of diamond synthesis. As more consumers request a specific growth method and gemological laboratories state the synthesis

method on their gemological reports, a quick analysis or a simple screening machine might give unclear results and not be sufficient to distinguish between mixed-growth diamonds and those grown using a single process.

Sean O'Neal and Guy Borenstein
Stuller Inc.
Lafayette, Louisiana

Diamond trader Ishaia Gol. It is always enlightening to encounter individuals who have left an indelible mark on the jewelry industry. Among these remarkable people is Ishaia Gol (figure 24), a multi-faceted diamond entrepreneur and owner of Ishaia Trading Corp. in New York.

In his early twenties, Gol arrived in New York in 1975 after five years of service in the Israeli army, including during the 1973 war. He had two goals: to attend New York University and start working with his older brother, David, who was in the gem and diamond business in Italy. David was the oldest of six brothers, and Gol was the youngest. To become a buyer in David's American office, Gol needed to become an expert in the trade, learn English, and earn a business degree as soon as possible.

Gol's merchant Jewish family originated in Afghanistan, where they bought furs and other goods in Russia and sold them locally. The family relocated to Israel shortly after it became a country in 1948. David began cutting diamonds in Israel, where this was a growing industry. But he became bored sitting at the cutting wheel for hours on end and started traveling to sell diamonds in 1956. He opened an office in Milan, and by 1960, he was buying sapphires, rubies, emeralds, and other colored stones from Mumbai. These were more profitable for him than diamonds, but they sold slowly. David then shifted his focus back to buying larger diamonds, frequently visiting New York to make purchases. With the opening of the New York office, David needed his brother to manage it.

At the start of his career, Gol's role was to purchase diamonds for distribution in Italy and throughout Europe. He balanced this responsibility with academic pursuits in New York, studying business at NYU and obtaining his Graduate Gemologist diploma in one of GIA's earliest New York classes. Throughout his studies, he took the F train daily from NYU to 47th Street, where he rapidly acquired the skills to saw, cut, and sort diamonds—all while learning English.

After obtaining his GG diploma, Gol would go to GIA's laboratory every morning to submit diamonds for grading and then ship them to his brother. GIA's "little office on 580 [Fifth Avenue]" was where he stood in line and chatted with other dealers. As demand grew, the laboratory expanded to two floors, with the second floor dedicated to diamonds under two carats and the tenth floor for larger stones. The lines on either floor were so long that submitting a diamond could take half a day. Dealers with diamonds in both size categories had to wait in two lines. Gol would arrive early and have his secretary hold his place

for hours. Some people even set up a business queueing for others. Gol recalled, "The corridors would be packed with hundreds. It was crazy!"

Gol quickly found himself immersed in New York's tight-knit gem community. Dealers and cutters would share coffee, jokes, and advice. As a newcomer, Gol sought their opinions on the stones he was considering. Once he established himself as a reputable gemologist, they soon asked for his advice. Gol's opinion was held in such high esteem that William Goldberg would consult him to resolve family disputes over stones. "We had an amazing friendship," Gol said of Goldberg. Lazar Wolf was another important influence: "He understood diamonds like no other person in the world," Gol noted.

As a dealer in New York in the late 1970s, Gol hired another gemologist. Since then, he has always had another staff gemologist, and as a team, they developed a formidable reputation. Dealers trusted Gol to check or even polish diamonds for them. One important assignment involved cleaning up the famous but badly bruised 41.37 ct Ashoka diamond. Gol also helped sell other important diamonds, including the 76.02 ct Archduke Joseph, with perfect D color and Internally Flawless clarity, which originated from the ancient Golconda mines of India. Gol's team attended major auctions, where they would study the offered diamonds for hours. Many of them did not carry a grading report. The team would buy some of these large diamonds, have them graded, and sell them for a good profit.

Gol's first recommendation for any aspiring gemologist who wants to work with big diamonds: "Dive headfirst into the world of auctions and gain confidence there. Don't be shy—attend them all, from quaint little affairs to bustling sales in Paris and beyond. Be willing to travel to the farthest corners of the globe to lay eyes on a single extraordinary stone." He also notes, "To truly understand a gemstone, it must be viewed under consistent conditions. Always carry the same portable light source, ensuring each diamond is seen in the same familiar glow. Examining all stones against a white, nonfluorescent plastic backdrop will help better compare their unique characteristics." Gol swears by his trusty tweezers, which he uses with 10× and



Figure 24. Diamond entrepreneur Ishaia Gol, interviewed in June 2024. Photo by Pedro Padua.

14× loupes, and a set of master stones he has used for color comparison for more than four decades.

Ishaia Gol's final piece of advice is to never stop learning. He urges aspiring gemologists to soak up as much education as possible: "Take every class you can get your hands on—it is the key to unlocking a successful career in this field."

This June 2024 interview with Ishaia Gol was captured on video as part of GIA's Oral History Project to be used by future historians. To see more, go to www.gia.edu/gems-gemology/summer-2025-gemnews-ishaia-gol.

Al Gilbertson
GIA, Carlsbad

TREATMENTS

Diffusion-induced blue spinel-like layer on natural sapphire. Recently, the GGTL laboratory in Geneva received three gems for identification weighing 1.43, 1.55, and 2.65 ct and exhibiting a blue coloration fairly typical of cobalt-bearing gems such as spinel (figure 25, left). Microscopic observation revealed the presence of inclusions, some

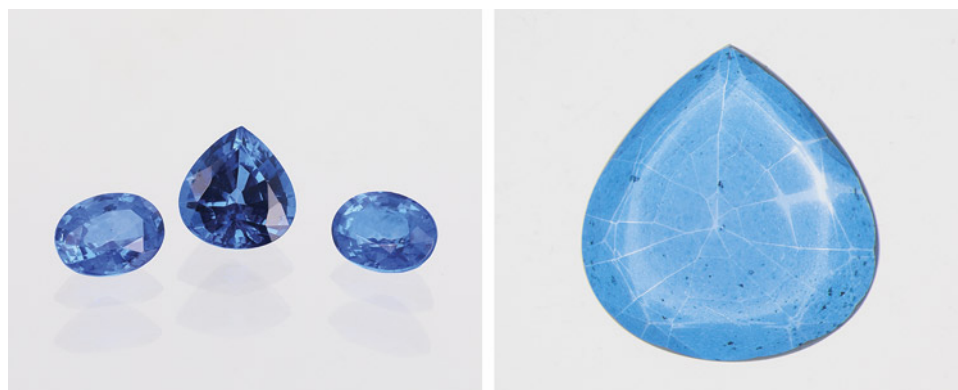


Figure 25. Left: Sapphires, weighing 1.43, 1.55, and 2.65 ct, diffused with cobalt and zinc, which formed a surface layer of blue spinel. Right: The 2.65 ct sample in immersion with brightfield illumination showing the typical spiderweb effect of diffused stones. Photos by Féodor Blumentritt.

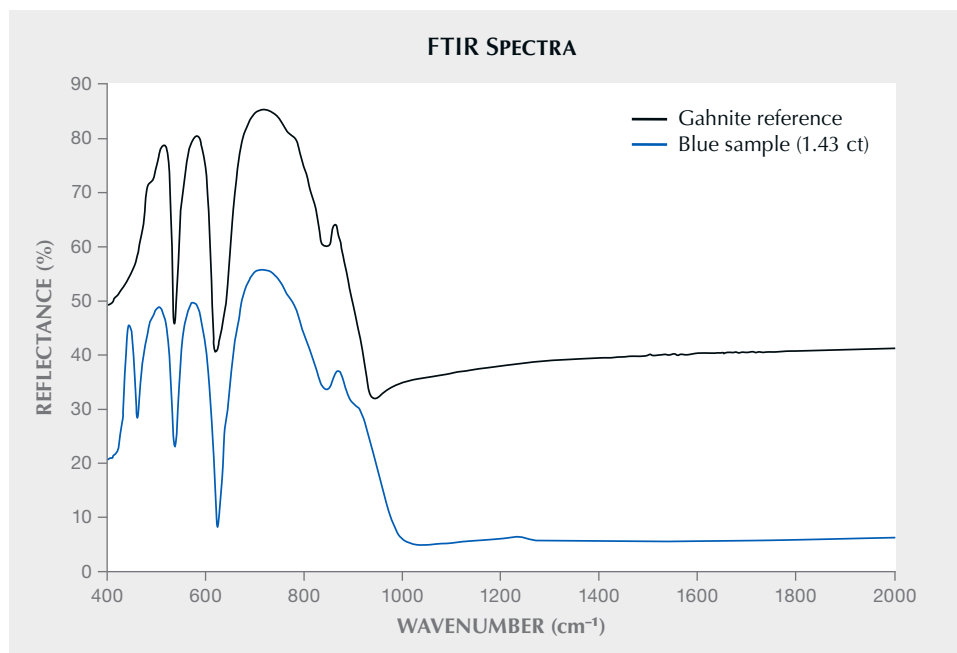


Figure 26. Infrared spectra in specular reflectance mode of a natural gahnite reference sample from Madagascar and the 1.43 ct blue sapphire sample. Spectra are offset vertically for clarity.

altered, such as rutile needles, mineral inclusions surrounded by discoidal fractures, and Rose channels. However, the surface condition and color zonation indicated the presence of diffusion. Some facets that were visibly unpolished following treatment displayed a granular appearance. In immersion fluid, it was observed that some of the edges and facets underwent repolishing, result-

ing in colorless surfaces (figure 25, right). On one of the stones, the color zonation was clearly visible on the surface of the facets and appeared as a cloudy pattern.

The identification of these stones by means of specular reflectance infrared spectroscopy demonstrated a clear correlation with gahnite (ZnAl_2O_4 ; figure 26). However, analysis of the stones' luminescence under long-wave

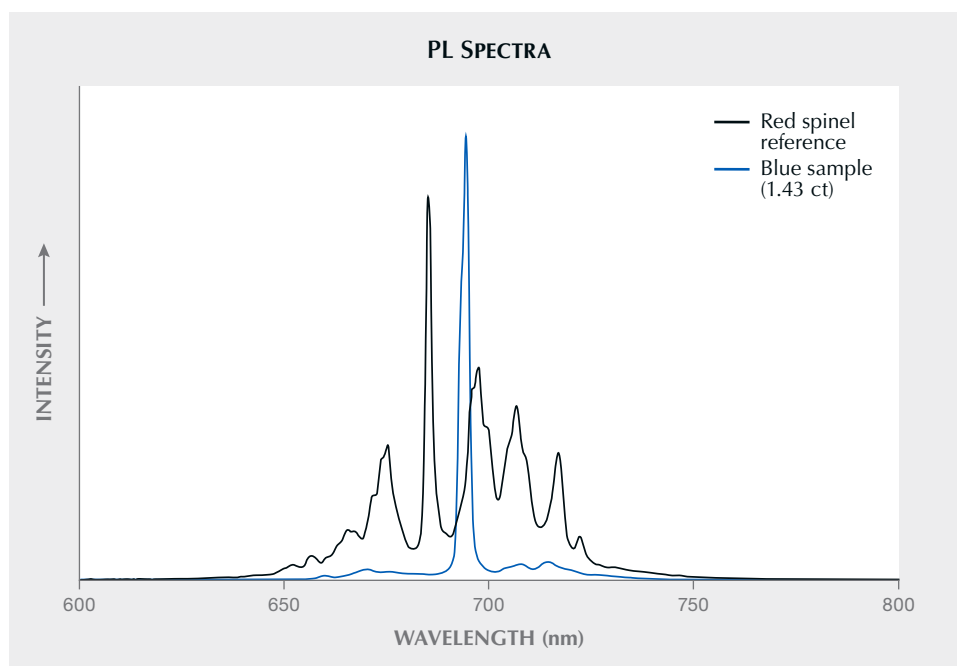


Figure 27. Typical luminescence spectrum of a red spinel reference sample compared with the luminescence spectrum of the 1.43 ct blue sapphire sample that matched the usual luminescence of Cr^{3+} in corundum. Note that the resolution of the spectrometer was not high enough to distinguish the two R1 and R2 transitions at about 694 nm.

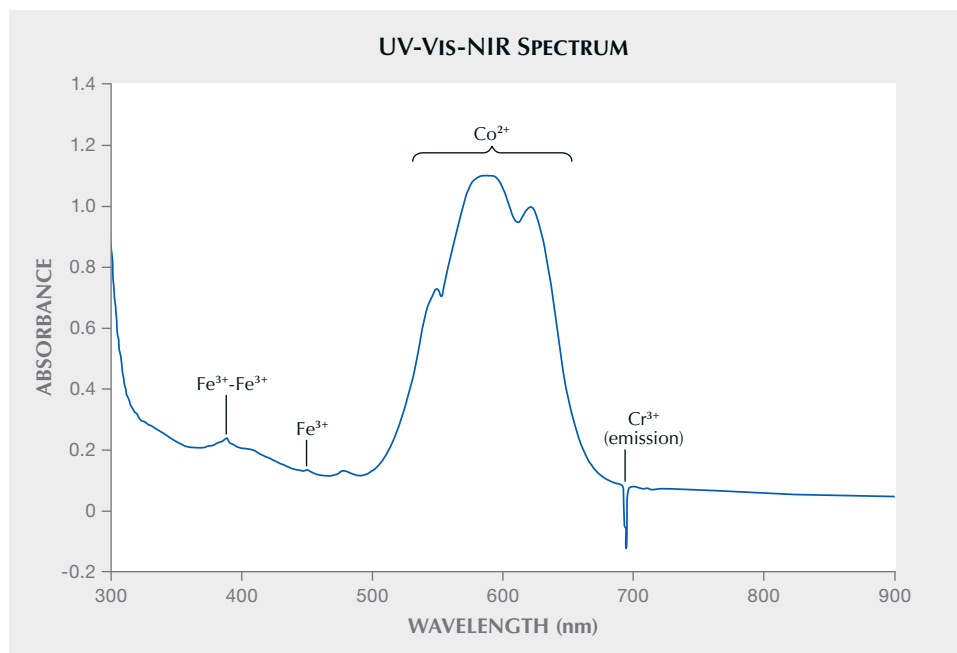


Figure 28. Absorption spectrum of the 1.43 ct sample showing characteristic features of Co^{2+} usually measured in spinel, superimposed to usual iron absorption features of sapphire.

ultraviolet (365 nm) light revealed a Cr^{3+} luminescence spectrum, characteristic of an octahedral environment in corundum (T. Kushida and Y. Tanaka, "Direct optical excitation into excited states of Cr^{3+} pairs in ruby," *Solid State Communications*, Vol. 11, No. 10, 1972, pp. 1341–1344), rather than in spinel structure (figure 27; see e.g., I. Malíčková et al., "Optical and luminescence spectroscopy of varicolored gem spinel from Mogok, Myanmar and Lục Yên, Vietnam," *Minerals*, Vol. 11, No. 2, 2021, article no. 169). This luminescence was homogeneous across the stones, and it was confirmed that it did not emanate solely from the surface by illuminating the colorless zonation of the stones. The results of an energy-dispersive X-ray fluorescence semi-quantitative chemical analysis provided evidence to support the inconsistency between the infrared spectrum and luminescence, with a majority proportion of aluminum (~89.9 wt.% of Al_2O_3) and, to a lesser extent, zinc (~6.5 wt.% of ZnO). The proportions of the two elements do not correspond to a spinel structural formula. Instead, they were consistent with the hypothesis of the coexistence of spinel and corundum structures.

Moreover, the detection of large quantities of cobalt (~3.4 wt.% of Co_3O_4) was consistent with the ultraviolet/visible/near-infrared (UV-Vis-NIR) absorption spectrum, supporting cobalt as the main cause of color (figure 28; D.K. Sardar et al., "Spectroscopic properties of Co^{2+} in related spinels," *Journal of Applied Physics*, Vol. 91, No. 8, 2002, pp. 4846–4852). A previous publication already documented "cobalt-diffused sapphires" (R.E. Kane et al., "The identification of blue diffusion-treated sapphires," Summer 1990 *G&G*, pp. 115–133), but the presence of Co^{2+} in a corundum structure remained unclear despite a parallel

made with the color of cobalt-blue synthetic spinel. One later article (Summer 2002 Gem Trade Lab Notes, p. 167) discussed a possible interaction of cobalt with the corundum surface without being more specific.

The aforementioned analyses led to the identification of these stones as natural sapphire partly owing to the typical Cr^{3+} luminescence. These sapphires likely underwent an attempt at diffusion of zinc and cobalt, resulting in the crystallization of a layer of blue spinel structure (gahnite) on the surface, which was identified by reflectance infrared spectroscopy. This treatment serves to demonstrate the considerable inventiveness required to induce a cobalt-bearing spinel color in corundum.

Féodor Blumentritt, Guillaume Zuber, Candice Caplan,
and Franck Notari
GGTL Laboratories, Switzerland

For online access to all issues of
Gems & Gemology from 1934 to the
present, visit: gia.edu/gems-gemology



Ben Kho: From Rough Beginnings to Brilliant Mastery

Jennifer Stone-Sundberg | GIA, Carlsbad

During the 2025 Tucson AGTA GemFair, a 12.88 ct Portuguese cushion-cut rhodochrosite from Colorado won the 2024 Cutting Edge Buyer's Choice Award. This vibrant red gem is a testament to both the cutter's skill and perseverance (figure 1). Rhodochrosite is notoriously difficult to cut because it is a soft material with perfect cleavage in three directions, heat sensitive, and rarely facet grade. Why cut such a difficult stone for a competition? The story of gem cutter Ben Kho (Ben Kho Gems, Decatur, Georgia), a man who has persevered throughout his life in the face of adversity, may help explain this choice.

Kho's extraordinary story began in the 1960s. Growing up in Battambang, Cambodia, Kho demonstrated an entrepreneurial spirit at a young age. At 11 years old, he set up a stand and rented comic books and magazines to people waiting at theaters and outdoor markets. At 12, he took trains to the Cambodia-Thailand border to buy Thai goods to wholesale in Cambodia. At 14, he lived with a Burmese family in Pailin, where he packaged and transported heavy loads of rambutan fruit back to Battambang for his parents to wholesale to vendors.

In Pailin, Kho heard tales of large ruby and sapphire rough found in nearby mines and dreamed of mining them himself, with hopes of making a big discovery. When the rambutan harvest season was over, he and a friend bought a 6 × 3 m parcel of land. They

would dig down about 2 meters and carry the dirt to the river for sifting using a shoulder pole and two rice bags. This difficult work was much harder when water entered their plot, making the dirt even heavier to dig out and carry. The process of sifting through the transported dirt at the river's edge was extremely labor-intensive, as the few dense corundum pieces were inevitably at the bottoms of their baskets. After a year, they had found only very small crystals, worth less than what they had paid for the land.

Realizing that his mining efforts were not yielding significant discoveries, Kho decided to pursue gem cutting. The family he was staying with had a friend who ran a small lapidary operation behind his house with six employees. At 15, Kho spent three months as an apprentice and learned to facet gems by hand. After becoming proficient, he was paid by the carat. He aspired to be a gem cutter as well as a wholesaler of the cut gems. After a year, he had made enough money to start purchasing rough from the miners. He invested in a moped and drove to the mines near the end of each workday to buy the rough found that day. During this time, he honed his skills of rough selection and orientation to maximize face-up color. He would then preform the rough to properly position the color at the bottoms of the stones.

Knowing how to cut gems meant that Kho knew the desirable qualities of rough and its value. He became a confident buyer of



Figure 1. Ben Kho (second from left) fashioned this 12.88 ct Portuguese cushion-cut rhodochrosite from Colorado's Sweet Home mine (right) to win both the 2024 AGTA Cutting Edge Buyer's Choice Award and second place in the North American Gemstones category. Photo by Jeff Mason Photography (right); courtesy of Ben Kho.



Figure 2. Ben and Molly Kho in Cambodia in the early 1970s. Courtesy of Ben Kho.

stones and a keen negotiator. He would cut and polish groups of 10–20 gems and visit the opulent homes of the gem wholesaler “big bosses” to see how much riel (the Cambodian currency) they would offer for his collection. His stones then went to Bangkok’s gem market for purchase by international buyers.

Kho spent four years building his business, until the devastation of the Khmer Rouge regime takeover displaced him and his wife, Molly, (figure 2) and their families and friends to the jungle in 1975, during the mass genocide of Cambodians known as “the Killing Fields.”

Kho and his family and friends were forced to work in the rice fields under the supervision of armed Communists. The goal was to survive without being noticed. Each worker was allowed only a small bowl of rice a day. The drinking water was dirty, and many people became sick or starved to death. There was no medicine. People caught and ate frogs, snakes, and insects in the fields to get enough protein to stay alive. For Kho, the worst feeling of all was trying to go to sleep while extraordinarily hungry. For shelter, they built huts, and for sleeping, they made hammocks from rice bags and sticks.

Kho recalled gazing up at the moon after an exhausting day of hard labor. *Somewhere in the world, someone living in freedom is looking up at this same moon*, he thought. This gave him some small hope that he would survive this nightmare and one day provide a better life for his family.

In 1979, Kho and his family heard bombing. Instead of fear, they felt hope that finally this oppressive regime would be defeated, and their torture would be over. Indeed, Vietnam had invaded and taken over Cambodia. He and his family went back to Battambang, but they were not allowed to return to their home and were once again forced to build their shelter, a hut of leaves and sticks. Many Cambodians escaped to Thailand during this time, and Kho and his parents, wife, baby girl, six brothers, and two sisters decided to do the same. They walked for three days and nights to the border and encountered many dangers, including land mines and aggressive thieves.

At the border, the Thai government blocked them and thousands of other refugees. Soldiers rounded them up, drove them a couple of hours away, and left them in the jungle. There was no food or shelter, and again they had to build their own huts, forage for food, drink dirty water, and fend off mosquitoes carrying malaria.

After several months, the United Nations offered to take refugees to countries such as Australia, Germany, and the United States. Kho’s family was taken to a refugee camp, where they were each given a can of rice per day. They chose to relocate to the United States without speaking any English. Kho was willing to work any job as long as he and his family could get three meals a day. On October 2, 1979, sponsored by the Covenant Presbyterian Church, they left Thailand for Atlanta, Georgia. Kho’s family lived in a house on the church property for a couple of years.

Based on Kho’s background as a gem cutter, he was introduced to Tim Roark of Tim Roark Imports, who needed a cutter for his wholesale gemstone business. Roark introduced Kho to another cutter, Mark Songer, who spent a month training Kho to use a Facatron. In December 1979, Kho went to work for Roark. Between Roark’s business and the government, he made US\$3 per hour. Over the next six years, he worked for Roark for 14–16 hours a day, helping him build the business. During this time, he learned how to cut a large variety of gem materials and honed his craft. His passion was growing, and he appreciated the great beauty of the gems he was creating. In 1987, he wanted to start his own business and gave three months’ notice, with a promise to train anyone before leaving.

Kho launched his business in the basement of the home he had purchased with his brother. His reputation as an exceptional cutter had begun to spread, and dealers started asking him to cut their stones. Soon he was cutting for many large companies as well. By 1990, Kho was buying rough and going to several gem shows, with vendors from different countries—Nigeria, Brazil, Sri Lanka, and Thailand. He had a keen eye for quality material. He purchased large parcels so he could cut the stones and sell them



Figure 3. Converting a parcel of rhodochrosite rough into finished gems, from inspecting and grinding the rough (left) to the preformed and dopped rough (right). Courtesy of Ben Kho.

wholesale to big companies. Kho also learned how to make jewelry and set stones, eventually selling both jewelry and gemstones on consignment to Atlanta's many jewelry stores.

In 1990, Kho started selling gems at the Holidome show in Tucson, Arizona. Around that time, he met award-winning gem cutter and dealer Bill Day, who introduced him to the AGTA Spectrum and Cutting Edge Award competitions. After receiving his first award for an 8.68 ct fantasy cushion-cut sphalerite in 1995, he applied for AGTA membership and in 1996 obtained a small booth at the show. Today, the business is still family-owned and operated. Kho and Molly run the gem shows with their daughter, Angela, who designs jewelry; their son, Andrew, who manages the website and social media; and other family members, who run the Decatur office.

Kho's prowess as one of the world's best cutters of difficult stones has given him unique access to rare material. He began cutting rhodochrosite in 1992, after being introduced to the owner of Colorado's Sweet Home mine. He loved the challenge of cutting such a difficult material and has been dubbed the "Rhodochrosite King." In 2005, he was sought out by the owner of the benitoite mine in California to cut a newly discovered large benitoite rough. The result was a magnificent 8.05 ct oval, the third-largest faceted benitoite in the world.

Kho described his process for cutting a stone for a competition: he takes several days to study the rough for inspiration for a cutting design, designs the cut, and then practices on a lower-quality piece of rough (figure 3).

Since 1995, Kho has won more than 30 AGTA Cutting Edge Awards (figure 4). Kho achieved a clean sweep in the 2022 AGTA Cutting Edge All Other Cut Gemstones category—an honor recognizing exceptional lapidary artistry and mastery featuring

traditional gemstone cutting techniques. In Tucson this year, his three winning entries from the 2024 competition were on display: the rhodochrosite, which won both the Buyer's Choice Award and second place in the North American Mined Gemstones cat-

Figure 4. Ben and Molly Kho at the 2024 AGTA Spectrum Awards Gala held in Tucson, Arizona. Courtesy of Ben Kho.



egory; a 109.92 ct trilliant-cut bright bluish green fluorite from New Hampshire, the third-place winner in the same category; and a 50.52 ct custom cushion-cut seafoam green beryl, an honorable mention in the All Other Cut Gemstones category (see photo gallery).

Ben Kho, an unassuming man with a kindly smile, has all the ingredients for success: great talent, a strong work ethic, an entrepreneurial spirit, and the ability to overcome seemingly insurmountable challenges. He is deeply grateful to live in the U.S.

and for the opportunities it has brought him. With the freedom to pursue his passion, he has built a thriving business and created a brighter future for his family.

At the AGTA shows, one can find exquisite examples of his masterfully cut fine gems, both loose and set in jewelry. His booth is filled with a constant flow of repeat customers and old friends coming by to say hello and make their annual purchases, and newcomers attracted by the array of color fortunate enough to meet this one-of-a-kind gem cutter.

Photo Gallery

The photo gallery shows images of various AGTA Cutting Edge Award–winning gemstones cut by Ben Kho. The photos are by Jeff Mason Photography and the stones are courtesy of Ben Kho Gems.



109.92 ct trilliant-cut ocean fluorite from New Hampshire, 2024 North American Mined Gemstones, third place.



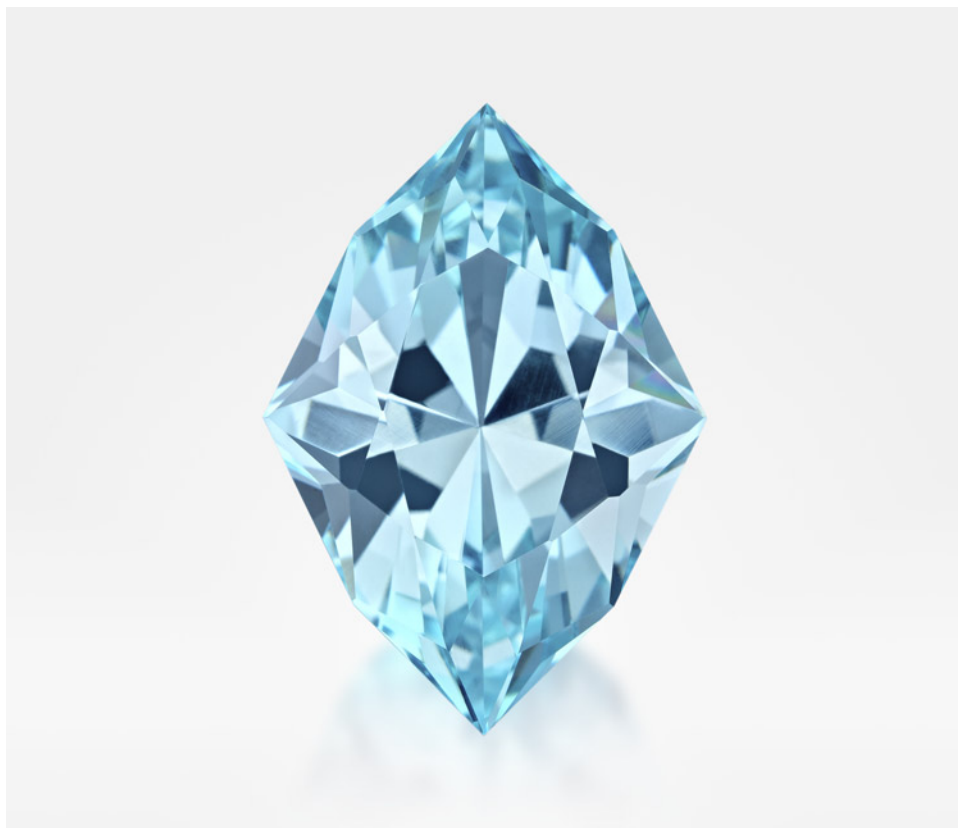
50.52 ct custom cushion-cut seafoam green beryl, 2024 All Other Cut Gemstones, honorable mention.



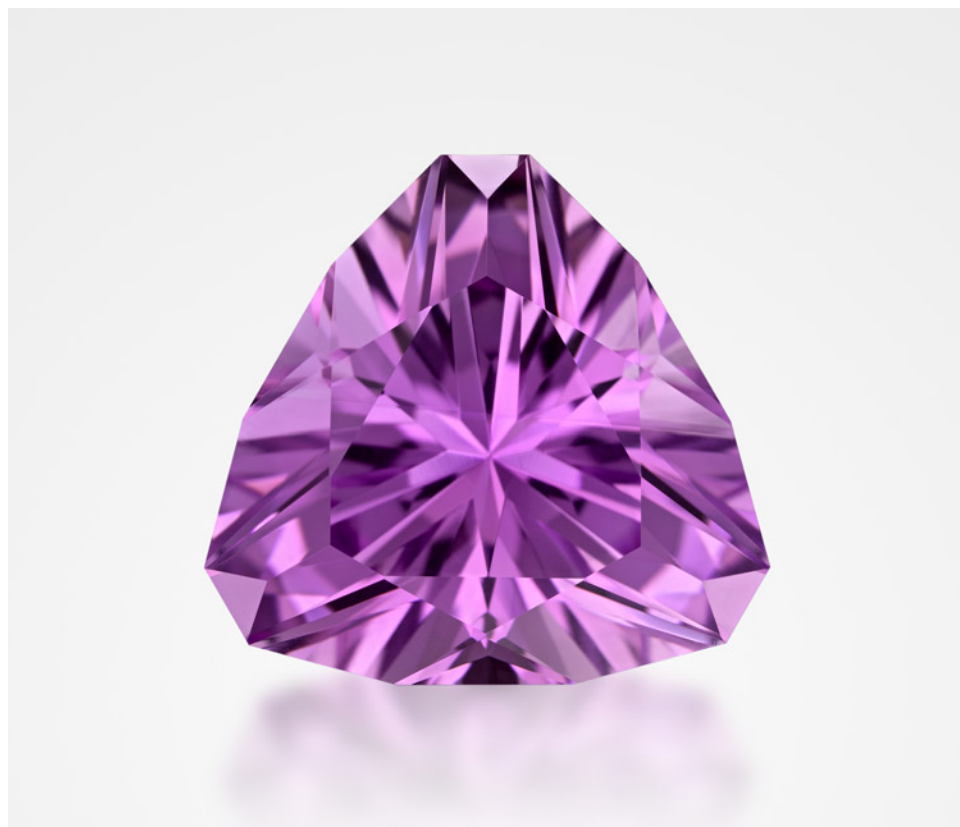
11.46 ct antique cushion-cut rhodochrosite from Colorado, 2022 North American Mined Gemstones, first place.



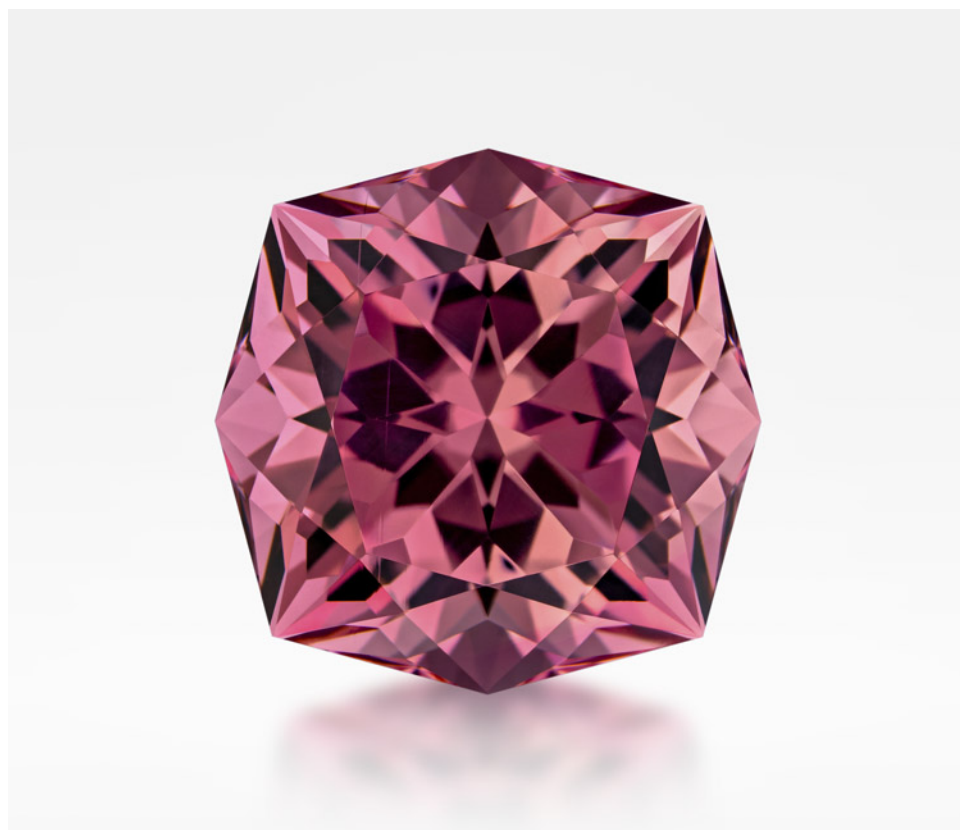
*32.50 ct sunburst-cut kunzite,
2022 All Other Cut Gemstones,
first place.*



*14.70 ct diamond-shaped apatite,
2022 All Other Cut Gemstones,
second place.*



*34.98 ct fancy trillion-cut kunzite,
2022 All Other Cut Gemstones,
third place.*



*28.61 ct pink tourmaline, 2022
All Other Cut Gemstones,
honorable mention.*